

# **Deformation behavior of Nb, Nb-1Zr and Nb-1Zr-0.1C**

*By*

**Shri Ananta Narayan Behera**

PHYS01201204011

**Bhabha Atomic Research Centre, Mumbai**

*A thesis submitted to the  
Board of Studies in Physical Sciences*

*In partial fulfillment of requirements  
for the Degree of*

**DOCTOR OF PHILOSOPHY**

*of*

**HOMI BHABHA NATIONAL INSTITUTE**



**November, 2018**



# Homi Bhabha National Institute<sup>1</sup>

## Recommendations of the Viva Voce Committee

As members of the Viva Voce Committee, we certify that we have read the dissertation prepared by Shri Ananta Narayan Behera entitled “Deformation behavior of Nb, Nb-1Zr and Nb-1Zr-0.1C ” and recommend that it may be accepted as fulfilling the thesis requirement for the award of Degree of Doctor of Philosophy.

---

Chairman - Dr. D. Srivastava

**Date:**

---

Guide / Dr. R. Kapoor

**Date:**

---

Examiner - Dr. M. J. N. V. Prasad

**Date:**

---

Member - Dr. M. K. Samal

**Date:**

---

Member - Dr. S. Ghorui

**Date:**

---

Final approval and acceptance of this thesis is contingent upon the candidate's submission of the final copies of the thesis to HBNI.

I hereby certify that I have read this thesis prepared under my direction and recommend that it may be accepted as fulfilling the thesis requirement.

**Date:**

**Place:**

**Dr. R. Kapoor**  
**Guide**

---

<sup>1</sup> This page is to be included only for final submission after successful completion of viva voce.



## **STATEMENT BY AUTHOR**

This dissertation has been submitted in partial fulfillment of requirements for an advanced degree at Homi Bhabha National Institute (HBNI) and is deposited in the Library to be made available to borrowers under rules of the HBNI.

Brief quotations from this dissertation are allowable without special permission, provided that accurate acknowledgement of source is made. Requests for permission for extended quotation from or reproduction of this manuscript in whole or in part may be granted by the Competent Authority of HBNI when in his or her judgment the proposed use of the material is in the interests of scholarship. In all other instances, however, permission must be obtained from the author.

Ananta Narayan Behera



# **DECLARATION**

I, hereby declare that the investigation presented in the thesis has been carried out by me. The work is original and has not been submitted earlier as a whole or in part for a degree / diploma at this or any other Institution / University.

Ananta Narayan Behera



# List of Publications arising from the thesis

## Journals

1. Hot deformation behaviour of niobium in temperature range 700 - 1500 °C, **A. N. Behera**, R. Kapoor, A. Sarkar, J. K. Chakravartty, *Materials Science and Technology*, 30(6) (2014) 637 - 644.
2. High temperature deformation behavior of Nb - 1wt.% Zr alloy, **A. N. Behera** , A. Chaudhuri , R. Kapoor, J. K. Chakravartty, S. Suwas, *Materials and Design* 92 (2016) 750 - 759.
3. Effect of strain on evolution of dynamic recrystallization in Nb - 1wt% Zr - 0.1wt% C alloy at 1500 and 1600 °C , **A. N. Behera**, R. Kapoor , B. Paul, J.K. Chakravartty, *Materials Characterization* 126 (2017) 135 - 143.

## Conferences

- i. Hot deformation of Niobium and its alloys; **A. N. Behera**, R. Kapoor, J. K. Chakravartty, V. Kumar, Poster Presentation at IIT - BHU, *NMD - ATM, IIM*, Nov 12 - 15, 2013.
- ii. Accelerated creep studies of Nb alloys ; R. Kapoor, A.N. Behera, J.K. Chakravartty, A Patel, Oral Presentation at IIT Madras, *National Conference on Thermo-mechanical Simulation using Gleeble Systems, GUWI 2014*, July 10 - 12, 2014.
- iii. Hot deformation and dynamic recrystallization behavior of Niobium and its alloys; A. N. Behera, R. Kapoor, A. Sarkar, J. K. Chakravartty, V. Kumar, Oral presentation at *National Conference on 'Thermo-mechanical Processing of Steels' & 5th Gleeble Users' Workshop India 2015 (GUW -2015)* , CSIR-NML Jamshedpur, Aug 6-7, 2015.
- iv. High temperature deformation behavior of Nb-1Zr and Nb-1Zr-0.1C alloy, R. Kapoor, A. N. Behera, A. Sarkar, J. K. Chakravartty, *BARC Newsletter*, July - August 2015, pp. 8 - 11.
- v. Kinetics of dynamic recrystallization behavior of Nb-1Zr and Nb-1Zr-0.1C alloys ; **A. N. Behera**, R. Kapoor, A. Sarkar, *Oral presentation at National Conference on Physical Simulation of Thermal-Mechanical Processing of Materials & 6th Gleeble Users' Workshop India 2017 (GUWI-2017)* , IIT Bombay, July 15-17, 2017

Ananta Narayan Behera



*Dedicated  
to  
my Parents*



## **ACKNOWLEDGEMENTS**

I would like to express my deepest sense of gratitude to my guide and mentor, Dr. Rajeev Kapoor, Head, DSS, MMD, BARC for his supervision, constructive criticisms and constant encouragement. His clear directions and suggestions, active involvement in the experiments and analysis helped me throughout the work. I am indebted to him for all the excellent ideas, approach and prescriptions.

I am also indebted to our Ex- Group Director Dr. J. K. Chakravartty, who has guided me in each step of my work without which I could have not completed the work. I also take this opportunity to express my sincere regards to Dr. A. K. Bhaduri, Director IGCAR for sharing his technical expertise during the annual progress reviews meeting.

I would take this opportunity to thank the respected members of my doctoral committee Dr. D. Srivastava (Chairman, CEO, NFC Hyderabad), Dr. M. K. Samal (Member, SO / G, RED, BARC), Prof. M. J. N. V. Prasad (Member, Associate Professor, IIT Bombay) and Dr. Srikumar Ghorui (Member, SO / G, L & PTD BARC) for their critical reviews and valuable suggestions during the annual progress reviews and pre-synopsis presentation.

I sincerely thank Dr. R N Singh (Head, MMS, MMD, BARC) and Dr. J. B. Singh (Head, SMS, MMD, BARC) for sharing their scientific expertise. It gives me a great pleasure to acknowledge my colleague Dr. Apu Sarkar, Dr. Amit Verma, Dr. Arpan Das, Shabana Khan, Shri Sourav Sunil and Shri Bhupender Kumawat for their continuous support and motivation.



I would like to take opportunity to thank my collaborators Dr. Satyam Suwas (Professor, IISc Bangalore) and Dr. Atanu Chaudhuri (Scholar, IISc Bangalore) who have provided their technical support and exchanged their scientific expertise during experiments and analysis. It gives me a great pleasure to acknowledge Dr. Vinod Kumar (RDCIS, SAIL Ranchi) and Shri Alpesh Patel (Scientist, IPR Ahmadabad) for their co-operation during the high temperature experiments in Gleeble.

It is difficult to name all those who have helped in providing logistic, scientific and administrative support during various stages of executing the work reported in this thesis. I apologize for any omission.

I am thankful to all my friends, family members and relatives for their encouragement and support. Most importantly, I owe a lot to my parents, who encouraged and helped me at every stage of my life.

November, 2018

Ananta Narayan Behera



# Contents

	Page No.
<b>Synopsis</b> .....	xxi
<b>List of figures</b> .....	xxxviii
<b>List of tables</b> .....	xlviii
<b>List of abbreviations</b> .....	xlix
<b>List of symbols</b> .....	1
<b>Chapter 1. Introduction</b> .....	1
1.1 Structure of thesis.....	6
<b>Chapter 2. Background</b> .....	7
2.1 General deformation behaviour of metallic materials .....	7
2.1.1 Deformation by slip.....	7
2.1.2 Deformation twinning .....	8
2.1.3 Thermally activated deformation .....	9
2.2 Deformation of body centred cubic materials .....	14
2.3 Mechanical behaviour of Nb and its alloys .....	15
2.4 Microstructure of Nb and its alloys .....	20
2.5 Processing by hot deformation .....	23
2.5.1 Ashby map.....	23
2.5.2 Strain rate sensitivity map .....	24
2.6 High temperature deformation mechanisms.....	25
2.6.1 Dynamic recovery .....	25
2.6.2 Dynamic recrystallization.....	26
2.7 Gap areas .....	40
2.8 Objectives.....	40
<b>Chapter 3. Experimental methods</b> .....	43
3.1 Materials.....	43
3.2 Hot deformation .....	43

3.3	Quasistatic deformation from room temperature to 700 °C.....	45
3.3.1	Strain rate change test and stress relaxation test.....	45
3.4	Dynamic deformation from room temperature to 400 °C.....	51
3.4.1	Procedure for carrying out test in SHPB .....	51
3.4.2	Split Hopkinson Pressure Bar technique .....	52
3.5	Microstructural characterization.....	54
<b>Chapter 4.</b>	<b>Results and Discussion .....</b>	<b>55</b>
4.1	Hot deformation behavior.....	55
4.1.1	Flow stress behaviour of Nb.....	55
4.1.2	Stress- strain behaviour of Nb-1Zr .....	57
4.1.3	Stress- strain behaviour of Nb-1Zr-0.1C .....	58
4.1.4	Strain rate sensitivity .....	61
4.1.5	Strain Rate Sensitivity Map generation .....	63
4.1.6	Kinetic analysis.....	65
4.1.7	Microstructure and texture evolution.....	71
4.1.8	Microstructural characterization of Nb-1Zr-0.1C.....	82
4.1.9	Effect of strain on evolution of microstructure of Nb-1Zr-0.1C .....	86
4.2	Kinetics study of dynamic recrystallization behaviour of Nb alloy .....	101
4.2.1	Flow curve analysis to study the DRX characteristic .....	101
4.2.2	Reconstruction of DRV Curve .....	102
4.2.3	Evaluation of volume fraction of DRX grains.....	105
4.2.4	Application of Avrami kinetics to DRX.....	105
4.3	Deformation behavior of Nb-1Zr and Nb-1Zr-0.1C from room temperature to 700 °C.....	108
4.3.1	Strain rate change test.....	109
4.3.2	Stress relaxation test / multiple stress relaxation test .....	112
4.4	High strain rate deformation.....	117
4.5	Comparative study of Nb, Nb-1Zr and Nb-1Zr-0.1C alloy .....	120
4.5.1	Effect of alloy addition.....	120

4.5.2	Strain rate sensitivity and flow stress variation with temperature .....	125
<b>Chapter 5.</b>	<b>Summary and Conclusion .....</b>	<b>130</b>
5.1	Flow stress behavior.....	130
5.2	Optimum of hot processing conditions .....	130
5.3	Deformation Microstructure.....	131
5.4	Deformation mechanisms and comparison of deformation parameters .....	132
<b>References.....</b>	<b>.....</b>	<b>134</b>



# **SYNOPSIS**

## **1. Motivation**

Niobium and its alloys offer attractive high temperature properties, most of which are suitable for applications in nuclear environments including high temperature strength, good thermal conductivity, lower density as compared with other refractory metals and alloys and compatibility with most liquid metal coolants. Due to these superior properties the commercially produced Nb alloys, Nb-1wt.% Zr (Nb-1Zr) and Nb-1wt.% Zr-0.1wt.% C (Nb-1Zr-0.1C) have been used in space power systems [1-3]. Apart from these the other applications of Nb and its alloys are in superconducting wires [4], in aircraft gas turbine and vacuum tubes [5], biological applications [6] and in mint metal [7]. Zr addition to Nb acts as a solid solution strengthener whereas addition of 0.1wt.% of carbon provides dispersion strengthening to Nb matrix due to Nb and Zr carbides [8]. Nb-1Zr alloy has been closely associated with the nuclear industry because of its excellent elevated temperature strength in the range of 900 to 1200 °C [9-11]. Nb-Zr alloys are being actively considered for use in high temperature applications in compact high temperature reactor (CHTR) [12].

For last few decades many researchers have studied the mechanical and thermal creep properties of Nb-1wt.% Zr-0.1wt.% C (Nb-1Zr-0.1C) alloy. Titran et al. and Davidson et al. investigated the creep behavior and thermo-mechanical processing of Nb alloys [13-18]. McGreevy et al. studied the mechanical behavior of unirradiated and irradiated Nb-1Zr alloy [19]. Neigh et al. studied the effect of texture on the mechanical properties of Nb-1Zr alloy at 1100 °C [20]. Farkas et al. studied the creep properties of Nb-1Zr-0.1C alloy [21, 22]. Sarkar et al. reported the deformation behaviour of Nb-1Zr-0.1C alloy from 800 to 1700 °C [23]. Most of the above mentioned works are in the lower strain rates and do not cover temperatures higher than 1200 °C. To the authors knowledge apart from these there are no comprehensive studies on the mechanical behavior of Nb alloys at temperatures greater than 1200 °C. Studies at temperatures above 1200 °C are important as this is the range where restoration mechanisms such as dynamic recrystallization are expected. An understanding of the microstructure property correlation helps in the identification of the preferred domain of hot working.

## 2. Objectives

The main objectives of this dissertation are:

- i. To study the deformation behaviour of Niobium, Nb-1Zr and Nb-1Zr-0.1C alloy over a wide temperature range (25 to 1700 °C) and strain rate range ( $10^{-3}$  -  $10$  s $^{-1}$  and 1000 s $^{-1}$ ).
- ii. Optimization of hot working conditions.
- iii. Identifications of deformation mechanisms.
- iv. Structure properties correlation with deformation mechanisms.
- v. Influence of strain on the evolution of dynamic recrystallization in Nb alloys.
- vi. Kinetics studies of dynamic recrystallization of Nb-1Zr and Nb-1Zr-0.1C alloy

## 3. Experimental

Annealed Nb, Nb-1Zr and Nb-1Zr-0.1C alloy were used for this study. Uniaxial compression tests were conducted in a thermo-mechanical simulator (deformation dilatometer, Gleeble 3800 and Zwick screw driven machine) on solid cylindrical samples at room temperature to 1700 °C in steps of 100 °C, and at strain rates from  $10^{-3}$  to  $10$  s $^{-1}$  and at strain rate  $> 1000$  s $^{-1}$ . All high temperature tests were done in vacuum of  $10^{-3}$  mbar. The sample surface temperature was controlled with an accuracy of  $\pm 1$  °C. In Gleeble tests the samples were placed between WC platens with Ta foil and graphite between sample and platen to reduce friction. The samples were heated to the desired test temperature, held for 5 minutes, deformed to a true strain of 0.6 and quenched with argon gas to retain the microstructure prevailing during hot deformation. For high strain rates of 1 and  $10$  s $^{-1}$  the deformation conditions were adiabatic and the temperature rise ( $\Delta T$ ) during the hot deformation was calculated as

$$\Delta T = \left(1/\rho C_p\right) \int_0^{\epsilon} \sigma d\epsilon, \text{ where } \rho \text{ is the mass density and } C_p \text{ is the specific heat capacity [24].}$$

The flow stress at the starting temperature was obtained by interpolation of the stress vs. the actual temperature ( $T+\Delta T$ ) plot. Split Hopkinson Pressure Bar (SHPB) setup was used for high strain rate tests. For microstructural studies the deformed samples were sectioned along the compression axis, mounted in resin, mechanically polished and electro-polished using 5% perchloric acid (HClO<sub>4</sub>) and 95% methanol (CH<sub>3</sub>OH) solution. The microstructures were analyzed using electron backscatter diffraction (EBSD) technique. Since the average grain size was  $\geq 100$   $\mu\text{m}$  a large step size of 2  $\mu\text{m}$  was used for each scan. To acquire and analyze

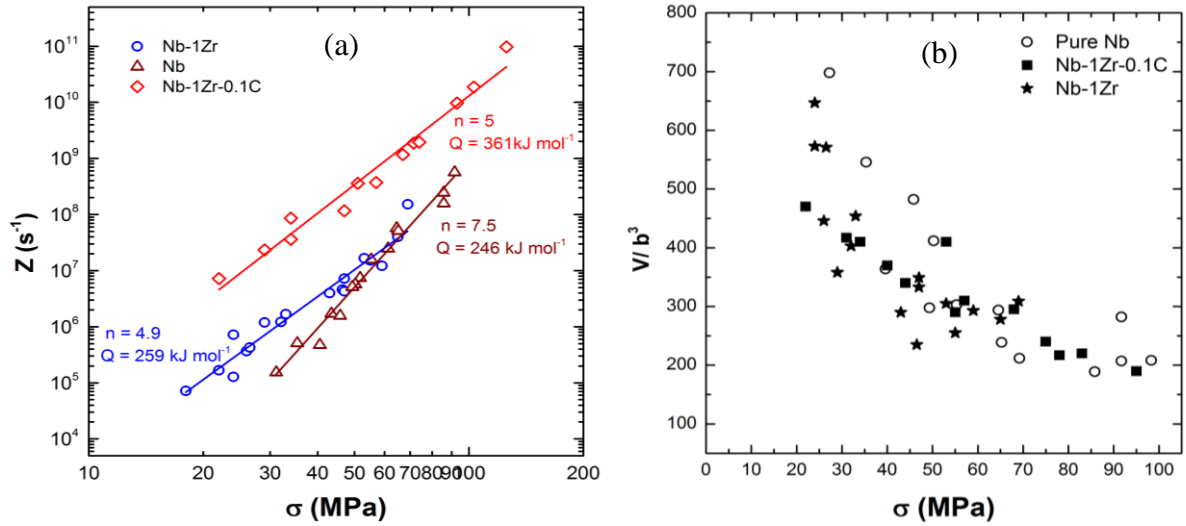
the data TSL-OIM data Collector and AZtec data Collector software and TSL-OIM analysis (Ver. 6.1) software and HKL - Channel 5 software were used. Average bulk textures of the deformed samples were measured using a Bruker D8-Discover X-ray texture goniometer (equipped with a Cu-K $\alpha$  source) based on Schultz reflection geometry. EBSD and X-ray texture measurement were done in the plane perpendicular to the compression axis. However as the deformation is uniaxial the EBSD maps and texture representation in terms of inverse pole figure for EBSD maps as well as X-ray texture plots were shown with respect to the compression axis.

## 4. Results and Discussion

### 4.1 Strain rate sensitivity

The strain rate sensitivity  $m = \Delta \ln \sigma / \Delta \ln \dot{\epsilon}$  of Nb, Nb-1Zr and Nb-1Zr-0.1C alloy were calculated for a true strain of 0.5 from the  $\sigma$ ,  $T$ ,  $\dot{\epsilon}$  data by fitting the  $\ln \sigma$  vs.  $\ln \dot{\epsilon}$  data to a cubic polynomial. The  $m$  was plotted as an iso-strain rate sensitivity contour plot as a function of temperature and strain rate as shown in Fig. 1. A domain of high strain rate sensitivity was observed starting from 1200 to 1500 °C and from strain rates of  $10^{-2}$  to  $1 \text{ s}^{-1}$  for pure Nb (Fig. 1 (a)). In this domain the strain rate sensitivity value varied between 0.12 to 0.2. The optimum domain of hot workability for Nb-1Zr alloy was determined to be from 1200 to 1500 °C for strain rates of  $10^{-3}$  to  $10^{-1} \text{ s}^{-1}$  and from 1600 to 1700 °C for strain rates of  $10^{-1}$  to  $1 \text{ s}^{-1}$  (Fig. 1 (b)). In this domain  $m$  varied from 0.15 to 0.25. The strain rate sensitivity map of Nb-1Zr-0.1C alloy exhibited a single domain starting at about 1300 °C and a maximum  $m$  at 1700 °C and  $2 \times 10^{-3} \text{ s}^{-1}$ . In this domain  $m$  increased from slightly positive to about 0.24 with increasing temperature and decreasing strain rate.





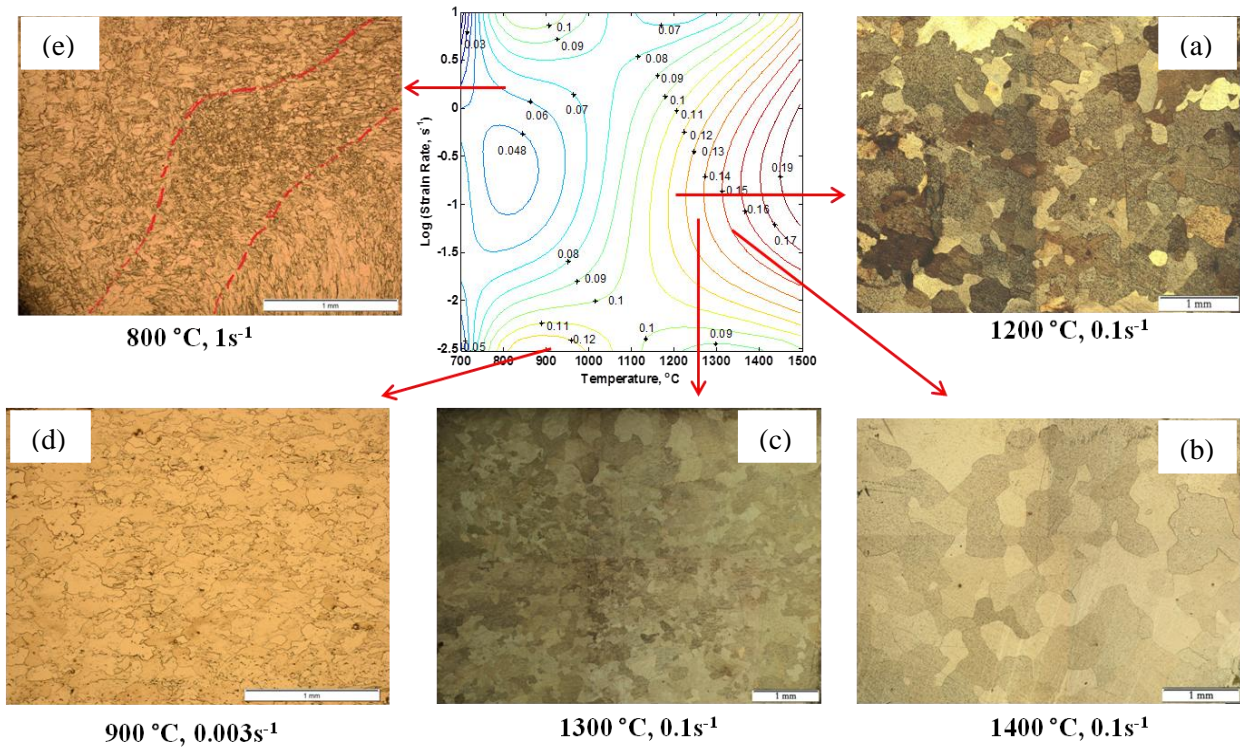
**Fig. 2:** (a) Zener-Hollomon parameter dependence on flow stress for Nb and its alloys within the deformation domain. The activation energy ( $Q$ ) and stress exponent ( $n$ ) are written on the plot. (b) Plot of activation volume (normalized with cube of magnitude of Burgers vector  $b$ ) vs. stress.

Table 1. A comparison of processing parameters of pure Nb, Nb-1Zr and Nb-1Zr-0.1C.

Material	High $m$ domain	Peak Strain rate sensitivity	$n$	$Q$ (kJ mol <sup>-1</sup> )	$V/b^3$
Nb	1200 - 1500 °C and $10^{-2} - 1 \text{ s}^{-1}$	0.19	7.5	246	200 - 700
Nb-1Zr	1200 - 1500 °C and $10^{-3}-0.1 \text{ s}^{-1}$ and 1600 - 1700 °C and $10^{-2} - 1 \text{ s}^{-1}$	0.24	4.9	259	230 - 650
Nb-1Zr-0.1C	1300 - 1700 °C and $10^{-3}- 1 \text{ s}^{-1}$	0.25	5	361	200 - 500

### 4.3 Microstructural characterization

For samples deformed at 1200 and 1300 °C at strain rate of  $10^{-1} \text{ s}^{-1}$  fine grains were observed suggesting dynamic recrystallization (DRX) microstructure (Fig. 3 (a), (b) and (c)). For samples deformed at 1400 °C the deformation appeared uniform throughout the sample with grains being equiaxed and larger than those at 1200 and 1300 °C. At 800 °C for strain rates of  $1 \text{ s}^{-1}$  regions of flow localization were observed as seen in Fig. 3 (e) (marked by dotted lines) whereas for 900 °C and  $3 \times 10^{-3} \text{ s}^{-1}$  (Fig. 3 (d)) elongated grains perpendicular to the deformation direction were observed suggesting the occurrence of dynamic recovery.



**Fig. 3:** Optical microstructure of the deformed samples at strain rate of  $10^{-1} \text{ s}^{-1}$  for (a) 1200, (b) 1400 and (c) 1300 °C and (d) at 900 °C for strain rate of  $3 \times 10^{-3} \text{ s}^{-1}$  and (e) 800 °C for strain rate of  $1 \text{ s}^{-1}$ .

The deformation microstructure of Nb-1Zr (Fig. 4) showed that the average grain size increased with decreasing strain rate and increasing temperature. At 1500 °C and  $10^{-1} \text{ s}^{-1}$  the equiaxed grains were finer as compared to that at other strain rates, with an average grain size of 329  $\mu\text{m}$ . The grains also appeared fully recrystallized and nearly equiaxed for the deformation condition of 1500 °C and  $10^{-2} \text{ s}^{-1}$ . At 1600 °C the grains were relatively large at  $10^{-2} \text{ s}^{-1}$  as compared to that at  $0.1 \text{ s}^{-1}$ , suggesting the occurrence of grain growth that occurs at higher temperatures and lower strain rates. Small new recrystallized grains formed at the boundaries of larger grains were seen at 1600 °C and  $10^{-2} \text{ s}^{-1}$ . At the higher strain rate of  $10^{-1} \text{ s}^{-1}$  few elongated grains were observed. Also the presence of equiaxed grains after deformation at these conditions (1600 °C for strain rates of  $10^{-2}$  and  $10^{-1} \text{ s}^{-1}$ ) suggests the occurrence of DRX. At temperature of 1700 °C and strain rates of  $10^{-1} \text{ s}^{-1}$  (Fig. 4) the grains were large and had straight boundaries as compared to that at other temperatures but the same strain rate.

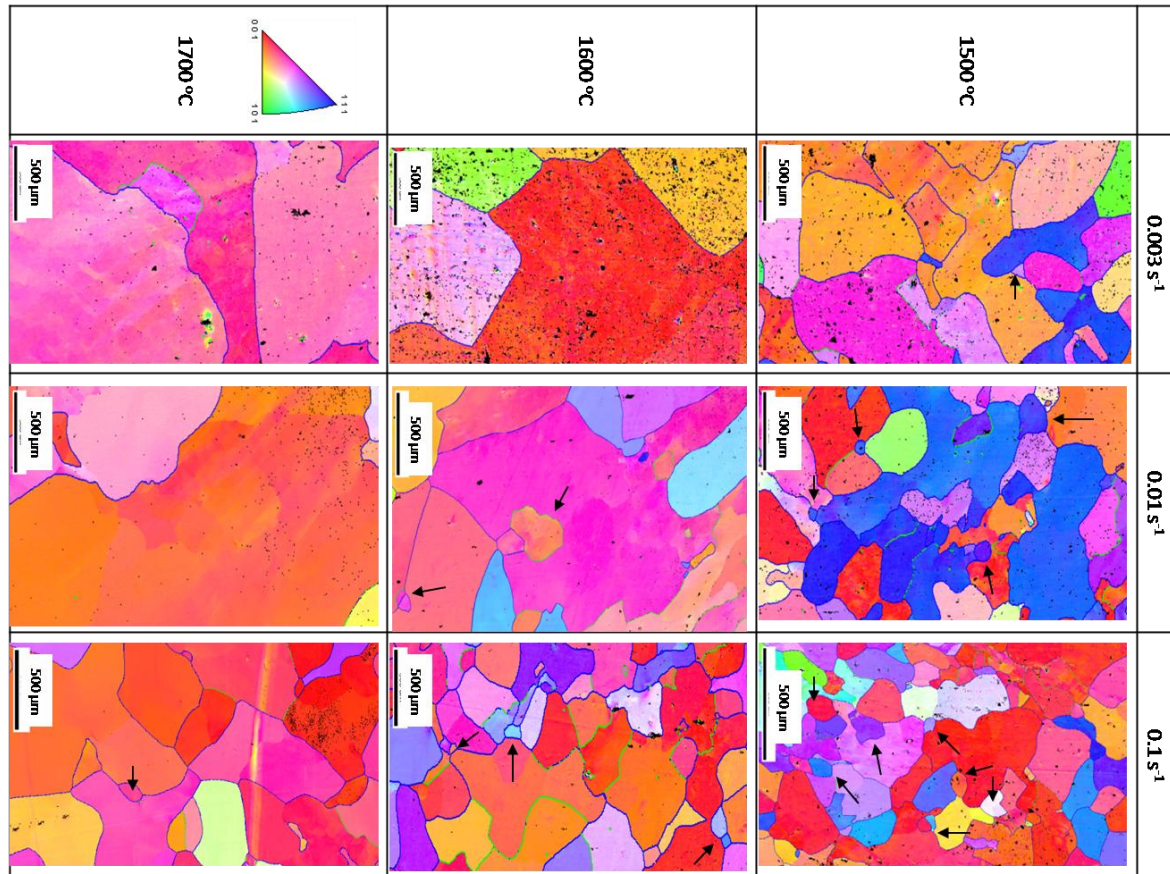


**Fig. 4.:** IPF map of the longitudinal section of Nb-1Zr samples deformed at 1500, 1600 and 1700 °C at strain rates of  $3 \times 10^{-3}$ ,  $10^{-2}$  and  $10^{-1} \text{ s}^{-1}$ . The compression axis is vertical. The colours represent the orientation with respect to the compression axis of the sample.

At 1500 to 1700 °C and  $10^{-1} \text{ s}^{-1}$  the microstructure of Nb-1Zr-0.1C (Fig. 5) consisted of many fine grains surrounding the larger grains forming the typical necklace structure, which is a characteristic feature of DRX. However, no such fine grains were observed at 1500 °C for lower strain rates of  $10^{-3}$  and  $10^{-2} \text{ s}^{-1}$  possibly due to grain growth. As the deformation microstructures were quite heterogeneous this suggested that DRX was incomplete at these deformation conditions. At  $10^{-3} \text{ s}^{-1}$  and 1500 - 1600 °C serrated high angle grain boundaries were observed whereas at  $10^{-2} \text{ s}^{-1}$  similar features were observed for only 1600 °C. However at  $10^{-1} \text{ s}^{-1}$  the serration of grain boundaries was very prominent only at 1700 °C. In the sample deformed at 1700 °C and  $10^{-1} \text{ s}^{-1}$  (Fig. 5) small new grains at boundaries of initial (larger) grains are observed, while the grain interior do not contain new grains. A similar microstructure is seen for sample tested at 1600 °C and  $10^{-2} \text{ s}^{-1}$  where wavy boundaries on large grains are actually indicative of boundaries of small newly recrystallized grains.

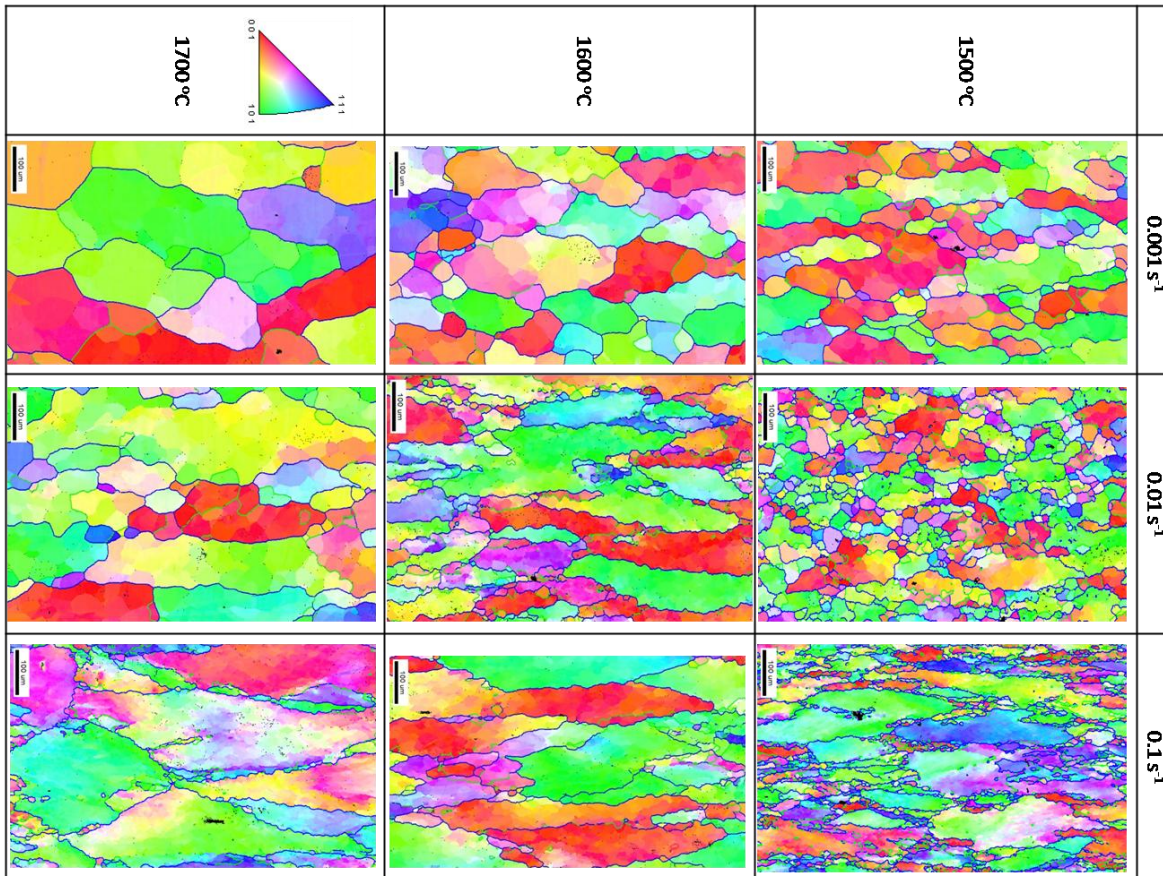


**Fig. 5:** IPF map of the longitudinal section of Nb-1Zr-0.1C samples deformed at 1500, 1600 and 1700 °C at strain rates of  $10^{-3}$ ,  $10^{-2}$  and  $10^{-1}$  s $^{-1}$ . The compression axis is vertical. The colours represent the orientation with respect to the compression axis of the sample.

In order to identify the dynamically recrystallized grains, the grains were partitioned based on grain orientation spread (GOS)  $< 2^\circ$ . As the DRX grains have lower dislocations density, the GOS value of DRX grains is expected to be low. Fig. 6 shows that in the microstructures of the samples deformed at higher strain rates, the number fraction of recrystallised grains is much higher as compared to those in the low strain rates.

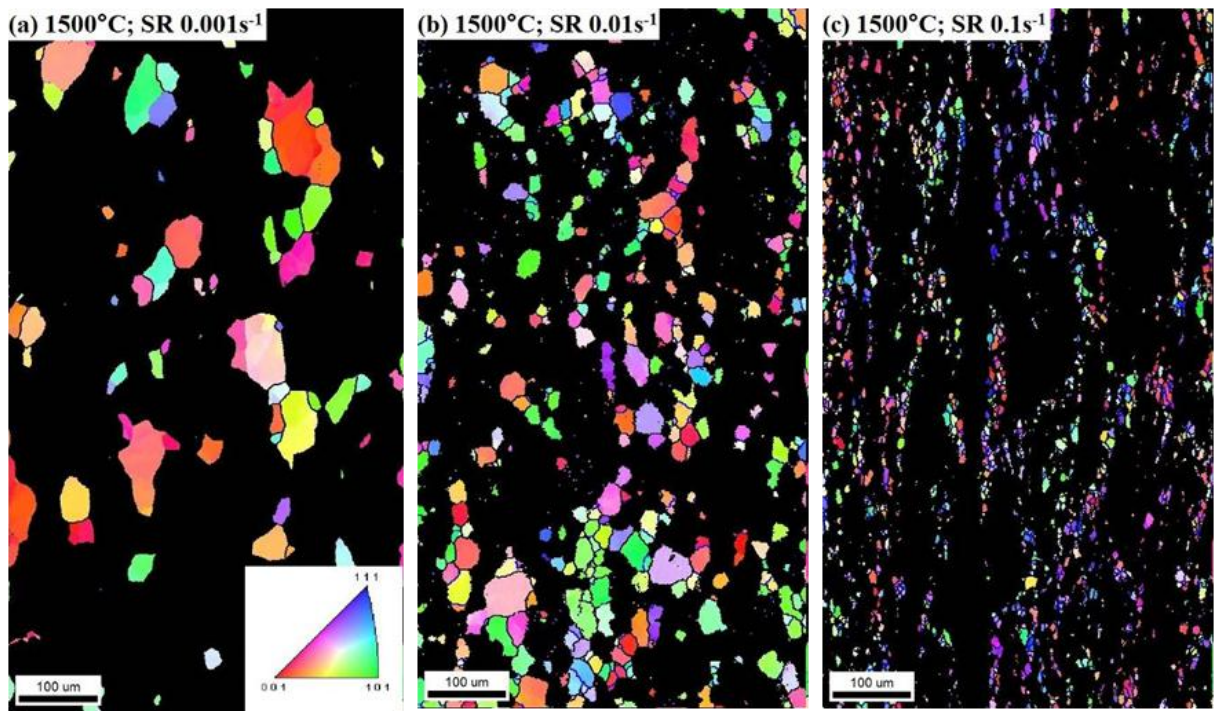


**Fig. 6:** Inverse pole figure map of the partitioned recrystallized grains of Nb-1Zr-0.1C (depending on Grain Orientation Spread ( $< 2^\circ$ )) for the deformation conditions as indicated.

#### 4.4 Evolution of DRX with strain

Nb-1Zr-0.1C sample deformed to a true strain of 0.3 at 1500 °C and  $10^{-1} \text{ s}^{-1}$  showed large grains with substructure (Fig. 7(a)). At this condition a large number of boundaries with  $2^\circ < \phi < 10^\circ$  were present. At true strain of 0.6 the grain boundaries appear serrated with increased subgrain boundaries within the grains. Small grains with high angle boundaries were seen at the corrugated site of the grain boundaries (Fig. 7 (b)). The average grain size of these fine grains was about 5  $\mu\text{m}$  and these form a necklace type of structure along the grain boundaries of the larger grains (grain size  $> 100 \mu\text{m}$ ). Few large grains contain well defined subgrains within them. At true strain of 0.9 elongated grains with wavy grain boundaries and well defined subgrains within were seen perpendicular to the compression axis (Fig. 7 (c)). The microstructure consisted of many fine equiaxed grains having high angle boundaries. For larger strain of 1.2 the elongated grains were seen to contain many fine grains with high angle boundaries (Fig. 7(d)). The homogeneous microstructure suggests the transformation of subgrain boundaries into grain boundaries at this deformation condition.

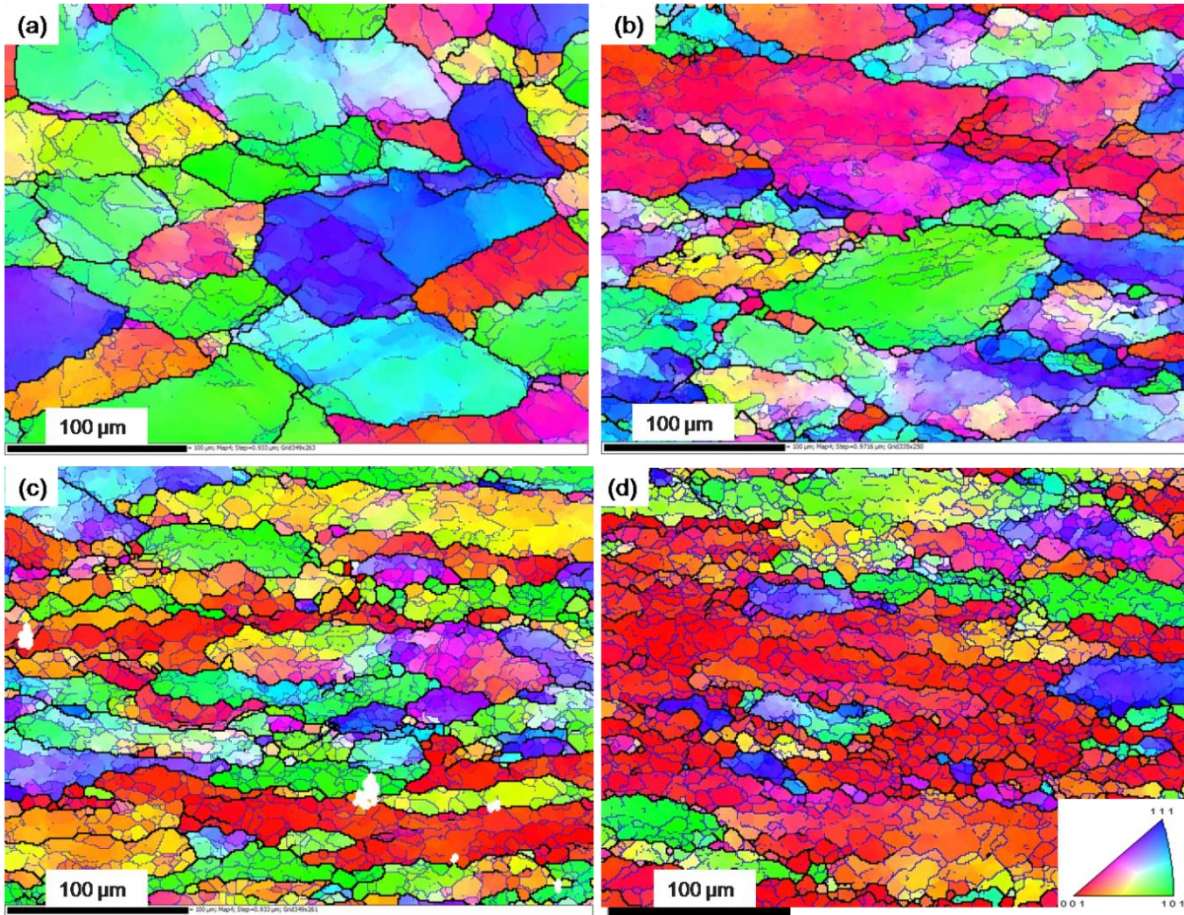


**Fig. 7:** IPF maps of Nb-1Zr-0.1C deformed at 1500 °C and  $10^{-1} \text{ s}^{-1}$  up to true strains of (a) 0.3, (b) 0.6, (c) 0.9 and (d) 1.2. The colours represent the orientation normal to the observation surface of the deformed sample. The stereographic triangle shows the orientation legend. The black lines represent high angle grain boundaries ( $\varphi > 10^\circ$ ) while the blue lines represent low angle boundaries ( $2 < \varphi < 10^\circ$ ).

The recrystallized grains were partitioned from the deformed grains and subgrains using the following criteria.

- 1) If the internal average misorientation angle within a grain exceeds  $2^\circ$  the grain is classified as being "deformed". The deformed grains are marked as grey in Fig. 8.
- 2) If grains consist of subgrains whose internal misorientation is under  $2^\circ$  but the misorientation from subgrain to subgrain is above  $2^\circ$  then the grain is classified as "substructured". These are marked as white.
- 3) All the remaining grains (i.e. neither deformed nor substructured) are classified as recrystallized and marked as red.

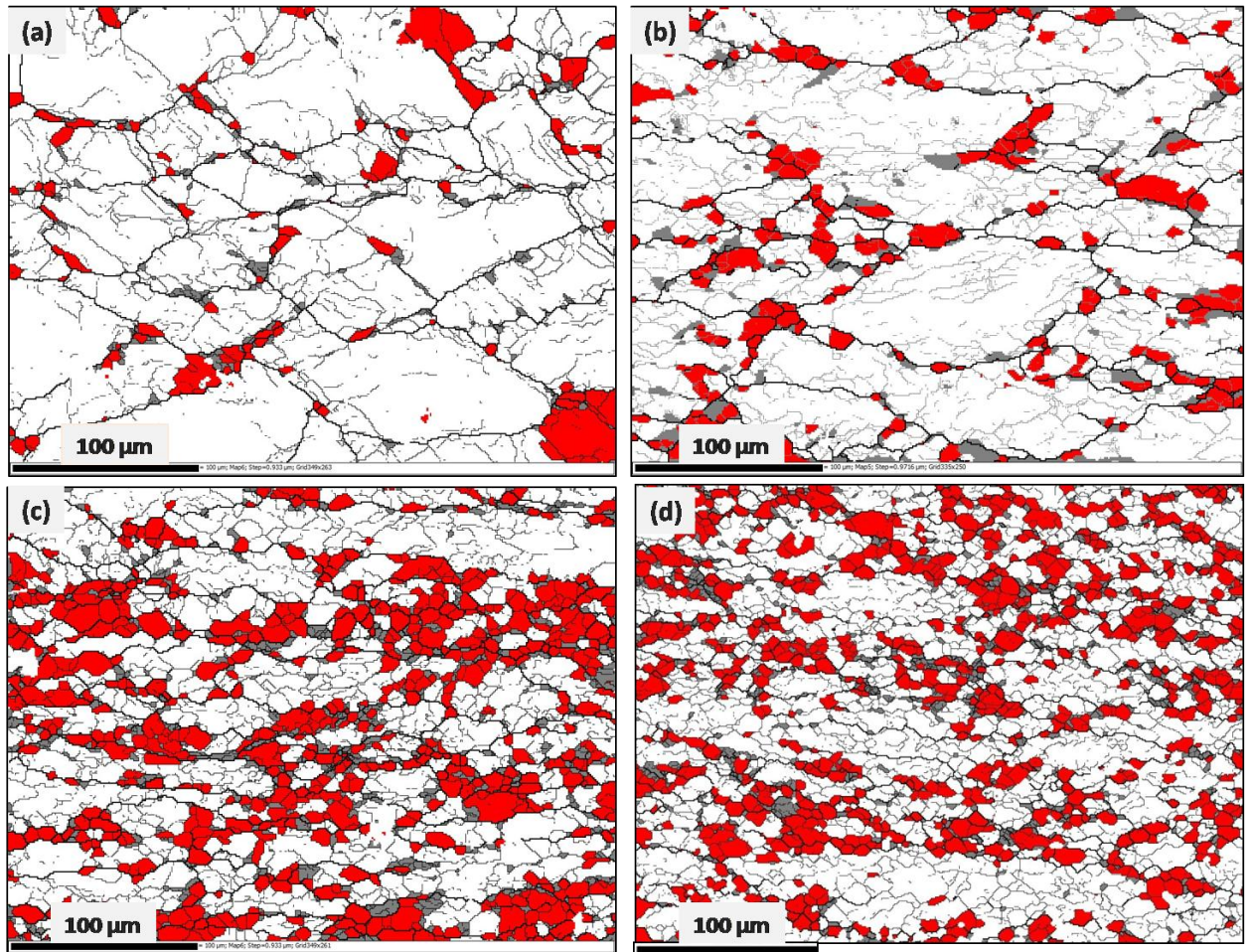


**Fig. 8:** EBSD map showing recrystallized grains obtained by partitioning the entire data set ( as explained in text) for Nb-1Zr-0.1C deformed at temperature of 1500 °C and strain rate of  $10^{-1} \text{ s}^{-1}$  for different true strains of (a) 0.3, (b) 0.6, (c) 0.9 and (d) 1.2. The red color represents the recrystallized grains, the white color represent grains with substructure and the gray color represent the deformed grains.

Nb-1Zr-0.1C deformed at 1500 °C and  $10^{-1} \text{ s}^{-1}$  up to a strain of 0.3 (Fig. 8 (a)) showed recrystallized grains along the boundaries of the large grains and the grain boundaries triple junctions. At a strain of 0.6 (Fig. 8 (b)) the recrystallized grains start to form the necklace structure. The presence of necklace type of microstructure at this condition, is a characteristics feature of DRX process, and signifies the non-uniform distribution of strain inside the grain. At 1500 °C and  $10^{-1} \text{ s}^{-1}$  for a strain of 0.9, most grains show a necklace structure signifying DRX. At 1500 °C and  $0.1 \text{ s}^{-1}$ , for strain of 1.2 an equiaxed grain structure with nearly similar grain sizes was observed. Deformation at 1500 °C and  $0.1 \text{ s}^{-1}$  to a large strain of 1.2 showed fine subgrains along the larger subgrain boundaries within the deformed grains.

## 4.5 Bulk Texture

Crystallographic texture measurements were carried out for the deformed samples of Nb-1Zr-0.1C alloy. The inverse pole figures were calculated from bulk XRD scans with respect to the compression axis for samples tested at 1500 °C and  $10^{-1} \text{ s}^{-1}$  and up to a strain of 0.3, 0.6, 0.9 and 1.2 (Fig. 9). At this deformation condition the predominant texture was along the  $\langle 001 \rangle$  poles. As the strain increased the texture evolution along the  $\langle 001 \rangle$  component became stronger. The strongest intensity of the  $\langle 001 \rangle$  pole texture was observed at the test condition of 1500 °C and  $0.1 \text{ s}^{-1}$  for strain of 1.2. At 1500 °C and  $0.1 \text{ s}^{-1}$  all fibers  $\langle 001 \rangle$ ,  $\langle 101 \rangle$  and  $\langle 111 \rangle$  were present for strain of 0.9, whereas  $\langle 111 \rangle$  component became weak at a strain of 1.2.

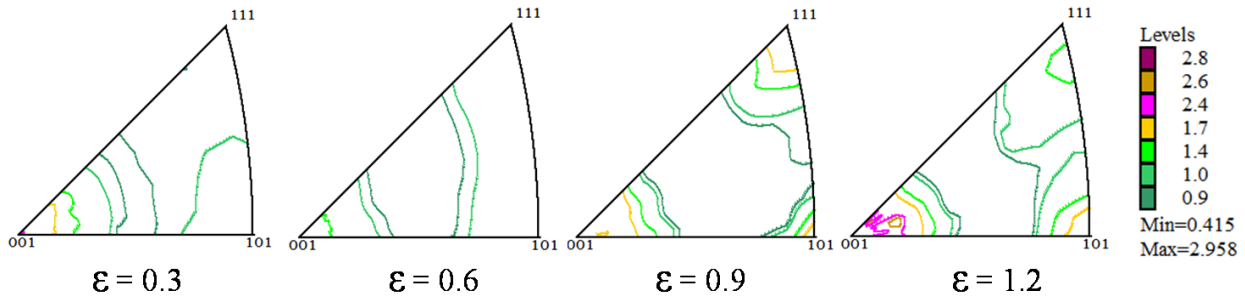


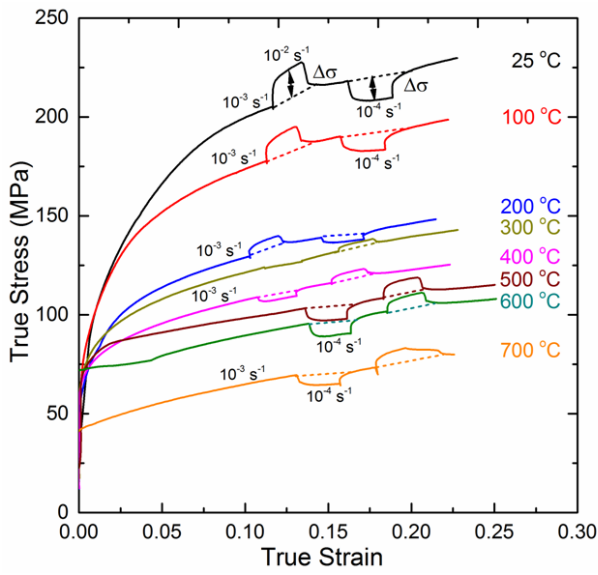
**Fig. 9:** Inverse pole figures from bulk XRD texture measurements with respect to compression axis for Nb-1Zr-0.1C alloy deformed at 1500 °C and strain rate of  $10^{-1} \text{ s}^{-1}$  to different strains.

## 4.6 Quasi-static deformation from 25 to 600 °C

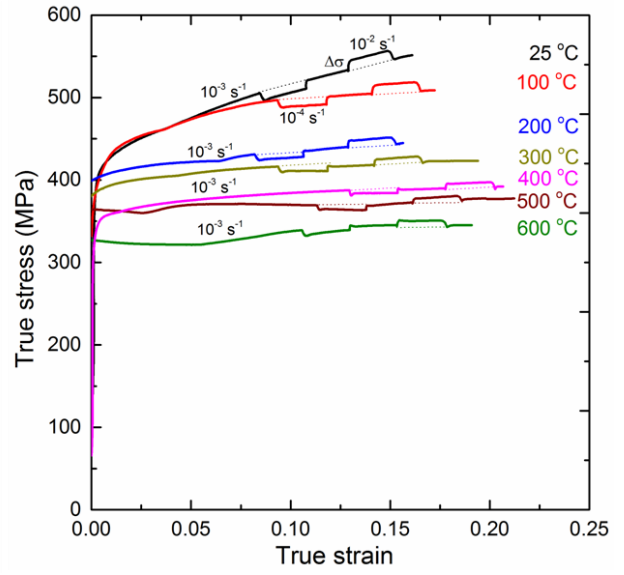
From the strain rate change tests carried out from 25 to 700 °C at strain rate of  $10^{-3} \text{ s}^{-1}$  (Fig. 10) the strain rate sensitivity was obtained and the activation volume ( $V$ ) was calculated. Results of successive stress relaxations and strain rate change tests were compared for Nb-1Zr and Nb-1Zr-0.1C alloy.

## 4.7 High strain rate deformation from 25 to 400 °C

Nb-1Zr and Nb-1Zr-0.1C alloys were tested from room temperature (25 °C) to 400 °C in the temperature interval of 100 °C up to strain of 0.25 and the strain rates were obtained as  $1700 \text{ s}^{-1}$  and  $1100 \text{ s}^{-1}$  respectively (Fig. 11). The flow curves show work-hardening behaviour of Nb alloys. Also the flow stress was seen to decrease with temperature.

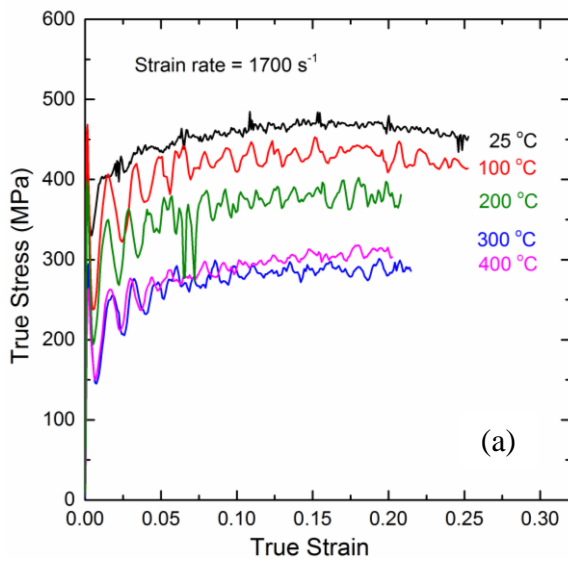


(a) Nb-1Zr

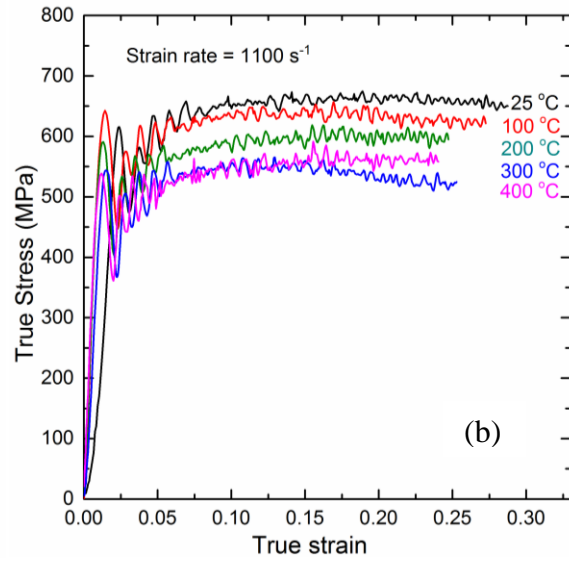


(b) Nb-1Zr-0.1C

**Fig. 10:** The true stress - true strain plot of (a) Nb-1Zr and (b) Nb-1Zr-0.1C alloy during strain rate change test from room temperature to 700 °C at strain rate of  $10^{-3} \text{ s}^{-1}$ .



(a)



(b)

**Fig. 11:** The stress- strain plot of (a) Nb-1Zr at strain rate of  $1750 \text{ s}^{-1}$  and (b) Nb-1Zr-0.1C alloy at strain rate of  $1125 \text{ s}^{-1}$  from room temperature to 400 °C.

## 4.8 Flow stress and strain rate sensitivity variation with temperature

Fig. 12 (a) shows the comparison of variation of strain rate sensitivity with temperature for Nb-1Zr and Nb-1Zr-0.1C alloy. The strain rate sensitivity was nearly same for Nb-1Zr and Nb-1Zr-0.1C alloy from room temperature to 600 °C. However at higher temperature up to 1400 °C Nb-1Zr alloy has higher strain rate sensitivity than Nb-1Zr-0.1C alloy. For Nb-1Zr alloy the strain rate sensitivity increased with temperature up to 1300 °C and then decreased with temperature. Also for Nb-1Zr-0.1C alloy the strain rate sensitivity increases linearly from 900 to 1700 °C. Fig. 12 (b) shows that the flow stress decreased from room temperature to 600 °C and was insensitive from 600 to 900 °C. At temperatures higher than 1000 °C the flow stress again starts to decrease with increasing temperature.

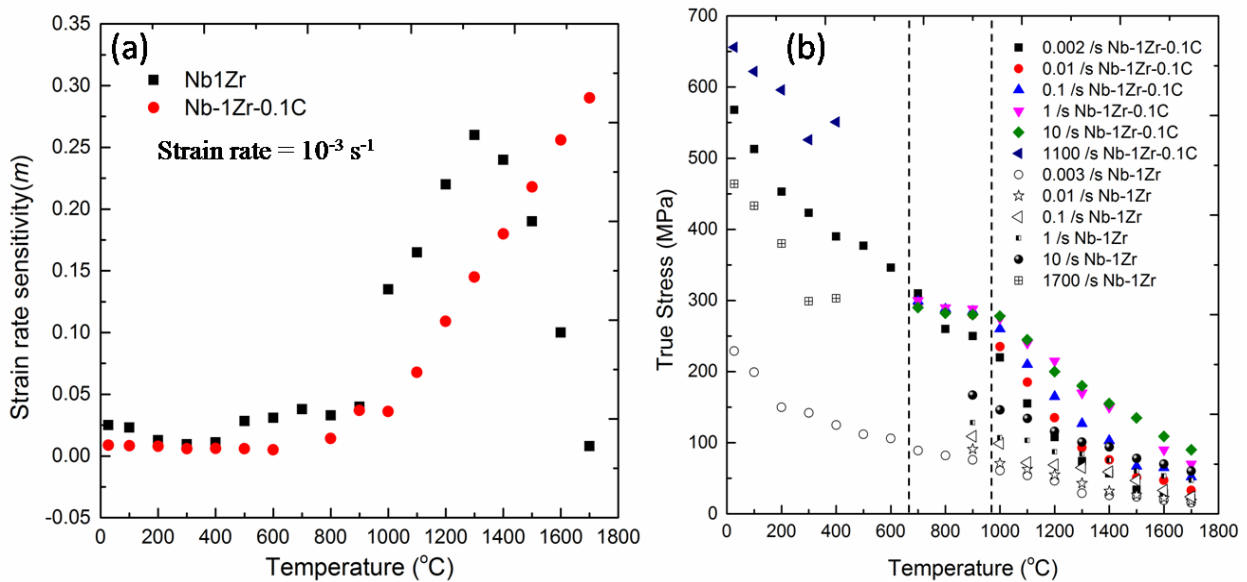


**Fig. 12:** The variation of (a) strain rate sensitivity ( $m$ ) at strain rate of  $10^{-3} \text{ s}^{-1}$  and (b) true stress different strain rates with temperature for Nb-1Zr and Nb-1Zr-0.1C alloy from room temperature to 1700 °C.

## 5. Conclusions

- i. Nb and its alloy showed a high strain rate sensitivity domain at temperature greater than 1300 °C and strain rate of  $10^{-3}$  to  $0.1 \text{ s}^{-1}$ .
- ii. At the same deformation conditions Nb-1Zr-0.1C showed a higher flow stress and finer microstructure as compared to that of Nb-1Zr.

- iii. The flow stress of Nb alloys decreased from room temperature to 600 °C and was insensitive from 600 to 900 °C. With further increase in temperature the flow stress decreased.
- iv. Microstructure of Nb, Nb-1Zr and Nb-1Zr-0.1C samples deformed within the high *m* domain revealed a dynamically recrystallized microstructure.
- v. The necklace structure of recrystallized grains for Nb-1Zr-0.1C alloy was seen along the serrated large grain boundaries at strain of 0.6 and 0.9 for temperature of 1500 and 1600 °C, respectively.
- vi. The activation energy of deformation suggests that dislocation core diffusion is the dominant mechanism during high temperature deformation (from 1300 to 1700 °C).
- vii. The predominant texture is along the <001> poles for all deformation conditions of the Nb-1Zr and Nb-1Zr-0.1C alloy.

## References

- [1] R. H. Titran, J. R. Stephens, D. W. Petrasek, Refractory Metal Alloys and Composites for Space Nuclear Power Systems, DOE / NASA / 16310 - 8 NASA TM - 101364 (1988).
- [2] J. R. Distefano, Review of alkali metal and refractory alloy compatibility for rankine cycle applications, Journal of Materials Engineering, 11 (1989) 215 - 225.
- [3] J. Hebda, Niobium alloys and high temperature applications, Niobium Science & Technology: Proceedings of the International Symposium Niobium 2001, Orlando, Florida, USA, 2001.
- [4] W. A. Fietz, M. R. Beasley, J. Silcox, W. W. Webb, Magnetization of Superconducting Nb-25% Zr Wire, Physical Review, 136 (1964) A 335 - 345.
- [5] J. S. Park, S. Lee, B. K. Ju, J. Jang, D. Jeon, M. H. Oh, Fabrication and estimation of characteristics for Nb-silicide FEAs Asian Symposium on Information Display, 1999 pp. 49 - 52.
- [6] H. Matsuno, A. Yokoyama, F. Watari, M. Uo, T. Kawasaki, Biocompatibility and osteogenesis of refractory metal implants, titanium, hafnium, niobium, tantalum and rhenium, Biomaterials, 22 (2001) 1253 - 1262.
- [7] R. Grill, A. Gnadenberger, Niobium as mint metal: Production & properties & processing, International Journal of Refractory Metals and Hard Materials, 24 (2006) 275 - 282.

- [8] E. J. Delgrosso, C. E. Carlson, J. J. Kaminsky, Development of niobium-zirconium-carbon alloys, *Journal of Less Common Metals*, 12 (1967) 173 - 201.
- [9] S. J. Zinkle, L. J. Ott, D.T. Ingersoll, R. J. Ellis, M. L. Grossbeck, Overview of materials technologies for space nuclear power and propulsion, *AIP Conference Proceedings*, 608 (2002) 1063 - 1073.
- [10] R. E. Gold, D. L. Harrod, Refractory metal alloys for fusion reactor applications, *Journal of Nuclear Materials*, 85 & 86, Part 2 (1979) 805 - 815.
- [11] D. J. Mazey, C. A. English, Role of refractory metal alloys in fusion reactor applications, *Journal of the Less Common Metals*, 100 (1984) 385 - 427.
- [12] I. V. Dulera, A. Basak, P. P. Kelkar, R. K. Sinha, Compact High Temperature Reactor, *BARC Newsletter*, 2006, pp. 172 - 179.
- [13] R. H. Titran, Creep strength of niobium alloys, Nb-1% Zr and PWC-11, DOE / NASA / 16310 - 13, NASA TM - 102390 (1990).
- [14] M. J. Davidson, M. Biberger, A. K. Mukherjee, Creep of niobium and solid solution strengthened Nb-1wt.% Zr, *Scripta Metallurgica et. Materialia*, 27 (1992) 1829 - 1834.
- [15] R. H. Titran, Long-time creep behavior of Nb-1Zr alloy containing carbon, DOE / NASA/ 16310 - 4, NASA TM - 100142 (1986).
- [16] R. H. Titran, M. Uz, Effects of thermomechanical processing on the microstructure and mechanical properties of Nb-1Zr-C alloys, NASA TM 107207 (1993).
- [17] M. Uz, R. H. Titran, Characterization of the microstructure of Nb-1wt.% Zr-0.1wt.% C tubes as affected by thermomechanical processing, DOE / NASA / 16310 - 21, NASA TM - 106381 (1994).
- [18] M. Uz, R. H. Titran, Processing and microstructure of Nb-1% Zr-0.1% C alloy sheet, NASA TM - 105921,1993 (1993).
- [19] T. E. McGreevy, C. E. Duty, K. J. Leonard, F. W. Wiffen, Z. S. J., The mechanical behavior of Nb-1Zr, *Proceedings of the space nuclear conference*, San Diego, California, 2005, pp. 303 - 308.
- [20] T. G. Nieh, M. Zhang, S. J. Zinkle, T. E. McGreevy, D. T. Hoelzer, S. A. Speakman, Effect of texture on the high temperature mechanical properties of Nb-1% Zr alloy, *Scripta Materialia*, 55 (2006) 719 - 722.
- [21] D. M. Farkas, A. K. Mukherjee, Creep behavior and microstructural correlation of a particle-strengthened Nb-1Zr-0.1C alloy, *Journal of Materials Research*, 11 (1996) 2198 - 2205.

- [22] D. M. Farkas, A. K. Mukherjee, Stress cycle testing during creep of a particle strengthened Nb-1Zr-0.1C alloy, *Materials Science and Engineering: A*, 222 (1997) 21 - 27.
- [23] A. Sarkar, R. Kapoor, A. Verma, J. K. Chakravartty, A. K. Suri, Hot deformation behavior of Nb-1Zr-0.1C alloy in the temperature range 700 - 1700 °C, *Journal of Nuclear Materials*, 422 (2012) 1 - 7.
- [24] R. Kapoor, S. Nemat-Nasser, Determination of temperature rise during high strain rate deformation, *Mechanics of Materials*, 27 (1998) 1 - 12.
- [25] A. N. Behera, R. Kapoor, A. Sarkar, J. K. Chakravartty, Hot deformation behaviour of niobium in temperature range 700 - 1500 °C, *Materials Science and Technology (United Kingdom)*, 30 (2014) 637 - 644.
- [26] H. J. Frost, M. F. Ashby, *Deformation Mechanism Maps: The Plasticity and Creep of Metals and Ceramics*, Pergamon Press, 1982.
- [27] G. Taylor, Thermally-activated deformation of BCC metals and alloys, *Progress in Materials Science*, 36 (1992) 29 - 61.
- [28] Q. Wei, S. Cheng, K. T. Ramesh, E. Ma, Effect of nanocrystalline and ultrafine grain sizes on the strain rate sensitivity and activation volume: fcc versus bcc metals, *Materials Science and Engineering A*, 381 (2004) 71 - 79.

## List of Figures

Figure	Page No.
1.1 Nb-Zr binary alloy equilibrium phase diagram	2
1.2 Nb-C binary alloy equilibrium phase diagram	3
1.3 Different hot deformation mechanisms	5
2.1 Dependence of critical resolved shear stress for brass on concentration and temperature [42]	15
2.2 (a) Isothermal stress vs. strain curves at strain rate of $10^{-3} \text{ s}^{-1}$ and (b) adiabatic stress vs. strain curves at strain rate of $3300 \text{ s}^{-1}$ for Nb for indicated temperatures [46]	17
2.3 Creep-rate as a function of temperature for the 0C, 1C and 10C alloys at 100 MPa [71]	20
2.4 Optical microstructure of as-cast microstructure of Nb-1Zr-0.1C alloy (a) low magnified image showing big grains and (b) high magnified image showing needle shape precipitates within the grain [79]	21
2.5 TEM micrograph of the (a) needle and (b) rectangular shape precipitate present in the deformed Nb-1Zr-0.1C alloy and the inset figure shows the SAED patterns of the precipitate and matrix [79]	22
2.6 IPF images of the Nb-1Zr-0.1C alloy samples heat treated at (a) $1300 \text{ }^{\circ}\text{C}$ for 3 h and (b) $1500 \text{ }^{\circ}\text{C}$ for 2 h show nearly recrystallized microstructure. The sample annealed at $1500 \text{ }^{\circ}\text{C}$ showed larger presence of carbides at grain boundaries of recrystallized grains [79]	22
2.7 Schematic summary of the microstructural changes occurring during dynamic recovery [91]	26

2.8	Schematic representation of the discontinuous static recrystallization (dSRX) taking place during the annealing of strained materials [93]	27
2.9	Schematic of grain boundaries pinch off where opposite serrations meet in case of gDRX [105]	31
2.10	Three types of dislocation density distribution developed in a microstructure undergoing dDRX: (a) a dDRX grain, (b) a growing dDRX grain and (c) a critically strain harden dDRX grain. The current state is represented by full lines and one or more earlier states by broken lines. $\rho_o$ is the initial (annealed) dislocation density, $\rho_c$ is the critical value required for nucleation, and D is the current dynamic grain size [115]	34
2.11	Schematic representation of the nucleation of DRX grain (a) Boundary corrugation accompanied by the evolution of sub-boundaries. (b) Partial grain boundary sliding / shearing, leading to the development of inhomogeneous local strains. (c) Bulging of parts of a serrated grain boundary accompanied with the evolution of dislocation sub-boundaries or twinning, leading to the formation of a new DRX grain [132]	38
3.1	Schematic profile of temperature vs. time for a hot deformation test	45
3.2	Schematic representation of stress relaxation test	46
3.3	Multiple relaxation curves for Nb-1Zr-0.1C alloy at 200 °C	48
3.4	Schematic of split-Hopkinson pressure bar (SHPB)	52
3.5	A typical pulse signal recorded through strain gauges using momentum trap	53
3.6	Schematics of EBSD and X-ray texture data measurement plane. The representation of IPF was done with respect to compression axis	54
4.1	Plots of true stress vs. true strain of Nb at strain rates of 0.003, 0.01, 0.1,	56

	1.0, 10 s <sup>-1</sup> and at different temperatures as mentioned along each curve	
4.2	Plots of true stress vs. true strain of Nb-1Zr at strain rates of (a) 0.003, (b) 0.01, (c) 0.1, (d) 1 and (e) 10 s <sup>-1</sup> and different temperatures as indicated	59
4.3	Plots of true stress vs. true strain of Nb-1Zr-0.1C at strain rates of (a) 0.002, (b) 0.01, (c) 0.1, (d) 1 and (e) 10 s <sup>-1</sup> and different temperatures as indicated	60
4.4	Flow stress vs. strain rates at a true strain of 0.5 for (a) Nb, (b) Nb-1Zr and (c) Nb-1Zr-0.1C alloy at different temperatures	62
4.5	Flow stress vs. temperature at a true strain of 0.5 for (a) Nb, (b) Nb-1Zr and (c) Nb-1Zr-0.1C alloy at different strain rates. The lines connecting the data points are shown for clarity	63
4.6	Iso-strain rate sensitivity contour map of (a) pure Nb, (b) Nb-1Zr alloy and (c) Nb-1Zr-0.1C alloy for a true strain of 0.5. The values on the contours indicate strain rate sensitivity ( <i>m</i> )	65
4.7	Zener-Hollomon parameter ( <i>Z</i> ) dependence on flow stress for Nb, Nb-1Zr and Nb-1Zr-0.1C alloys within the deformation domain. The activation energies ( <i>Q</i> ) and stress exponents ( <i>n</i> ) as determined by using Eq. (4.1) are written on the plot	68
4.8	Zener-Hollomon parameter dependence on grain size for Nb, Nb-1Zr and Nb-1Zr-0.1C alloys within each of their deformation domain. The numbers next to the data points indicate the test conditions	70
4.9	Plot of activation volume (normalized with cube of magnitude of Burgers vector <i>b</i> ) vs. stress for data within high <i>m</i> domain	71
4.10	Optical microstructures of (a) starting Nb material and (b) Nb deformed at 1500 °C, 0.1 s <sup>-1</sup>	72

- 4.11 Optical microstructure of the deformed Nb samples at strain rate of  $0.1 \text{ s}^{-1}$  73  
for (a) 1200, (b) 1300 and (c) 1400 °C at conditions as shown in the map.  
Each of the micrographs show the near complete sample with the top and  
bottom of the micrograph being near the top and bottom faces and the  
sides are near the lateral faces which show bulging
- 4.12 Optical microstructure of the Nb samples deformed at 1400 °C and at 73  
strain rates of (a)  $0.01 \text{ s}^{-1}$  and (b)  $10 \text{ s}^{-1}$
- 4.13 Optical microstructure of the deformed Nb sample at 800 °C for strain 74  
rate of  $1 \text{ s}^{-1}$  and at 900 °C for strain rate of  $0.003 \text{ s}^{-1}$ . The flow  
localization was marked by the dotted line for sample deformed at 800 °C  
for strain rate of  $1 \text{ s}^{-1}$ . The red line portion in the iso-*m* map shows the  
high *m* domain
- 4.14 Inverse pole figures (IPF) maps of EBSD microstructure for deformed 75  
samples of Nb at (a) 1300 °C,  $0.1 \text{ s}^{-1}$  and (b) 1400 °C,  $0.1 \text{ s}^{-1}$ . The scale  
for 1300 °C,  $0.1 \text{ s}^{-1}$  is 300 μm whereas for 1400 °C,  $0.1 \text{ s}^{-1}$  it is 200 μm
- 4.15 IPF map of longitudinal section for starting material of Nb-1Zr alloy. 76  
The colours represent the orientation with respect to the compression axis  
of the deformed sample. The stereographic triangle shows the orientation  
legend
- 4.16 IPF maps of the longitudinal section of Nb-1Zr samples deformed at 77  
1500, 1600 and 1700 °C at strain rates of 0.003, 0.01 and  $0.1 \text{ s}^{-1}$ . The  
compression axis is horizontal. The blue lines represent high angle grain  
boundaries (misorientation  $\phi > 15^\circ$ ) while the green lines represent low  
angle boundaries (misorientation  $2^\circ < \phi < 15^\circ$ ). The colours represent the  
orientation with respect to the compression axis of the sample. The arrow

	shows the fine recrystallized new grains	
4.17	IPF map of the longitudinal section of samples deformed at 1700 °C for strain rate of 10 s <sup>-1</sup> conditions. The colours represent orientation with respect to compression axis of the sample (vertical in figure)	78
4.18	Cumulative distribution of KAM with misorientation angle less than 5° for samples deformed at strain rates of (a) 0.1 s <sup>-1</sup> and (b) 0.01 s <sup>-1</sup> for temperature of 1500, 1600 and 1700 °C. Similar distribution of samples deformed at temperatures of (c) 1500 °C and (d) 1700 °C for strain rates of 0.003, 0.01, 0.1 and 10 s <sup>-1</sup>	79
4.19	Inverse pole figures for texture with respect to compression axis of deformed samples of Nb-1Zr alloy at different testing conditions	81
4.20	Inverse pole figure map of the as received sample of Nb-1Zr-0.1C alloy	82
4.21	IPF map of the longitudinal section of Nb-1Zr-0.1C samples deformed at 1500, 1600 and 1700 °C at strain rates of 0.001, 0.01 and 0.1 s <sup>-1</sup> . The compression axis is horizontal. The blue lines represent high angle grain boundaries (misorientation $\varphi > 10^\circ$ ) while the green lines represent low angle boundaries (misorientation $2 < \varphi < 10^\circ$ ). The colours represent the orientation with respect to the compression axis of the sample. The arrow marks shows the fine recrystallized new grains	84
4.22	Image quality map of Nb-1Zr-0.1C alloy deformed at temperature of 1500 °C and strain rates of (a) 0.001 s <sup>-1</sup> , (b) 0.01 s <sup>-1</sup> and (c) 0.1 s <sup>-1</sup> . The dark lines represents misorientation angle $> 10^\circ$ and grey lines $2^\circ - 10^\circ$	85
4.23	Inverse pole figure map of the partitioned recrystallized grains (depending on Grain Orientation Spread ( $< 2^\circ$ )) for the deformation of Nb-1Zr-0.1C at conditions as indicated	86

- 4.24 True stress vs. true strain plot of Nb-1Zr-0.1C alloy (a) at 1500 and 87  
1600 °C and at strain rates 0.1 s<sup>-1</sup> up to a true strain of 1.2, (b) at 1500 °C  
and strain rate of 0.1 s<sup>-1</sup> showing curves of different tests to true strains of  
0.3, 0.6, 0.9 and 1.2
- 4.25 Inverse pole figure (IPF) map of Nb-1Zr-0.1C deformed at temperature of 88  
1500 °C and strain rate of 0.1 s<sup>-1</sup> up to true strains of (a) 0.3, (b) 0.6, (c)  
0.9 and (d) 1.2. The colours represent the orientation normal to the  
observation surface of the deformed sample. The stereographic triangle  
shows the orientation legend. The black lines represent high angle grain  
boundaries ( $\varphi > 10^\circ$ ) while the blue lines represent low angle boundaries  
( $2 < \varphi < 10^\circ$ )
- 4.26 Cumulative grain size distribution for all grains with misorientation angle 90  
( $\varphi$ ) greater than 2° and (b) Cumulative distribution of misorientation  
angle for samples deformed at 1500 °C and 0.1 s<sup>-1</sup> at different strains
- 4.27 Inverse Pole Figure map of Nb-1Zr-0.1C deformed at temperature of 91  
1600 °C and strain rate of 0.1 s<sup>-1</sup> for different true strain as (a) 0.3, (b) 0.6,  
(c) 0.9 and (d) 1.2. The colours represent the orientation normal to the  
observed plane of the deformed sample. The stereographic triangle  
shows the orientation legend. The black lines represent high angle grain  
boundaries ( $\varphi > 10^\circ$ ) while the blue lines represent low angle boundaries  
( $2^\circ < \varphi < 10^\circ$ )
- 4.28 (a) Cumulative grain size distribution for all grains with misorientation 92  
angle greater than 2° and (b) Cumulative distribution of misorientation  
angle for samples deformed at 1600 °C and 0.1 s<sup>-1</sup> up to different strains
- 4.29 Local average misorientation distribution for misorientation below 2° of 93

- samples deformed at (a) 1500 and (b) 1600 °C for strain rate of 0.1 s<sup>-1</sup>
- 4.30 Inverse pole figures from bulk XRD texture measurements with respect to 94  
compression axis for Nb-1Zr-0.1C alloy deformed at 1500 °C and strain  
rate of 0.1 s<sup>-1</sup> to different strains
- 4.31 Inverse pole figures from EBSD measurements with respect to 94  
compression axis of Nb-1Zr-0.1C alloy deformed at 1500 and 1600 °C at  
strain rate of 0.1 s<sup>-1</sup> and at different strains. The legend represents the  
levels of multiple uniform density
- 4.32 EBSD map showing recrystallized grains obtained by partitioning the 96  
entire data set (as explained in text) for Nb-1Zr-0.1C deformed at  
temperature of 1500 °C and strain rate of 0.1 s<sup>-1</sup> for different true strains  
of (a) 0.3, (b) 0.6, (c) 0.9 and (d) 1.2. The red color represents the  
recrystallized grains, the white color represent grains with substructure  
and the gray color represent the deformed grains
- 4.33 Inverse pole figure map of Nb-1Zr-0.1C deformed at temperature of 97  
1500 °C and strain rate of 0.1 s<sup>-1</sup> up to a true strain of 1.2. The necklace  
structure formed at the boundary of subgrains are marked by circle and  
magnified at the right side of the figure. Fine subgrains are seen at the  
boundary of larger subgrains (marked by arrow)
- 4.34 EBSD map showing recrystallized grains obtained by partitioning the 98  
entire data set (explained in text) for samples deformed at temperature of  
1600 °C and strain rate of 0.1 s<sup>-1</sup> for different true strains of (a) 0.3, (b)  
0.6, (c) 0.9 and (d) 1.2. The red color represents recrystallized grains, the  
white color represents substructure and the gray color represent the  
deformed grains

4.35	Comparisons of grain orientation spread (GOS) $< 2^\circ$ at different test conditions as mentioned in the plot	99
4.36	Inverse pole figures with respect to compression axis obtained from EBSD of only the DRX grains for Nb-1Zr-0.1C alloy deformed at 1500 and 1600 °C for strain rate of $0.1 \text{ s}^{-1}$ . The legend represents the levels of multiple uniform density	100
4.37	Schematic of the difference between the $\sigma_{DRV}$ (reconstructed) and $\sigma_{DRX}$ (experimental obtained) curves for the calculation of recrystallized volume fraction ( $X$ )	102
4.38	(a) Plot of $\theta \cdot \sigma$ vs. $\sigma^2$ for determination of $\sigma_{\text{sat}}$ and (b) plot of $-(d\theta/d\sigma)$ vs. $\sigma$ for determination of $\sigma_c$ for deformation condition of 1500 °C at strain rate of $0.1 \text{ s}^{-1}$	103
4.39	Reconstructed dynamic recovery (DRV) curve plotted along with the experimental DRX curve for Nb-1Zr-0.1C alloy at deformation conditions of 1500 and 1600 °C for strain rate of $0.1 \text{ s}^{-1}$	104
4.40	Variation of recrystallization fraction with $(\varepsilon - \varepsilon_c)$ for Nb-1Zr-0.1C alloy	106
4.41	Avrami plots for Nb-1Zr-0.1C alloy at different deformation conditions	107
4.42	Variation of recrystallization fraction with strain for 1500 and 1600 °C at strain rate of $0.1 \text{ s}^{-1}$ as calculated from EBSD data	108
4.43	Strain rate jump test of Nb-1Zr alloy at different deformation conditions as mentioned	110
4.44	Strain rate jump test of Nb-1Zr-0.1C alloy at different deformation conditions as mentioned	111
4.45	Strain rate change test of Nb-1Zr-0.1C alloy at temperature of 700 °C and strain rate of $10^{-3} \text{ s}^{-1}$ . Serrations and negative strain rate sensitivity	112

	indicate occurrence of dynamic strain aging (DSA)	
4.46	Stress relaxation curve for Nb-1Zr-0.1C alloy at a stress of 556 MPa for room temperature	113
4.47	Variation of activation volume with number of relaxations for Nb alloys at different temperatures as indicated	114
4.48	Variation of activation volume with flow stress of Nb alloys. Activation volume is calculated from stress relaxation data using Eq. (3.11)	115
4.49	The time decrease of the mobile dislocation density (dislocation exhaustion rate) during four stress relaxation cycles of Nb-1Zr-0.1C alloy at 600 °C	116
4.50	Strain rate variation with strain for (a) Nb-1Zr and (b) Nb-1Zr-0.1C alloy at temperature of 25 to 400 °C	118
4.51	Stress - strain curve for (a) Nb-1Zr and (b) Nb-1Zr-0.1C alloy at strain rate of 1700 s <sup>-1</sup> and 1100 s <sup>-1</sup> respectively	119
4.52	The true stress variation of Nb alloys with temperature at a strain of 0.2 for high strain rates as indicated in the figure	120
4.53	Comparison of flow stress vs. strain rate for Nb-1Zr, pure Nb [158] and Nb-1Zr-0.1C [47] at 900 °C and 1000 °C	121
4.54	Comparison of steady state strain rate vs. flow stress for pure Nb at 1000 °C (taken from experiment), Nb-1Zr-0.1C at 1000 °C and Nb-1Zr and Nb-1Zr-0.1C at 1027 °C (taken from ref. [67])	124
4.55	The variation of strain rate sensitivity ( <i>m</i> ) at strain rate of 10 <sup>-3</sup> s <sup>-1</sup> with temperature for Nb-1Zr and Nb-1Zr-0.1C alloy from room temperature to 1700 °C	125
4.56	The variation of true stress with temperature for (a) Nb-1Zr and	127

(b) Nb-1Zr-0.1C alloy from room temperature to 1700 °C at different strain rates

4.57 Comparison of the variation of true stress at different strain rates with 129 temperature for Nb-1Zr and Nb-1Zr-0.1C alloy from room temperature to 1700 °C

## List of Tables

Table	Page No.
3.1 Elemental analysis of pure niobium in wt.%	43
3.2 Elemental analysis of Nb-1Zr alloy in wt.%	43
3.3 Elemental analysis of Nb-1Zr-0.1C alloy in wt.%	43
4.1 Average grain size of Nb-1Zr at different deformation conditions	78
4.2 Details of high strain rate test parameters for Nb-1Zr	117
4.3 Details of high strain rate test parameters for Nb-1Zr-0.1C	118
4.4 A comparison of deformation domain, strain rate sensitivity( $m$ ), stress exponent ( $n$ ), activation energy ( $Q$ ) and activation volume ( $V/b^3$ ) values of pure Nb, Nb-1Zr and Nb-1Zr-0.1C	123
4.5 Activation energy ( $Q$ ) for Nb-1Zr and Nb-1Zr-0.1C alloy at low temperature	128

## List of Abbreviations

cDRX	Continuous dynamic recrystallization
DRX	Dynamic recrystallization
dDRX	Discontinuous dynamic recrystallization
dSRX	Discontinuous static recrystallization
EBSD	Electron backscatter diffraction
gDRX	Geometric dynamic recrystallization
GNB	Geometrically necessary boundary
GND	Geometrically necessary dislocation
GOS	Grain orientation spread
HAGB	High angle grain boundary
IPF	Inverse pole figure
KAM	Kernel Average Misorientation
LAGB	Low angle grain boundary
mDRX	Meta dynamic recrystallization
SFE	Stacking fault energy

## List of Symbols

$\varepsilon$	True strain
$\varepsilon_p$	Plastic strain
$\rho_m$	Mobile dislocation density
$\dot{\gamma}$	Shear strain rate
$v$	Mean velocity of dislocations
$k$	Boltzmann's constant
$\varphi$	Misorientation angle
$\sigma$	True stress
$\tau$	Shear stress
$\tau^*$	Effective shear stress
$\tau_i$	Long range internal stress
$v_d$	Debye frequency
$\gamma$	Shear strain
$\mu$	Shear modulus
$A^l$	Area swept by dislocation segment $l$
$A_o$	Initial cross-sectional area of sample
$b$	Burgers vector
$C_0$	Wave velocity in the bar
$C_p$	Specific heat capacity
$d$	Grain size
$D$	Diffusivity
$D_v$	Diffusion constant

$e$	Engineering strain
$E$	Combined modulus of machine and sample
$L_o$	Initial length of sample
$n$	Stress exponent
$Q$	Activation energy for deformation
$Q_{SD}$	Activation energy for self diffusion
$R$	Universal gas constant
$S$	Engineering stress
$T$	Absolute temperature
$T_m$	Melting point temperature of material
$V$	Activation volume
$V_a$	Apparent activation volume
$X$	Recrystallized fraction
$Z$	Zener-Hollomon parameter



## Chapter 1. Introduction

Niobium and its alloy come under the refractory metals and alloys group. Niobium is a metal having body centred cubic (bcc) lattice. The melting point and boiling point of niobium are 2468 °C and 4744 °C respectively. It has the highest low temperature ductility of 20% at -173 °C, the highest solubility of interstitial elements and the least sensitivity in ductility with interstitial content of all the refractory elements. It is a superconductor below the critical temperature  $T_C \sim 9.3$  K [1]. Niobium resists attack by most gases below 200 °C. However, as with other refractory metals (Mo, Ta and W) it begins to oxidize at about 500 °C. It reacts with nitrogen above 300 °C and is embrittled by hydrogen above 250 °C. Nb metal finds application for a wide temperature range from 4 to 1400 K. The applications of Nb are in superconducting wires [2], in aircraft gas turbine and vacuum tubes [3] and in mint metal [4]. An important application for niobium is as an alloying element to strengthen high-strength-low-alloy steels used to build automobiles and high pressure gas transmission pipelines [5, 6]. An important secondary role for niobium is to provide creep strength in super-alloys operating in the hot section of aircraft gas turbine engines [7]. Niobium is also utilized in the production of superconducting niobium-titanium alloys used for building magnetic resonance imaging (MRI) magnets [8]. Minor applications include electronic ceramics and camera lenses.

Niobium alloys fall into three major groups: moderately strengthened alloys for nuclear applications, high strength alloys for aerospace applications, and superconducting alloys for electronic applications. Niobium and its alloys offer attractive high-temperature properties, most of which are suitable for applications in nuclear environments including high temperature strength, long term creep strength, good thermal conductivity, low neutron absorption cross-section and compatibility with most liquid metal coolants [9-12]. As

niobium has the lowest density ( $8.57 \text{ g cm}^{-3}$ ) and best workability among the group of refractory metals its alloys are typically suitable for cold-working and fabrication of complex structures [13, 14] and find use as the structural components in nuclear reactors [15]. Due to their poor oxidization resistance at high temperatures niobium base alloys must be coated before use in high temperatures environments. Niobium and some niobium base alloys also have been used for heat shields in high temperature vacuum furnaces. Also they are used in several biological applications [16]. Nb-Zr alloys with and without carbon have been designated for advanced space power system applications due to their superior corrosion resistance to liquid alkali metal environment and having lower density as compared to other refractory metal alloys [17, 18]. Nb-1Zr alloy has been closely associated with the nuclear industry because of its excellent elevated temperature strength in the range of 900 to 1200 °C [15, 19, 20]. Fig. 1.1 shows that addition of 1wt.% Zr to Nb retains in solid solution. This acts as a solid solution strengthener in Nb-1wt.% Zr (Nb-1Zr) alloy.

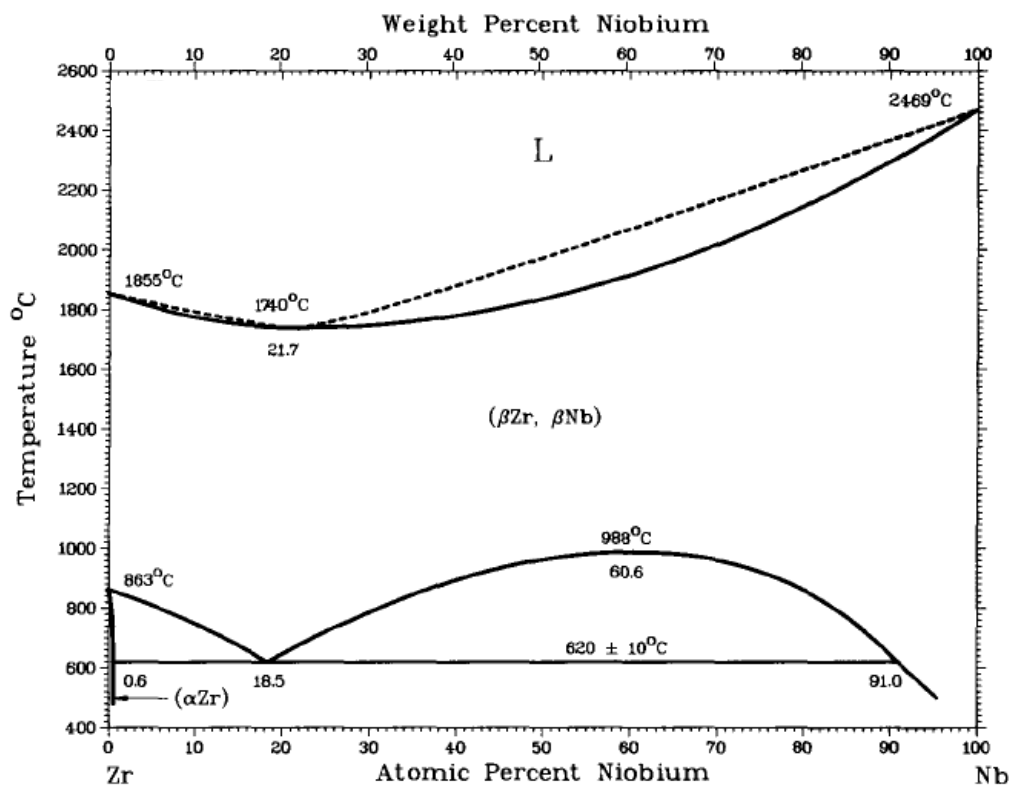
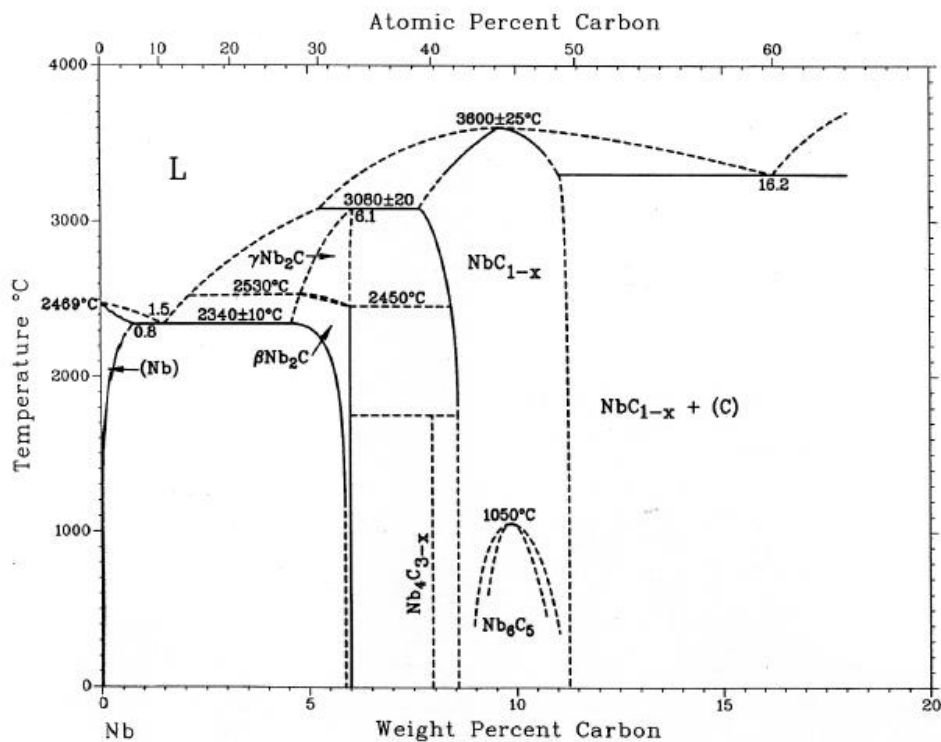


Fig. 1.1: Nb-Zr binary alloy equilibrium phase diagram.

One of the commercially produced Nb-alloys is Nb-1wt.% Zr-0.1wt.% C (Nb-1Zr-0.1C) for use in space power systems due to its good high temperature strength, lower density as compared with other refractory metals and alloys and good compatibility with liquid alkali metals [21-23]. The addition of 0.1wt.% of carbon promotes precipitation (Fig. 1.2) which was found to be effective in improving the creep strength of Nb-1Zr alloy. Nb-1Zr-0.1C alloy is a potential material for use in high temperature nuclear reactors [24-26]. Nb-Zr alloys are being actively considered for use in high temperature applications in compact high temperature reactor (CHTR) [27].



**Fig. 1.2:** Nb-C binary alloy equilibrium phase diagram.

The different steps in industrial processing for the fabrication of materials are:

- a. Melting and casting,
- b. Thermo mechanical processing – Hot deformation,
- c. Secondary processing steps,
- d. Final product.

An essential part in the processing of materials is hot deformation. The flow behaviour of metals and alloys during hot working play an important role for designers of metal forming processes. In order to study the workability and to establish the optimum hot processing parameters for metals and alloys, the thermo-mechanical experiments have been carried out over wide temperatures and strain-rates range, and some constitutive equations are developed to describe the hot deformation behaviours. Materials are transformed into high quality components by the set of operations of thermo-mechanical processing. The main objectives of thermo-mechanical processing is to break the cast microstructure, control of product microstructure, produce product without micro / macro defect or flow instabilities and finally to obtain product properties on a repeatable basis to minimize variability. Thermo-mechanical processing can result in the following defect free microstructural modifications:

- i. Grain refinement,
- ii. Special boundaries,
- iii. Texture,
- iv. Defect free / free of adiabatic shear band,

and can provide a suitable microstructure for secondary processing.

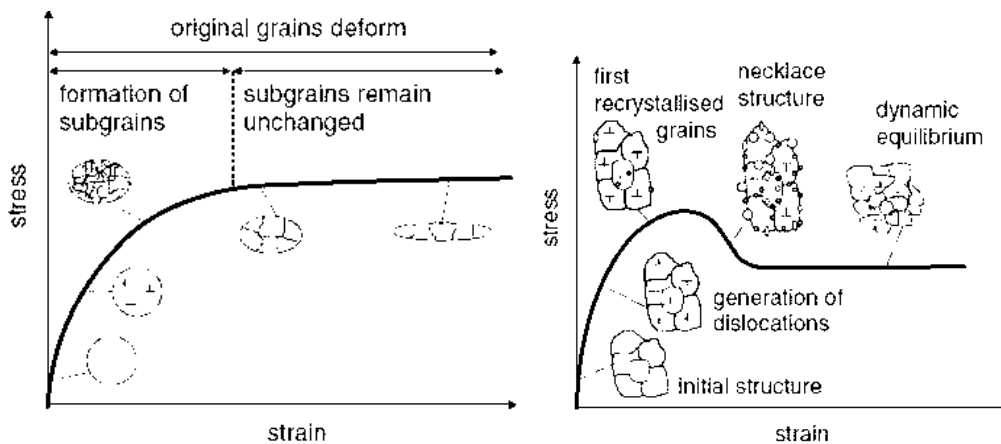
Forming operations may be carried out at room temperature or at elevated temperatures, and at a low or a high rate of deformation. Based upon temperature, deformation process can be classified as either hot deformation or warm deformation. The manufacture of advanced materials often includes deformation processes at elevated temperatures, typically in the hot working regime. Some forms of small-scale simulative tests are used to select the temperature and deformation rate for such operations. From these tests the optimum conditions of both workability and microstructure development are readily identified. In addition, such tests provide estimations of the flow stress dependence on the level of deformation, deformation rate, and temperature, or information which is valuable in

selecting equipment as well as in the design of preforms and tooling via increasingly popular numerical techniques. For bulk forming operations, such as forging, rolling, and extrusion, the isothermal hot compression test is often used as a simulative test because of its similarity to the actual forming operation in terms of stress state and achievable deformation rates.

During hot deformation the primary micro-mechanisms operating are (Fig. 1.3):

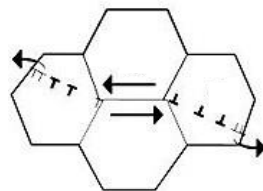
- i. Dynamic Recovery (DRV),
- ii. Dynamic Recrystallization (DRX),
- iii. Grain Boundary deformation.

The most significant of the many changes associated with recrystallization and other annealing phenomena is the decrease in the dislocation density.



(a) Dynamic Recovery

(b) Dynamic Recrystallization



(c) Grain boundary sliding

**Fig. 1.3:** Different hot deformation mechanisms.

DRX is preferred in industrial processing because it reduces the crystalline defect (dislocation) density and hence reduces the load required for processing. It also helps to homogenize and reconstitute the microstructure and control texture of the deformed material. DRX results in a product which is free of defects such as cracks, adiabatic shear bands, etc. to provide a suitable microstructure for secondary processing. The ductility is enhanced and large deformation can be imparted to the materials.

## **1.1 Structure of thesis**

In this investigation the deformation behavior of Nb and Nb-1Zr and Nb-1Zr-0.1C alloys were studied from room temperature to 1700 °C and wide strain rates range. Chapter 1 introduces the topic. In chapter 2 a literature review about the deformation of bcc metals and alloys (specifically recent deformation studies on Nb alloys) are highlighted. Also uses of Nb based alloy and microstructural and texture evolution studies of Nb alloys are included. Chapter 3 deals with the details of experimental methods employed for deformation and the microstructural characterization techniques used. Chapter 4 deals with the results and discussion of the deformation behavior and microstructural evolution of Nb, Nb-1Zr and Nb-1Zr-0.1C alloys. Also the kinetics of dynamic recrystallization of Nb alloys is discussed in this chapter. The summary of the current topic is given in Chapter 5.

## **Chapter 2. Background**

This chapter deals with the literature on six aspects of present studies. The first aspect deals with general deformation behavior of metallic materials. The second aspect describes the deformation of bcc metals and alloys. The third aspect discusses the deformation studies on mechanical behavior of Nb and its alloys. The fourth aspect focus on microstructure and texture development of Nb alloys during deformation process. The fifth aspect discusses processing by hot deformation and the six aspect highlights different high temperature deformation mechanisms. Given this literature survey the gaps in the literature are identified and the objectives of the dissertation are mentioned.

### **2.1 General deformation behaviour of metallic materials**

Plastic deformation of materials primarily involves dislocation slip and twinning [28]. Slip entails the movement of dislocations and their generation resulting from dislocation-dislocation interaction. These mechanisms can occur for different processing conditions and crystal structures of materials. At high temperatures diffusive processes start dominating, either aiding the movement of dislocations or deforming by purely diffusive mechanisms. At high temperatures because fine grained alloys have a larger fraction of grain boundaries, grain boundary sliding becomes the dominant deformation mechanism. Thus at a given temperature a combination of these mechanisms determine the macroscopic mechanical behaviour of materials.

#### **2.1.1 Deformation by slip**

Plastic deformation on a microscopic scale consists of the movement of large numbers of atoms in response to an applied stress. The Burgers vector ( $\mathbf{b}$ ) describes the magnitude and direction of the lattice distortion induced by a dislocation. To accommodate plastic deformation, dislocations slip on preferred slip planes along preferred slip directions

(direction of dislocation movement). There are two basic types of dislocation movements (a) glide (conservative motion) and (b) climb (non-conservative motion). In glide the dislocation moves on the plane which contains both its line and  $\mathbf{b}$ , whereas in climb the dislocation aided by diffusion, moves out of the glide plane. Glide of many dislocations results in slip, which is the most common manifestation of plastic deformation in crystalline solids. Dislocations glide if an applied stress reaches a critical resolved shear stress for a given slip system. Dislocations can attract or repel each other depending on their orientation [29]. Dislocation annihilation occurs more frequently when a dislocation can move from one slip plane to another [30]. The dislocation annihilation process occurs by (a) cross slip which is driven by thermally activated glide at low temperatures ( $T < 0.3T_m$ , where  $T_m$  is the absolute melting temperature) and (b) climb which is driven by vacancy assisted dislocation at high temperatures ( $T > 0.6T_m$ ). At intermediate temperatures ( $0.3T_m < T < 0.6T_m$ ) both processes take place, exhibiting a mixed behaviour. Cross slip is thermally activated and is responsible for dislocation generation, annihilation and cell formation. This mechanism is more difficult to activate in metals with low stacking fault energy, as dislocation dissociation is more favourable.

### **2.1.2 Deformation twinning**

Deformation twinning is an important plastic deformation mechanism in materials. One of the mechanisms of twinning is based on the localised stress concentrations due to pile up of dislocations at grain boundaries which favours the splitting of dislocations into partials and whose movements then nucleate twins. The stress required to form a twin is generally much larger than that required to cause slip. Twinning tends to occur in instances where plastic deformation via slip is hindered and occurs along with slip. Twinning is also less sensitive to temperature. Twinning involves shear displacements on specific crystallographic planes and in specific crystallographic directions. Deformation twinning in coarse-grained materials has

been reviewed by Christian and Mahajan [31]. They reported the detailed insight into the twin interface and twinning dislocations and the influence of material variables (grain size, pre-strain, texture, alloy composition and precipitates) on twinning. In fcc and bcc materials, stacking faults and deformation twins usually occur in metals and alloys with low stacking fault energy whereas in hcp metals and alloys, twinning is a common deformation mechanism because of their small number of slip systems. Tome et al. [32] showed that in polycrystals of less than cubic crystal symmetry (Zr alloys), when plastic deformation is dominated by twinning the texture development too is controlled by twinning. Also Randle showed the indirect role of annealing twinning on processing route schedules to produce successfully a grain boundary engineered microstructure with improved properties [33].

### 2.1.3 Thermally activated deformation

The important feature of bcc pure metals and alloys is the strong temperature dependence of the yield and flow stresses at low temperatures and its concomitant effect on slip geometry. Taylor reviewed the thermodynamical aspects of theory of deformation. He showed the relation between the thermodynamical quantities to experimental measurements and discussed the selection of experimental results covering the range of bcc metals and alloys [34]. To describe various deformation behavior the starting point is a mechanical transport equation proposed by Orowan as [35]

$$\dot{\gamma} = A \rho_m b v \quad (2.1)$$

where  $\dot{\gamma}$  is the shear strain rate,

$v$  is the mean velocity of dislocations with Burgers vector magnitude  $b$

$\rho_m$  is the dislocation density

and  $A$  is a geometrical coefficient.

The mobile dislocation segments of average length  $l$ , are held up by the shear stress  $\tau$  against the energy barrier at position  $y_0$ , while  $y_c$  is the threshold position of the dislocation while by-passing this barrier. The change of Gibbs free energy of the sample as the dislocation moves from  $y_0$  to  $y_c$  is called  $\Delta G$ . It is used to characterize the energy barrier opposing dislocation motion. Then the shear strain rate is given as

$$\dot{\gamma} = A \rho_m b \left( \frac{A^l}{l} \right) \nu_l \exp\left( \frac{-\Delta G}{kT} \right) \quad (2.2)$$

where  $k$  is Boltzmann's constant and

$T$  is the absolute temperature

$\Delta G$  is the change in Gibbs free energy of activation (strongly dependent on the shear stress  $\tau$ ),

$A^l$  is the area swept by segment  $l$  between two successive obstacles

and  $\nu_l = b \nu_d / l$ ,  $\nu_d$  being the Debye frequency  $\approx 10^{13} \text{ s}^{-1}$ .

The thermodynamical analysis of deformation was done by the rate equation for plastic flow which is controlled by thermal fluctuations as

$$\dot{\gamma} = \dot{\gamma}_0 \exp\left( \frac{-\Delta G}{kT} \right) \quad (2.3)$$

$$\text{where } \dot{\gamma}_0 = A \rho_m b \left( \frac{A^l}{l} \right) \nu_l \quad (2.4)$$

### 2.1.3.1 Activation volume

The stress experienced by an individual dislocation in a crystal is a combination of the applied resolved shear stress,  $\tau_a$ , and stresses from other sources. An effective shear stress,  $\tau^*$ , is therefore defined as

$$\tau^* = \tau_a - \tau_i \quad (2.5)$$

where  $\tau_i$  is a long-range internal stress arising from the elastic strain fields of other dislocations or the back stress due to curvature of the glide dislocation. The internal stress

may be positive or negative but when considering thermally-activated motion of dislocations over short-range obstacles, it is always subtracted from the applied stress because in regions of the crystal where  $\tau_i$  aids slip, the obstacle's effectiveness is nullified. The activation volume is defined as

$$V = - \left( \frac{\partial G^*}{\partial \tau^*} \right) = kT \left( \frac{\partial \ln \left( \frac{\dot{\gamma}}{\dot{\gamma}_0} \right)}{\partial \tau^*} \right) \quad (2.6)$$

The activation volume value gives the signature of the dislocation mechanism. The activation volume is further described in section 4.2 of results and discussion.

### 2.1.3.2 Peierls stress

The stress required to move a dislocation in an otherwise perfect lattice is known as the Peierls stress or the Peierls-Nabarro stress or the lattice friction stress. The Peierls stress arises from changes in the core energy of a dislocation with its exact position in the crystal lattice. The energy changes have a periodicity equal to a unit lattice vector in the direction of motion. The large yield stress and the strong temperature dependence of body centred cubic (bcc) metals is a consequence of a large Peierls stress as compared to face centred cubic (fcc) or hexagonal closed pack (hcp) metals. The Peierls barrier in bcc crystals is critically dependent on the character of the dislocation. Edge and mixed dislocations have planar cores and relatively low Peierls stresses. The screw dislocation, on the other hand, has its core spread over several intersecting planes and consequently is much harder to move. The screw dislocation is responsible for the strong temperature dependence of the yield and flow stresses observed in bcc metals. At low stresses the length of activated segment is unlikely to remain fixed so that  $\Delta G$  (the change in free energy of activation) will be stress dependent; certainly all experiments show an increasing activation volume as the effective stress decreases. For

Peierls barrier model the thermal activation analysis of Nb-Zr solid solution showed that the activation volume is  $v^* < 10 b^3$ , the activation enthalpy is  $H^* < 19.3 \text{ kJ mol}^{-1}$  and the total enthalpy  $H_0 \sim 154.4 \text{ kJ mol}^{-1}$  at low temperatures [34].

### 2.1.3.3 High temperature deformation

The mechanical behavior of materials at elevated temperature is controlled primarily by thermally activated processes. The strength of materials at high temperatures is strongly dependent on strain rate and temperature. In the high temperature regime the strength of materials decreases and ductility increases with increase in temperature. This is due to increase in equilibrium concentration of vacancies with temperature which results in increase in mobility of atoms. Dislocation climb occurs as the rate controlling step in atomic diffusion via diffusion of vacancies or interstitials. At high temperature the mobility of dislocations is enhanced by the mechanism of climb. It is also known that diffusion controlled processes have a very significant effect on high temperature mechanical properties and non-conservative deformation mechanisms come into play at elevated temperatures. The time dependent deformation behavior of a material at a constant load is called creep. The basic mechanisms of hot deformation and high temperature creep may be depending on strain rate and temperature regime. In that regime both processes can be described by a power law relation. The steady state creep rate for intermediate to high stress levels at temperature above  $0.5T_m$  is given by a power law relation as,

$$\dot{\varepsilon}_s = \frac{AD_v \mu b}{kT} \left( \frac{\sigma}{\mu} \right)^n \quad (2.7)$$

where  $\mu$  is the shear modulus,  $A$  and  $n$  are material constants and  $D_v$  is the diffusion constant. Eq. (2.7) can be rewritten as

$$\dot{\varepsilon}_s = B\sigma^n \exp(-Q/kT) \quad (2.8)$$

Sherby showed that crystal structure, melting temperature, valence and elastic modulus are the important factors in determining the high temperature creep strength of pure polycrystalline metals [36]. According to his results diamond has the best structure for highest creep resistance with its covalent bonds; the second best structure is the close-packed structure, namely the fcc and hcp; and third is the more open bcc structure. The higher values of the melting temperature, valence and elastic modulus of the pure material gives better creep resistance of the material. Also he showed that at high stresses Weertman's theory of creep based on dislocation motion and climb is best to describe the experimental data for creep of pure metals. At low stresses the Nabarro-Herring theory of creep based on atomic diffusion (without dislocation motion) appears to become the controlling mechanism. Also Shreby and Burke studied the high temperature mechanical behavior of crystalline solids at elevated temperature [37]. They discussed the strength of materials in terms of creep resistance. Their results showed that the creep rate is controlled by the rate of atom mobility and is proportional to the diffusion coefficient  $D$ . They concluded that the influence of composition, temperature and crystal structure on the high temperature strength can be explained by the influence of these variables on the diffusion coefficient.

Mukherjee et al. described the elevated temperature crystalline plasticity through a constitutive relation that links the stress, strain rate, grain size and temperature [38]. In generalized form the equation is:

$$\dot{\varepsilon} = A \frac{D\mu b}{kT} \left(\frac{b}{d}\right)^p \left(\frac{\sigma}{\mu}\right)^n \quad (2.9)$$

where  $\dot{\varepsilon}$  is the steady-state strain rate,

$D$  is the appropriate diffusivity (lattice or grain boundary),

$d$  is the grain size,

$p$  is the grain size exponent,

$\sigma$  is the applied stress,

and  $n$  is the strain rate sensitivity of the flow stress.

This correlation (Eq. 2.9) known as Mukherjee-Bird-Dorn (MBD) correlation provide a quantitative estimation of the steady-state creep rate in the creep damage accumulation relationship. This correlation made the depiction of deformation mechanism maps in normalized coordinates. Mukherjee suggested that a universal creep curve can be constructed from the steady-state creep rate estimated from the MBD correlation [39].

## 2.2 Deformation of body centred cubic materials

Plastic deformation of bcc metals mostly occurs by dislocation slip. This process is driven by thermally activated kink pair migration which leads to dislocation cross slip for both dislocation generation and annihilation [40]. The dislocation mobility and climb process are enhanced by the presence of vacancies. The annihilation of dislocations occurs via vacancies segregation around the dislocation's core. At higher temperatures vacancy assisted dislocation climb becomes the dominant annihilation mechanism.

Taylor showed that all bcc metals and alloys exhibit thermally-activated flow of dislocations over a Peierls barrier at sufficiently low temperatures [34]. Also Christian has pointed out that the flow stress in bcc metals features three regimes with respect to temperature variations, being the transition points between the ranges  $\sim 0.15 T_m$  and  $\sim 0.33 T_m$  [41]. The concentration of alloying elements and temperature have a significant effect on flow stress of metals and alloys to initiate plastic deformation (Fig. 2.1) as reviewed by Honeycombe [42]. In bcc metals and alloys, small additions of alloying elements have been shown to decrease the temperature dependence of the yield stresses, flow stresses or hardness at low temperature (below  $0.15 T_m$ ) and is referred to as alloy softening [43]. The critical

concentration for the maximum alloy softening effect increases as the temperature is reduced and is about 2 - 10 at.% for substitutional alloys and 0.02 - 0.05 at.% for interstitial alloys.

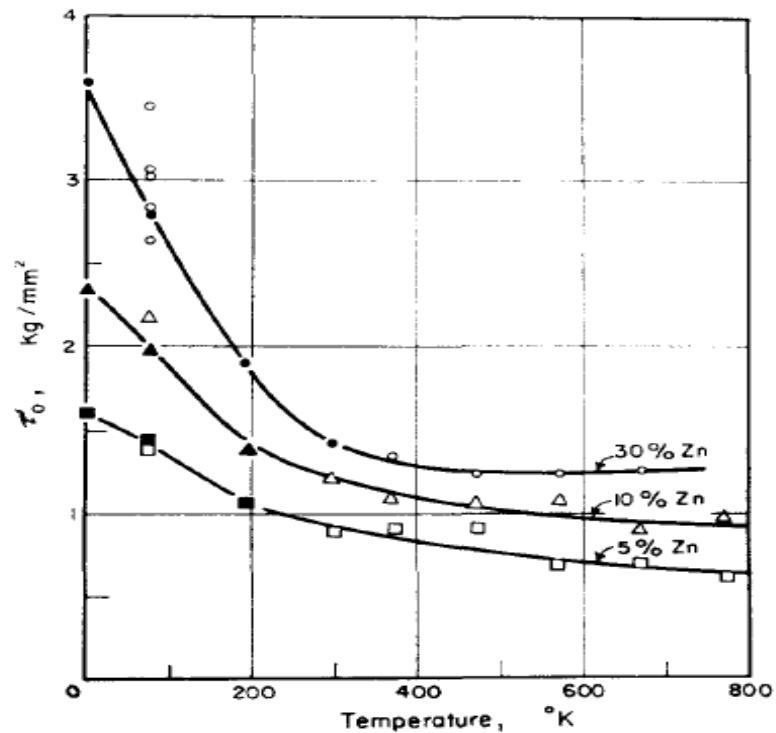


**Fig. 2.1:** Dependence of critical resolved shear stress for brass on concentration and temperature [42].

Meyers et al. studied the mechanical response of metals by constitutive description of dynamic deformation by the four interrelated aspects as (a) instability; (b) the slip-twinning transition; (c) grain-size effects; and (d) shock compression [44]. Armstrong and Walley reviewed the high strain rate mechanical properties of metals and alloys [45]. They described the dependence of flow stress from a dislocation mechanics viewpoint over a large range of experimental results.

### 2.3 Mechanical behaviour of Nb and its alloys

The deformation behavior of Nb and its alloys such as creep and the general high temperature mechanical behavior ranging over strain rates of  $10^{-3} \text{ s}^{-1}$  and 3000 to 8000  $\text{s}^{-1}$  and temperature range of -196 to 527  $^{\circ}\text{C}$  have been studied [46-52]. Fourdeux and Wronski studied the tensile

properties of niobium at 25 and -196 °C [53]. They also investigated the effects of grain size, purity, testing speed and dislocation structure on the deformation properties of niobium [54]. Torne and Thomas made a detailed comparison of the substructures and mechanical properties of polycrystalline niobium deformed at room temperature [55]. They showed that impurities are not responsible for the temperature dependence of the yield stress. Also the yield drop is due to dislocation multiplication and the effect of grain size on the yield and flow stress appears to be significant through the dislocation density. Dislocation cell structures are formed only in impure Nb containing dispersed precipitates. Briggs and Campbell showed that the rate sensitivities of the yield and flow stress of niobium increase with increasing stress at strain rates of  $1.7 \times 10^{-4}$  to  $10^2 \text{ s}^{-1}$  and temperatures from -196 to 327 °C [56]. They mentioned that the work-hardening rate is independent of temperature and decreases slightly with increasing strain rate at these deformation conditions. Further the plastic flow of Nb is significantly affected by the strain-rate history.

Flow stress of commercially pure niobium over a temperature range of -196 to 527 °C and strain rates of  $10^{-3}$  to  $8000 \text{ s}^{-1}$  was investigated in quasi-static and dynamic compression by Nemat-Nasser and Guo (Fig. 2.2) [46]. Their results showed that below room temperature the flow stress at low strain rates was more sensitive to temperature and that different deformation mechanisms exist at low and high strain rates. Also adiabatic shear bands occur at low temperatures and high strain rates. The physical and mechanical properties of polycrystalline and single crystal niobium were studied by Myneni for superconducting radio frequency (SRF) cavity [57]. Banani et al. analysed theoretically the high temperature deformations of niobium by decoupling the thermal phenomena from the elastic-thermal reaction [58]. Zamiri et al. studied the mechanical properties of the superconducting niobium and proposed the optimal microstructure and texture for fabricating cavities from high purity niobium [59].

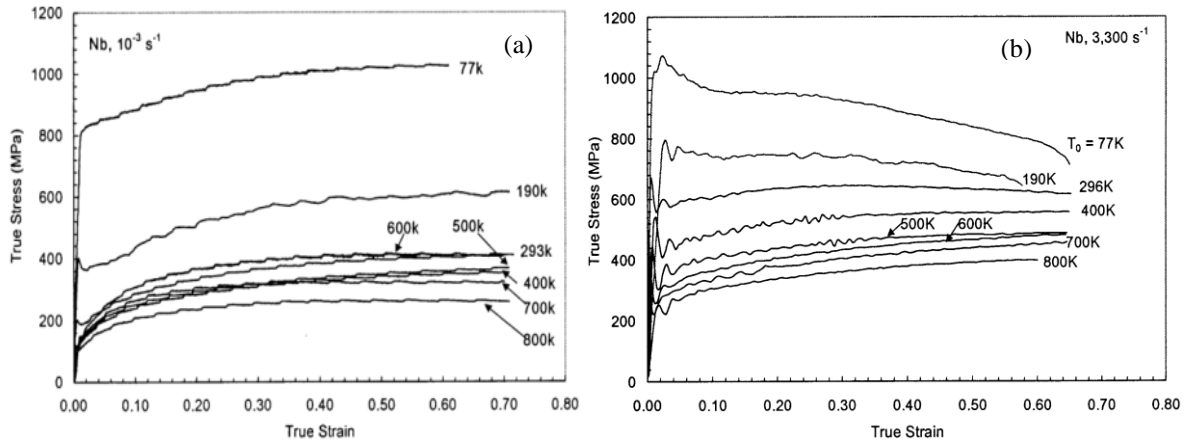


**Fig. 2.2:** (a) Isothermal stress vs. strain curves at strain rate of  $10^{-3} \text{ s}^{-1}$  and (b) adiabatic stress vs. strain curves at strain rate of  $3300 \text{ s}^{-1}$  for Nb for indicated temperatures [46].

Begley and Bechtold reported that the addition of vanadium and chromium to Nb resulted in the largest increase of the room temperature mechanical strength of Nb, whereas addition of titanium and hafnium resulted in the smallest increase in strength and the remaining elements give intermediate strength [60]. At higher temperature of  $1095 \text{ }^{\circ}\text{C}$  addition of zirconium and vanadium give the largest increase in strength of Nb due to solid-solution strengthening, titanium has very little effect; molybdenum, tungsten and hafnium are intermediate strengtheners. Gill and Argent studied the hot working characteristics of several two-phase niobium-carbon alloys and discussed the results in terms of solid solution hardening and dispersion hardening [49]. They reported that commercial niobium containing about 0.01% C showed greater ductility than the carbon-containing alloys and a comparatively large increase in the amount of deformation at temperatures above  $1300 \text{ }^{\circ}\text{C}$ . A similar increase was reported by them for carbon-containing alloys at about  $1550 \text{ }^{\circ}\text{C}$ . McCoy evaluated the creep properties of the Nb-1Zr alloy at  $982$  and  $1204 \text{ }^{\circ}\text{C}$  [61]. They showed that solution annealing of Nb-1Zr alloy at  $1200$  to  $1700 \text{ }^{\circ}\text{C}$  for 1 hour significantly improved the creep properties due to both the decreased grain size and the changes in the grain boundary structure. At high stresses fine precipitate were formed normal to the applied stress at  $982 \text{ }^{\circ}\text{C}$ . Delgrosso et al.

developed different high strength Nb-Zr-C alloys and established mechanical properties of these Nb alloys [26]. They reported that Nb-3Zr-0.34C and Nb-3Zr-0.4C were the only alloys that exhibited concomitant maximum yield and 100 h rupture strength at 1315 °C. These Nb-Zr-C alloys show maximum strength at 1315 °C when carbides were dissolved during the extrusion process and reprecipitated as fine particles uniformly distributed throughout the matrix, as well as in subgrain boundaries and dislocation sub cell walls. Nb-1Zr-0.1C was completely ductile in both the as-welded and post heat treated conditions.

For last few decades many researchers have studied the mechanical and thermal creep properties of Nb-1Zr-0.1C alloy. Titran investigated the long time high vacuum creep behavior of Nb-1Zr alloy at 1077 °C [62]. The creep strength of the annealed Nb-1Zr-0.1C alloy at 1077 and 1127 °C was more than three times that of the annealed Nb-1Zr alloy due to the intergranular precipitates [10, 62]. Titran and Uz showed that Nb-1Zr sheets with 0.06 and 0.1 C have much better creep resistance than Nb-1Zr at 1077 °C and the creep resistance increased with increasing carbon content [62, 63]. The thermomechanical processing and the microstructural characterization studies of Nb-1Zr-0.1C alloy were done by Titran et al. [10, 63-65]. The creep strength of Nb-1Zr is higher than pure Nb at 1027 °C due to solid solution strengthening mechanisms as reported by Davidson et al. [66]. The monotonic creep behavior of precipitation strengthened Nb-1Zr-0.1C alloy was comparable with Nb-1Zr alloy (at high stresses) and is superior to pure niobium as reported by Farkas et al. [67]. The creep microstructure of Nb-1Zr-0.1C alloy showed a classic dislocation substructure whose cell size was inversely proportional to the applied stress except at very low stresses. Also they showed that the normalised effective stress was insensitive to the applied stress and temperature during steady-state creep conditions (constant structure) [68]. Neutron irradiation up to 1.8 dpa at temperatures of 800, 950 and 1100 °C resulted in increased strength and reduced elongation of Nb-1Zr [69]. McGreevy et al. studied the mechanical behavior of unirradiated

and irradiated Nb-1Zr alloy [52]. Watanabe et al. reported the microstructural evolution of neutron irradiated Nb-1Zr alloy at 520 to 730 °C from moderate to high doses as 47.2 dpa [70].

Texture has an effect on the high temperature mechanical properties of Nb-1Zr alloy at 1100 °C as reported by Nieh et al. [51]. According to their results the tensile deformation of Nb-1Zr at 1100 °C in the rolling direction had about 20% stronger texture than that oriented 30° to the rolling direction. Ding and Jones investigated the mechanical behaviour of Nb<sub>35</sub>Ti<sub>6</sub>Al<sub>5</sub>Cr<sub>8</sub>V (at.%) alloy containing different C contents (0, 1, 10 at.%) for both constant strain rate tests and creep tests [71]. The effect of temperature on steady-state creep-rate of the Nb alloys with different C contents is shown in Fig. 2.3. The activation energies values were obtained as 298 - 370 kJ mol<sup>-1</sup> for these Nb alloys. From TEM microstructural investigations they reported that the presence of extensive carbides resulted in a substantial increase in yield strength at room and high temperatures and also improved the creep resistance. The room temperature and high temperature strengths increase with increasing C content, whereas room temperature ductility of the alloy decreases due to the breaking of primary carbide during compression [72].

Sarkar et al. [47] showed that Nb-1Zr-0.1C underwent DRX at temperatures from 1400 to 1700 °C and at strain rates of 10<sup>-3</sup> to 1 s<sup>-1</sup>. Recently Chaudhuri et al. [73] showed that for Nb-1Zr-0.1C alloy substructures were formed and DRX occurred at 1500 to 1700 °C at strain rate of 10<sup>-1</sup> s<sup>-1</sup> and the necklace structure formation was more prominent at low strain rates of 10<sup>-3</sup> and 10<sup>-2</sup> s<sup>-1</sup>.

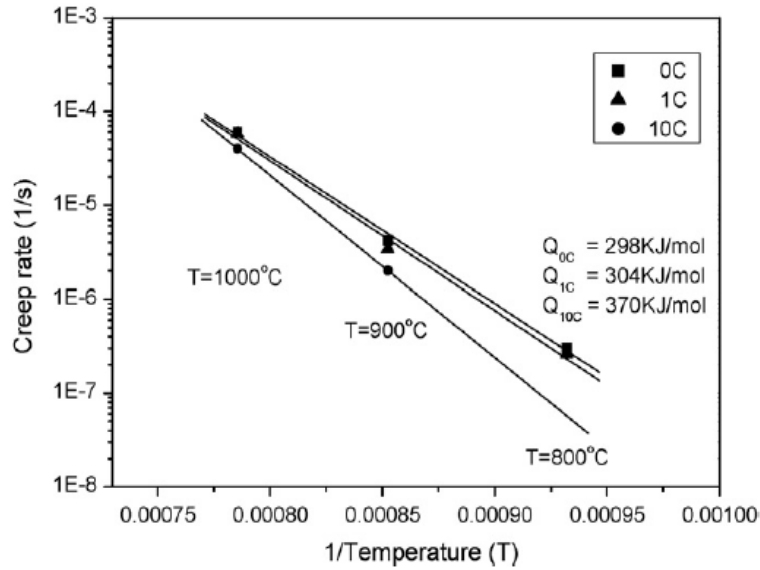


**Fig. 2.3:** Creep-rate as a function of temperature for the 0 C, 1 C and 10 C alloys at 100 MPa [71].

## 2.4 Microstructure of Nb and its alloys

The aspects of deformed microstructure as: (1) microstructural evolution, (2) dislocation boundaries and (3) macroscopic properties were discussed by Hansen [74]. The microstructural evolution during plastic deformation follows a pattern of grain subdivision [75]. He classified the dislocation boundaries into geometrically necessary boundaries (GNBs) and incidental dislocation boundaries (IDBs). By using this type of dislocation boundaries classification he analyzed the distribution of structural parameters such as misorientation angle and the boundary spacing. The dependence of structural parameters distributions on the strain comes out as a result of his work. He described the microstructural evolution in theoretical models based on general principles for the formation of dislocation structures during plastic deformation by slip. The microstructural characterization studies on Nb-Zr-C alloys have established that the precipitates are orthorhombic Nb<sub>2</sub>C and cubic (Zr,Nb)C [63, 76, 77]. The effects of initial extrusion temperature and the subsequent thermomechanical processing on the microstructure of Nb-1Zr-0.1C tubes was studied by Uz and Titran [65]. The microstructure and high temperature strength of Nb-Mo-Zr-C alloys

were investigated from room temperature to 1500 °C by Tan et al. [78]. They reported that the compressive yield strengths of Nb-Zr-C alloys were improved significantly with Mo addition from room to elevated temperature.

Vishwanadh et al. studied the microstructures of the as-cast, deformed and recrystallized samples of Nb-1Zr-0.1C alloy [79], and showed that along with the bcc phase carbides were also present. Electron microscopy and energy dispersive spectroscopic analyses revealed that the carbide precipitation undergoes various phase transformations. The as-cast structure of Nb-1Zr-0.1C alloy had hexagonal Nb<sub>2</sub>C precipitates (Fig. 2.4) in the Nb matrix and after extrusion, the deformed microstructure had two types of carbide precipitates: needle and rectangular morphology precipitates (Fig. 2.5). The needle shape precipitates were of (Nb, Zr)<sub>2</sub>C with orthorhombic structure and rectangular shape precipitates were of (Nb, Zr)<sub>3</sub>C<sub>2</sub> with hexagonal structure. After annealing, the recrystallized microstructures showed equilibrium structure (Fig. 2.6). Most of the prior existing carbides were dissolved and (Nb, Zr)C precipitates (fcc structure) in the Nb matrix during the recrystallization.

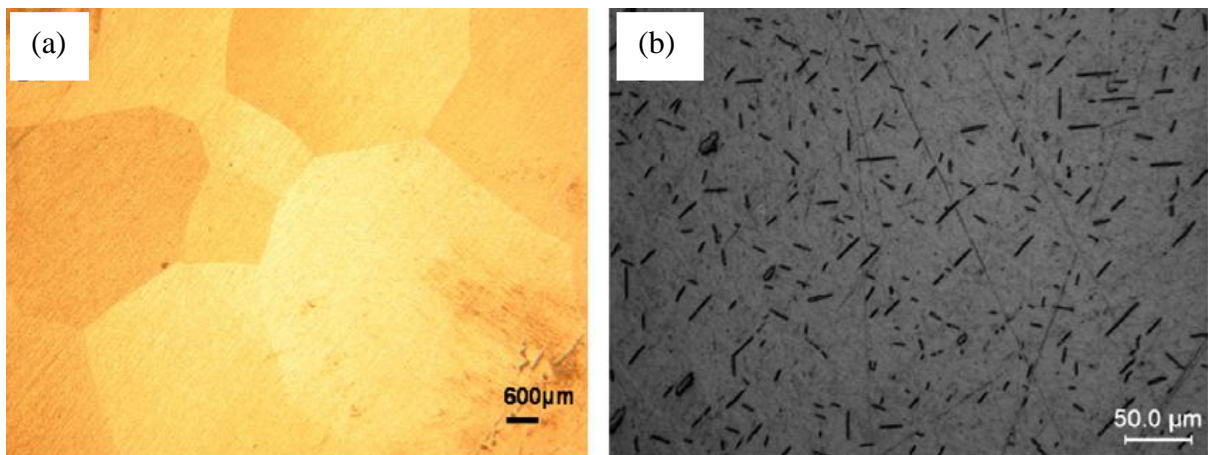


**Fig. 2.4:** Optical microstructure of as-cast microstructure of Nb-1Zr-0.1C alloy (a) low magnified image showing big grains and (b) high magnified image showing needle shape precipitates within the grain [79].

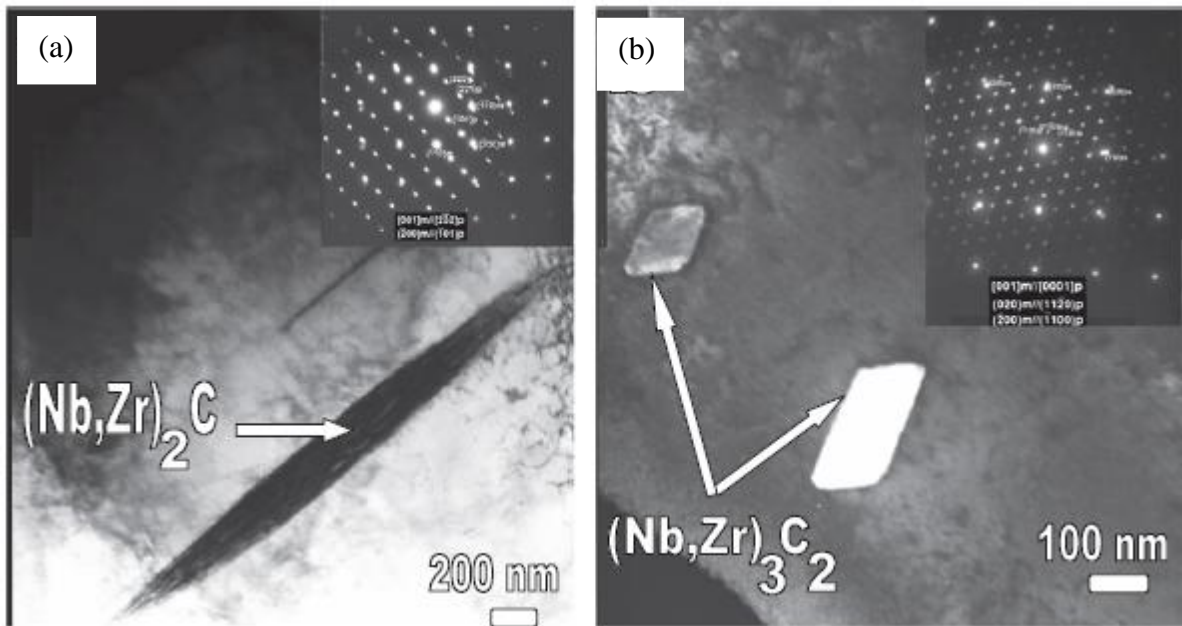


**Fig. 2.5:** TEM micrograph of the (a) needle and (b) rectangular shape precipitate present in the deformed Nb-1Zr-0.1C alloy and the inset figure shows the SAED patterns of the precipitate and matrix [79].

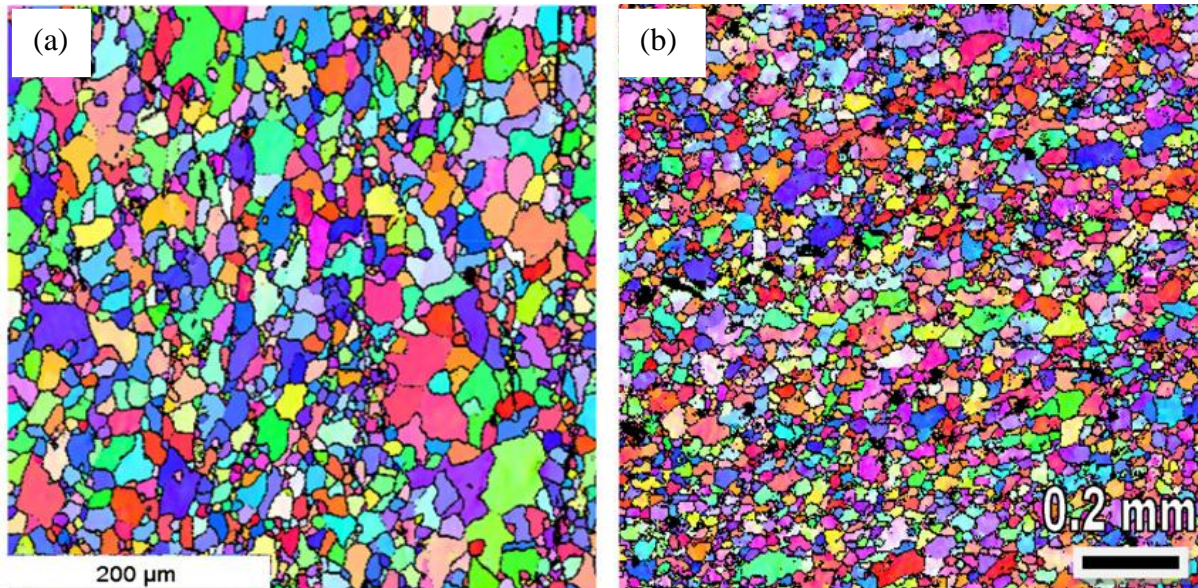


**Fig. 2.6:** IPF images of the Nb-1Zr-0.1C alloy samples heat treated at (a) 1300  $^{\circ}\text{C}$  for 3 h and (b) 1500  $^{\circ}\text{C}$  for 2 h show nearly recrystallized microstructure. The sample annealed at 1500  $^{\circ}\text{C}$  showed larger presence of carbides at grain boundaries of recrystallized grains [79].

## 2.5 Processing by hot deformation

### 2.5.1 Ashby map

Ashby introduced the idea of deformation mechanism map [80, 81]. This map displays the fields of stress and temperature in which a particular mechanism of plastic flow is dominant. As most materials deformed by several alternative and independent mechanisms for different deformation conditions, mechanisms like dislocation glide, diffusional flow and dislocation creep appear as a field on the map. A point on a map then identifies the dominant mechanism and indicates the resulting strain rate. The significance of this deformation map is based on the creep mechanisms applicable at lower strain rates. These maps are very useful for alloy design. Ashby discussed three applications of the maps as

- i.* The effect of crystal structure and atomic bonding on plastic flow.
- ii.* The design of experiments to study a given flow mechanism and in locating, identifying and characterizing missing mechanisms.
- iii.* A qualitative way for choosing a material for engineering applications for predicting the mechanism by which it deforms and the effects of strengthening mechanisms.

Knowledge of any two of the three variables of stress, temperature and strain rate locates a point on the map, identifies the dominant mechanism or mechanisms and gives the value of the third variable. As Ashby map considers modulus-compensated stress ( $\sigma/\mu$ ) as a function of homologous temperature ( $T/T_m$ ) at constant grain size (where  $\mu$  is the shear modulus,  $T_m$  is the melting point of the material) its application is limited to only steady state flow stress regime. Also several mechanisms fields are missing from the deformation mechanism map and the time or strain dependent effects are not included. They are useful in spite of their inexactness for both designing and interpreting experiments and in selecting and understanding the behaviour of materials for engineering applications.

### 2.5.2 Strain rate sensitivity map

Many materials processing are done at strain rates orders of magnitude higher than those observed during creep deformation and therefore they involve different microstructural regimes. These difficulties were addressed by Raj by considering strain rate as one of the direct variables and temperature as the other. He extended the concept of Ashby's maps to construct a processing map by atomistic approach [82]. The Raj processing map represents the limiting conditions for two damage mechanisms: (i) cavity formation at hard particles in a soft matrix occurring at lower temperatures and higher strain rates; (ii) wedge cracking at grain boundary triple junctions occurring at higher temperatures and lower strain rates. This map shows a safe region for processing where neither of the two damage mechanisms nor adiabatic heating occurs. The practical difficulties for use of the Raj map are due to the variation of the location of safe boundaries and a number of materials constants required for construction of the map. Also Raj map do not guide the workability optimisation directly and is not useful for commercial alloys. These issues of atomistic approach of Raj map was addressed by Prasad et al. by using the dynamic materials modelling (DMM) approach for describing the material behaviour under processing conditions [83]. This model forms a bridge between the continuum mechanics and the microstructural mechanisms occurring during hot deformation, and consists of principles of irreversible thermodynamics of large plastic flow [84]. The processing maps developed by using this model were used to optimize hot workability of materials and for process design in bulk metal working [85-87]. These processing maps have been applied to analyze several industrial problems including process optimization, product property control, and defect avoidance. However the fundamentals of the DMM model have been questioned [88] and lately strain rate sensitivity maps (SRS) maps have been used and correlated with microstructural evolution [47, 89, 90]. These SRS ( $m$ ) maps were constructed from the stress, temperature and strain rate data. The SRS map

exhibits domains of high strain rate sensitivity, which are considered as the domain of hot workability.

## **2.6 High temperature deformation mechanisms**

Hot working is generally carried out at strain rates in the range of 1 - 100 s<sup>-1</sup>. During deformation, energy is stored in the material mainly in the form of dislocations. This stored energy is released in three main processes as recovery, recrystallization, and grain coarsening (subsequent to recrystallization).

### **2.6.1 Dynamic recovery**

Dynamic recovery is a process in which dislocation rearrangement and annihilation occurs during plastic deformation (Fig. 1.3a). These are different from static recovery processes which are driven by defect interactions and are not strongly influenced by the applied stress. The decreasing rate of strain hardening in the course of plastic deformation at low temperatures is attributed to dynamic recovery processes. Dynamic recovery occurs via dislocation climb, cross-slip and glide, which result in the formation of low angle boundaries. The applied stress provides an additional driving force for the movement of low angle boundaries. Dislocations of opposite sign will be driven in opposite directions, and this stress assisted migration of dislocation boundaries may contribute significantly to the overall strain. Such migration results in some annihilation of dislocations in opposing boundaries and these enable the subgrains to remain approximately equiaxed during the deformation. Some reorientation of subgrains may also occur during hot deformation. The subgrains can therefore be considered to be transient microstructural features [91]. During the process of recovery, annihilation and rearrangement of dislocations lead to the formation of cell structure which transform with strain into subgrains (low angle boundaries). A constant density of dislocation is observed within the subgrains. After a strain of typically 0.5 to 1, the subgrain

structure often appears to achieve a steady state. The microstructural changes occurring during dynamic recovery are summarized schematically in Fig. 2.7. Dynamic recovery occurs only when dislocations move out of their slip planes by cross-slip and is much more sluggish when dislocations are widely extended [92].

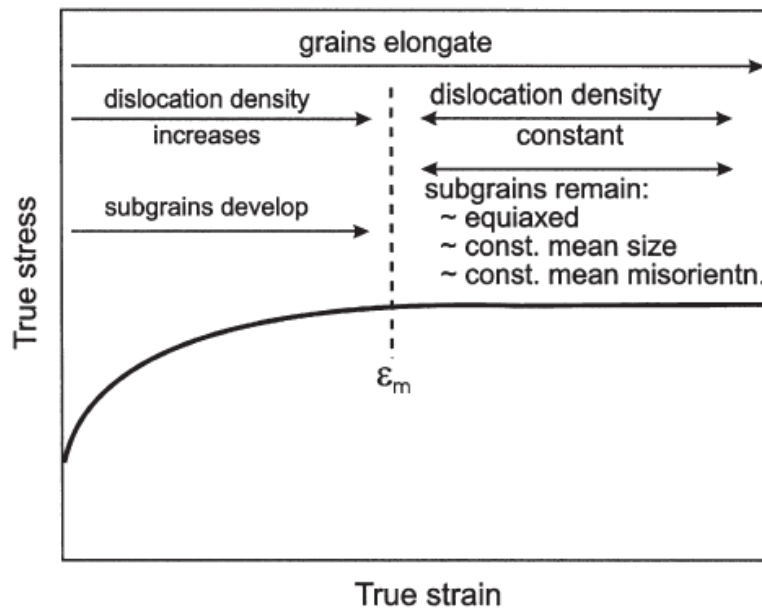


**Fig. 2.7:** Schematic summary of the microstructural changes occurring during dynamic recovery [91].

As recovery proceeds, the sequences of structural changes emerge as:

- a. The point defects and their clusters anneal out.
- b. The dislocations annihilate and rearrange into lower energy configurations.
- c. Polygonization leads to subgrain formation and subgrain growth occurs.

### 2.6.2 Dynamic recrystallization

Static recrystallization (SRX) is a process of replacement of a deformation microstructure by nucleation and growth of new grains during annealing (Fig. 2.8). In the early stages of SRX,

the nuclei are outlined by low angle boundaries, the misorientations of which gradually increase until they attain values typical of high angle boundaries (HABs). The microstructure consists a mixture of increasing amounts of recrystallized grains and decreasing amounts of strain hardened grains during annealing. This process is referred to as discontinuous static recrystallization (dSRX) [93]. Dynamic recrystallization (DRX) is defined as a process in which replacement of the deformation microstructure occur by new grains during deformation. DRX takes place during straining, as long as the temperature is above about  $0.5T_m$ . New DRX grains are produced and they grow by migration of the boundaries, which consume the strain hardened microstructure. The driving force for the growth of such new grains is the stored energy associated with the dislocations and sub-boundaries produced during prior straining.

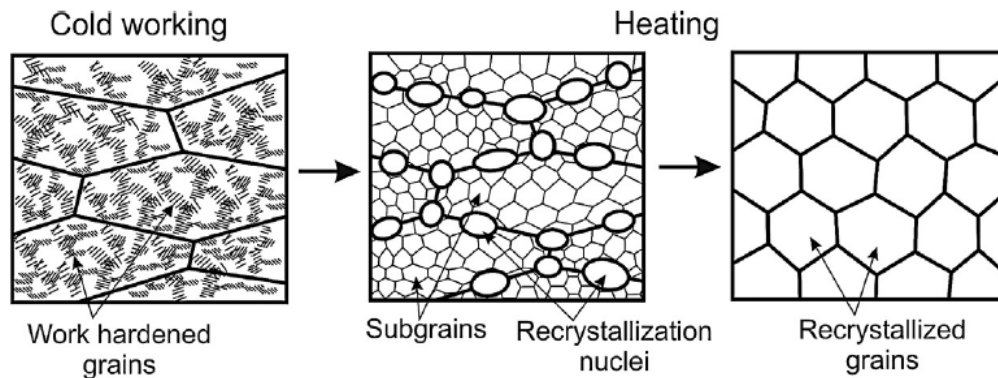


**Fig. 2.8:** Schematic representation of the discontinuous static recrystallization (dSRX) taking place during the annealing of strained materials [93].

The occurrence of recrystallization during deformation at elevated temperatures was surveyed by Honeycombe and Pethen [94]. They reported that dynamic recrystallization occurred after a critical strain which is stress dependent. They discuss the mechanism by which the new grains are nucleated. Their results showed that pinning of grain boundaries by sub-boundaries is a prime factor for initiation of dynamic recrystallization at grain boundary serrations. The critical strain for initiation of DRX depends on (a) the chemical composition of the material

under consideration, (b) the grain size prior to deformation, and (c) the deformation schedule (temperature and strain rate) [95-97]. McQueen developed the theory of DRX and characterized different types of DRX as [98]

(1) discontinuous dynamic recrystallization (dDRX);

(2) geometric dynamic recrystallization (gDRX);

(3) continuous reactions or continuous dynamic recrystallization (cDRX);

According to McQueen the nucleation and growth of new grains are attained by the migration of high angle grain boundaries that absorbs existing dislocations leaving behind a region with low dislocation density [99].

#### **2.6.2.1 Discontinuous dynamic recrystallization (dDRX)**

This type of recrystallization occurs during plastic deformation and is similar to static recrystallization where relatively strain free grains nucleate and grow and consume deformed grains. Like static recrystallization (SRX), it is more frequently observed at elevated temperatures, but it is now known that it is also observed in pure metals at relatively low temperatures, such as about  $0.3T_m$ , ( $T_m$  the melting temperature). The microstructure up to a strain of about 1 is that of the individual grains of the polycrystal containing low misorientation cell or subgrain walls in a low energy dislocation configuration. With DRX, this structure contains numerous small grains or nuclei that are initially relatively dislocation free. With continuing deformation these develop subgrains with a higher dislocation density. DRX may be particularly observed in lower stacking fault energy materials where dynamic recovery may be retarded due to inhibition of dislocation cross-slip. Discontinuous dynamic recrystallization occurs during high temperature deformation of a wide class of metals, such

as copper and copper alloys, austenitic plain carbon or stainless steels, nickel and nickel-based superalloys. The main phenomenological characteristics of dDRX are as follows [96]:

- i. It involves local repeated cycles of strain hardening and recrystallization, which generate quite inhomogeneous grain sizes and dislocation distributions.
- ii. Steady state is generally reached at moderate strains, typically  $\epsilon < 1$  and the steady-state flow stress and microstructural parameters are independent of the initial grain size [100].
- iii. An inverse power law relationship is commonly observed between the steady-state flow stress and the average steady-state grain size [101].
- iv. The strain rate sensitivity of the flow stress associated with dDRX is higher than that typical of dynamic recovery.

#### **2.6.2.2 Continuous dynamic recrystallization (cDRX)**

This mechanism begins with the recovery process where subgrain boundaries form within grains. These subgrain boundaries have misorientations of just a few degrees, much lower than high angle grain boundaries (typically  $10^\circ$  -  $62^\circ$  for cubic materials). Gourdet and Montheillet showed that continuous dynamic recrystallization is more prevalent in commercial purity aluminium than in pure aluminium and Al-Mg alloy. That means the transformation of low angle boundaries into high angle boundaries is faster when the recovery level is neither too high nor too low. They confirm that the strain path does not alter noticeably the cDRX kinetics [102]. High stacking fault energy (SFE) metals, such as aluminium, beta titanium alloys, and ferritic steels, undergo continuous (cDRX) rather than discontinuous dynamic recrystallization (dDRX) during high temperature deformation [103]. During cDRX geometrically necessary boundaries are gradually transformed into HABs [104].

The main characteristics of cDRX are:

- i. A steady state is observed at very large strains.
- ii. The crystallite size decreases strongly up to a strain  $\epsilon = 5$ ; it then increases slowly to reach a steady value at large strains ( $\epsilon = 30$ ).
- iii. Low angle grain boundaries are generated at low strains; part of them start to transform into HABs at moderate strains ( $\epsilon = 1$ ).
- iv. A strong crystallographic texture forms at large strains.

### **2.6.2.3 Geometric dynamic recrystallization (gDRX)**

McQueen et al. introduced the concept of geometric dynamic recrystallization (gDRX) in a commercial purity aluminium. In gDRX the shape of the original grains change during deformation and their boundaries become progressively serrated while subgrains form. Consequently, the grain boundary area per unit volume grows and an increasing fraction of subgrain facets is made from those initial grain boundaries. Ultimately, when the original grain thickness is reduced to about two subgrain sizes, the grain boundaries begin locally to come into contact with each other, causing the grains to pinch-off (Fig. 2.9) [105].

Geometric dynamic recrystallization has been observed at elevated temperatures where dynamic recovery has been observed, which includes subgrain boundary formation. gDRX has been confirmed in Al and Al–Mg alloys [9,10]. Kassner and Barrabes studied the development of gDRX. In gDRX substantial grain refinement occurs through a process of grain elongation and thinning leading to a dramatic increase in grain boundary area. The grain boundaries become serrated as a result of subgrain (low angle) boundary formation. Pinching off and annihilation of high angle grain boundaries occurs as the original grains thin to about twice the subgrain diameter to a steady-state structure. The gDRX is a general

phenomenon that can lead to grain refinement in the absence of any dDRX or cDRX processes [106].

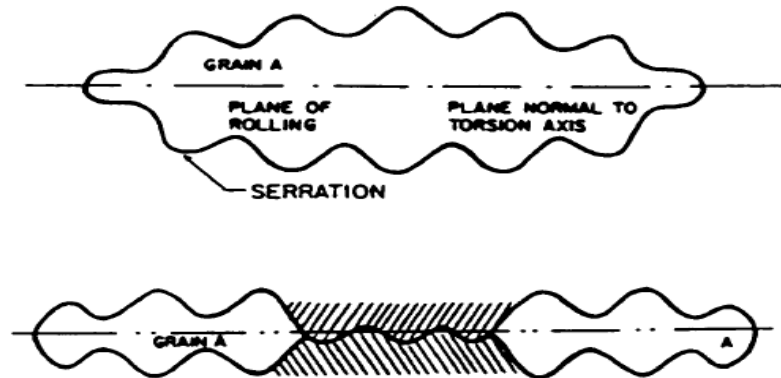


**Fig. 2.9:** Schematic of grain boundaries pinch off where opposite serrations meet in case of gDRX [105].

Blum et al. reported gDRX in an industrial Al alloy (5083) containing precipitate [107]. They showed that gDRX occurs not only by recombination of opposite boundaries of the thinned grain but also by pinching off of serrations in the grain boundaries. The size of the gDRX grains is about two to three times the subgrain size. Balasundar et al. [108] studied the geometric dynamic recrystallization (gDRX) or globularisation of lamellae of near alpha titanium alloy-TITAN 29A. The initiation and evolution of globularisation was investigated using the flow curve analysis method.

#### 2.6.2.4 Geometric necessary boundaries

During deformation, the individual grains of polycrystal can subdivide into smaller grains, each having a misorientation with respect to each other. These are now generally referred to as geometrically necessary boundaries (GNBs) and not generally considered a recrystallization phenomenon. These were shown to form in single crystals, even on slip planes with low Taylor factors [98]. GNBs separate regions that deform by different slip system combinations, strain amplitudes and strain. These GNBs appear to increase in misorientation with increasing strain.

### 2.6.2.5 Other Studies on DRX (Factors affect DRX)

The interstitial content in Nb has an influence on its recrystallisation temperature. For controlled purity niobium (50 ppm O<sub>2</sub>) recrystallisation occurs at the lowest temperature of  $0.34T_m$  as reported by Thompson and Flewitt [109]. Sandstrom and Lagneborg developed a theoretical model for both static recrystallization and dynamic recrystallization [110, 111]. Their model gives the volume distributions of dislocations in terms of work-hardening and recovery of the dislocation structure as well as recrystallization and continuous grain growth. Their model suggests that the distinct peak stress at high strain rate is an effect of the variation in grain size during the dynamic recrystallization. The flow stress, final grain size and ductility are mostly affected by the presence of dynamic recrystallisation [112]. Gottstein and Deshpande investigated the occurrence of dynamic recrystallization under changing deformation conditions, including changes of strain rate and strain path and the effect of annealing [113]. They reported that dynamic recrystallization can be delayed by pre-deformation at a higher strain rate or facilitated by intermediate annealing, load cycling or strain path changes. Also concluded that the occurrence of dynamic recrystallization is controlled by the dynamic recovery rate, and that dynamic recovery is much faster and more effective than static recovery in rearranging the microstructure. The initiation of DRX is preceded by growing fluctuations of the grain boundary shape. Serration and bulges develop and eventually new grains are generated along these prior grain boundaries by strain induced sub-boundary formation mechanism.

Ueki et al. [114] discussed the effect of the stacking fault energy, Zener-Hollomon parameter, the solute elements and the value of strain on DRX of copper, Cu-Al alloys and nickel. According to their study when cross-slip and climb of dislocations occur as the major controlling processes of dynamic recovery, metals of high SFE (low stacking fault width) would have lower activation energy for the processes than metals of low SFE (large stacking

fault width), because of the necessity of constriction of the separation. The ease with which dynamic recovery takes place in metals of high SFE makes it difficult to develop a high density of dislocations which is required for dynamic recrystallization. In metals, dislocations generated during deformation usually tend to recover easily into boundaries of subgrains with low misorientation. The motions of boundaries are extensively inhibited in metals of low SFE due to the large separation between the partials which result in a high dislocation density. This causes migration and the formation of boundaries. Thus, dynamic recrystallization occurs more easily in metals of low SFE as compared to those with high SFE, from the kinetics point of view. SFE is the most important factor controlling dynamic recrystallization especially in pure metals. Using the Zener-Hollomon parameter  $Z$ , it may be possible to define the flow stress transition from single to multiple peaks which is characteristic of dynamic recrystallization behavior. The addition of solute elements which lower the SFE further reduces the degree of dynamic recovery in substructures. These solutes also reduce the mobility of the grain boundary, retarding dynamic recrystallization and shifting the start of DRX to higher strains. Also dynamic recrystallization seems to occur in most materials given appropriate conditions independently of the SFE. The SFE affects only the kinetics of dynamic recrystallization. This means that the occurrence of dynamic recrystallization in materials of high SFE depends largely on the strain, strain rate and temperature.

Sakai and Ohashi investigated the dislocation substructures developed during hot deformation of pure nickel [115]. They classified the full DRX substructures which were distributed heterogeneously throughout the microstructure into three categories as shown in Fig. 2.10: (a) DRX nuclei, (b) growing DRX grains containing a dislocation density gradient, and (c) large DRX grains with a fairly homogeneous substructure. Once hot deformation has ceased, the just nucleated dDRX grains (Fig. 2.10a) continue to grow without requiring an incubation time, as indicated by the dashed lines in this figure. This is referred to as meta

dynamic recrystallization (mDRX), a term originally proposed by Jonas and co-workers. The growing dDRX grains (Fig. 2.10b) contain few dislocations near their boundaries, so classical nucleation is not possible in the grain interiors and they can only soften by static recovery (SRV). Finally, the fully strain-hardened dDRX grains (Fig. 2.10c) undergo SRV followed by nucleation, leading to classical SRX.

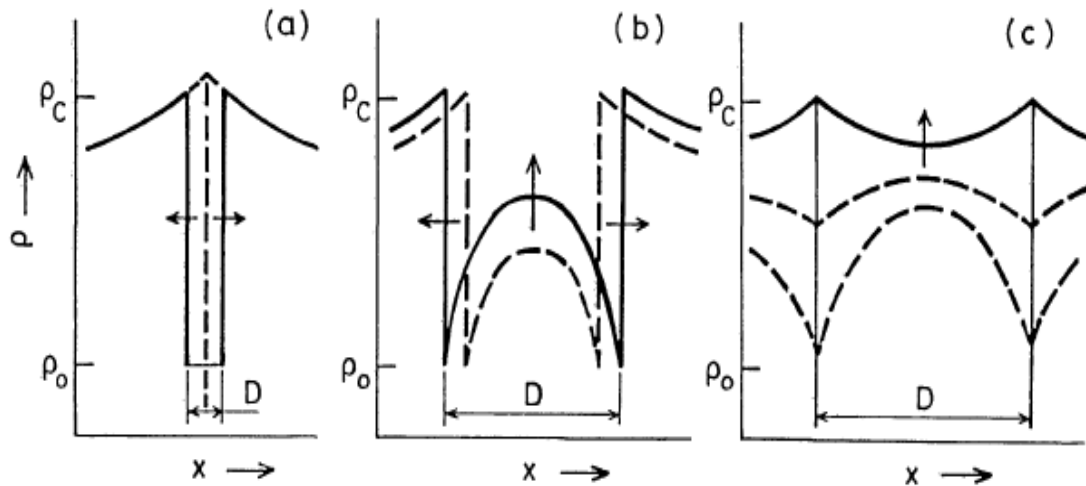


**Fig. 2.10:** Three types of dislocation density distribution developed in a microstructure undergoing dDRX: (a) a dDRX grain, (b) a growing dDRX grain and (c) a critically strain hardened dDRX grain. The current state is represented by full lines and one or more earlier states by broken lines.  $\rho_o$  is the initial (annealed) dislocation density,  $\rho_c$  is the critical value required for nucleation, and  $D$  is the current dynamic grain size [115].

The influence of the deformation temperature on recrystallization was investigated by Gottstein et al. [116]. The temperature dependence of the flow stress has to be accounted for when comparing recrystallization behavior at constant stress but at different deformation temperatures. They compared the recrystallization behavior at constant stress to study the effect of deformation temperature on recrystallization. Derby has given the empirical relation between the steady state grain size during dynamic recrystallisation and deformation stress for a number of metals and minerals as [101],

$$\frac{\sigma}{\mu} \left( \frac{D}{b} \right)^{2/3} = K . \quad (2.10)$$

The conditions to determine the critical values of flow stress, strain and strain hardening rate for the initiation of DRX under arbitrary deformation windows are (i) the local stored energy must attain a maximum and critical value and (ii) the rate of dissipation must decrease to a minimum value [117]. Ponge and Gottstein stated that the crucial step for nucleation of DRX in a subgrain structure is the generation of a mobile grain boundary [118]. For small angle grain boundaries, the mobility increases with growing misorientation, but a misorientation across boundary of 10 - 15° is assumed to be necessary for nucleation to occur. Rollett developed a Monte Carlo model for dynamic recrystallization which used to simulate static recrystallization and grain growth [119]. The model simulates dynamic recrystallization by adding recrystallization nuclei and stored energy continuously with time. The simulations reproduce many of the essential features of dynamic recrystallization. Jonas investigated the evidence for the occurrence of dynamic recrystallization under industrial forming conditions such as rolling and also explained the importance of DRX in scientific context for industrial applications [120].

#### **2.6.2.6 Recent studies on DRX**

A Monte Carlo model of dynamic recrystallization has been investigated by Peczak and Luton [121] which provides a comprehensive description of the dynamic recrystallization process and requires one strain rate dependent recovery parameter. Montheillet et al. [122] proposed a general model to describe the dDRX phenomena which includes strain hardening and dynamic recovery, nucleation, growth and shrinkage of grains. Computer simulations are used to study effects of an experimentally determined 3D distribution of nucleation sites on the recrystallization kinetics and on the evolution of the recrystallized microstructure as compared to simulations with random nucleation by Storm and Jensen [123]. Solhjo

developed a mathematical model to predict the stress-strain curves of alloy steel during hot deformation up to the peak stress and also the critical strain for initiation of dynamic recrystallization [124]. He developed a model to predict the flow stress and the critical strain for the onset of dynamic recrystallization of the stress-strain curves [125]. Favre et al. [126] studied the nucleation of recrystallization in fine grained materials by the Bailey-Hirsch criterion. In the framework of nucleation driven by dislocation density, the contribution of the grain boundary energy stored in the microstructure was included in the energy balance. The Bailey-Hirsch criterion was extended to the case of nucleation in small grain materials. Fan et al. [127] developed a theoretical model considering the fundamental metallurgical principles of DRX to describe stress-strain curves as well as microstructure evolution in DRX. The mobile grain boundary area and the immobile grain boundary area are introduced as internal state variables to model the phenomena of nucleation and grain growth in DRX. The model provides an essential link for microscopic dislocation activities, mesoscopic microstructure evolution and macroscopic flow stress behavior. Stress-strain curves, recrystallized grain size and the percentage of DRX predicted by the model agree well with the experimental observations. The model also reproduces many features of DRX, including: (i) oscillatory behavior of flow stress curves at high temperatures or low strain rates and one single peak at low temperatures and high strain rates; (ii) Recrystallized grain size and steady state flow stress are determined by processing conditions; (iii) the kinetics of the percentage of DRX takes an exponential format; and (iv) initial grain size influences the stress-strain curves and recrystallization kinetics but has no effect on steady state stress and recrystallized grain size.

Galindo-Nava and Castillo [128] characterized the grain size behavior during discontinuous dynamic recrystallization in alloys by a theoretical approach that combines a novel thermo-statistics framework, with classical grain nucleation and growth formulations.

An alternative approach for accounting for solute-drag effects was also proposed by them. They reported that the drag atmosphere linearly amounts to the atomic radius of solute atoms. Momeni et al. [129] proposed a physical model based on the evolution of subgrains size to describe the nucleation and growth processes during discontinuous dynamic recrystallization. They showed that the evolution of subgrains to recrystallization nuclei occurred at very low strains. Afterwards, the number of stable nuclei increased (sigmoidal) with strain and reached a saturated state at about 0.6 times the peak strain. The dependence of nucleation rate on strain was modeled using an Avrami type equation. The driving force for the growth of recrystallized nuclei was similarly modeled in terms of strain. It is also shown that site saturation is the governing mechanism for the initiation of the discontinuous dynamic recrystallization at the grain boundaries. The flow stress of the material was calculated using the law of mixture of recrystallized and unrecrystallized regions with fractional softening as the stress-partitioning factor.

Cram et al. [130] developed a physically based model for nucleation during discontinuous dynamic recrystallization (dDRX) which was coupled with poly-phase plasticity and grain growth models to predict the macroscopic stress and grain size evolution during straining. The nucleation model is based on a recent description for static recrystallization and considers the dynamically evolving substructure size. Model predictions are compared with literature results on dDRX in pure Cu as a function of initial grain size, deformation temperature and strain rate. The characteristic DRX features such as single to multiple peak stress transitions, convergence towards a steady-state stress and grain size and a power law relationship between the stress and grain size are quantitatively reproduced by the model. The critical conditions for the onset of nucleation in the model are shown to compare well with Gottstein et al. [131] experimentally determined critical stress criteria. Wusatowska-Sarnek et al. [132] investigated the microstructure and microtexture evolved

under dynamic recrystallization in compression of polycrystalline copper. They concluded that DRX grains can be nucleated by bulging of some portions of serrated grain boundaries accompanied with the formation of GNBs or twinning (Fig. 2.11).

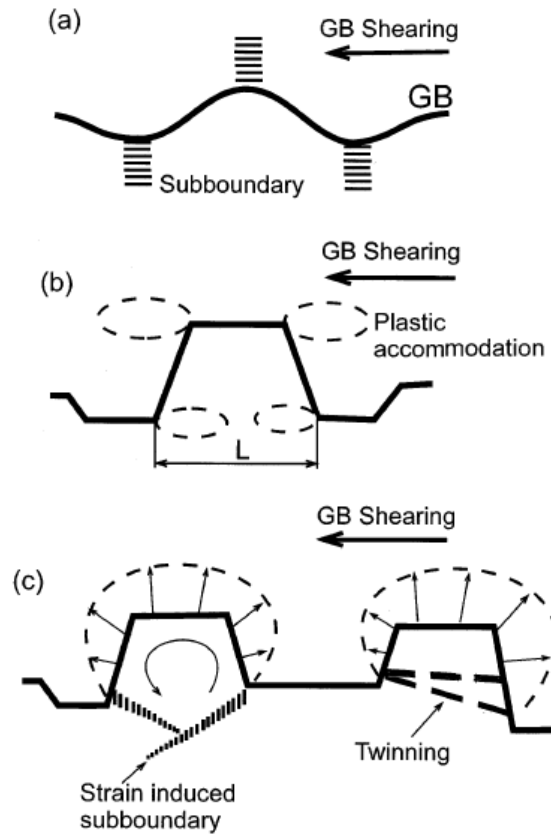


**Fig. 2.11:** Schematic representation of the nucleation of DRX grain (a) Boundary corrugation accompanied by the evolution of sub-boundaries. (b) Partial grain boundary sliding / shearing, leading to the development of inhomogeneous local strains. (c) Bulging of parts of a serrated grain boundary accompanied with the evolution of dislocation sub-boundaries or twinning, leading to the formation of a new DRX grain [131].

The steady-state behaviour of dynamic recrystallization (DRX) was studied in commercially pure copper and the austenitic steel alloy 800H by Graetz and Gottstein [133]. They investigated the grain size sensitivity of the flow stress behaviour during strain-rate and temperature change tests in the steady-state regime. The results confirmed the predicted connection of DRX grain size and deformation induced subgrain size. The grain size

distribution during steady-state DRX was evaluated and found to remain constant. A continuity equation of the growing and shrinking grain distributions is proposed which allows the steady-state flow stress to be calculated. Wang et al. [134] proposed a mathematical model for predicting flow stress up to the critical strain.

Ding and Guo [135] suggested that the oscillation of the stress-strain curve not only depends on thermomechanical processing parameters (strain rate and temperature) but also the initial microstructure. They reported that the mean recrystallized grain size is only a function of the Zener-Hollomon parameter. However, the percentage of DRX is not only related with the Zener-Hollomon parameter, but also influenced by the nucleation rate and the initial microstructure. Andrade et al. [136] studied plastic deformation of Copper at high strain (3 - 4) and high strain rate ( $10^{-4} \text{ s}^{-1}$ ). They suggested that the microstructure developed by dynamic recrystallization, which is enabled by the adiabatic temperature rise.

Price [137] showed that the Johnson-Mehl-Avrami relation provides only limited correlation with experimental data at low volume fractions, whereas the Speich-Fisher relation provides reasonably good correlation up to at least volume fractions of 0.95. He suggested that the simultaneous recovery can contribute to the strong negative deviation from linear Kolmogorov-Johnson-Mehl-Avram (KJMA) kinetics. He discussed the extent to which subcritical recovery treatments can affect subsequent recrystallization and the possibility that simultaneous recovery could prevail over non-uniform deformation as a cause of negative deviation from linear KJMA behavior. He reviewed strong evidence for the simultaneous occurrence of recovery during recrystallization [138]. An equation was suggested by Stuwe et al. [139] for an analysis of the influence of the rate of recovery on the Avrami-Johnson-Mehl-Kolmogorov equation which is meant to describe the kinetics of recrystallization.

Zahiri et al. [140] proposed a new method to quantify progress of dynamic recrystallization in polycrystalline metals during deformation. This approach utilizes the

stress-strain curve of the material to quantify the progress of dynamic softening. The effects on recrystallization kinetics and microstructure of growth rate distributions rather than a single growth rate for recrystallizing grains were investigated by Godiksen et. al. [141].

## 2.7 Gap areas

Most of the previous mentioned works on Nb alloys are in the lower strain rates (creep rate) regime and do not cover temperatures higher than 1200 °C. Further, there are no comprehensive studies on the mechanical behavior of Nb alloys at temperatures greater than 1200 °C. Also very few high strain rate deformation studies were carried out for Nb and practically none for Nb-Zr alloys. From the literature survey we find out the gap areas as

- i. Deformation behavior from 25 to 1700 °C for Nb-1Zr-0.1C alloy is not available
- ii. Effect of strain rate on deformation of Nb alloys are not fully studied
- iii. Microstructural characterizations are not carried out beyond 1200 °C
- iv. Evolution of microstructure with strain in DRX regime is not studied.

## 2.8 Objectives

Given the gap areas the objective of the dissertation is to study the deformation behaviour of Niobium, Nb-1Zr alloy and Nb-1Zr-0.1C alloy over a wide temperature range (27 to 1700 °C) and strain rate range ( $10^{-3}$  -  $10$  s<sup>-1</sup> and  $1000$  s<sup>-1</sup>). Specifically the present study includes the following.

- i. *Optimization of hot processing conditions.*

Optimum hot working conditions are determined by constructing processing maps and correlating these to the microstructural evolution. These maps are iso-contour plots of either strain rate sensitivity or its function plotted out on a temperature strain rate space.

These processing maps have been used to model the hot deformation behaviour of Nb and its alloys over a range of temperatures and strain rates. Also these iso-contour plots are used to understand the microstructural evolution with a view to optimize the hot workability at these temperatures.

*ii. Identifications of deformation mechanisms.*

Along with microstructural investigations, kinetics analysis can be used to identify the dislocation mechanisms associated with restoration mechanisms during high temperature deformation of Nb and its alloy. The deformation mechanisms of Nb alloys at high temperatures were identified by fitting the  $\sigma$ ,  $\dot{\epsilon}$  and  $T$  data at or near the high strain rate sensitivity domain to a power-law kinetic rate equation. The hot deformation mechanisms such as dynamic recovery (DRV), dynamic recrystallization (DRX) and grain growth are identified along with the characteristics features at high temperatures.

*iii. Structure - property correlation with deformation mechanism.*

As microstructure and texture are primarily used to establish the hot working condition for many metals and alloys, in this work attempt has been made to understand the microstructural development during high temperature deformation of Nb and its alloys. In order to correlate the flow behaviour with microstructural evolution of niobium alloy, the microstructure of samples deformed within the domain of hot workability were examined by using the optical microscopy and electron backscatter diffraction (EBSD) technique.

*iv. Evolution of dynamic recrystallization microstructure of Nb alloys.*

Since DRX is used as a tool for controlling the microstructure during secondary metallurgical processing, the microstructure and texture of the deformed samples of Nb-1Zr and Nb-1Zr-0.1C alloys were analysed in detail. In previous studies the microstructure was observed only at the final strain of around 0.6, where depending on the deformation condition, DRX had either completed or was in an intermediate stage; the

evolution of DRX with strain for Nb alloys has not been reported earlier. The start and completion of DRX and the favorable conditions for the necklace type of microstructures were not reported in previous studies. The detailed microstructural evolution of Nb-1Zr and Nb-1Zr-0.1C alloys with strain were characterized at deformation temperatures of 1400 to 1600 °C and at strain rate of  $0.1 \text{ s}^{-1}$ . The microstructural evolution was correlated with the deformation mechanisms along with identification of the start and completion of the DRX process.

v. *Kinetics studies of dynamic recrystallization of Nb-1Zr and Nb-1Zr-0.1C alloy.*

As DRX is considered to be the most important restoration mechanism during thermo-mechanical processing a detailed knowledge of DRX kinetics is essential during the processing steps. The present study focus on the kinetics of DRX behavior of Nb-1Zr and Nb-1Zr-0.1C alloy. The critical condition for the initiation of DRX was determined. The recrystallized fraction was estimated from the difference between the DRX flow curve as obtained by experiment and the corresponding dynamic recovery flow curve (reconstructed) assuming that recovery was the only operative restoration process. The difference between these two curves is the net softening and is directly attributed to DRX. The Avrami equation was used to describe the relationships between the DRX volume fraction and strain at given deformation temperature and strain rate.

## Chapter 3. Experimental methods

### 3.1 Materials

Annealed Nb, Nb-1Zr and Nb-1Zr-0.1C alloy were used for this study. The composition of Nb, Nb-1Zr and Nb-1Zr-0.1C alloys are given in Table 3.1, Table 3.2 and Table 3.3 respectively. The starting microstructures of these three materials are given in section 4.1.7 of microstructure and texture evolution.

**Table 3.1:** Elemental analysis of pure niobium in wt.%.

Element	Zr	Fe	Al	Nb
wt. %	0.1	0.08	0.05	Balance

**Table 3.2:** Elemental analysis of Nb-1Zr alloy in wt.%.

Element	H	C	N	Zr	O	Nb
wt. %	0.03	0.0114	0.06	1	0.04	Balance

**Table 3.3:** Elemental analysis of Nb-1Zr-0.1C alloy in wt.%.

Element	H	C	N	O	Zr	Nb
wt. %	0.02	0.067	0.02	0.03	1	Balance

### 3.2 Hot deformation

Uniaxial compression tests were conducted in a thermo-mechanical simulator (Gleeble 3800) on solid cylindrical samples of diameter 10 mm and height 15 mm at temperatures from 900 - 1700 °C in steps of 100 °C, and at strain rates from  $10^{-3}$  to  $10$  s<sup>-1</sup>. As Nb and its alloys are prone to oxidation at high temperatures all tests were done in vacuum of  $10^{-3}$  mbar. The samples were resistance heated with a type-C thermocouple spot-welded to the sample surface

to monitor and control the test temperature with an accuracy of  $\pm 1$  °C. To avoid friction the samples were placed between WC platens with Ta foil and graphite between sample and platen. The testing program profile is shown in Fig. 3.1. The samples were heated to the desired test temperature, held for 5 minutes, deformed to a true strain of 0.6 and quenched with argon gas to retain the microstructure prevailing during hot deformation. The average cooling rate during quenching was  $75$  °C  $s^{-1}$  for initial 7 s beyond which the cooling rate was slower but high enough to prevent any microstructural change. The load ( $F$ ) - displacement ( $d$ ) data obtained from the compression tests were first corrected to obtain plastic strain as

$$e = e_{total} - S/E \quad (3.1)$$

where  $e_{total}$  is the total strain and  $E$  is the combined modulus of machine and sample.  $S = F/A_o$  is the engineering stress and  $e = d/L_o$  is the engineering strain.  $A_o$  and  $L_o$  are the initial cross-sectional area and length of the sample respectively.

These were then converted into true stress ( $\sigma$ ) vs. true strain ( $\epsilon$ ) curves using standard equations of

$$\sigma = S(1 - e) \quad (3.2)$$

$$\text{and } \epsilon = -\ln(1 - e) \quad (3.3)$$

For high strain rates of 1 and 10  $s^{-1}$  the deformation conditions are adiabatic and the temperature rise ( $\Delta T$ ) during the hot deformation was calculated as

$$\Delta T = \frac{1}{\rho C_p} \int_0^\epsilon \sigma d\epsilon \quad (3.4)$$

where  $\rho$  is the mass density and  $C_p$  is the specific heat capacity [142]. The flow stress at the starting temperature was obtained by interpolation of the stress vs. the actual temperature ( $T + \Delta T$ ) plot.

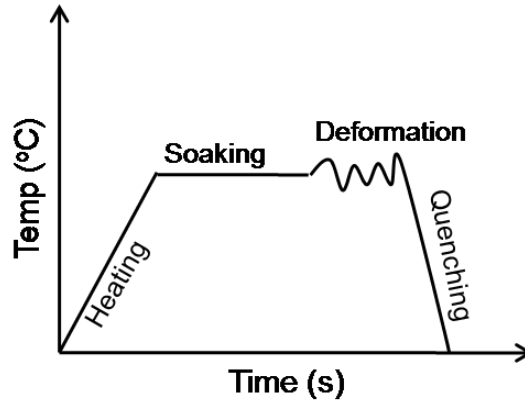


**Fig. 3.1:** Schematic profile of temperature vs. time for a hot deformation test.

### 3.3 Quasistatic deformation from room temperature to 700 °C

#### 3.3.1 Strain rate change test and stress relaxation test

The quasistatic behaviour of Nb-1Zr and Nb-1Zr-0.1C alloys were studied by uniaxial compression tests on a Zwick tensile testing machine. Solid cylindrical samples having dimensions of 5 mm diameter and 5 mm length were used for these compression tests. All deformation tests were done from room temperature to 700 °C by using the radiant heating furnace. The deformation tests from room temperature to 400 °C carried out at air atmosphere where as tests from 500 to 700 °C were done by glass coating of the samples. The temperature stability achieved during the mechanical test was  $\pm 1$  °C. In order to determine strain rate sensitivity and activation volume two different types of tests at starting strain rate of  $10^{-3} \text{ s}^{-1}$  were performed: (1) strain rate change test at different stress levels where strain rate was increased or decreased by a factor of ten (from  $10^{-3} \text{ s}^{-1}$  to  $10^{-4} \text{ s}^{-1}$  and again to  $10^{-3} \text{ s}^{-1}$  to  $10^{-2} \text{ s}^{-1}$ ), and (2) four successive stress relaxation runs of 15 seconds each at each stress level. The stress relaxation test was performed by stopping the cross-head of the testing machine at certain strain so that the applied total strain rate is zero during relaxation process (as total strain constant). The decrease in stress  $\Delta\sigma(t)$  (a negative quantity) was recorded with time (Fig. 3.2). This decrease in stress is accounted for by an increase of plastic strain  $\epsilon_p$  which

relieves the elastic strain  $\sigma/E_{eff}$ , where  $E_{eff}$  is the effective elastic modulus of specimen and machine.

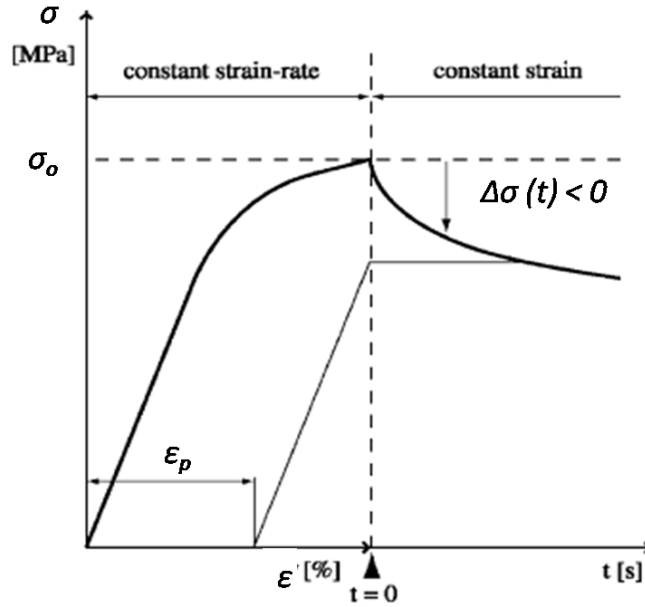


**Fig. 3.2:** Schematic representation of stress relaxation test.

The equation of the specimen and machine assembly during the relaxation is

$$\varepsilon = \left( \frac{\sigma}{E_{eff}} \right) + \varepsilon_p \quad (3.5)$$

The time derivative of the above equation is

$$\dot{\varepsilon} = \left( \frac{\dot{\sigma}}{E_{eff}} \right) + \dot{\varepsilon}_p \quad (3.6)$$

As total strain is constant during relaxation the LHS of above equation is zero and the equation becomes

$$\dot{\varepsilon}_p = - \left( \frac{\dot{\sigma}}{E_{eff}} \right) \quad (3.7)$$

The slope of the above relaxation curve gives the plastic strain rate at time  $t$ .

The relaxation curves can exhibit a logarithmic variation of stress with time, which is described by [143]:

$$\Delta\sigma = -\left(\frac{kT}{V_a}\right) \ln\left(1 + \frac{t}{c_r}\right) \quad (3.8)$$

where  $c_r$  is a time constant and  $V_a$  has the dimension of a volume. Fitting this relation with the relaxation curve provides  $V_a$  and  $c_r$ . Taking the time derivative of above equation and using the Eq. (3.7) the plastic strain rate during the relaxation is

$$\dot{\varepsilon}_p = -\left(\frac{kT}{MV_a}\right) \left(\frac{1}{t + c_r}\right) \quad (3.9)$$

The plastic strain rate which is calculated from the derivative of the relaxation curve during the test was used for the calculation of apparent activation volume ( $V_a$ ). For stress relaxations, it is worth noting that  $V_a$  is the apparent activation volume. The stress relaxation test consists of a repeated relaxation test with constant durations ( $\Delta t$ ), which starts at a given stress level ( $\sigma_o$ ). The first stress relaxation was done at stress  $\sigma_o$  over a time interval of  $\Delta t$ , which results in decrease of stress  $\Delta\sigma_1$ . The specimen is then reloaded to  $\sigma_o$  fast enough to obtain quasi-elastic conditions and is allowed to relax for the same time  $\Delta t$ , the decrease in stress is now  $\Delta\sigma_2$ , then again reloaded to  $\sigma_o$ , and this cycle repeated. In the present work four stress relaxations of 15 s each were carried out for Nb-1Zr and Nb-1Zr-0.1C alloy at temperatures range of 25 to 600 °C (in steps of 100 °C) and at a strain rate of  $10^{-3} \text{ s}^{-1}$ . Fig. 3.3 shows the multiple relaxation curves for Nb-1Zr-0.1C alloy at 200 °C. The relaxation curves exhibit a logarithmic variation of stress with time as describe above and this relaxation is used for the calculation of the plastic strain rate for each cycle. The strain rates  $\dot{\varepsilon}_{f1}$  and  $\dot{\varepsilon}_{i2}$  correspond to the end of stress relaxation 1 and the onset of stress relaxation 2 respectively (Fig. 3.3) were compared.

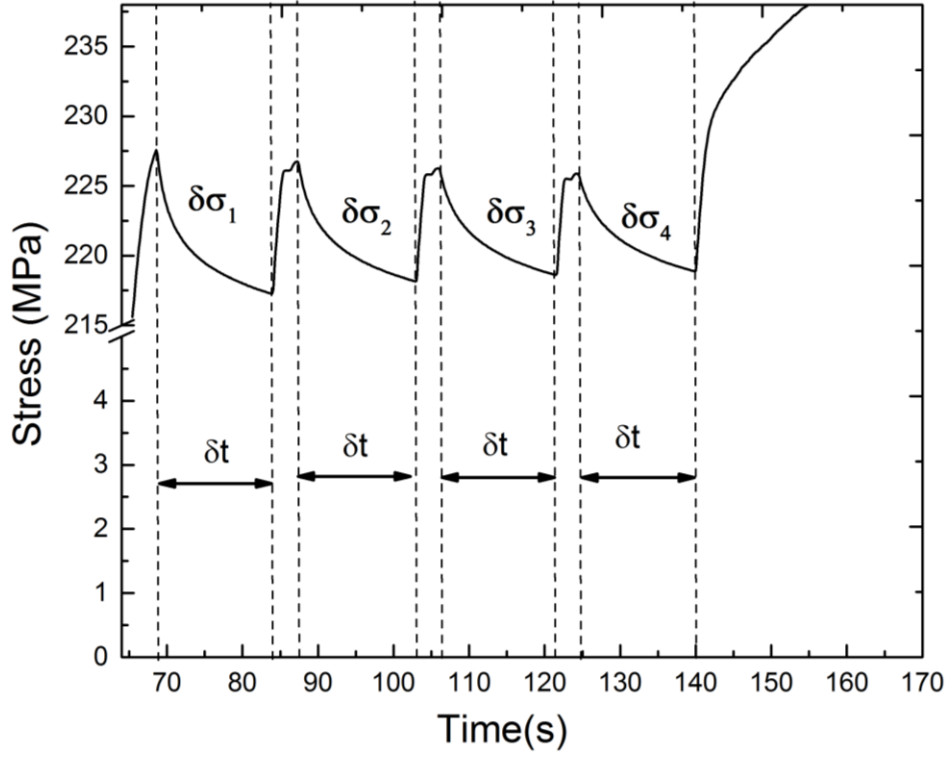


**Fig. 3.3:** Multiple relaxation curves for Nb-1Zr-0.1C alloy at 200 °C.

The end of one relaxation and start of the next relaxation have the same mobile dislocation density. Therefore, the activation volume calculated from the first and second relaxation curves is:

$$V = kT \left( \frac{\ln \left( \frac{\dot{\epsilon}_{i2}}{\dot{\epsilon}_{f1}} \right)}{\Delta \sigma_1} \right) \quad (3.10)$$

The activation volume is measured for repeated relaxation tests through the relation as

$$V = kT \left( \frac{\ln \left( \frac{\dot{\epsilon}_{i2}}{\dot{\epsilon}_{f1}} \right)}{\Delta \sigma} \right) \quad (3.11)$$

The interpretation of repeated relaxation tests relies on the following assumptions:

(i) The applied shear stress  $\tau$  can be decomposed into an athermal stress  $\tau_\mu$  and an effective stress  $\tau^*$  [144]

$$\tau = \tau_\mu + \tau^* \quad (3.12)$$

$\tau^*$  is temperature and strain rate dependent and corresponds to localized obstacles or energy barriers, such as impurities, solute atoms, forest dislocations, etc. for thermal activation of dislocation motion.  $\tau_\mu$  corresponds to the long range elastic interactions and is not thermally activated. It depends very much on the history of the sample, in particular on strain. The change in the internal stress is considered to be proportional to the change in strain for this condition as [144]

$$\Delta \tau_\mu = K_r \Delta \gamma_p \quad (3.13)$$

By some mathematical operations

$$\tau^* = (1 + K_r/M) \Delta \tau \quad (3.14)$$

where  $K_r$  is the work-hardening coefficients.

(ii) The dislocation velocity  $v$  is thermally activated:

$$v = v_d \exp(\Delta G/kT) \quad (3.15)$$

where  $\Delta G$  is the change in activation free energy of the mobility mechanism,  $v$  is the vibration frequency of the average dislocation segment and  $d$  is the distance over which this segment moves after a successful activation event. The activation volume  $V$  of the dislocation velocity is defined as:

$$V = - \frac{\partial G}{\partial \tau^*} \quad (3.16)$$

$V$  is obviously different from  $V_a$  and therefore cannot be determined via a single transient experiment. During the short transient, provided the change in effective stress  $\Delta \tau^*$  is small

enough and the pre-exponential factor in Eq. (3.15) is constant, the corresponding change in activation energy is  $-\Delta\tau^*V$ . Then the dislocation velocity is

$$v = v_0 \exp(V\Delta\tau^*/kT) \quad (3.17)$$

$v_0$  being the velocity at the onset of the transient (i.e. when  $\Delta\tau^* = 0$ ).

(iii) The mobile dislocation density is assumed to be a power function of the velocity, as suggested by a few experiments [145]

$$\frac{\rho_m}{\rho_{m0}} = \left(\frac{v}{v_0}\right)^\beta \quad (3.18)$$

$\rho_{m0}$  being the mobile density at the onset of the transient.

After some mathematical calculations the relation between  $V$  and  $V_a$  is

$$\Omega_r = \frac{V_a}{V} \quad (3.19)$$

$$\text{with } \Omega_r = (1 + \beta_r) \left[ \frac{1 + K_r}{M} \right] \quad (3.20)$$

$\Omega_r$  can be determined as follows: In a repeated relaxation tests  $V_a$  is obtained usually by a fit of the first relaxation curve (the longest one) with the logarithmic law (3.8).  $V$  can be computed using relation (3.11).

If  $V_a$  and  $V$  are known, relation (3.20) shows that information can be gained about the structural parameters  $\beta$  and  $K_r$ . By using Eq. (3.8) and (3.17) to (3.20) the time decrease of the mobile dislocation density during a stress relaxation test is calculated as

$$\frac{\rho_m}{\rho_{m0}} = \left( \frac{c_r}{c_r + t} \right)^{\beta_r/1+\beta_r} \quad (3.21)$$

During stress relaxation tests, both the plastic strain as well as the athermal stress increase (Eq. 3.13). Though each relaxation test starts at the same stress  $\tau_0$ , the corresponding effective stress  $\tau_0^*$  and therefore the dislocation velocity are smaller as the relaxation number increases. The mobile dislocation density is smaller too under the same conditions. Therefore, the initial deformation rate decreases along a series for the two above reasons.

### **3.4 Dynamic deformation from room temperature to 400 °C**

#### **3.4.1 Procedure for carrying out test in SHPB**

Split Hopkinson Pressure Bar (SHPB) setup is suitable for high strain rate test in strain rate range of 100 to 10000  $s^{-1}$ . The high strain rate flow behavior of Nb-1Zr and Nb-1Zr-0.1C alloys were studied by SHPB setup from 25 to 400 °C in the interval of 100 °C at a strain rate  $> 1000 s^{-1}$ . The schematic diagram of split-Hopkinson pressure bar is shown in Fig. 3.4. To achieve force equilibrium in sample within shorter time, solid cylindrical samples having dimensions of 5 mm diameter and 5 mm length were used for these high strain rate tests. All the tests were done for a strain of 0.25. Molybdenum disulphide powder was used as lubricant between specimen and bars of set-up to reduce friction between the bars and the specimen. The elevated temperature tests were carried out by heating the sample using a small resistance coil furnace (not shown in Fig. 3.4).

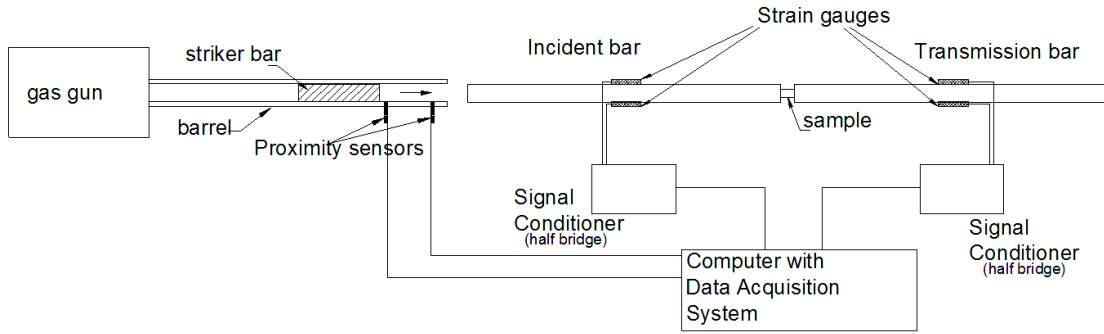


**Fig. 3.4:** Schematic of split-Hopkinson pressure bar (SHPB).

### 3.4.2 Split Hopkinson Pressure Bar technique

The mechanism in SHPB test is the propagation of a one dimensional stress wave along a thin long bar. A gas gun launches a striker bar that impact upon the end of the incident bar (Fig. 3.4). A stress wave is generated that travels down the bar and is recorded sequentially by the first and second strain gauges mounted longitudinally on the bar. The stress wave then passes through the solid cylindrical samples of Nb alloys which are sandwiched between the incident and transmission bar. These samples undergo a uniaxial stress deformation. Part of the stress wave is reflected in the form of a tensile pulse and is recorded by the strain gauges mounted on the incident bar. Part of the wave energy is transmitted to the transmission bar and recorded by the strain gauges mounted on the transmission bar. The pulse signal of elastic strain generated in the incident and transmitted bar are used to calculate the stress-strain behavior of the material.

The basic theory and functioning details of split-Hopkinson pressure bar are described elsewhere [146]. However the equations that are used for the calculation of the flow stress

( $\sigma_s$ ), strain ( $\varepsilon_s$ ) and strain rate ( $\dot{\varepsilon}_s$ ) of the specimen are

$$\sigma_s = \frac{A_0 E \varepsilon_t}{A_s} \quad (3.22)$$

$$\dot{\varepsilon}_s = \frac{2\varepsilon_r C_0}{L_s} \quad (3.23)$$

$$\varepsilon_s = 2 \frac{C_0}{L_s} \int_0^t \varepsilon_r dt \quad (3.24)$$

where  $C_0$  is the wave velocity in the bar,  $L_s$  is the length of the sample,  $A_s$  and  $A_0$  are the cross sectional area of the specimen and bar respectively,  $\varepsilon_r$  and  $\varepsilon_t$  are the reflected and transmitted strain measured in the incident and transmitted bar respectively.

As all high strain rate tests are adiabatic in nature, i.e. the heat generated during high strain rate deformation does not have sufficient time to dissipate, the heat generated raises the temperature of the sample. The temperature rise  $\Delta T$  is calculated by using Eq. (3.4). Fig. 3.5 shows typical pulse forms with momentum trapping during the test.

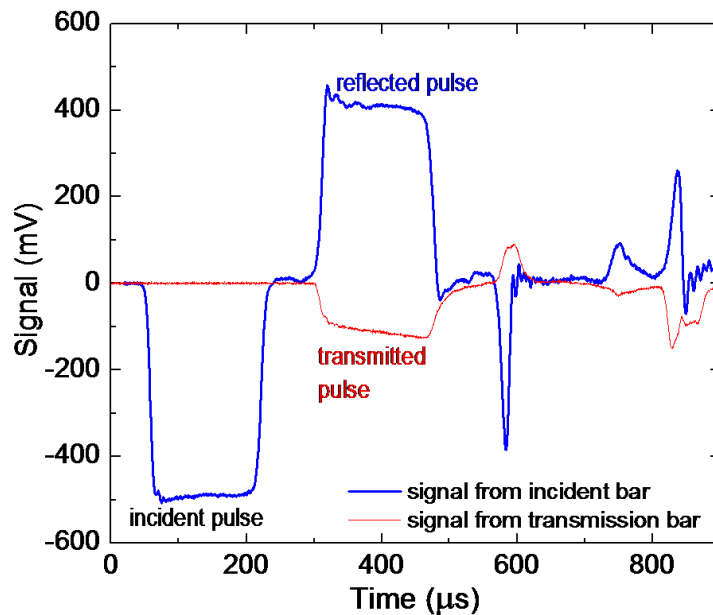


**Fig. 3.5:** A typical pulse signal recorded through strain gauges using momentum trap.

### 3.5 Microstructural characterization

The deformed samples were sectioned along the compression axis, mounted, mechanically polished and electropolished using 5% perchloric acid ( $\text{HClO}_4$ ) and 95% methanol ( $\text{CH}_3\text{OH}$ ) solution. The microstructures were analyzed using electron backscatter diffraction technique (EBSD) in a FEI scanning electron microscope (SEM) with a tungsten source operated at 25 kV. Since the average grain size was  $\geq 100 \mu\text{m}$  a large step size of  $2 \mu\text{m}$  was used for each scan. To acquire and analyze the data TSL-OIM data Collector and AZtec data Collector software and TSL-OIM analysis (Ver. 6.1) software and HKL-Channel 5 software were used. Average bulk textures of the deformed samples were measured using a Bruker D8-Discover X-ray texture goniometer (equipped with a  $\text{Cu-K}\alpha$  source) based on Schultz reflection geometry. X-ray texture measurements were done in the plane perpendicular to the compression axis. However as the deformation is uniaxial the EBSD maps and texture representation in terms of inverse pole figure for EBSD maps as well as X-ray texture plots were shown with respect to the compression axis. Schematics of the data measurement plane with respect to deformed sample and compression axis is shown in Fig. 3.6.

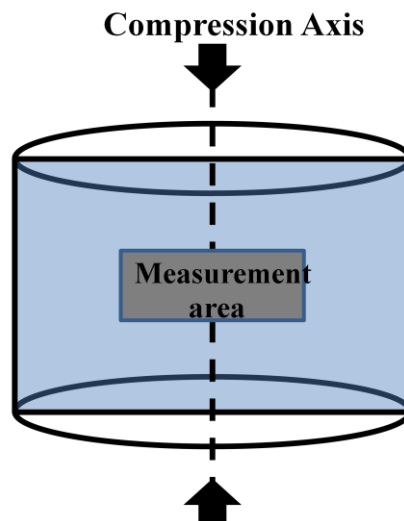


**Fig. 3.6:** Schematics of EBSD and X-ray texture data measurement plane. The representation of IPF was done with respect to compression axis.

## Chapter 4. Results and Discussion

### 4.1 Hot deformation behavior

#### 4.1.1 Flow stress behaviour of Nb

The true stress-true strain curve of niobium, compressed at various test temperatures from 700 to 1500 °C and at strain rates of 0.003, 0.01, 0.1, 1 and 10 s<sup>-1</sup> are shown in Fig. 4.1. The flow stress ( $\sigma$ ) of Nb shows a strong dependence on deformation temperature and strain rate. The following can be observed from the Fig. 4.1.

- a) At the lower temperatures of 700 and 800 °C, Nb shows an increasing work-hardening rate with increasing strain rate (compare different plots for 700 °C). At 700 °C and lower strain rates of  $3 \times 10^{-3}$  and 10<sup>-1</sup> s<sup>-1</sup> a sharp yield point is observed. Sharp yield points are the indicative of strong solute dislocation interaction [147, 148].
- b) For tests at 900 °C and higher, and at lower strain rates of  $3 \times 10^{-3}$  and 10<sup>-2</sup> s<sup>-1</sup> the flow stress increases to a maximum beyond which it softens to a steady state value. This is typical of a sample undergoing dynamic recrystallization (DRX). Similar  $\sigma - \epsilon$  behaviour has been reported during DRX of several metals and alloys [90, 149, 150].
- c) As the strain rate increases the temperatures at which softening is observed also increases. For example at low strain rates of 0.003 and 0.01 s<sup>-1</sup> softening occurs at temperatures of 800 °C and above. At strain rates of 0.1 s<sup>-1</sup> softening starts at 1100 °C and above and at strain rates of 1 s<sup>-1</sup> softening starts at 1400 °C and above. At strain rate of 10 s<sup>-1</sup> no softening is observed.

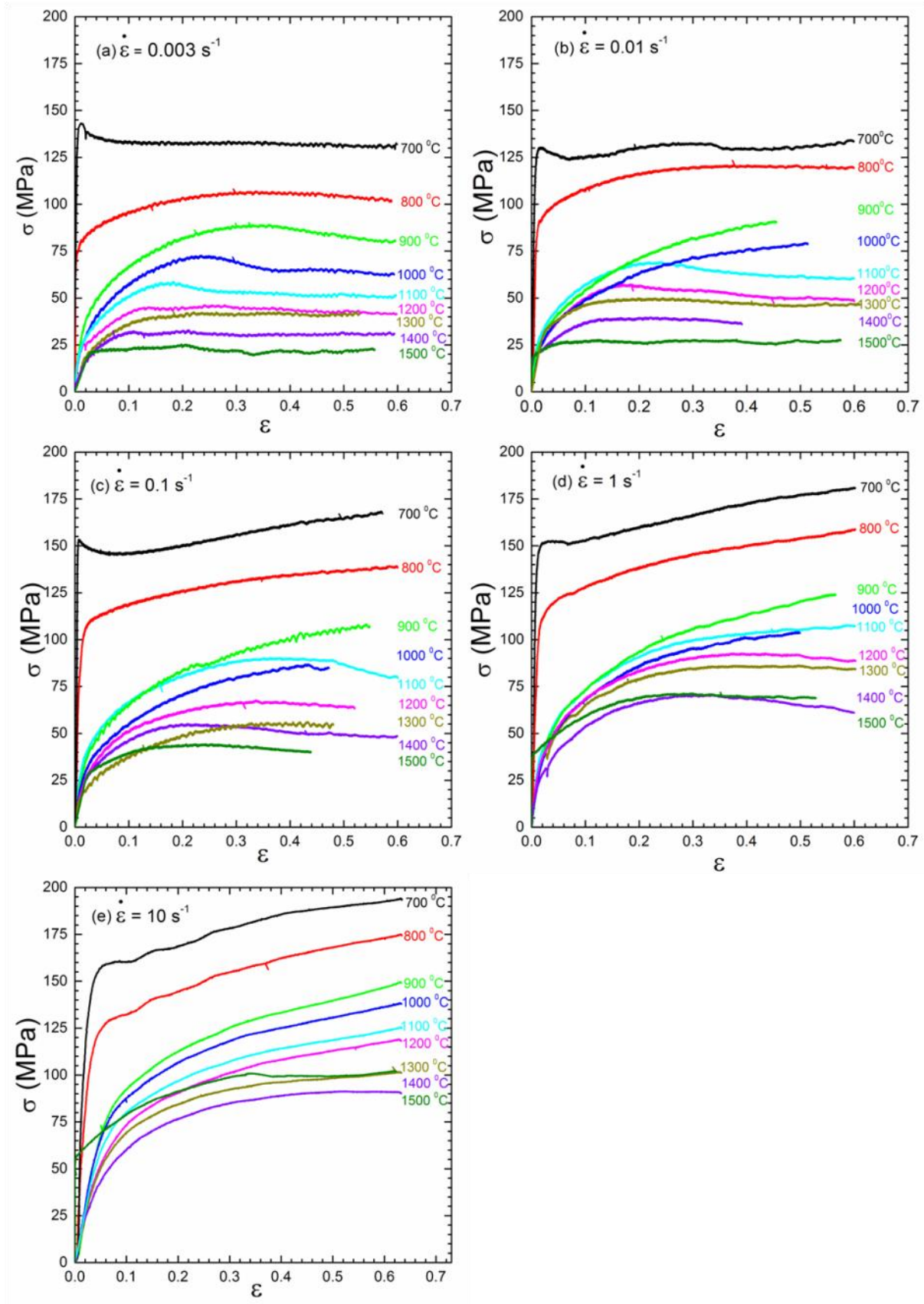


**Fig. 4.1:** Plots of true stress vs. true strain of Nb at strain rates of 0.003, 0.01, 0.1, 1.0, 10  $\text{s}^{-1}$  and at different temperatures as mentioned along each curve.

#### 4.1.2 Stress- strain behaviour of Nb-1Zr

The true stress-true strain curves for Nb-1Zr alloy compressed at various test temperatures from 900 to 1700 °C and at strain rates of 0.003, 0.01, 0.1, 1 and 10 s<sup>-1</sup> are shown in Fig. 4.2. The flow stress shows a strong dependence on deformation temperature and strain rate. The following can be observed from Fig. 4.2.

- a) There are two types of flow curves exhibited by Nb-1Zr – those which show work-hardening behavior throughout the strain range and those which achieve steady state (or softening behavior).
- b) At temperatures of 900 to 1200 °C work-hardening was seen in the entire strain and strain rate range.
- c) At each strain rate it was seen that with increasing temperature the flow behavior changed from a hardening to a steady state behavior and that the temperature of this transition increased with increasing strain rate.
- d) At strain rate of 0.003 s<sup>-1</sup> the transition from work hardening to steady state takes place at 1300 °C, and with increasing strain rate of 0.01, 0.1 and 1 s<sup>-1</sup> the transition takes place at 1400, 1500 and 1600 °C, respectively. At a strain rate of 10 s<sup>-1</sup> work-hardening was seen at all temperatures.

A single peak followed by the flow softening was observed during a temperature range of 1400 to 1700 °C and for strain rates of 0.003 and 0.01 s<sup>-1</sup>. This feature of a peak in flow stress followed by softening is usually attributed to the occurrence of dynamic recrystallisation (DRX). Similar  $\sigma - \epsilon$  behaviour has been reported during DRX of several metals and alloys [89, 94, 151, 152]. For strain rate of 0.1 s<sup>-1</sup> and temperatures of 1500 to 1700 °C steady state flow behaviour was observed after an initial hardening. At higher strain rates of 1 and 10 s<sup>-1</sup> the flow curves continue to show hardening and only at higher temperatures do they attain

flow saturation. This hardening behaviour followed by saturation is typical of dynamic recovery [153].

#### **4.1.3 Stress- strain behaviour of Nb-1Zr-0.1C**

The true stress-true strain curves for Nb-1Zr-0.1C alloy compressed at various test temperatures from 900 to 1700 °C and at strain rates of 0.003, 0.01, 0.1, 1 and 10 s<sup>-1</sup> are shown in Fig. 4.3. The nature of the flow curves exhibited by the material can be broadly classified into three types:

- a) At temperatures lower than 1000 °C and at all strain rates the flow curves are clustered together indicating that the flow stress is virtually independent of temperature and strain rate.
- b) At temperatures of 1000 °C and up to 1400 °C and strain rates higher than 0.1 s<sup>-1</sup>, the flow curves show a high strain hardening behavior.
- c) At strain rates lower than 0.1 s<sup>-1</sup> and at temperatures in the range 1000 to 1700 °C, the flow curves exhibit an initial rapid work-hardening at lower strains followed by a tendency to reach steady-state stress levels at large strains.

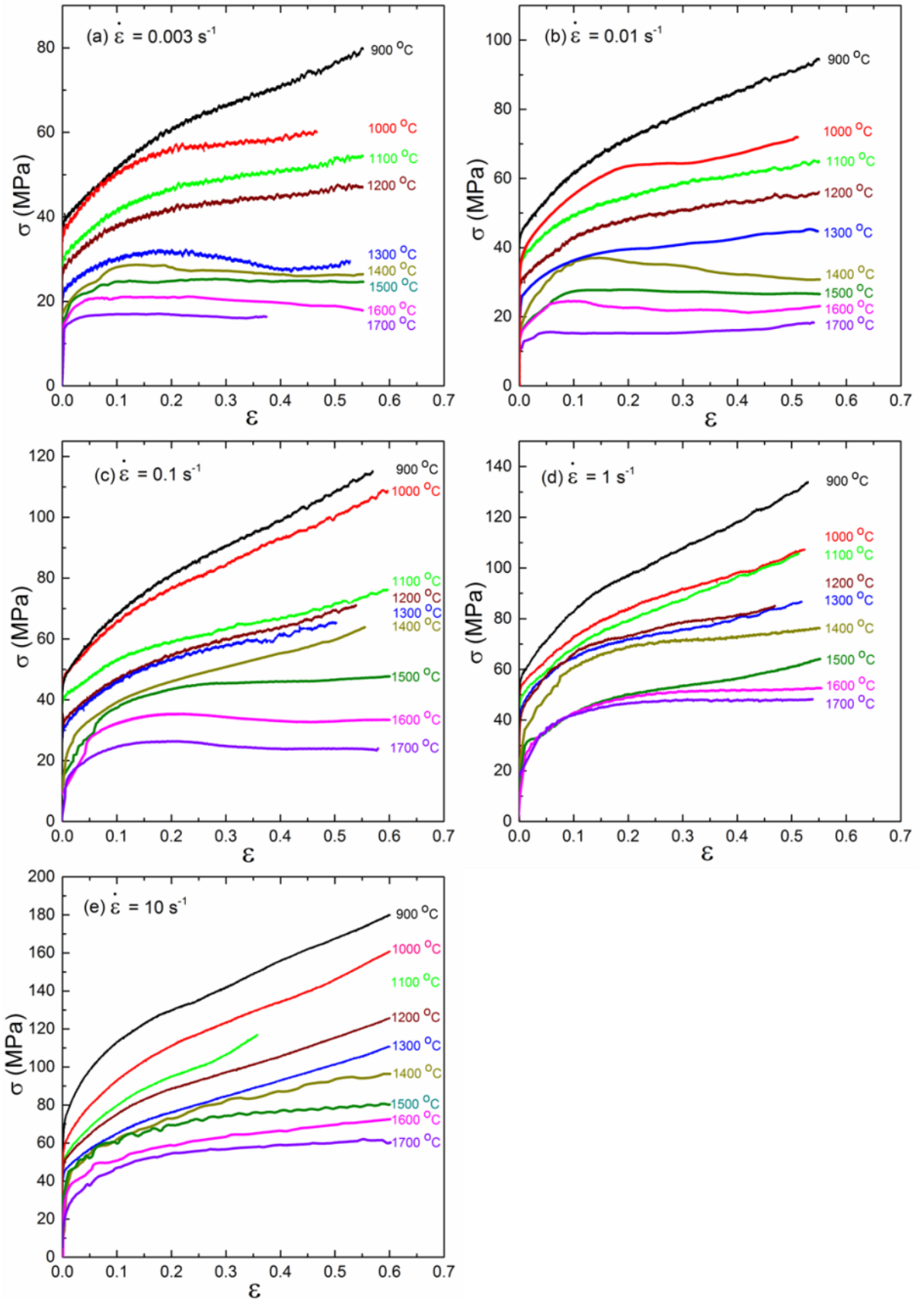


**Fig. 4.2:** Plots of true stress vs. true strain of Nb-1Zr at strain rates of (a) 0.003, (b) 0.01, (c) 0.1, (d) 1 and (e)  $10 \text{ s}^{-1}$  and different temperatures as indicated.

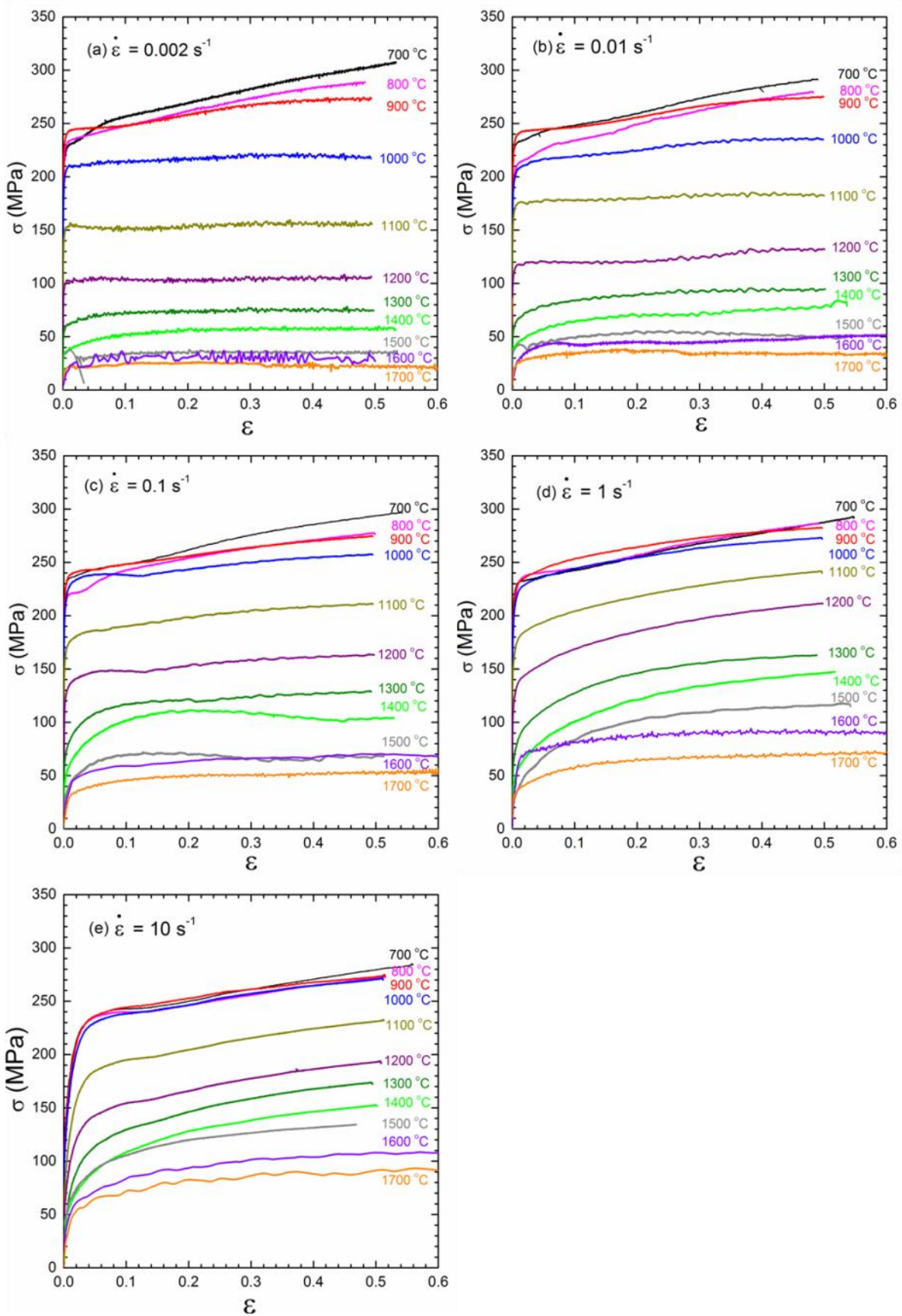


**Fig. 4.3:** Plots of true stress vs. true strain of Nb-1Zr-0.1C at strain rates of (a) 0.002, (b) 0.01, (c) 0.1, (d) 1 and (e)  $10 \text{ s}^{-1}$  and different temperature as indicated.

#### 4.1.4 Strain rate sensitivity

The variation of  $\sigma$  with strain rate  $\dot{\epsilon}$  at constant  $T$  and the variation of  $\sigma$  with  $T$  at constant  $\dot{\epsilon}$  are shown in Fig. 4.4 and Fig. 4.5 respectively. The flow stress increased with strain rate and decreased with temperature (increasing  $1/T$ ) signifying that the deformation is thermally activated. For Nb, Nb-1Zr and Nb-1Zr-0.1C with increasing temperature the strain rate sensitivity  $m = \Delta \ln \sigma / \Delta \ln \dot{\epsilon}$  (the slope of  $\log \sigma$  vs.  $\log \dot{\epsilon}$  plot) increased and the slope was high at the lower strain rates and low at the higher strain rates.

For pure Nb at temperatures higher than 1100 °C and at strain rates lower than 0.1 s<sup>-1</sup> the slope of  $\log \sigma$  vs.  $\log \dot{\epsilon}$  was observed to be higher than that below 1100 °C. For Nb-1Zr alloy at higher temperatures (1200 - 1700 °C) and lower strain rates (0.01 and 0.003 s<sup>-1</sup>),  $m$  was high as compared to lower temperatures (900 - 1100 °C) and higher strain rates (1 and 10 s<sup>-1</sup>). Fig 4.5 shows that for Nb-1Zr-0.1C alloy the flow stress has weak dependence on temperature and strain rate up to 900 °C. The flow stress is independent of temperature up to 1000 °C at higher strain rates. At temperatures higher than 1000 °C and at all strain rates, the flow stress is found to change significantly with strain rate and temperature, indicating that the flow behavior is thermally activated. The strain rate sensitivity  $m$  increases with increasing temperature and is strain rate dependent.

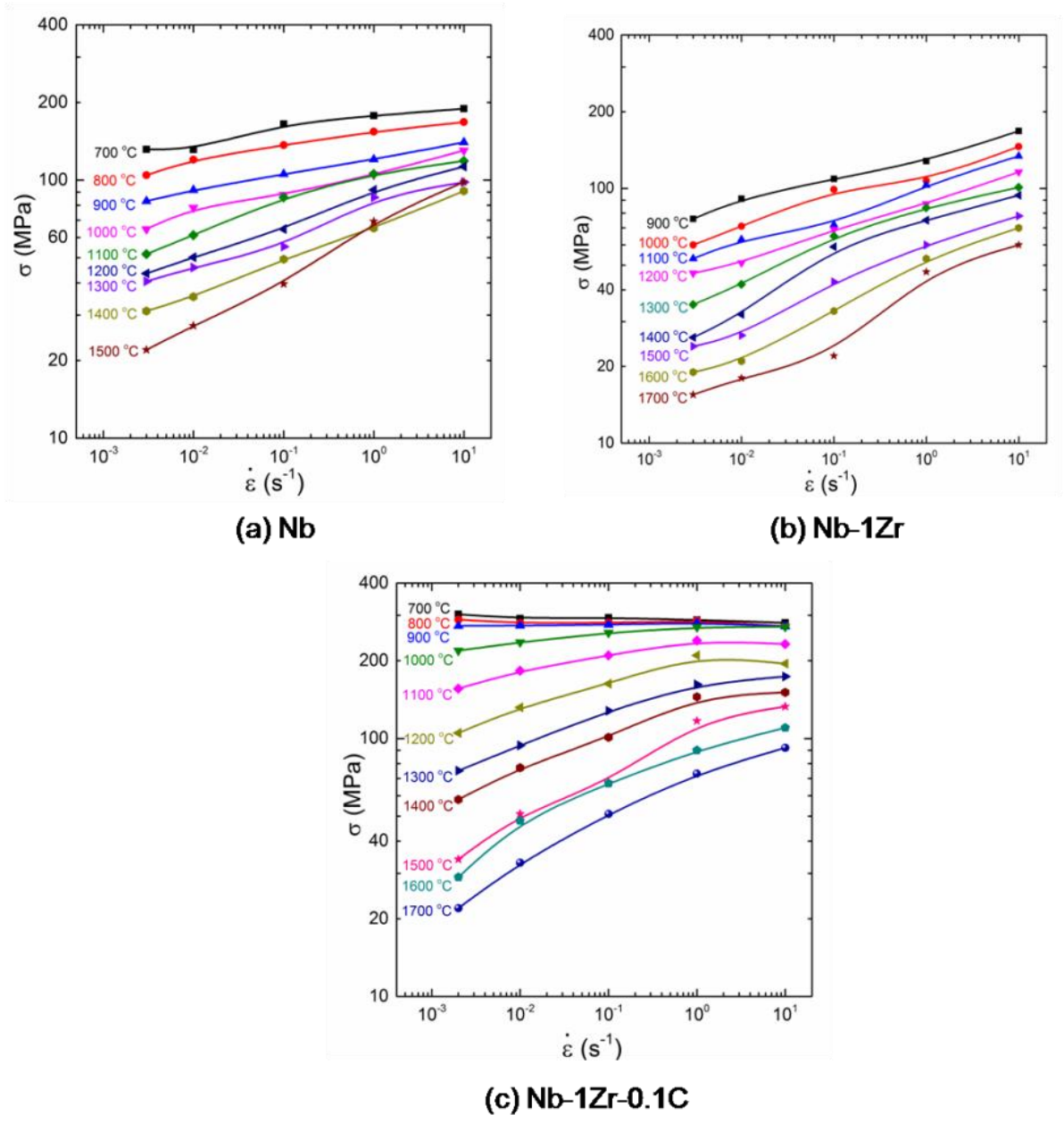


**Fig. 4.4:** Flow stress vs. strain rates at a true strain of 0.5 for (a) Nb, (b) Nb-1Zr and (c) Nb-1Zr-0.1C alloy at different temperatures.

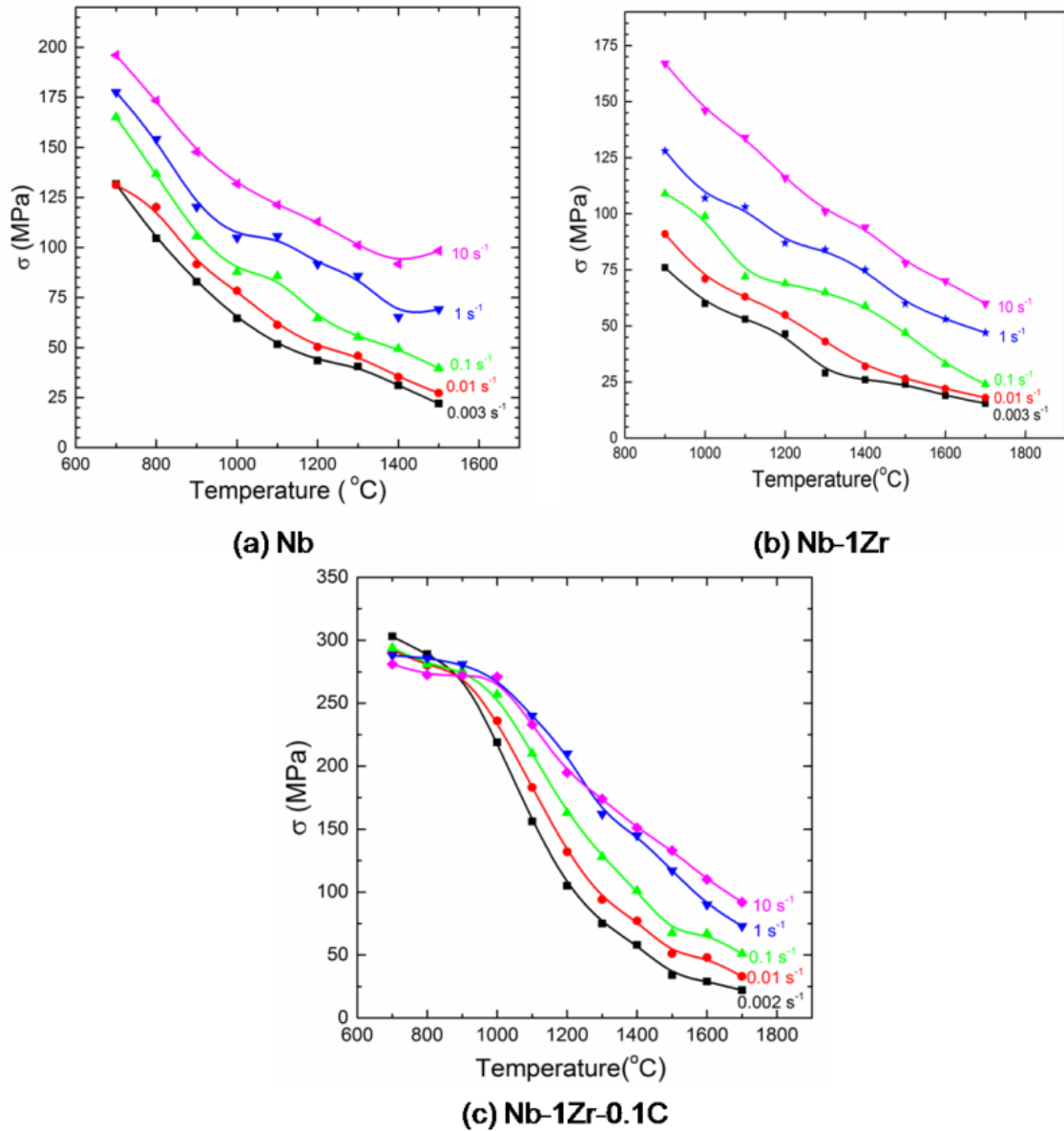


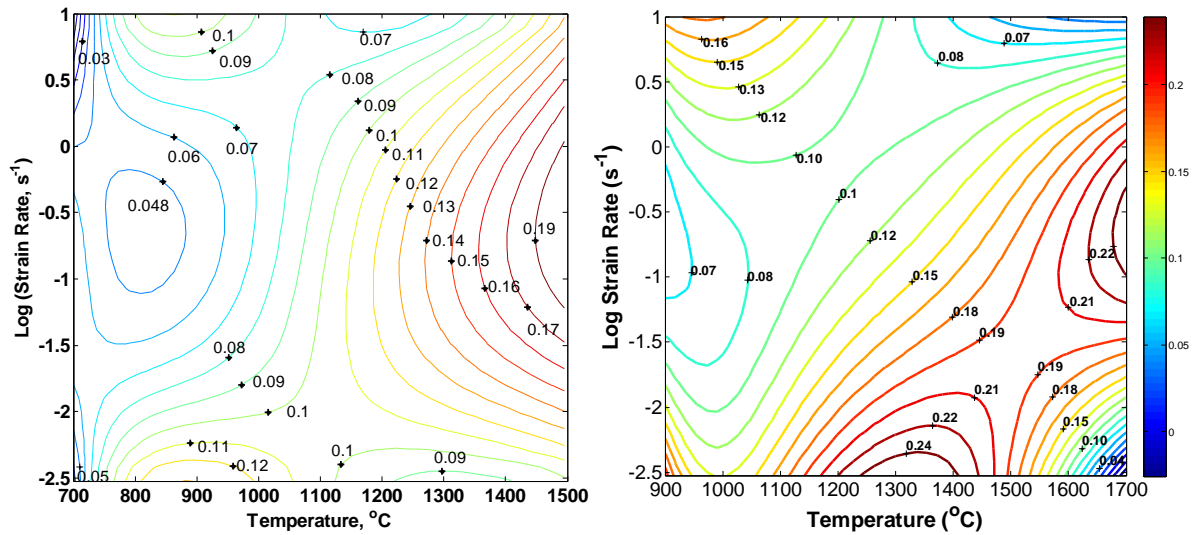
**Fig. 4.5:** Flow stress vs. temperature at a true strain of 0.5 for (a) Nb, (b) Nb-1Zr and (c) Nb-1Zr-0.1C alloy at different strain rates. The lines connecting the data points are shown for clarity.

#### 4.1.5 Strain Rate Sensitivity Map generation

The strain rate sensitivity ( $m$ ) of Nb, Nb-1Zr and Nb-1Zr-0.1C alloy were calculated from the  $\sigma$ ,  $T$ ,  $\dot{\epsilon}$  data by fitting the  $\ln \sigma$  vs.  $\ln \dot{\epsilon}$  data to a cubic polynomial. From the plot of  $\sigma$  vs.  $T$  at different strain rates the stress values were interpolated in finely spaced  $\ln \dot{\epsilon}$  and  $1/T$  intervals. The strain rate sensitivity was obtained as described above for a true strain of 0.5 and was plotted as an iso-strain rate sensitivity contour plot as a function of temperature and strain rate

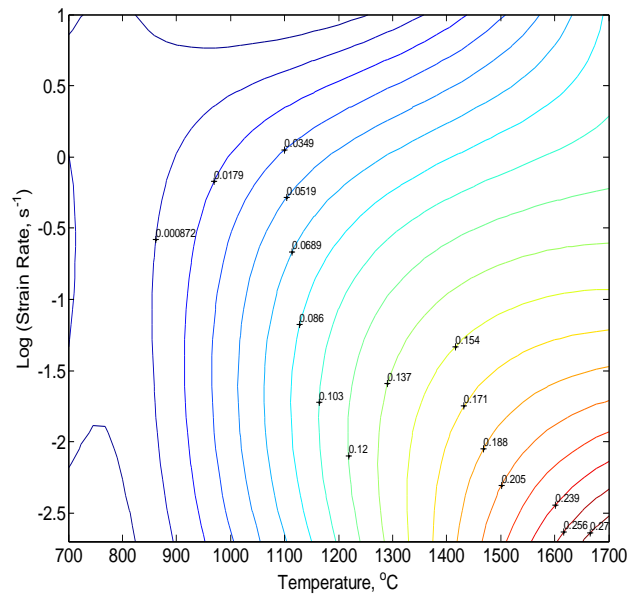
as shown in Fig. 4.6. A higher value of strain rate sensitivity ensures strain rate hardening, which delays necking in tension [154, 155] and prevents instabilities in compression [156]. Thus the parameters for optimum hot workability can be identified in terms of regimes of temperature and strain rate where strain rate sensitivity is high. Fig 4.6 (a) shows the strain rate sensitivity (SRS) map for pure Nb. A domain of high strain rate sensitivity was observed starting from 1200 to 1500 °C and from strain rates of  $10^{-2}$  to  $1 \text{ s}^{-1}$  for pure Nb. In this domain the strain rate sensitivity value varied between 0.12 to 0.2. As this is significantly positive the hot worked product is not expected to exhibit flow instability in this regime. A regime of low strain rate sensitivity (0.05) was observed at temperatures of 800 °C and lower and at strain rates around  $0.1 \text{ s}^{-1}$ .

For Nb-1Zr alloy a domain of high strain rate sensitivity was observed starting from 1200 to 1500 °C for strain rates of  $10^{-3}$  to  $10^{-1} \text{ s}^{-1}$  and from 1600 to 1700 °C for strain rates of  $10^{-1}$  to  $1 \text{ s}^{-1}$  (Fig 4.6b). In this domain the strain rate sensitivity varied from 0.15 to 0.25. This is considered as the optimum domain of hot workability. Throughout the strain rate and temperature range of this study  $m > 0$  and thus Nb-1Zr alloy is not expected to exhibit flow instability in this temperature and strain rate range [90, 151]. Nb-1Zr-0.1C alloy processing map exhibits a single domain starting at about 1300 °C and maximum  $m$  at 1700 °C and  $0.002 \text{ s}^{-1}$ . In this domain  $m$  increases from slightly positive to about 0.24 with increasing temperature and decreasing strain rate.



(a) Nb

(b) Nb-1Zr



(c) Nb-1Zr-0.1C

**Fig. 4.6:** Iso-strain rate sensitivity contour map of (a) pure Nb, (b) Nb-1Zr alloy and (c) Nb-1Zr-0.1C alloy for a true strain of 0.5. The values on the contours indicate strain rate sensitivity ( $m$ ).

#### 4.1.6 Kinetic analysis

As the deformation processes are thermally activated (Fig. 4.4 and Fig. 4.5), the dynamic restoration mechanisms depends upon temperature and strain rate. The kinetic analysis along with microstructural investigations can be used to identify the deformation mechanisms

associated with restoration mechanisms during high temperature deformation [47, 157]. The constitutive relation between the  $\sigma$ ,  $\dot{\varepsilon}$  and  $T$  is generally expressed as [153],

$$\dot{\varepsilon} = A \sigma^n \exp(-Q/RT) \quad (4.1a)$$

where,  $n$  is the stress exponent,  $Q$  is the activation energy for deformation,  $A$  is a constant independent of temperature and  $R$  is the universal gas constant ( $8.314 \text{ J K}^{-1} \text{ mol}^{-1}$ ). The constants  $n$ ,  $Q$  and  $A$  were determined through non-linear fitting of the  $\sigma$ ,  $\dot{\varepsilon}$ , and  $T$  data from high  $m$  domain (Fig. 4.5 and Fig. 4.6) to the above relation. For a given value of  $Q$  the Zener-Hollomon parameter  $Z \equiv \dot{\varepsilon} \exp(Q/RT)$  [157] values can be calculated by using Eq. (4.1a) as

$$\ln Z \equiv \ln \dot{\varepsilon} + Q/RT \quad (4.1b)$$

Using these values of  $\ln Z$  and the stress values the constants  $n$  and  $A$  values are obtained by fitting the data to the equation  $Z = A \sigma^n$  as

$$\ln Z = \ln A + n \ln \sigma \quad (4.1c)$$

Thus plot of  $\ln Z$  vs.  $\ln \sigma$  should give a straight line with slope  $n$ . However the best fit would be obtained by the correct value of  $Q$ . The goodness of fit is quantified by residue values as the sum of the square of the difference between the  $\ln Z$  (for  $Q_i$ ) and  $\ln Z$  (for  $n_i$  and  $A_i$ ). A range of  $Q$  values are chosen and the one which gives the least residue is the final  $Q$  value. The minimum residue value gives the final  $n$ ,  $Q$  and  $A$ . The power law dependence of the Zener-Hollomon parameter ( $Z$ ) on the flow stress for the data within the deformation domain (as seen in liner plot on a log-log scale Fig. 4.7) confirms a good fit to the experimental data. The temperature compensated strain rate parameter  $Z$  gives the information regarding the deformation conditions of hot deformation.

#### 4.1.6.1 Activation energy

For Nb, the activation energy was found to be  $246 \text{ kJ mol}^{-1}$  and the stress exponent to be 7.5 in the high  $m$  domain. This value of  $Q$  was lower than that for the activation energy for self diffusion of niobium which is  $374 \sim 400 \text{ kJ mol}^{-1}$  [81]. The high value of  $n$  indicates a dislocation based mechanisms for pure Nb. The lower value of  $Q$  could imply dislocation core diffusion during high temperature deformation of Nb. The non-linear fitting of the data for Nb-1Zr alloy to Eq. (4.1) gives  $n = 4.9$  and  $Q = 259 \text{ kJ mol}^{-1}$ . This value of the activation energy for deformation is similar to that of Nb ( $246 \text{ kJ mol}^{-1}$ ) [158] and lower than that of the activation energy for self diffusion ( $Q_{SD}$ ) which for Nb is  $374 \sim 400 \text{ kJ mol}^{-1}$  [81]. If lattice diffusion is involved during deformation and is rate controlling then activation energy of deformation and that of self diffusion should match. In this case  $Q < Q_{SD}$  which implies that the deformation is based on conservative motion of dislocations (glide or cross slip) and does not involve diffusion. Alternatively,  $Q \sim (2/3) Q_{SD}$  implies that either grain boundary or dislocation core diffusion plays a part during deformation. A stress exponent  $n > 3$  suggests dislocation based mechanisms for Nb-1Zr [81]. In the present case  $n = 4.9$  indicates a dislocation based mechanism and  $Q < Q_{SD}$  implies dislocation core diffusion during high temperature deformation process instead of lattice diffusion. The determined activation energy of deformation for Nb-1Zr-0.1C alloy is in reasonable agreement with the reported activation energy for self diffusion of Nb ( $Q_{SD} = 374 \sim 400 \text{ kJ mol}^{-1}$ ) [51]. The value of  $n = 5$  suggests a dislocation based mechanism for Nb-1Zr-0.1C alloy.

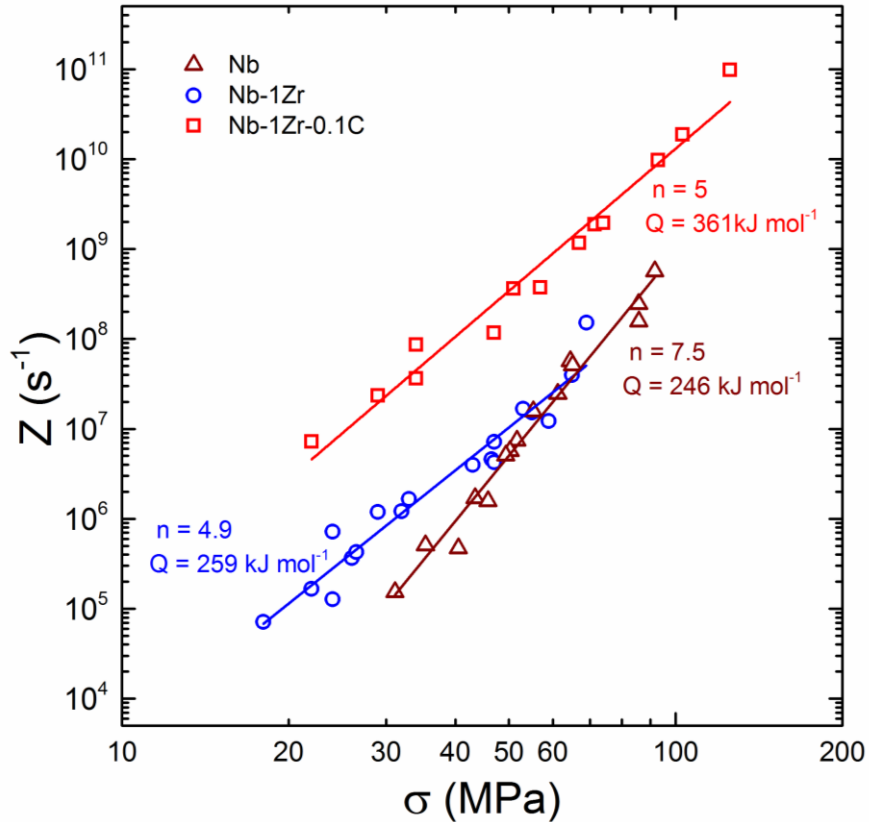


**Fig. 4.7:** Zener-Hollomon parameter ( $Z$ ) dependence on flow stress for Nb, Nb-1Zr and Nb-1Zr-0.1C alloys within the deformation domain. The activation energies ( $Q$ ) and stress exponents ( $n$ ) as determined by using Eq. (4.1) are written on the plot.

#### 4.1.6.2 Grain size- $Z$ relation

It was observed that the steady state grain size of the deformed samples varied with strain rate and temperature. Fig. 4.8 shows the variation of the steady state grain size with the temperature compensated strain rate parameter ( $Z$ ). Within the high  $m$  domain at strain rates ranging from  $10^{-3}$  to  $0.1 \text{ s}^{-1}$ , the grain size increased with decreasing temperature and increasing strain rate, i.e.  $\log Z$  decreased linearly with increasing  $\log$  of grain size (Fig. 4.8). It has been reported that in several alloy systems undergoing DRX the characteristic features of DRX is the inverse relation of the steady state recrystallized grain size with  $Z$  [159]. In present studies this characteristic feature of DRX confirms its occurrence in this high  $m$

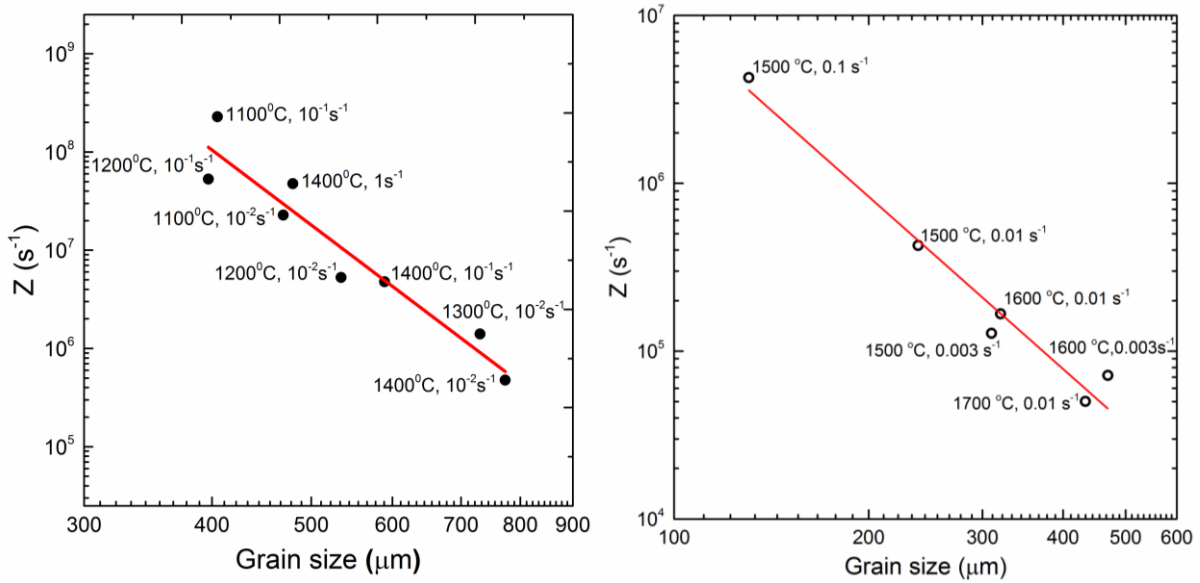
domain. The recrystallized grain size is dependent of the deformation temperature and strain rate implying dependence on  $Z$ .

#### 4.1.6.3 Activation Volume

Activation volume is a key parameter to understand the deformation mechanism in different metals and alloy systems. The activation volume  $V$  was calculated indirectly as

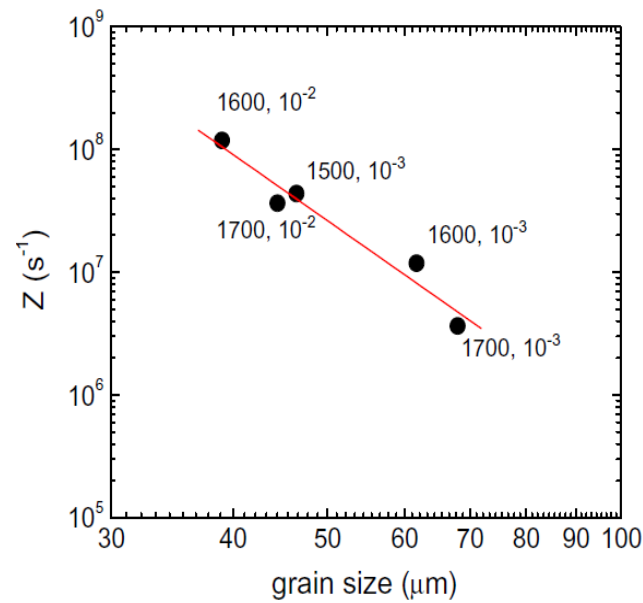
$$V = \frac{MkT}{\sigma m} \quad (4.2)$$

where  $M$  is the Taylor factor taken as 2.8 (for bcc metals and alloy),  $m$  is the strain rate sensitivity and  $k$  is the Boltzmann constant [34, 160]. Fig. 4.9 shows the variation of normalized activation volume with stress for data within the domain of high  $m$ . It is observed that the activation volume decreased with increasing stress from 700 to 200  $b^3$ , which is expected for a thermally activated process. These high values of activation volumes rules out climb as the rate controlling mechanism (activation volume for climb  $\approx 1$  to  $10 b^3$ ). This range of activation volume signifies barriers related to dislocation intersection based process. The activation volumes for Nb, Nb-1Zr and Nb-1Zr-0.1C at high stresses are similar whereas at low stresses pure Nb and Nb-1Zr have relatively higher activation volume as compared to its alloy. The lower activation volumes for the Nb-1Zr-0.1C alloy is expected as these have fine precipitates and would likely reduce the dislocation activation length thereby reducing activation volume.



(a) Nb

(b) Nb-1Zr



(c) Nb-1Zr-0.1C

**Fig. 4.8:** Zener-Hollomon parameter dependence on grain size for Nb, Nb-1Zr and Nb-1Zr-0.1C alloys within each of their deformation domain. The numbers next to the data points indicate the test conditions.

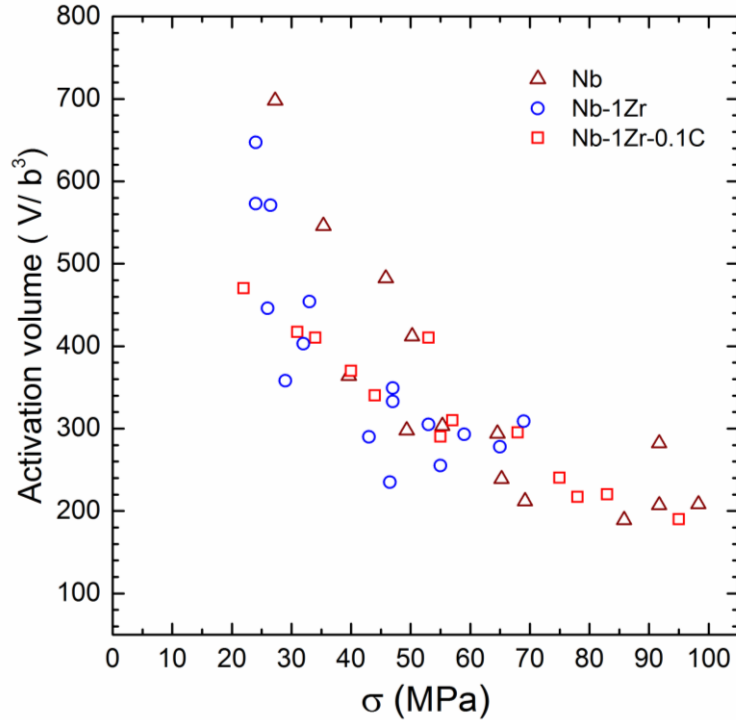


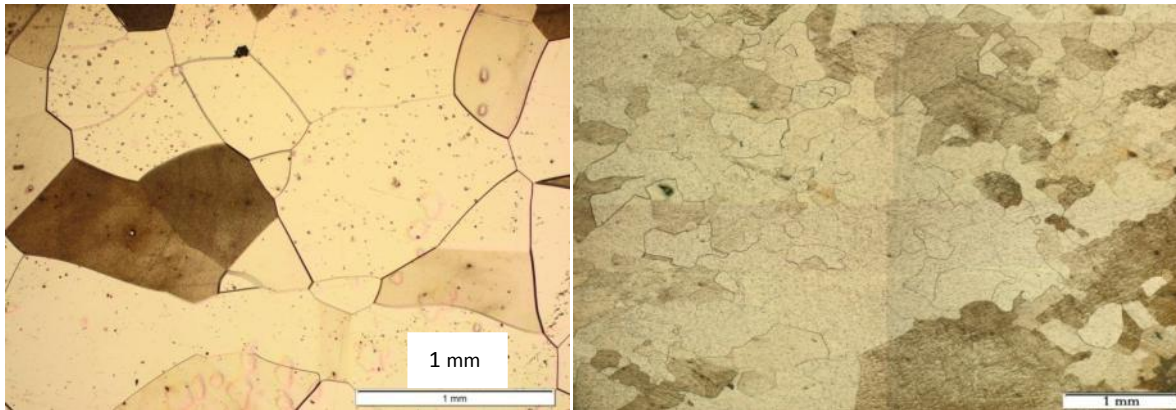
**Fig. 4.9:** Plot of activation volume (normalized with cube of magnitude of Burgers vector  $b$ ) vs. stress for data within high  $m$  domain.

#### 4.1.7 Microstructure and texture evolution

##### 4.1.7.1 Microstructure of Nb

In order to correlate the flow behavior with microstructural evolution and to reveal the deformation mechanisms of niobium, the microstructure of the deformed samples were examined using optical microscopy and electron backscatter diffraction (EBSD) technique. The starting material showed a well annealed microstructure with straight grain boundaries and large grains (Fig 4.10a). The microstructure of samples after deformation at strain rate of  $0.1 \text{ s}^{-1}$  and at  $1500 \text{ }^\circ\text{C}$  is shown in Fig. 4.10 (b) and at  $1200$ ,  $1300$  and  $1400 \text{ }^\circ\text{C}$  shown in Fig 4.11. For samples deformed at  $1200$  and  $1300 \text{ }^\circ\text{C}$  at strain rate of  $0.1 \text{ s}^{-1}$  fine grains were observed suggesting modification of initial microstructure. The grain boundaries are no longer straight and the grains no longer as large as in the undeformed sample (compare with Fig. 4.10a). For samples deformed at  $1400$  and  $1500 \text{ }^\circ\text{C}$  the deformation appeared uniform

throughout the sample with grains being equiaxed and larger than those at 1200 and 1300 °C. The presence of equiaxed grains after deformation at these conditions suggests the occurrence of dynamic recrystallization.



(a) Starting Nb material

(b) 1500 °C, 0.1 s<sup>-1</sup>

**Fig. 4.10:** Optical microstructures of (a) starting Nb material and (b) Nb deformed at 1500 °C, 0.1 s<sup>-1</sup>.

The effect of strain rate on the grain size of samples deformed at 1400 °C is shown in Fig. 4.12. On increasing the strain rate from 0.01 to 10 s<sup>-1</sup> at 1400 °C, the resulting grain size was seen to decrease; the grains however still remained equiaxed. It is thus possible to control grain size of the hot worked product by suitable choice of strain rate and temperature. For the sample tested at 800 °C for strain rates of 0.1 and 1 s<sup>-1</sup> regions of flow localization were observed as seen in Fig. 4.13 (marked by dotted lines). For the sample tested at 900 °C and 0.003 s<sup>-1</sup> (Fig. 4.13) elongated grains perpendicular to the deformation direction were observed suggesting the occurrence of dynamic recovery. The iso-*m* map in Fig. 4.6 (a) also shows a small domain around this condition with  $m \approx 0.13$ .

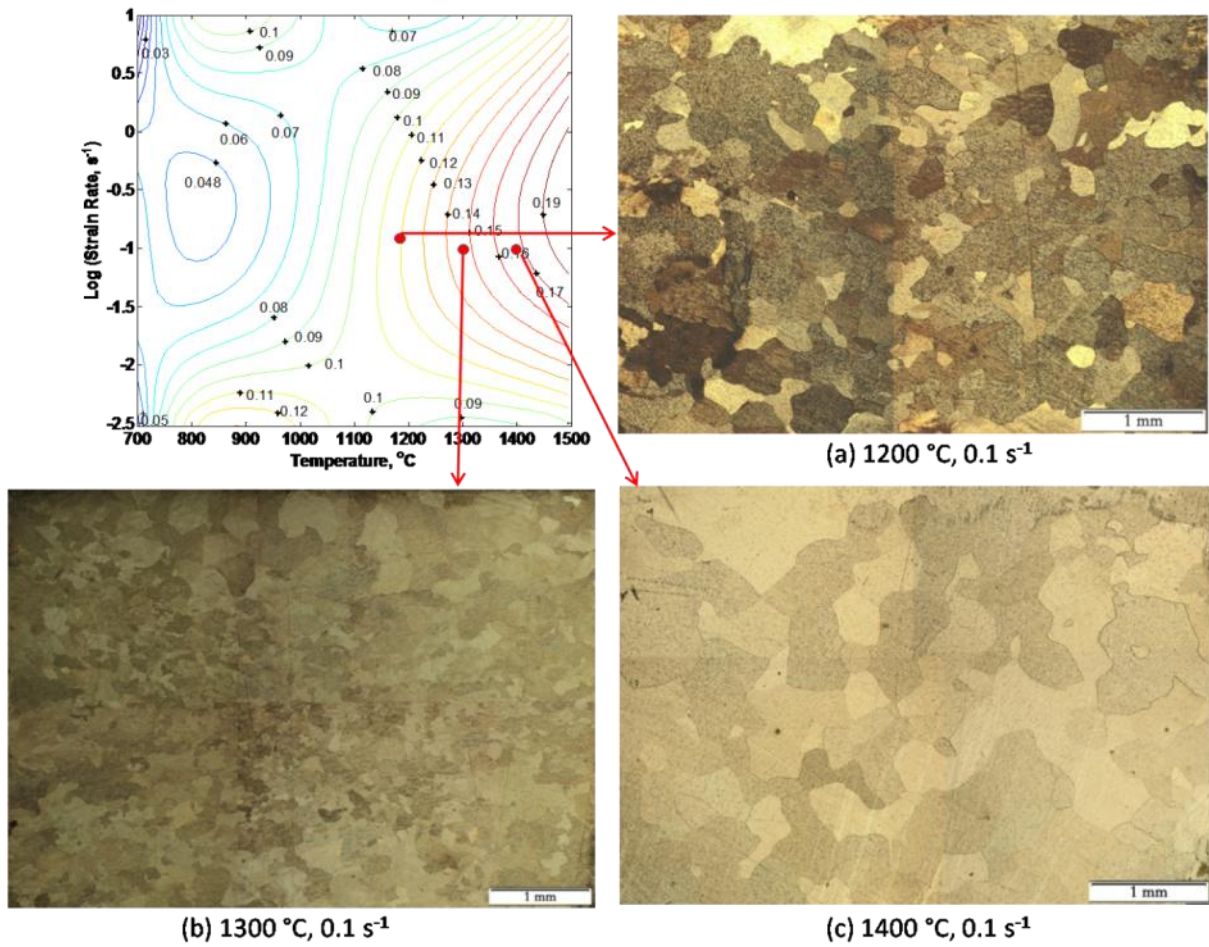


**Fig. 4.11:** Optical microstructure of the deformed Nb samples at strain rate of  $0.1 \text{ s}^{-1}$  for (a) 1200, (b) 1300 and (c) 1400 °C at conditions as shown in the map. Each of the micrographs show the near complete sample with the top and bottom of the micrograph being near the top and bottom faces and the sides are near the lateral faces which show bulging.

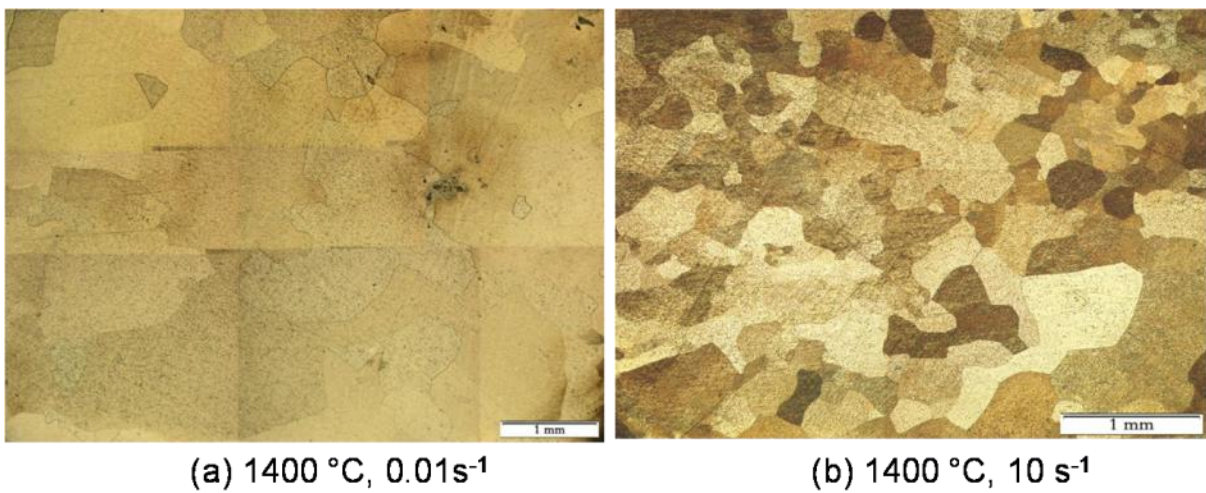


**Fig. 4.12:** Optical microstructure of the Nb samples deformed at 1400 °C and at strain rates of (a)  $0.01 \text{ s}^{-1}$  and (b)  $10 \text{ s}^{-1}$ .

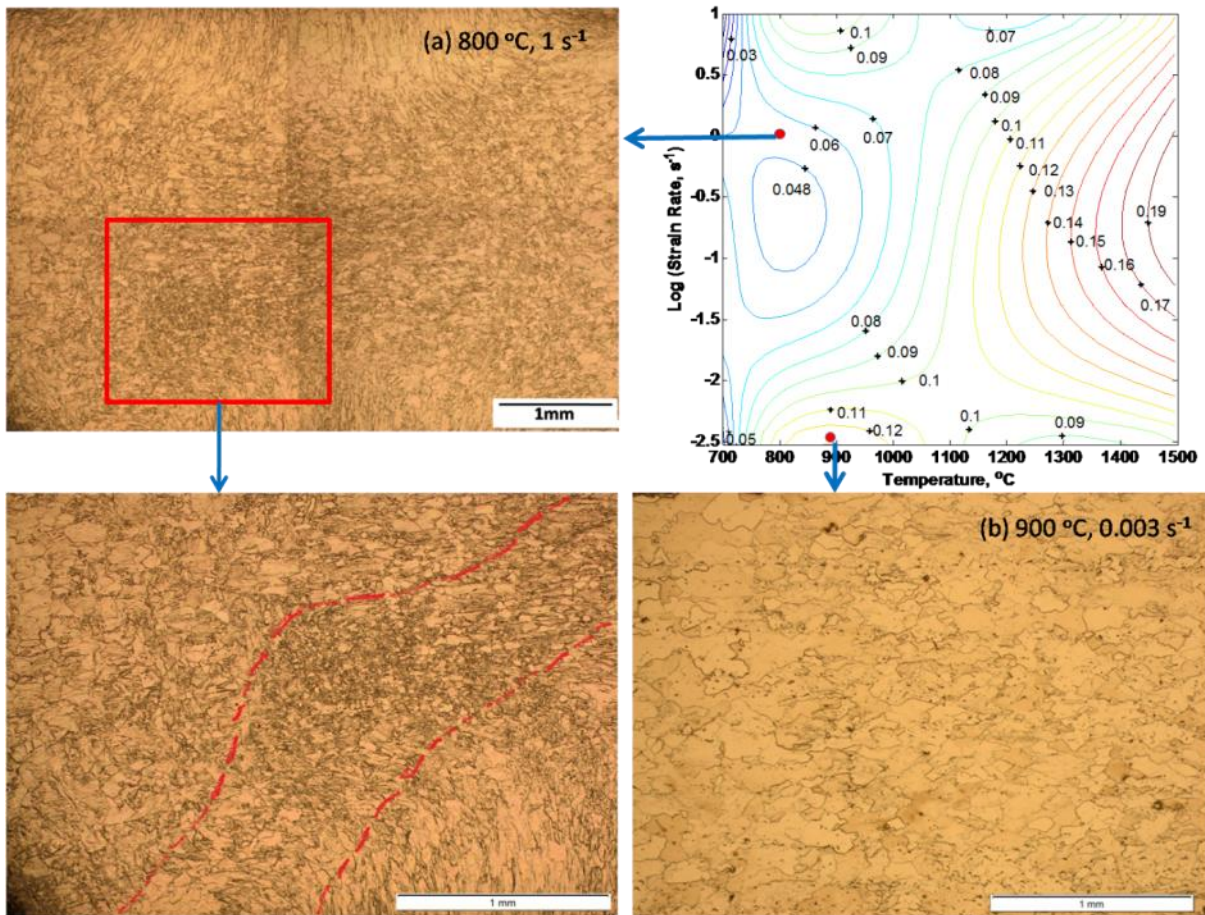


**Fig. 4.13:** Optical microstructure of the deformed Nb sample at 800 °C for strain rate of  $1 \text{ s}^{-1}$  and at 900 °C for strain rate of  $0.003 \text{ s}^{-1}$ . The flow localization was marked by the dotted line for sample deformed at 800 °C for strain rate of  $1 \text{ s}^{-1}$ . The red line portion in the iso- $m$  map shows the high  $m$  domain.

Fig. 4.14 shows the microstructure and micro-texture for deformed samples of pure Nb at 1300 and 1400 °C for strain rate of  $0.1 \text{ s}^{-1}$  with respect to compression axis. At 1300 °C and strain rate of  $0.1 \text{ s}^{-1}$  the microstructure consists of fine recrystallized grains. The strongest intensity of  $\langle 001 \rangle$  pole micro-texture was observed for 1300 °C and strain rate of  $0.1 \text{ s}^{-1}$ .

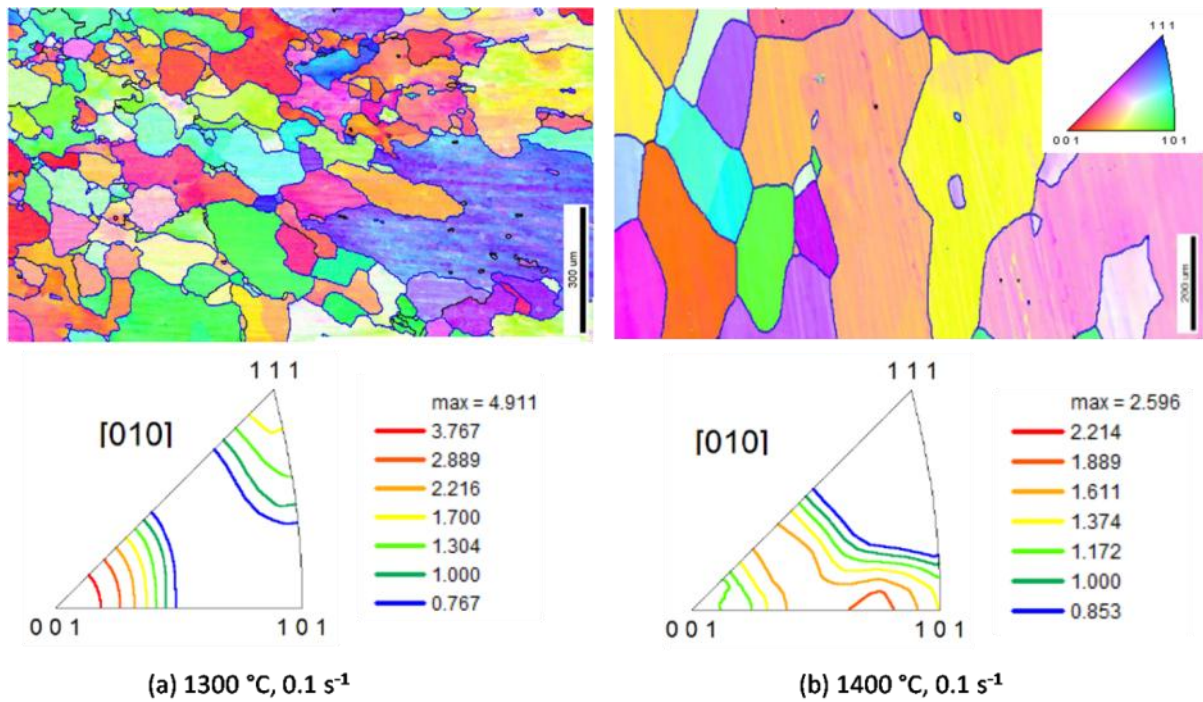


**Fig. 4.14:** Inverse pole figures (IPF) maps of EBSD microstructure for deformed samples of Nb at (a) 1300 °C, 0.1 s<sup>-1</sup> and (b) 1400 °C, 0.1 s<sup>-1</sup>. The scale for 1300 °C, 0.1 s<sup>-1</sup> is 300 μm whereas for 1400 °C, 0.1 s<sup>-1</sup> it is 200 μm.

#### 4.1.7.2 Microstructural characterization of Nb-1Zr

In order to correlate the flow behavior with microstructural evolution and to determine the deformation mechanisms of Nb-1Zr alloy, the microstructure of samples deformed within the domain of hot workability were examined by using the electron backscatter diffraction (EBSD) technique. The starting microstructure of Nb-1Zr (Fig. 4.15) showed well annealed grains with average size of about 138 μm. The microstructure of Nb-1Zr after deformation at temperature of 1500, 1600 and 1700 °C for strain rates of 0.003, 0.01 and 0.1 s<sup>-1</sup> (Fig. 4.16) showed that the average grain size increased with decreasing strain rate and increasing temperature; the grains however still remained equiaxed. At 1500 °C and 0.1 s<sup>-1</sup> the equiaxed grains were the finest as compared to that at other strain rates, with an average grain size of 329 μm. The grains also appeared fully recrystallized and nearly equiaxed for the

deformation condition of 1500 °C and 0.01 s<sup>-1</sup>. Table 4.1 shows the average grain size of Nb-1Zr alloy after deformation at different test conditions.

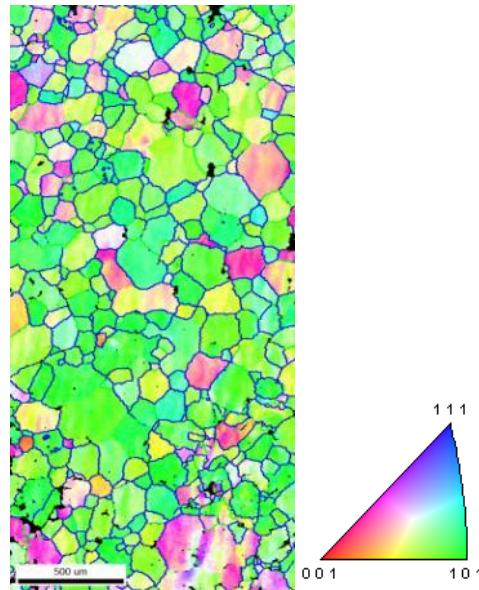


**Fig. 4.15:** IPF map of longitudinal section for starting material of Nb-1Zr alloy. The colours represent the orientation with respect to the compression axis of the deformed sample. The stereographic triangle shows the orientation legend.

At 1600 °C the grains were relatively large at 0.01 s<sup>-1</sup> as compared to that at 0.1 s<sup>-1</sup>, suggesting the occurrence of grain growth at higher temperatures and lower strain rates. Small new recrystallized grains formed at the boundaries of larger grains were seen at 1600 °C and 0.01 s<sup>-1</sup> and marked by arrows in Fig. 4.16. At the higher strain rate of 0.1 s<sup>-1</sup> few elongated grains were observed. Also the presence of equiaxed grains after deformation at these conditions (1600 °C for strain rates of 0.01 and 0.1 s<sup>-1</sup>) suggests the occurrence of dynamic recrystallization. At temperature of 1700 °C and strain rates of 0.1 s<sup>-1</sup> (Fig. 4.16) and 10 s<sup>-1</sup> (Fig. 4.17) the grains were large and boundaries straight as compared to microstructures at other temperature but the same strain rate. The microstructures of the deformed samples within high *m* domain exhibit nearly equiaxed grain morphology.

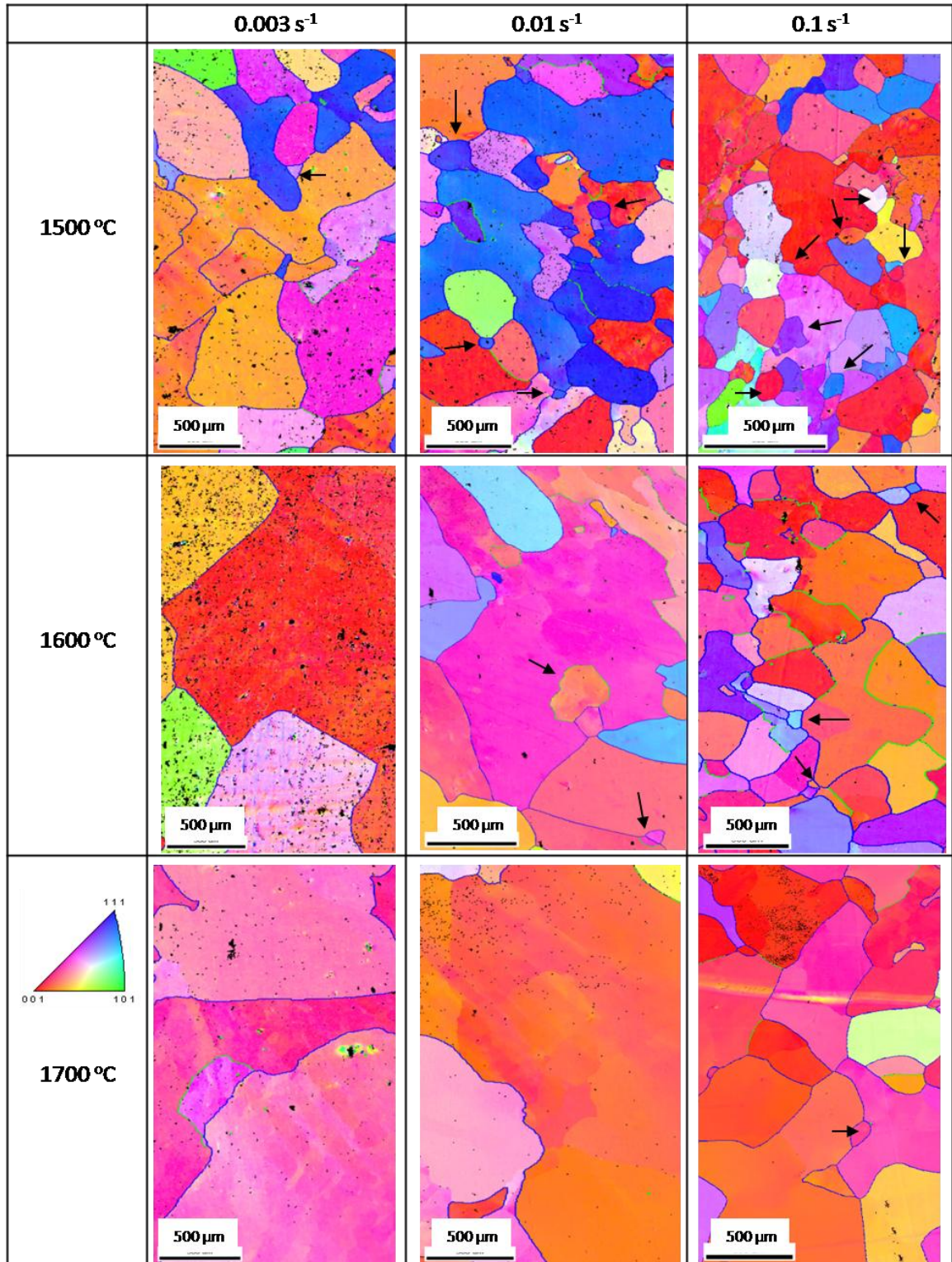


**Fig. 4.16:** IPF maps of the longitudinal section of Nb-1Zr samples deformed at 1500, 1600 and 1700 °C at strain rates of 0.003, 0.01 and 0.1  $\text{s}^{-1}$ . The compression axis is horizontal. The blue lines represent high angle grain boundaries (misorientation  $\phi > 15^\circ$ ) while the green lines represent low angle boundaries (misorientation  $2^\circ < \phi < 15^\circ$ ). The colours represent the orientation with respect to the compression axis of the sample. The arrow shows the fine recrystallized new grains.

**Table 4.1:** Average grain size of Nb-1Zr at different deformation conditions.

Strain rate (s <sup>-1</sup> )	Average grain size (μm) ± standard deviation		
	1500 °C	1600 °C	1700 °C
0.003	827 ± 400	*	*
0.01	613 ± 257	1290 ± 813	*
0.1	329 ± 176	567 ± 296	668 ± 258

\* The number of grains in scan was very few to obtain any meaningful average value.

The equiaxed nature of grains in conjunction with the flow stress behavior of a peak followed by flow softening towards steady state (Fig. 4.2a, b and c) strongly suggest the occurrence of dynamic recrystallization. The larger grain sizes at higher temperatures and lower strain rates suggest the occurrence of grain growth after DRX. DRX is considered as an important restoration mechanism during thermo-mechanical processing and such features of DRX during hot deformation are seen for many metals alloy systems, e.g. [90, 95, 96, 149, 161].

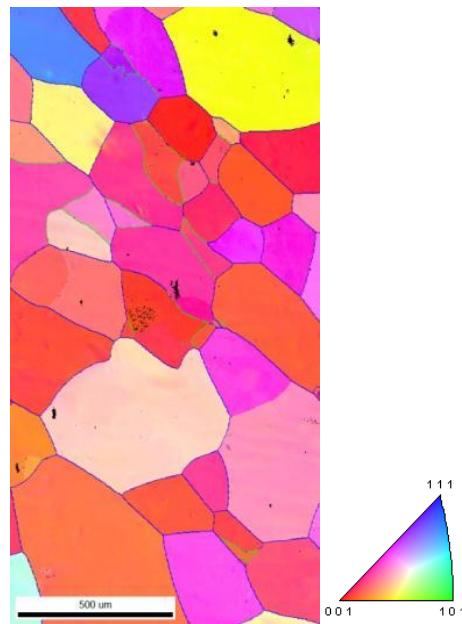


**Fig. 4.17:** IPF map of the longitudinal section of samples deformed at 1700 °C for strain rate of 10 s<sup>-1</sup> conditions. The colours represent orientation with respect to compression axis of the sample (vertical in figure).

The Kernel Average Misorientation (KAM) or the local average misorientation represents the average misorientation between each data point and all its nearest neighboring points, except those whose misorientation angle is greater than  $5^\circ$ . KAM relates to the geometrically necessary dislocation (GND) density present within subgrains or grains. Fig. 4.18 shows the KAM of deformed samples at different test conditions. For strain rate of 0.1 and 0.01  $\text{s}^{-1}$  the KAM value decreased with increase in temperature (Fig 4.18a and b).

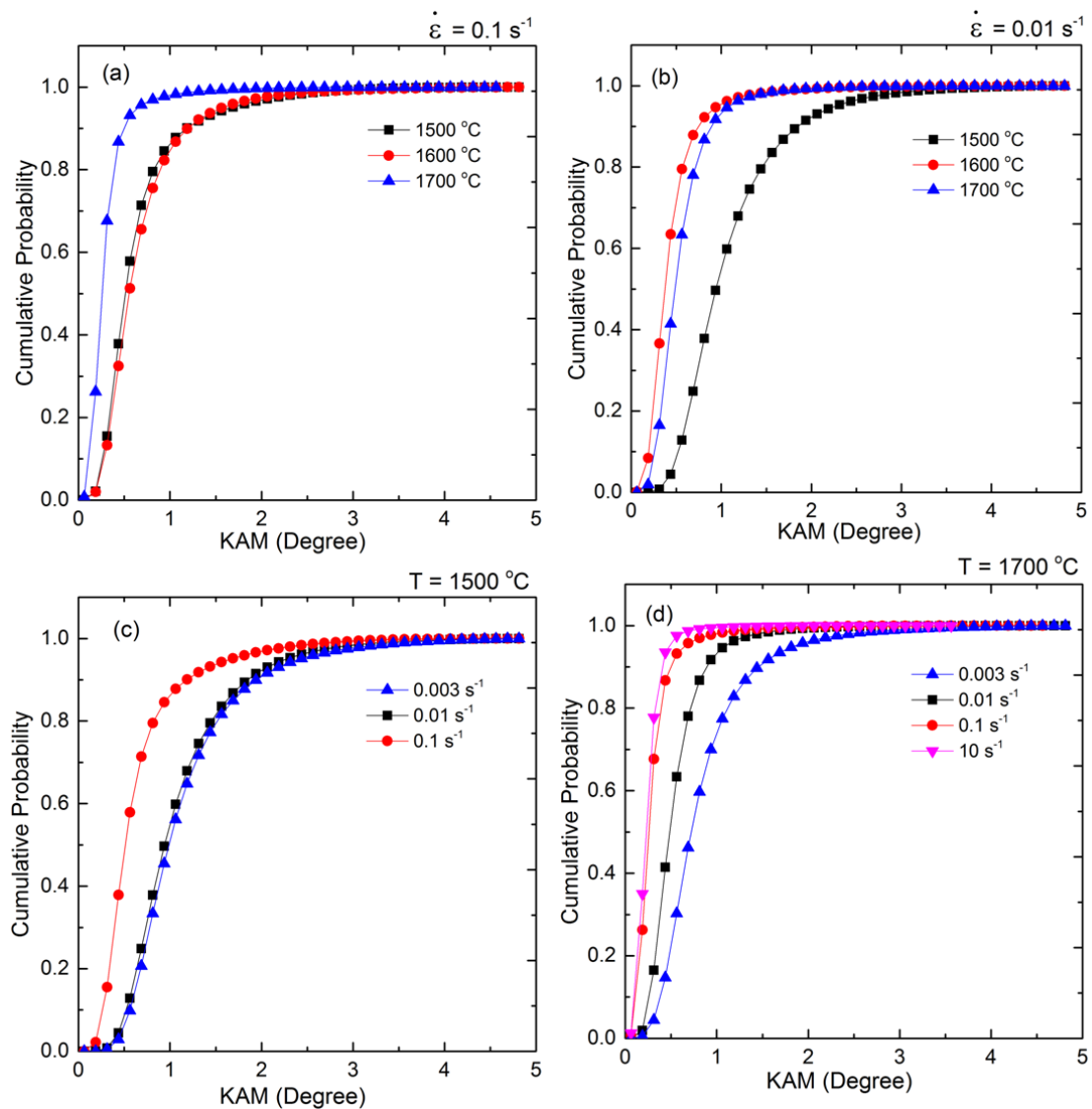


**Fig 4.18:** Cumulative distribution of KAM with misorientation angle less than  $5^\circ$  for samples deformed at strain rates of (a)  $0.1 \text{ s}^{-1}$  and (b)  $0.01 \text{ s}^{-1}$  for temperature of 1500, 1600 and 1700 °C. Similar distribution of samples deformed at temperatures of (c) 1500 °C and (d) 1700 °C for strain rates of 0.003, 0.01, 0.1 and  $10 \text{ s}^{-1}$ .

Similarly for temperature of 1500 and 1700 °C KAM values decreased with increase in strain rates Fig. 4.18 (c) and (d). This signifies that at 1500 to 1700 °C and 0.003 to 0.1 s<sup>-1</sup> there was either recovery or recrystallization taking place. The extent of recovery or recrystallization increases with temperature and decreases with strain rate.

#### **4.1.7.2.1 Texture**

The crystallographic texture information was obtained from bulk XRD scans. The inverse pole figures (IPF) calculated with respect to the compression axis for samples tested at different conditions are shown in Fig. 4.19. For deformation conditions in high *m* domain shown in (Fig. 4.19) (for high *m* domain) the predominant texture was along the <001> poles. The strongest intensity of the <001> pole texture was observed at the test condition of 1500 °C and 0.1 s<sup>-1</sup>. At 0.1 s<sup>-1</sup> the <001> fiber texture was weaker at 1700 °C as compared to 1500 °C. In comparison Nb-1Zr-0.1C too showed a strong fiber texture of <001> at 1500 °C and 10<sup>-1</sup> and 10<sup>-2</sup> s<sup>-1</sup> [73]. Nb-1Zr-0.1C deformed at 1700 °C and 10<sup>-3</sup> s<sup>-1</sup> showed the fiber texture at both <001> and <111> pole.

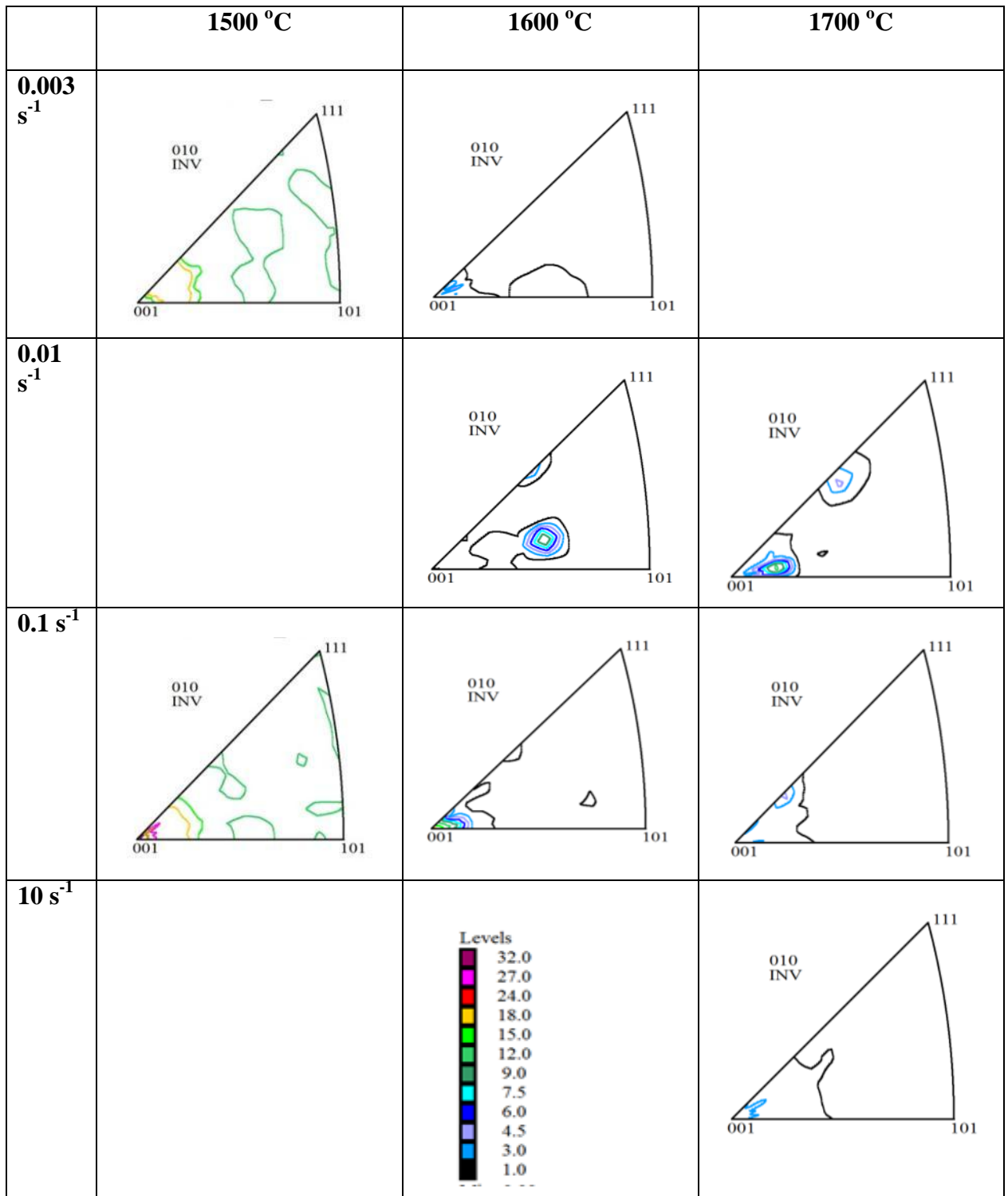


**Fig. 4.19:** Inverse pole figures for texture with respect to compression axis of deformed samples of Nb-1Zr alloy at different testing conditions.

#### 4.1.8 Microstructural characterization of Nb-1Zr-0.1C

Fig. 4.20 shows the inverse pole figure image of the as received sample of Nb-1Zr-0.1C alloy. It has been observed that prior to deformation, the sample has large grains and average grain size of  $\sim 30 \mu\text{m}$ . Also the fraction of high angle grain boundaries is high as seen from the Fig. 4.20. The deformed microstructures (Fig. 4.21) reveal significant modifications of the starting microstructure (Fig. 4.20) and exhibit nearly equiaxed grain morphology.

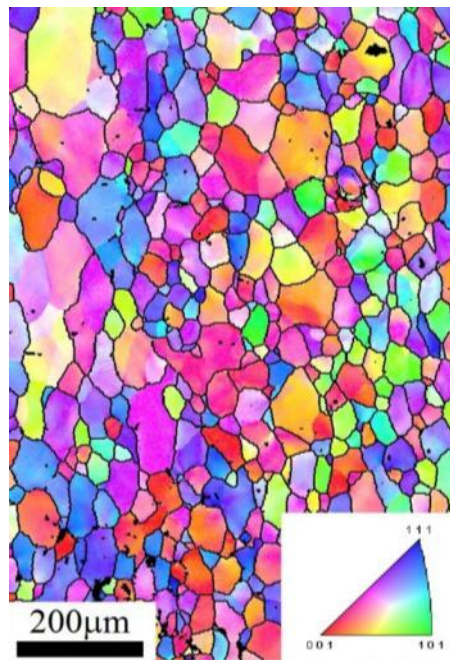


**Fig. 4.20:** Inverse pole figure map of the as received sample of Nb-1Zr-0.1C alloy.

Fig. 4.21 shows the IPF images of longitudinal section of Nb-1Zr-0.1C samples deformed at 1500, 1600 and 1700 °C at strain rates of 0.001, 0.01 and 0.1  $\text{s}^{-1}$ . High angle boundaries ( $> 15^\circ$ ) are marked as thick black lines in these images. At temperature of 1500 °C and strain rate of  $10^{-1} \text{s}^{-1}$  the microstructure consists of many fine grains surrounding the larger grains. Similar features have been observed for the samples deformed at 1600 and 1700 °C and at the strain rate  $10^{-1} \text{s}^{-1}$ , where fine grains surround larger grains forming the typical necklace structure, which is a characteristic feature of dynamic recrystallisation (DRX). However, no

such fine grains are observed at 1500 °C for lower strain rates of  $10^{-3}$  and  $10^{-2}$  s<sup>-1</sup>. It is likely that at lower strain rates grain growth occurred for all the test temperatures. The grain growth is most notable at 1700 °C and strain rate of 0.001 s<sup>-1</sup>. As the deformation microstructures are quite heterogeneous this suggests fact that the DRX is incomplete at these deformation conditions. At strain rate of 0.001 s<sup>-1</sup> and temperatures of 1500 to 1600 °C, serrated high angle grain boundaries are observed whereas at strain rate of 0.01 s<sup>-1</sup> similar features are observed only at temperature of 1600 °C. However at strain rate of 0.1 s<sup>-1</sup> the serration of grain boundaries is very prominent at 1700 °C. In the sample deformed at 1700 °C and 0.1 s<sup>-1</sup> (Fig. 4.21) small new grains at boundaries of initial (larger) grains are observed, while the grain interior do not contain new grains. A similar microstructure is seen for sample tested at 1600 °C and 0.01 s<sup>-1</sup> where wavy boundaries on large grains are actually indicative of boundaries of small newly recrystallized grains. Further, it is observed that the grain size of deformed samples varies with strain rate and temperature of deformation within the high *m* domain as seen in Fig. 4.21. These observations suggest that the Nb-1Zr-0.1C alloy undergoes DRX when deformed within the high *m* domain.

In Fig. 4.22 the thick black lines represent the HAGBs ( $\varphi > 10^\circ$ ) and the grey lines represents LAGBs ( $\varphi \sim 2^\circ - 10^\circ$ ). It was observed that with increase in strain rate the subgrain size becomes finer and at the high strain rate of 0.1 s<sup>-1</sup> subgrains are undeveloped in the mid-regions of grains.

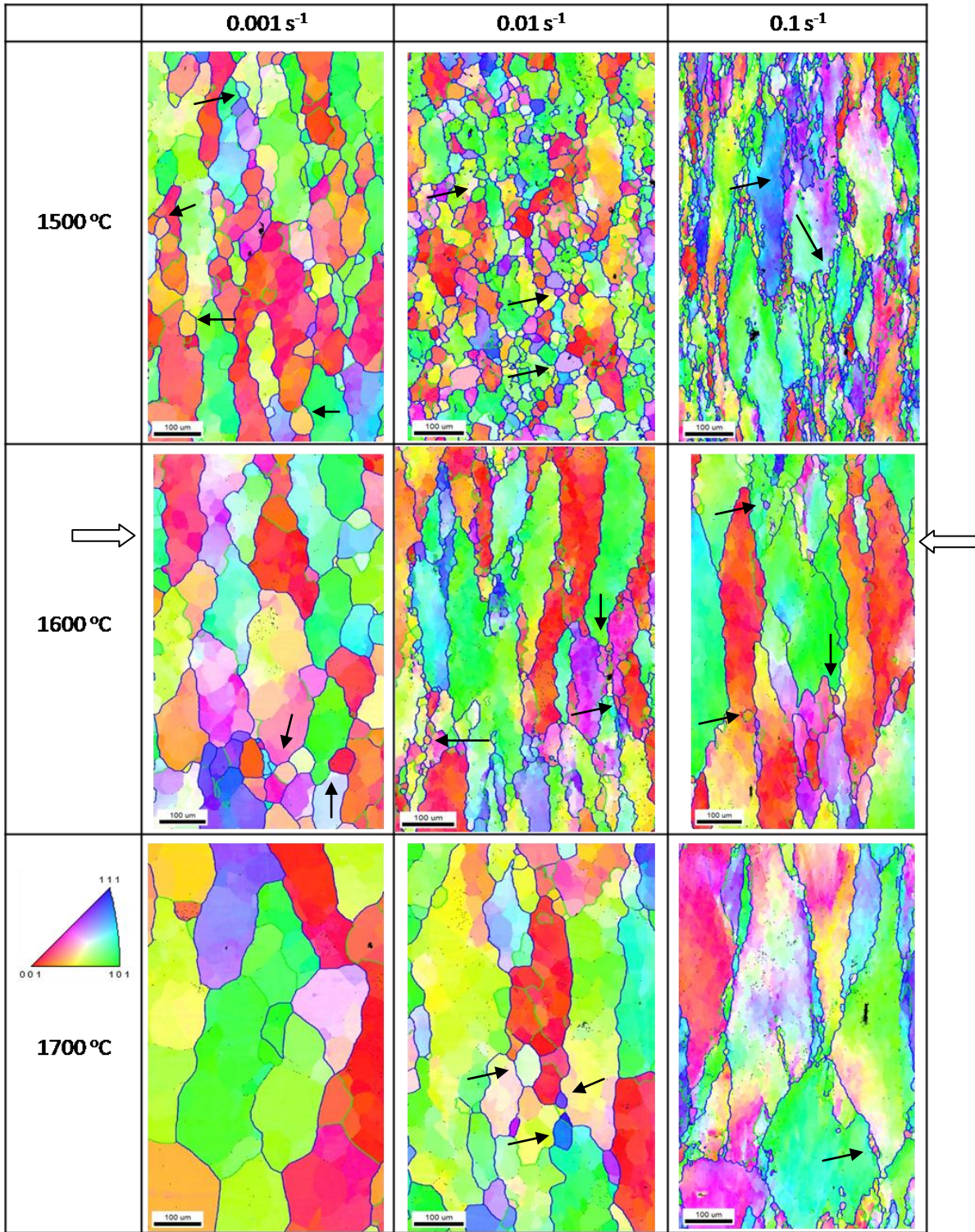


**Fig. 4.21:** IPF map of the longitudinal section of Nb-1Zr-0.1C samples deformed at 1500, 1600 and 1700 °C at strain rates of 0.001, 0.01 and 0.1 s<sup>-1</sup>. The compression axis is horizontal. The blue lines represent high angle grain boundaries (misorientation  $\phi > 10^\circ$ ) while the green lines represent low angle boundaries (misorientation  $2^\circ < \phi < 10^\circ$ ). The colours represent the orientation with respect to the compression axis of the sample. The arrow marks shows the fine recrystallized new grains.

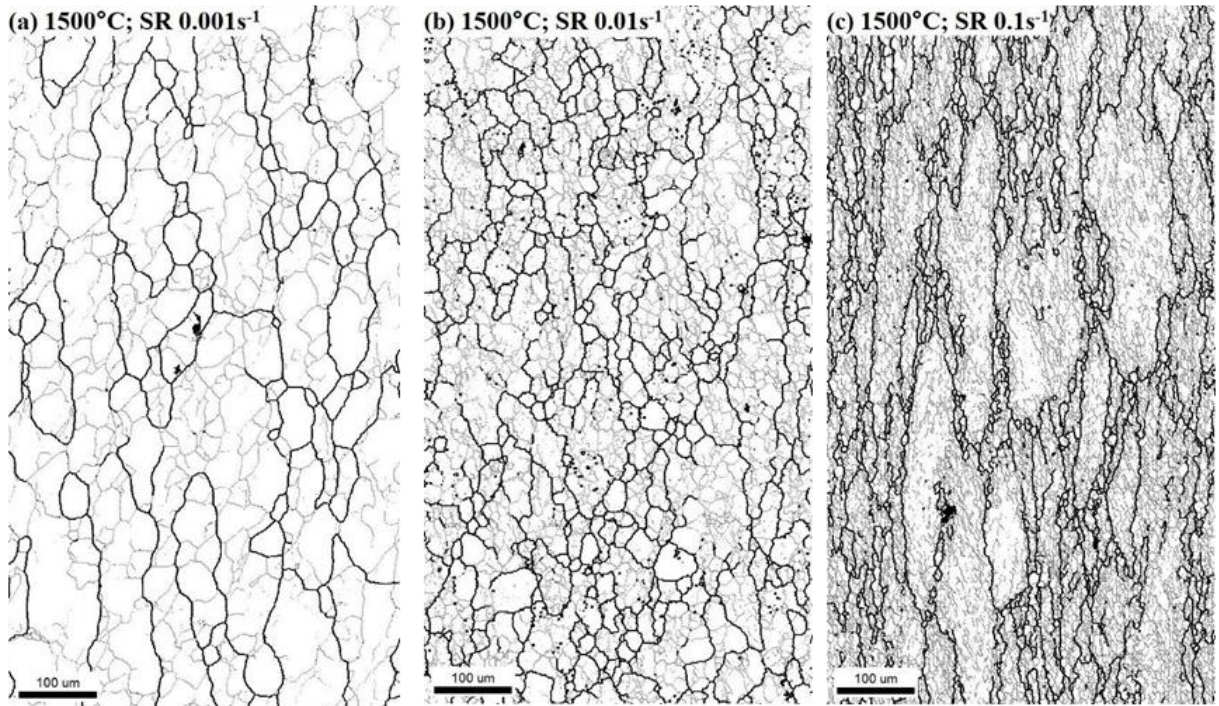


**Fig. 4.22:** Image quality map of Nb-1Zr-0.1C alloy deformed at temperature of 1500 °C and strain rates of (a)  $0.001 \text{ s}^{-1}$ , (b)  $0.01 \text{ s}^{-1}$  and (c)  $0.1 \text{ s}^{-1}$ . The dark lines represent misorientation angle  $> 10^\circ$  and grey lines  $2^\circ - 10^\circ$ .

In order to understand the mechanism of dynamic recrystallization, the recrystallised grains were partitioned out in the EBSD images using the criterion as grain orientation spread (GOS)  $< 2^\circ$  (Fig. 4.23). A GOS value less than  $2^\circ$  is used as an approximation to distinguish the recrystallized grains from the other deformed grains. As the dislocation densities of DRX grains are lower than that of deformed grains, the GOS value of DRX grains is to be low. Fig. 4.23 shows that the size of DRX grains decreases with increasing strain rate. Also the number fraction of recrystallised grains (GOS  $< 2^\circ$ ) is much higher in the samples deformed at higher strain rates, as compared to those in the low strain rates.

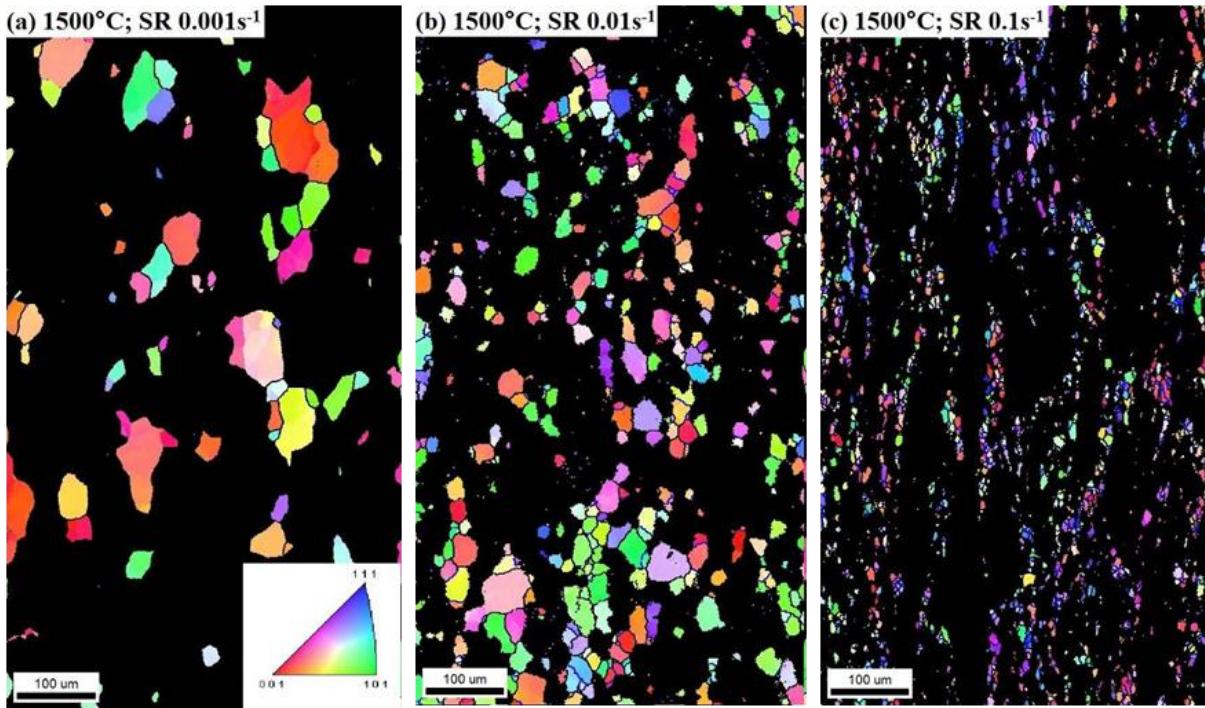


**Fig. 4.23:** Inverse pole figure map of the partitioned recrystallized grains (depending on Grain Orientation Spread ( $< 2^\circ$ )) for the deformation of Nb-1Zr-0.1C at conditions as indicated.

#### 4.1.9 Effect of strain on evolution of microstructure of Nb-1Zr-0.1C

##### 4.1.9.1 Flow Stress behaviour

To study the evolution of DRX, compression tests were carried out at the optimum condition of 1500 - 1600°C and  $0.1 \text{ s}^{-1}$  to strains of 0.3, 0.6, 0.9 and 1.2. Fig. 4.24 (a) shows the true stress-true strain curves for Nb-1Zr-0.1C alloy compressed at test temperatures of 1500 and 1600 °C and at strain rate of  $0.1 \text{ s}^{-1}$ . Fig. 4.24 (b) shows the true stress-true strain curves for Nb-1Zr-0.1C alloy compressed at test temperature of 1500 °C and at strain rate of  $0.1 \text{ s}^{-1}$  for different tests up to true strains of 0.3, 0.6, 0.9 and 1.2. The curves lie on each other suggesting good repeatability of the experiments. The flow curves for Nb-1Zr-0.1C alloy showed a strong dependence on deformation temperature and strain rate. The flow curves showed an initial work-hardening to a maximum stress followed by softening. This softening

of flow stress after an initial hardening is a characteristic feature of dynamic recrystallisation (DRX) [96, 162].

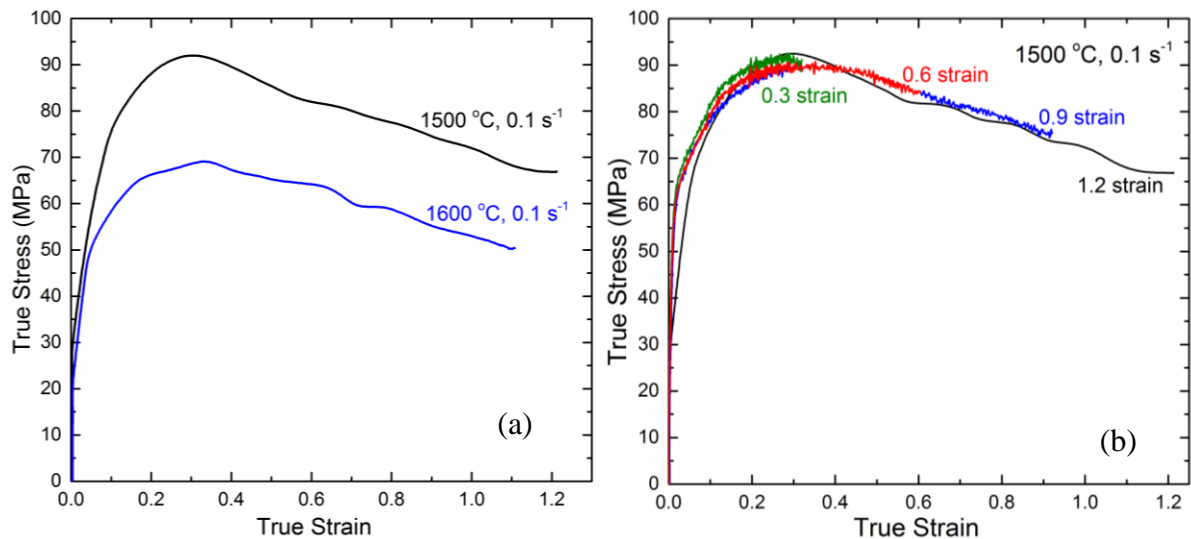


**Fig. 4.24:** True stress vs. true strain plot of Nb-1Zr-0.1C alloy (a) at 1500 and 1600 °C and at strain rates 0.1 s<sup>-1</sup> up to a true strain of 1.2, (b) at 1500 °C and strain rate of 0.1 s<sup>-1</sup> showing curves of different tests to true strains of 0.3, 0.6, 0.9 and 1.2.

#### 4.1.9.2 Microstructural characterization

The microstructural evolution of Nb-1Zr-0.1C alloy deformed to a true strain of 0.3, 0.6, 0.9 and 1.2 at temperatures of 1500 and 1600 °C and strain rate of 0.1 s<sup>-1</sup> was examined by using EBSD. Fig. 4.25 shows the inverse pole figure (IPF) map of Nb-1Zr-0.1C alloy deformed at 1500 °C and 0.1 s<sup>-1</sup>. In Fig. 4.25 the black lines represent high angle grain boundaries (HAGB misorientation angle,  $\phi > 10^\circ$ ) and the blue lines represent low angle grain boundaries (LAGB,  $2^\circ < \phi < 10^\circ$ ). At a true strain of 0.3 at the deformation condition of 1500 °C and 0.1 s<sup>-1</sup> large grains with substructure were observed with a large number of boundaries with  $2^\circ < \phi < 10^\circ$  (Fig. 4.25a). At this deformation condition work-hardening dominates. Similar type of dislocation substructures developed during dynamic recrystallisation (DRX) were observed for polycrystalline nickel [115]. At true strain of 0.6 the grain boundaries appear serrated with increased subgrain boundaries within the grains. Small grains with high angle

boundaries were seen at the corrugated site of the grain boundaries (Fig. 4.25b). The average grain size of these fine grains is about 5  $\mu\text{m}$  and these form a necklace type of structure along the grain boundaries of the larger grains (grain size  $> 100 \mu\text{m}$ ) as seen in Fig. 4.25 (b). Similar type of microstructures were also reported for this alloy by others at this deformation condition [47, 73]. Fig. 4.25 (b) also shows that few large grains contain well defined subgrains within them. At 1500  $^{\circ}\text{C}$  and  $0.1 \text{ s}^{-1}$  deformed to a true strain of 0.9 elongated grains were seen perpendicular to the compression axis (Fig. 4.25c).

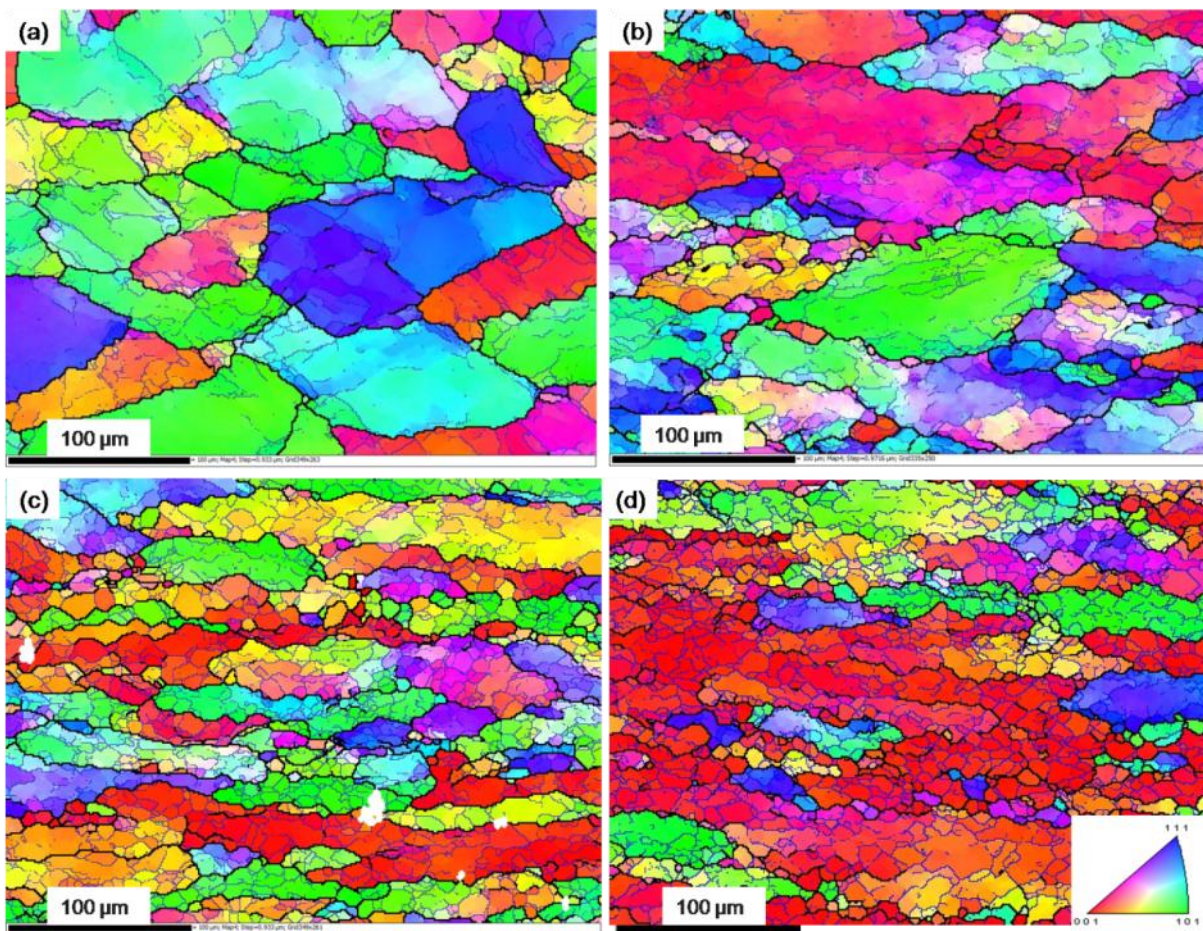


**Fig. 4.25:** Inverse pole figure (IPF) map of Nb-1Zr-0.1C deformed at temperature of 1500  $^{\circ}\text{C}$  and strain rate of  $0.1 \text{ s}^{-1}$  up to true strains of (a) 0.3, (b) 0.6, (c) 0.9 and (d) 1.2. The colours represent the orientation normal to the observation surface of the deformed sample. The stereographic triangle shows the orientation legend. The black lines represent high angle grain boundaries ( $\phi > 10^{\circ}$ ) while the blue lines represent low angle boundaries ( $2^{\circ} < \phi < 10^{\circ}$ ).

The elongated large grains had wavy grain boundaries with well defined subgrains within. The microstructure consisted of many fine equiaxed grains having high angle boundaries. This deformation condition showed grain refinement as compared to that at strain of 0.6. For larger strain of 1.2 the elongated grains were seen to contain many fine grains with high angle boundaries (Fig. 4.25d). The homogeneous microstructure suggests the transformation of subgrain boundaries into grain boundaries at this deformation condition.

Fig. 4.26 (a) shows the cumulative grain size distribution for all grains after deformation at 1500 °C and 0.1 s<sup>-1</sup> up to different strains. The boundary spacing is measured between all boundaries with  $\phi > 2^\circ$  (including both subgrain and grain boundaries). The distribution showed that as the strain increased the curves shifted to left, i.e. the median value of the distribution decreased. At 1500 °C the lowest median value was at a strain of 0.9 implying the lowest subgrain size distribution at this condition as compared to other deformed conditions. Fig. 4.26 (b) shows cumulative distribution of misorientation angle for samples after deformation at 1500 °C and 0.1 s<sup>-1</sup> up to different strains. The correlated distribution was obtained by taking the minimum angle of 2°. The misorientation angle (or angular distance) between two orientations is defined as the smallest angle of rotation leading from one orientation to the other. The misorientation angle distribution showed that at all the deformation conditions the microstructure consisted of mostly low angle boundaries ( $\phi < 10^\circ$ ). However as the deformation strain increased the fraction of HAGB also increased (from a value of 0.24 at strains of 0.3 and 0.6 to a value of 0.3 at strains of 0.9 and 1.2) as reflected in the observed microstructure of Fig. 4.25.

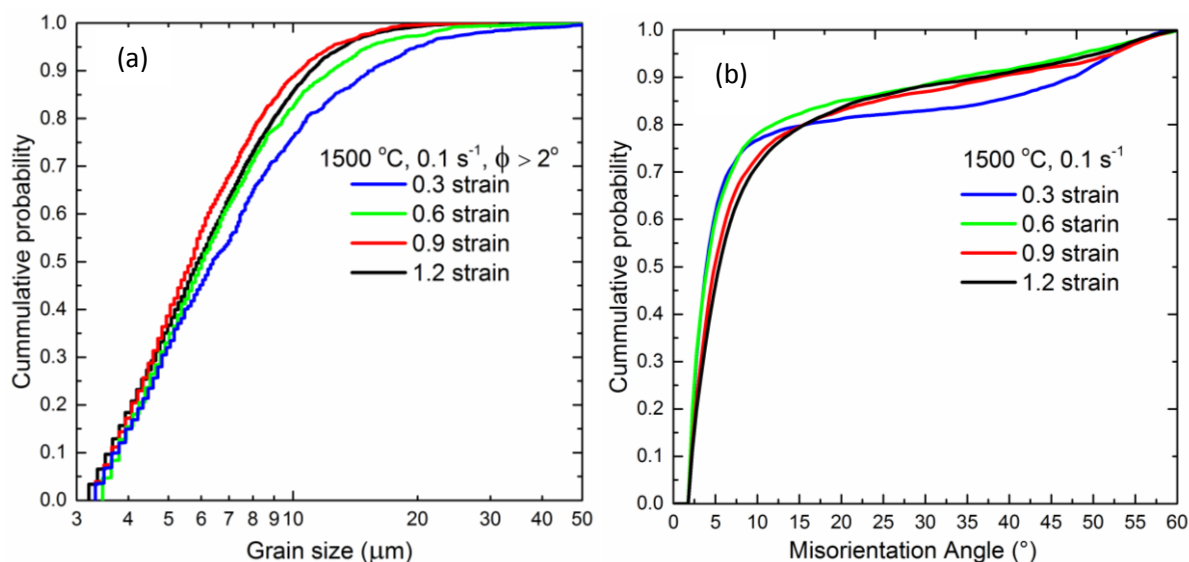


**Fig. 4.26:** (a) Cumulative grain size distribution for all grains with misorientation angle ( $\phi$ ) greater than  $2^\circ$  and (b) Cumulative distribution of misorientation angle for samples deformed at  $1500^\circ\text{C}$  and  $0.1\text{ s}^{-1}$  at different strains.

The IPF map for strain of 0.3 after deformation at  $1600^\circ\text{C}$  and  $0.1\text{ s}^{-1}$  (Fig. 4.27a) showed few large grains containing few subgrain boundaries. At strain of 0.6 these large grains were elongated perpendicular to the compression direction (Fig. 4.27b). Also small subgrains were seen inside the large deformed grain. A small number of fine grains having high angle boundaries were formed along the deformed grain boundaries. At this deformation condition the fraction of low angle boundaries was 0.77. At a strain of 0.9 corrugated boundaries were seen with a large subgrain structure within the grains. Small grains at the serrated grain boundaries were also observed (Fig. 4.27c). Similar kind of microstructure was also observed for this alloy deformed to strain of 0.6 at  $1600^\circ\text{C}$  and  $0.01\text{ s}^{-1}$  [47]. In the present study at strain of 0.6 and 0.9 the grain interior showed the formation of small subgrains. At this deformation condition necklace type of recrystallized microstructure was also observed along the boundary of the large elongated grain. At this elevated temperature there was substantial grain growth at the large strain of 1.2. Fig. 4.27 (d) shows the equiaxed microstructure at strain of 1.2 for temperature of  $1600^\circ\text{C}$  and strain rate of  $0.1\text{ s}^{-1}$ . Some

regions containing substructure continue to be present at this large strain (steady state flow stress). The new equiaxed grains appear to replace the initial substructure completely.

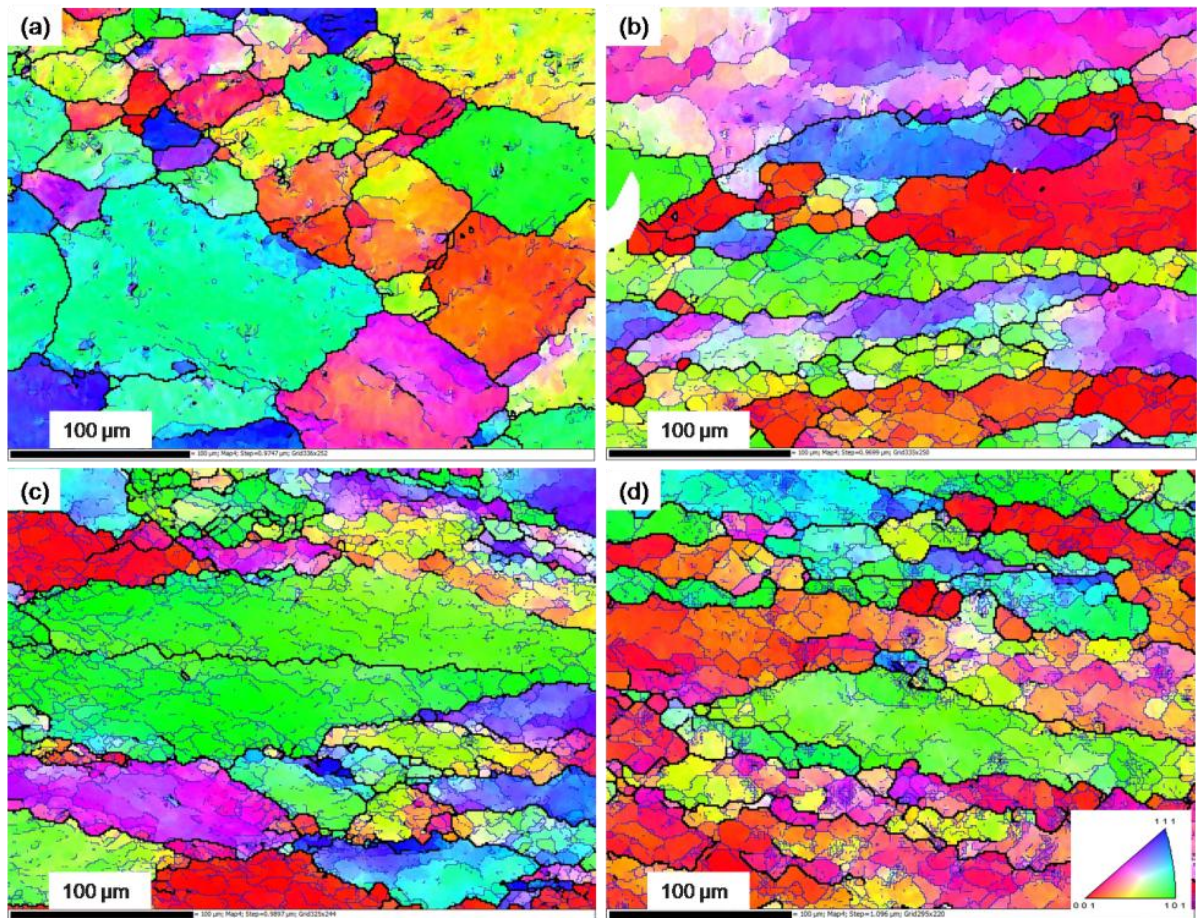


**Fig. 4.27:** Inverse Pole Figure map of Nb-1Zr-0.1C deformed at temperature of 1600 °C and strain rate of 0.1 s<sup>-1</sup> for different true strain as (a) 0.3, (b) 0.6, (c) 0.9 and (d) 1.2. The colours represent the orientation normal to the observed plane of the deformed sample. The stereographic triangle shows the orientation legend. The black lines represent high angle grain boundaries ( $\varphi > 10^\circ$ ) while the blue lines represent low angle boundaries ( $2^\circ < \varphi < 10^\circ$ ).

Fig. 4.28 (a) shows the grain size distribution determined from the EBSD data for temperature of 1600 °C and strain rate of 0.1 s<sup>-1</sup>. The distribution of grain size for all grains with misorientation angle greater than 2° showed that at a strain of 0.6 Nb-1Zr-0.1C had the highest median value whereas for strain of 0.9 it had the lowest value. The cumulative distribution of misorientation angle for Nb-1Zr-0.1C deformed at 1600 °C and 0.1 s<sup>-1</sup> up to

different strains is shown in Fig. 4.28 (b). The correlated distribution was obtained by taking the minimum angle of  $2^\circ$ . The fraction of low angle boundaries (value of cumulative probability at  $\phi = 10^\circ$ ) increased with strain (Fig. 4.28b). The low angle misorientation structure corresponds to a dislocation substructure. The distribution showed that the microstructures of all the deformed samples consisted of mostly low angle boundaries ( $\phi < 10^\circ$ ).

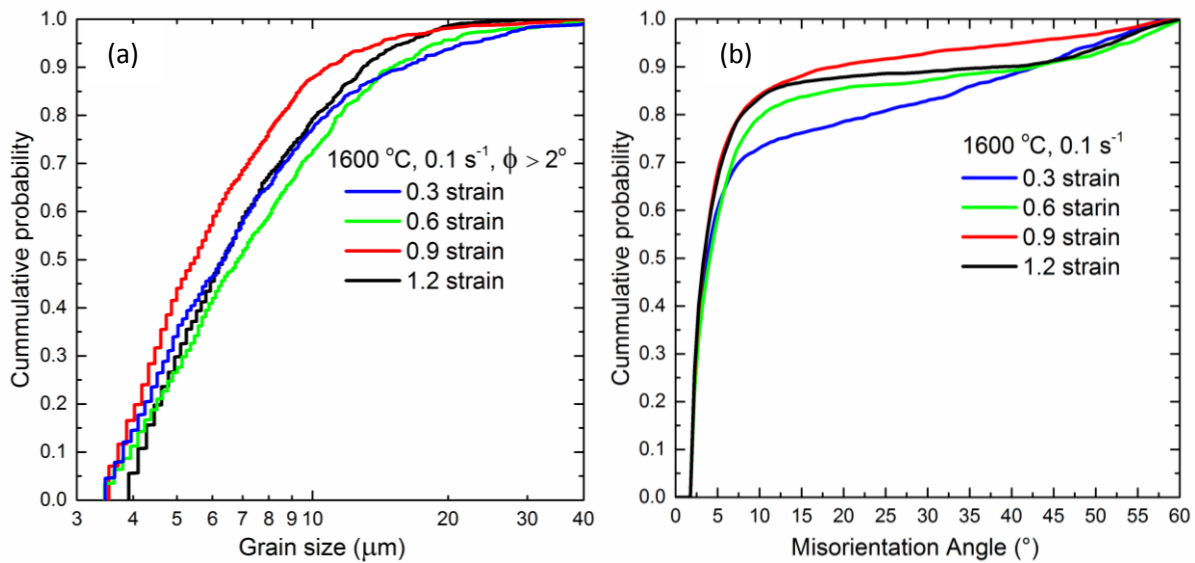


**Fig. 4.28:** (a) Cumulative grain size distribution for all grains with misorientation angle greater than  $2^\circ$  and (b) Cumulative distribution of misorientation angle for samples deformed at 1600 °C and  $0.1 \text{ s}^{-1}$  up to different strains.

#### 4.1.9.3 Local average misorientation distribution

The local misorientation distribution of Nb-1Zr-0.1C at 1500 and 1600 °C at  $0.1 \text{ s}^{-1}$  and at different strains were compared in Fig. 4.29. Local misorientations signify excess of geometrically necessary dislocations (GND) within subgrains. Fig. 4.29 shows a comparison of local average misorientation distribution for misorientation below  $2^\circ$  for samples deformed at 1500 and 1600 °C for strain rate of  $0.1 \text{ s}^{-1}$ . At the deformation condition of 1500 °C and  $0.1 \text{ s}^{-1}$  the local average misorientation distribution was low at strain of 0.9. This suggests

low GND density within subgrains at this condition. At 1600 °C and 0.1 s<sup>-1</sup> the local average misorientation increased with increasing strain. The distribution was low at strain of 0.3 and 0.6. This was unlike that at 1500 °C where the distribution was shifted to low values for strain of 0.9.

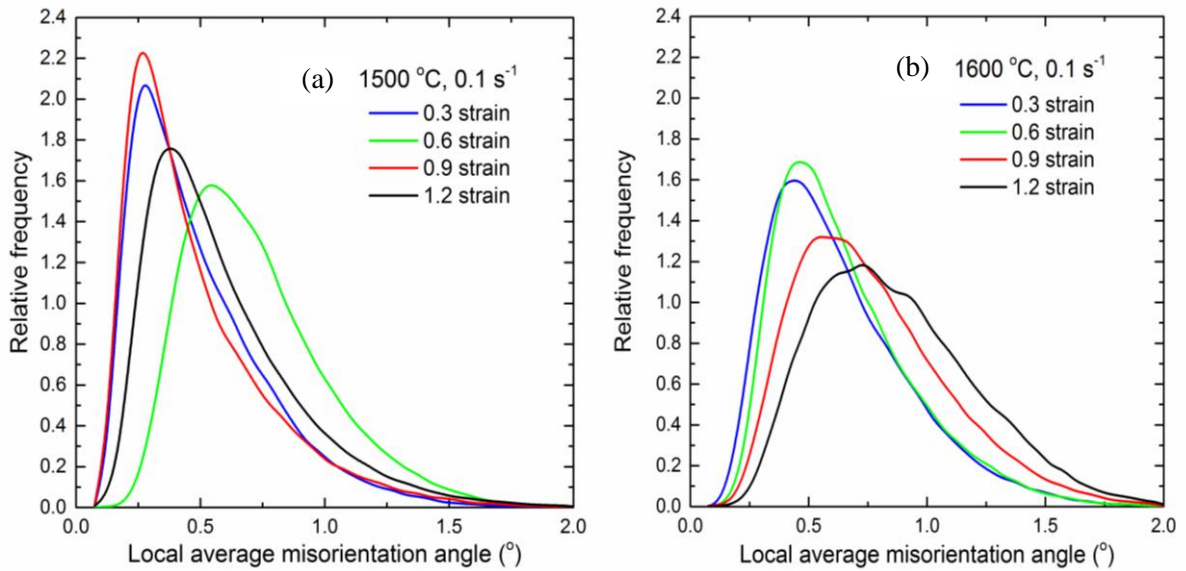


**Fig. 4.29:** Local average misorientation distribution for misorientation below 2° of samples deformed at (a) 1500 and (b) 1600 °C for strain rate of 0.1 s<sup>-1</sup>.

#### 4.1.9.4 Texture

For an understanding of deformation behavior crystallographic texture measurements were carried out for the deformed samples of Nb-1Zr-0.1C alloy. The inverse pole figures were calculated from bulk XRD scans with respect to the compression axis for samples tested at 1500 °C and 0.1 s<sup>-1</sup> and up to a strain of 0.3, 0.6, 0.9 and 1.2 (Fig. 4.30). At this deformation condition the predominant texture was along the <001> poles. As the strain increased the texture evolution along the <001> component became stronger. The strongest intensity of the <001> pole texture was observed at the test condition of 1500 °C and 0.1 s<sup>-1</sup> for strain of 1.2. At 1500 °C and 0.1 s<sup>-1</sup> all fibers <001>, <101> and <111> were present for strain of 0.9, whereas <111> component became weak at a strain of 1.2.

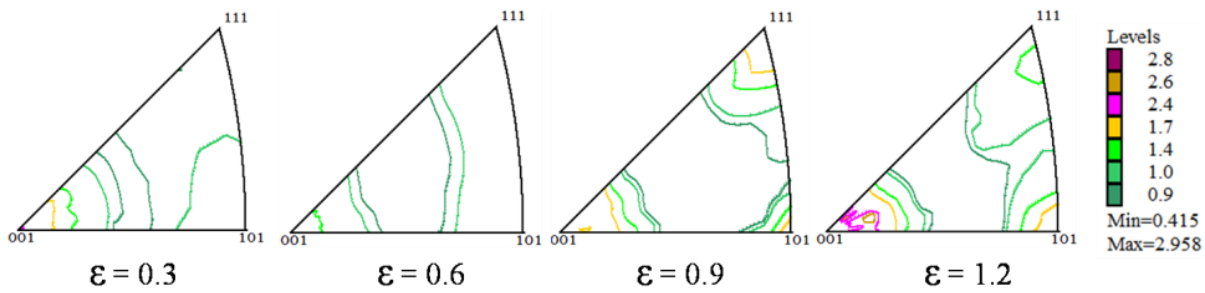


**Fig. 4.30:** Inverse pole figures from bulk XRD texture measurements with respect to compression axis for Nb-1Zr-0.1C alloy deformed at 1500 °C and strain rate of 0.1 s<sup>-1</sup> to different strains.

Fig. 4.31 shows the micro-texture with respect to compression axis for Nb-1Zr-0.1C alloy deformed at 1500 and 1600 °C at strain rate of 0.1 s<sup>-1</sup>. The strongest intensity of <001> pole micro-texture was observed for a strain of 1.2 after deformation at 1500 °C and 0.1 s<sup>-1</sup>. This is very similar to the bulk texture at 1500 °C and 0.1 s<sup>-1</sup> (Fig. 4.30). At 1600 °C and 0.1 s<sup>-1</sup>, a strong intensity of <001> component was obtained for strain of 0.6 as compared to other strain conditions.

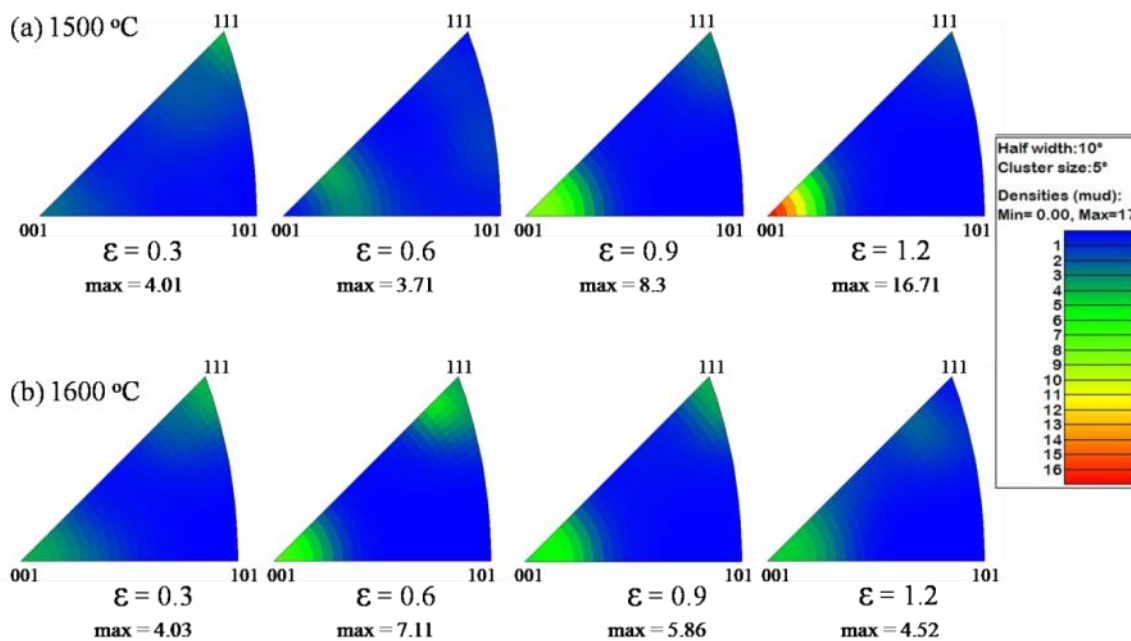


**Fig. 4.31:** Inverse pole figures from EBSD measurements with respect to compression axis of Nb-1Zr-0.1C alloy deformed at 1500 and 1600 °C at strain rate of 0.1 s<sup>-1</sup> and at different strains. The legend represents the levels of multiple uniform density.

#### **4.1.9.5 Discussion on evolution of DRX of Nb-1Zr-0.1C with strain**

##### **4.1.9.5.1 Flow stress softening and microstructural evolution**

Nb-1Zr-0.1C hot deformed at 1500 and 1600 °C at strain rate of 0.1 s<sup>-1</sup> showed an initial hardening followed by a decrease in flow stress to a steady value. With increasing strain the grains developed a substructure, the grain boundaries showed corrugation and fine grains with high angle boundaries were seen in a necklace type formation (Fig. 4.25b and 4.27c). The necklace structure of DRX grains were observed at strains of 0.6 and 0.9 after deformation at 1500 and 1600 °C, respectively. These features suggest that Nb-1Zr-0.1C alloy deformed at these conditions undergoes dynamic recrystallization. Of the various dynamic recrystallization processes the discontinuous dynamic recrystallization process (dDRX) is known to show necklace formation. dDRX is a two step process consisting of nucleation of strain free grains and their growth. The presence of serrated grain boundaries and the necklace structure on them is an evidence of discontinuous dynamic recrystallization [28, 93, 163, 164]. The results of the present study show this necklace type formation of fine grains suggesting that Nb-1Zr-0.1C undergoes discontinuous dynamic recrystallization when deformed at 1500 and 1600 °C at strain rate of 0.1 s<sup>-1</sup>. It was seen that at a large strain of 1.2 (Fig. 4.25d) the grains were fairly equiaxed and homogeneously distributed with significant fraction of high angle boundaries.

##### **4.1.9.5.2 Identification of DRX grains**

The recrystallized grains were partitioned from the deformed grains and subgrains using the following criteria.

- 1) If the internal average misorientation angle within a grain exceeds 2° the grain is classified as being "deformed". The deformed grains are marked as grey in Fig. 4.32.

- 2) If grains consist of subgrains whose internal misorientation is under  $2^\circ$  but the misorientation from subgrain to subgrain is above  $2^\circ$  then the grain is classified as "substructured". These are marked as white.
- 3) All the remaining grains (i.e. neither deformed nor substructured) are classified as recrystallized and marked as red.

Nb-1Zr-0.1C deformed at  $1500\text{ }^\circ\text{C}$  and  $0.1\text{ s}^{-1}$  up to a strain of 0.3 (Fig. 4.32a) showed recrystallized grains along the boundaries of the large grains and the grain boundaries triple junctions.

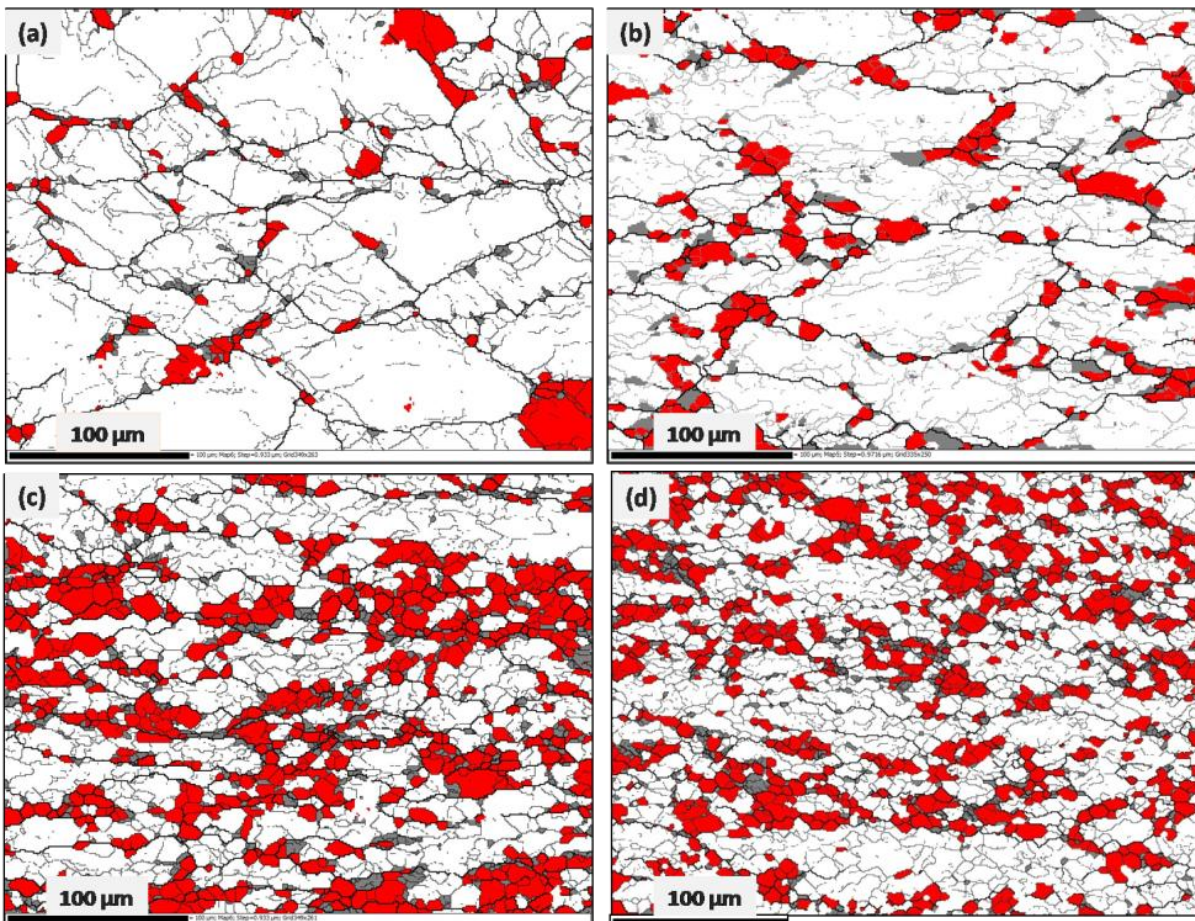


**Fig. 4.32:** EBSD map showing recrystallized grains obtained by partitioning the entire data set (as explained in text) for Nb-1Zr-0.1C deformed at temperature of  $1500\text{ }^\circ\text{C}$  and strain rate of  $0.1\text{ s}^{-1}$  for different true strains of (a) 0.3, (b) 0.6, (c) 0.9 and (d) 1.2. The red color represents the recrystallized grains, the white color represent grains with substructure and the gray color represent the deformed grains.

At a strain of 0.6 (Fig. 4.32b) the recrystallized grains start to form the necklace structure. The presence of necklace type of microstructure (a characteristic feature of DRX process) signifies the non-uniform distribution of strain inside the grain. The volume fraction of recrystallized grains was found to be highest for strain of 0.9 (30 %) as compared to other strains (Fig. 4.32c). At 1500 °C and  $0.1 \text{ s}^{-1}$  for a strain of 0.9, most grains show a necklace structure signifying DRX. The recrystallization volume fraction at strain of 1.2 was slightly less (27 %) than that at strain of 0.9. This could be because at larger strains substructure starts forming within the DRX grains as shown in Fig. 4.33. At 1500 °C and  $0.1 \text{ s}^{-1}$ , for strain of 1.2 an equiaxed grain structure with nearly similar grain sizes was observed. The necklace structure of dynamically recrystallized grains were seen along the old serrated grain boundaries at strain of 0.6 for temperature of 1500 °C and strain rate of  $0.1 \text{ s}^{-1}$  (Fig. 4.25b). Deformation at 1500 °C and  $0.1 \text{ s}^{-1}$  to a large strain of 1.2 showed fine subgrains along the larger subgrain boundaries within the deformed grains.

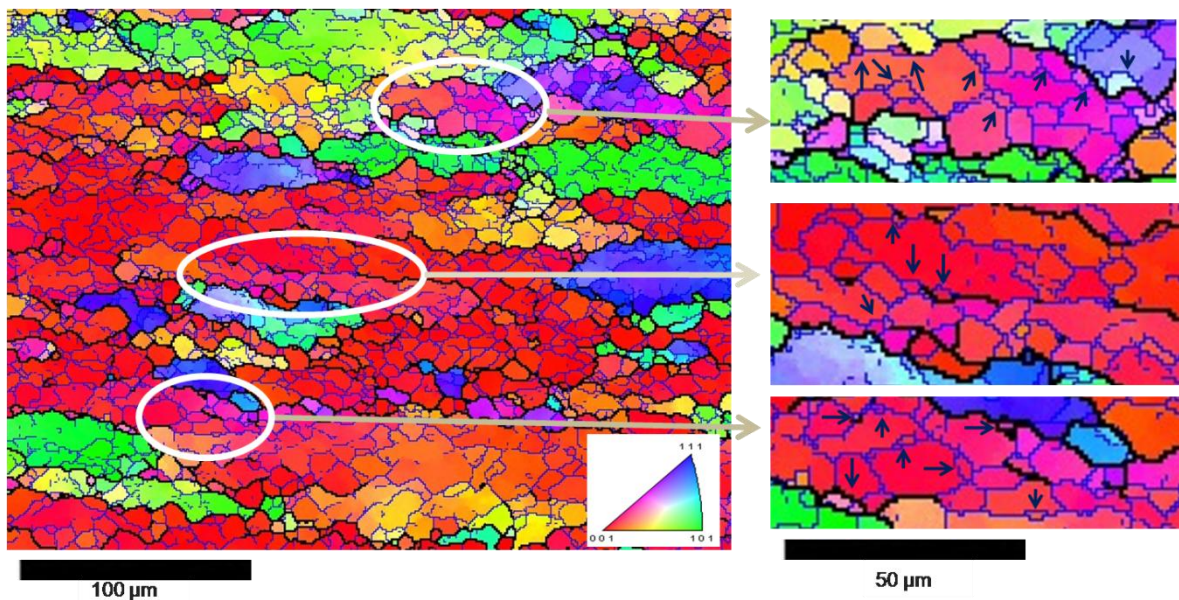


**Fig. 4.33:** Inverse pole figure map of Nb-1Zr-0.1C deformed at temperature of 1500 °C and strain rate of  $0.1 \text{ s}^{-1}$  up to a true strain of 1.2. The necklace structure formed at the boundary of subgrains are marked by circle and magnified at the right side of the figure. Fine subgrains are seen at the boundary of larger subgrains (marked by arrow).

Nb-1Zr-0.1C deformed at 1600 °C and 0.1 s<sup>-1</sup> up to strain of 0.3 showed small recrystallized grains at the boundaries and triple junctions (Fig. 4.34a). The DRX grains were seen along the original grain boundaries for strain of 0.6 (Fig. 4.34b) and 0.9 (Fig. 4.34c) forming a partial necklace structure. The difference in dislocation density between centre of the subgrain and grain boundaries is the driving force for the growth of subgrains. For the deformation condition of 1600 °C and 0.1 s<sup>-1</sup> the recrystallization fraction increased with strain and was highest for strain of 1.2. Equiaxed DRX grains were seen at a strain of 1.2 (Fig. 4.34d). At this deformation condition the fraction of deformed grains was also the highest. Equiaxed microstructure was seen for larger strain of 1.2 for both 1500 and 1600 °C.

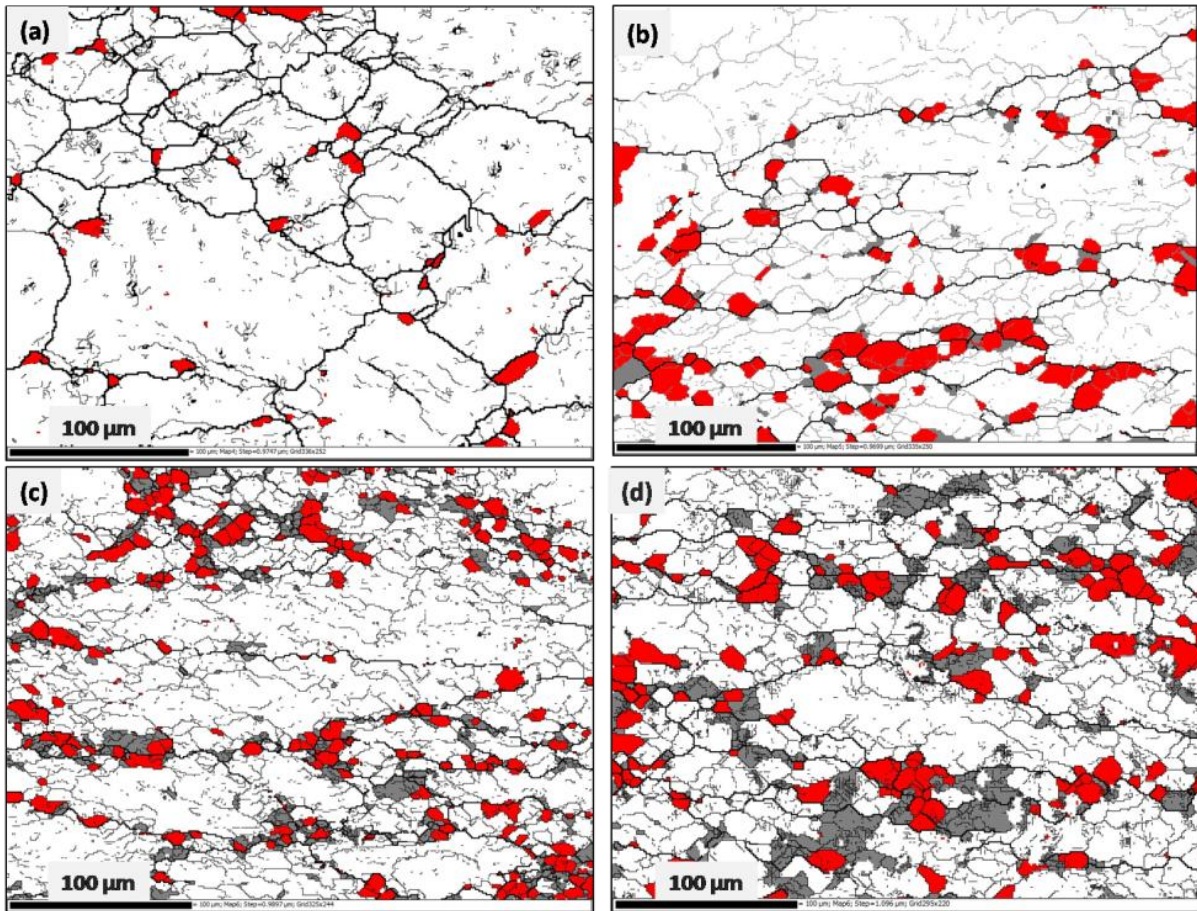


**Fig. 4.34:** EBSD map showing recrystallized grains obtained by partitioning the entire data set (explained in text) for samples deformed at temperature of 1600 °C and strain rate of 0.1 s<sup>-1</sup> for different true strains of (a) 0.3, (b) 0.6, (c) 0.9 and (d) 1.2. The red color represents recrystallized grains, the white color represents substructure and the gray color represent the deformed grains.

The fraction of recrystallization was higher at 1500 °C as compared to that at 1600 °C. The grain refinement of starting coarse grain was reflected in the single peak type flow curve [96]. Since Nb-1Zr-0.1C alloy was deformed in the high strain rate sensitivity regime, as expected there was no signature of flow instability such as cracks, shear or deformation bands [47].

#### 4.1.9.5.3 Grain orientation spread (GOS)

Any point pair with misorientation exceeding  $2^\circ$  is considered as a boundary. Grain orientation spread (GOS) is the angular deviation between any point within the grain and the average orientation of the grain. Here the boundary is defined by the critical misorientation value of  $2^\circ$ . It is expected that DRX grains would have a low GOS. Fig. 4.35 shows the comparisons of  $GOS < 2^\circ$  at temperatures of 1500 and 1600 °C for strain rate of  $0.1 \text{ s}^{-1}$  and true strains of 0.3, 0.6, 0.9 and 1.2. For deformation condition of 1500 °C and  $0.1 \text{ s}^{-1}$ , the mean GOS value was higher for strain of 0.6 than 0.9 and 1.2, which suggests that 0.6 strain is an intermediate stage of the dDRX process as compared to strain of 0.9 and 1.2 in which dDRX more developed.

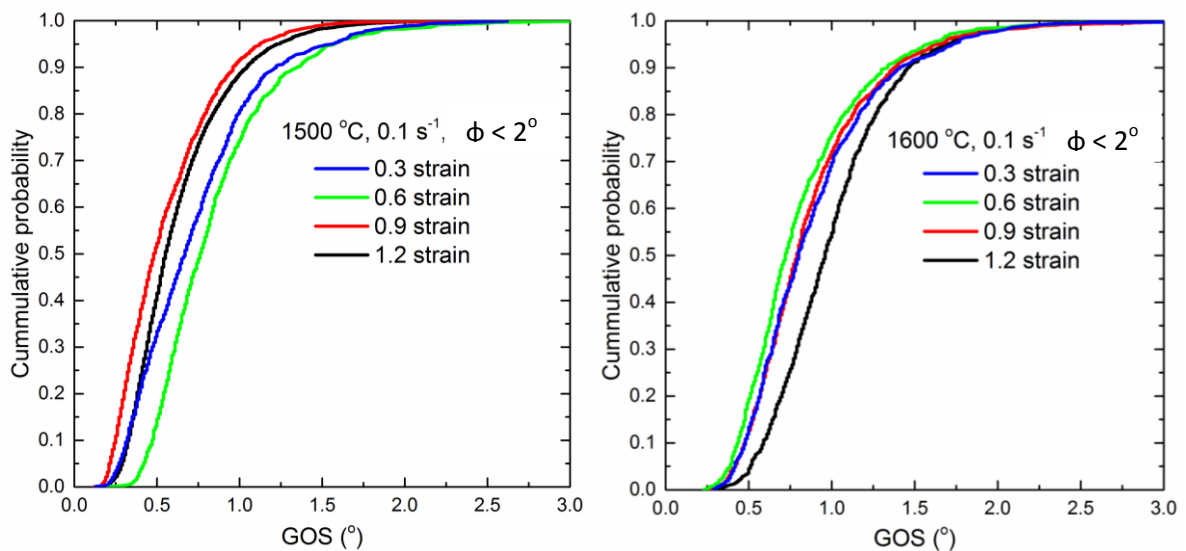


**Fig. 4.35:** Comparisons of grain orientation spread ( $GOS < 2^\circ$ ) at different test conditions as mentioned in the plot.

At 1600 °C and 0.1 s<sup>-1</sup> the GOS value was lowest for strain of 0.6 because of newly formed DRX grains, while GOS value was higher at strain of 1.2.

#### 4.1.9.5.4 Texture of partitioned recrystallized grains

The inverse pole figures with respect to compression axis for only the recrystallized grains are shown in Fig. 4.36. The recrystallized grains were partitioned by setting the conditions as mentioned earlier. The <001> pole texture evolved for all the deformation conditions. The <001> component evolved as the deformation strain was increased for 1500 °C and strain rate of 0.1 s<sup>-1</sup>. The micro-texture for 1600 °C and strain rate of 0.1 s<sup>-1</sup> showed that <001> pole texture was strongest at strain of 0.6 whereas in all other strain conditions the <001> pole texture weakens. For the <001> orientation, all the measured misorientations were lower than 10°, even at strain of 1.2. Furthermore, no micro-texture evolution is noticeable for strain of 0.9 and 1.2 at 1600 °C and strain rate of 0.1 s<sup>-1</sup>.

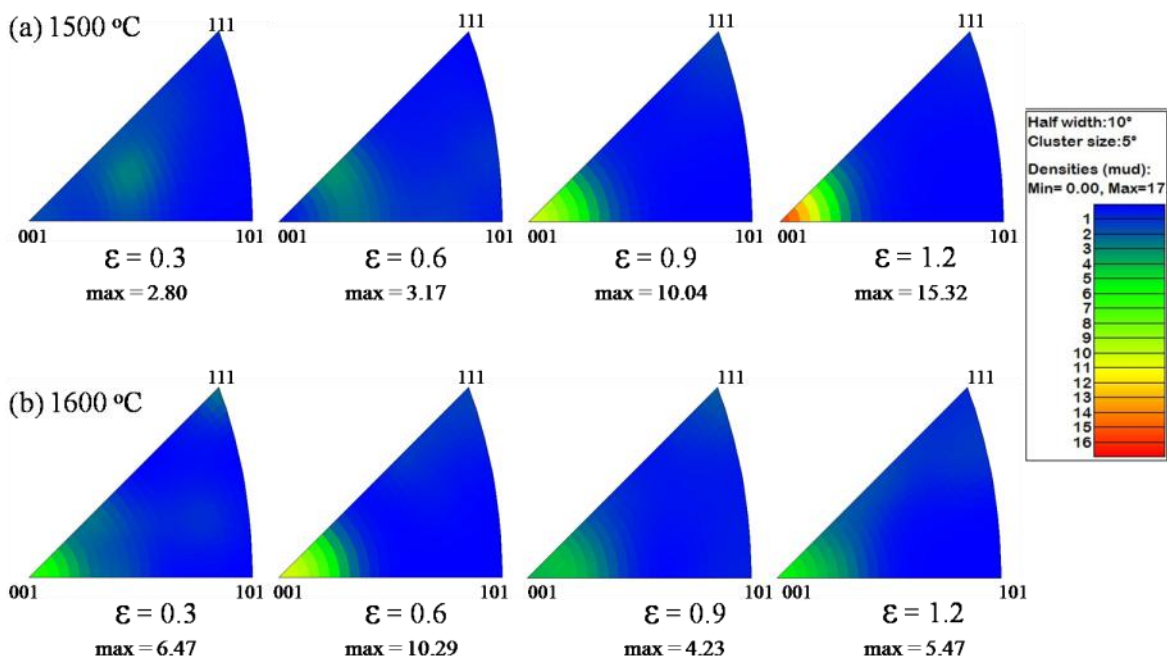


**Fig. 4.36:** Inverse pole figures with respect to compression axis obtained from EBSD of only the DRX grains for Nb-1Zr-0.1C alloy deformed at 1500 and 1600 °C for strain rate of 0.1 s<sup>-1</sup>. The legend represents the levels of multiple uniform density.

## 4.2 Kinetics study of dynamic recrystallization behaviour of Nb alloy

### 4.2.1 Flow curve analysis to study the DRX characteristic

The stress-strain curves of Nb alloys are used to quantify the progress of dynamic softening during deformation. As dynamic recrystallization (DRX) is considered to be the most important restoration mechanism during thermo-mechanical processing, a detailed knowledge of DRX kinetics is essential during the processing steps. Nb-1Zr-0.1C alloy was hot deformed in DRX regimes of 1500 to 1600 °C at strain rate of 0.1 and 0.01 s<sup>-1</sup>. Fig. 4.37 shows the schematic of a DRX flow curve. During the DRX process of Nb-1Zr-0.1C alloy, the flow curve rises initially as a result of work hardening and recovery processes to a peak value ( $\sigma_p$ ). It has been shown that a critical strain ( $\epsilon_c$ ) is required for the nucleation of relatively dislocation free regions initiating DRX process [94, 117, 118]. The corresponding critical stress ( $\sigma_c$ ) occurs before the peak stress ( $\sigma_p$ ). The critical condition for the initiation of DRX was determined by the inflection point in the work-hardening vs. stress plot. The onset of DRX corresponds to a deviation in work hardening curve [165]. Subsequently the flow stress at large strain reaches a steady state value ( $\sigma_{ss}$ ) which results from a balance between work softening and hardening. For dynamic recovery process the generation and accumulation of dislocations due to work-hardening is balanced by dislocation rearrangement and annihilation (Fig. 4.37 marked as DRV curve). At large strain the flow stress reaches a steady state ( $\sigma_{sat}$ ) value which results from a balance between work softening and hardening.

The recrystallized fraction is related to the loss of dislocations and it is estimated from the difference between the DRX flow curve as obtained by experiment and the corresponding dynamic recovery flow curve (reconstructed) assuming that recovery was the only operative restoration process predicted. The difference between these two curves is the net softening and is directly attributed to DRX. The Avrami equation is used to describe the relationships between the DRX volume fraction and strain at given deformation temperature and strain rate.

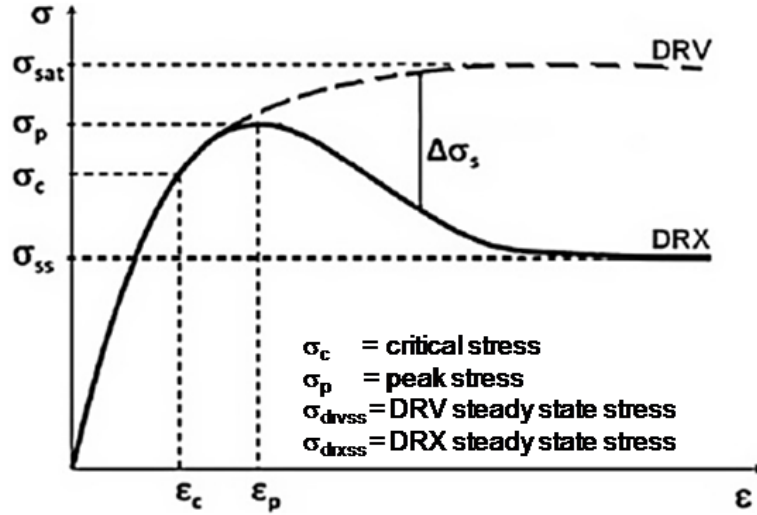


**Fig. 4.37:** Schematic of the difference between the  $\sigma_{DRV}$  (reconstructed) and  $\sigma_{DRX}$  (experimental obtained) curves for the calculation of recrystallized volume fraction ( $X$ ).

#### 4.2.2 Reconstruction of DRV Curve

The evolution of dislocation density with strain is given by [166]

$$\frac{d\rho}{d\varepsilon} = h - r\rho \quad (4.2)$$

$h$  is the athermal work hardening rate and  $r$  is the rate of dynamic recovery. Both are independent of strain. For materials in which the spacing of barriers (precipitate as barriers) is constant with strain the hardening term is constant in Eq. (4.2) [166]. Flow stress for dynamic recovery as derived from the above equation is [165]

$$\sigma = (\sigma_{sat}^2 - (\sigma_{sat}^2 - \sigma_0^2) \exp(-r\varepsilon))^{1/2} \quad (4.3)$$

where  $\sigma_0$  is the yield stress and can be determined from the experimental flow curve. Using some simple algebraic substitutions the following relationship was established

$$\sigma \frac{d\sigma}{d\varepsilon} = \sigma \cdot \theta = 0.5r\sigma_{sat}^2 - 0.5r\sigma^2 \quad (4.4)$$

This is the equation of the tangent to the curve shown in Fig. 4.38 (a). The value of the recovery parameter  $r$  is obtained from the slope ( $-0.5r$ ) and that of  $\sigma_{sat}$  from the intercept on X- axis. Using these values the work-hardening curve pertaining to the regions that have not yet undergone DRX can now be constructed. The critical stress ( $\sigma_c$ ) is determined from the plot of  $-(d\theta/d\sigma)$  vs.  $\sigma$  as shown in Fig. 4.38 (b) (for deformation condition of 1500 °C at strain rate of 0.1 s<sup>-1</sup>). The corresponding critical strain ( $\epsilon_c$ ) for the initiation of DRX process of Nb-1Zr-0.1C alloy is obtained from the stress - strain plot. The critical strain for dDRX of Nb-1Zr-0.1C alloy decreases with increasing temperature. At temperature of 1500 °C and strain rate of 0.1 s<sup>-1</sup> the peak strain ( $\epsilon_p$ ) and critical strain ( $\epsilon_c$ ) were found as 0.29 and 0.18 respectively. It shows that  $\epsilon_p > \epsilon_c$  and  $\epsilon_c = 0.62 \epsilon_p$  as reported by many authors for DRX process [150, 165].

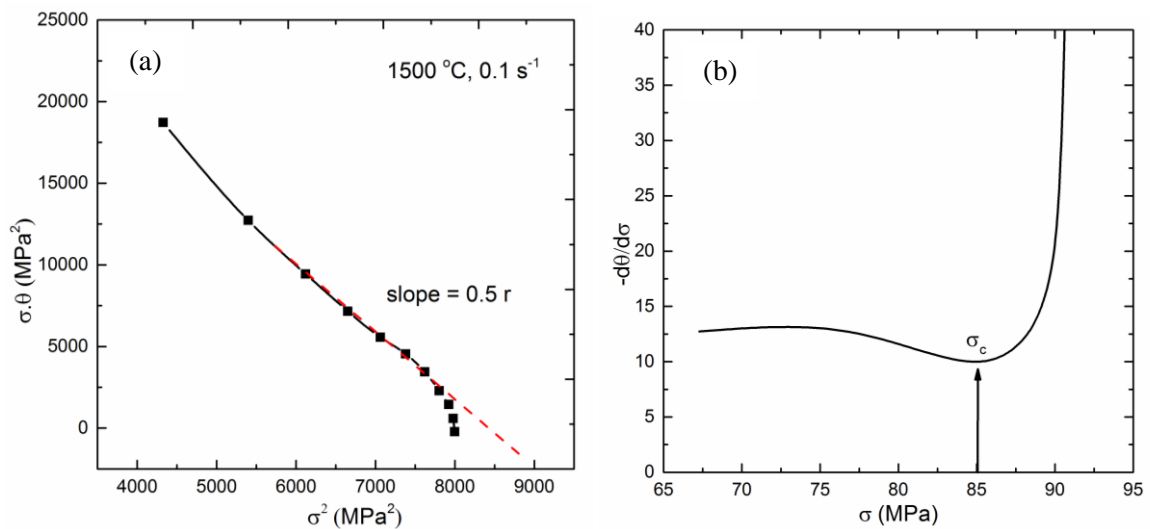


**Fig. 4.38:** (a) Plot of  $\theta \cdot \sigma$  vs.  $\sigma^2$  for determination of  $\sigma_{sat}$  and (b) plot of  $-(d\theta/d\sigma)$  vs.  $\sigma$  for determination of  $\sigma_c$  for deformation condition of 1500 °C at strain rate of 0.1 s<sup>-1</sup>.

In the case of DRV, slope of  $\theta - \sigma$  curve remains constant above  $\sigma_c$ .

When  $\theta = 0$  then  $\sigma = \sigma_{drvss}$

For  $\sigma_c \leq \sigma_{drv} \leq \sigma_{drvss}$  the work hardening is

$$\theta = \frac{d\sigma}{d\varepsilon} = m' \sigma_{drv} + c \quad (4.5)$$

Using the boundary conditions as:

$$\theta = \theta_c, \sigma_{drv} = \sigma_c$$

$$\theta = 0, \sigma_{drv} = \sigma_{drvss}$$

The DRV curve can also be constructed by using the relation as

$$\varepsilon_{drv} = \varepsilon_c + \frac{\sigma_{drvss} - \sigma_c}{\theta_c} \ln \left( \frac{\sigma_c - \sigma_{drvss}}{\sigma - \sigma_{drvss}} \right) \quad (4.6)$$

Using the data of Fig. 4.38 (a) and the above procedure, DRV curve is constructed as shown in Fig. 4.39 (reconstruction curve shown as red colour curve).

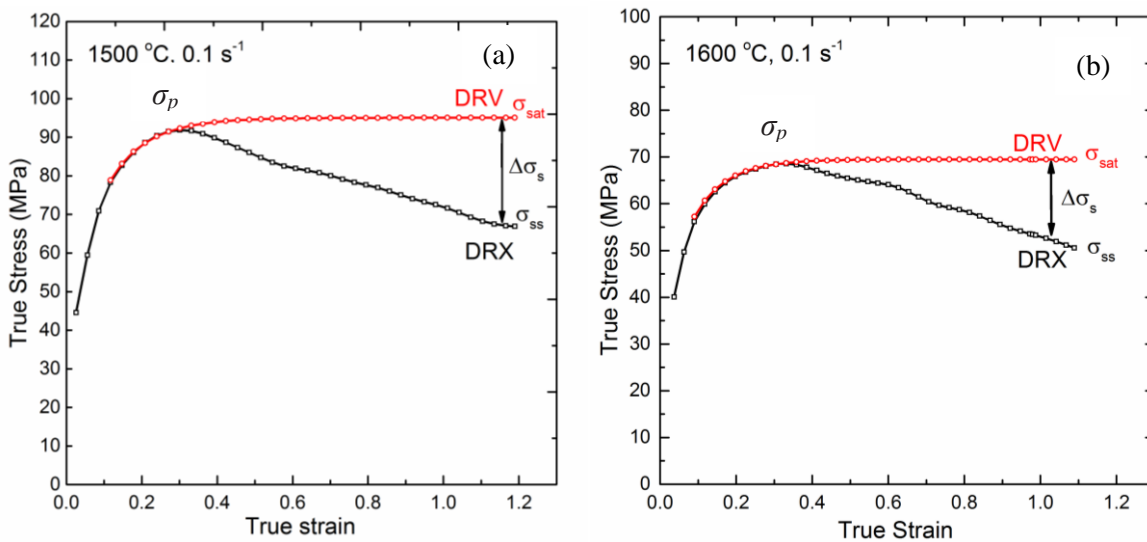


**Fig. 4.39:** Reconstructed dynamic recovery (DRV) curve plotted along with the experimental DRX curve for Nb-1Zr-0.1C alloy at deformation conditions of 1500 and 1600 °C for strain rate of 0.1 s<sup>-1</sup>.

### 4.2.3 Evaluation of volume fraction of DRX grains

The recrystallized volume fraction ( $X$ ) is related to the loss of dislocations and it can be calculated from the difference between the DRX flow curve (obtained by experiment) and the corresponding DRV flow curve (expected stress - strain behaviour if recovery were the only operative restoration process) predicted under similar conditions of deformation of DRX. The difference between these two curves ( $\Delta\sigma_s$ ) is the net softening and the maximum value of  $\Delta\sigma_s$  is  $(\sigma_{sat} - \sigma_{ss})$ , where  $\sigma_{ss}$  is the steady state stress under DRX conditions. As the flow curve is the net result of the simultaneous operation of DRV and DRX, the recrystallized volume fraction ( $X$ ) (Fig. 4.37) is expressed as [165]

$$X = \frac{\Delta\sigma_s}{(\sigma_{sat}) - (\sigma_{ss})} \quad (4.7)$$

In this study a modified equation was used for the calculation of recrystallized fraction ( $X$ ) as given by Zahiri et al. is [140]

$$X = \frac{(\sigma_{drvx})^2 - (\sigma_{drxx})^2}{(\sigma_{drvss})^2 - (\sigma_{drxss})^2} \quad (4.8)$$

The above relation (Eq. 4.8) gives the fraction recrystallized as function of flow stress.

### 4.2.4 Application of Avrami kinetics to DRX

The kinetics of DRX can be described in terms of the recrystallized volume expressed as a function of time as

$$X = 1 - \exp(-k t^n) \quad (4.9)$$

where  $X$  is the recrystallized volume fraction,  $k$  is the Avrami constant,  $n$  is the time exponent and  $t$  is time for the start of DRX.

In a constant strain rate test, time can be replaced with strain ( $\varepsilon - \varepsilon_c$ ) [149] and recrystallized volume fraction can be expressed by modified Avrami equation as a function of strain. The Avrami equation that used to describe the relationships between the DRX volume fraction and strain at given deformation temperature and strain rate is [165]

$$X = 1 - \exp(-k' (\varepsilon_x - \varepsilon_c)^n) \quad (4.10)$$

The above relation provides the fraction recrystallized value as function of strain. Fig. 4.40 shows the variation of recrystallization fraction with ( $\varepsilon - \varepsilon_c$ ) which was calculated by using the modified Eq. (4.8) and subsequently fitted to the Avrami Eq. (4.10).

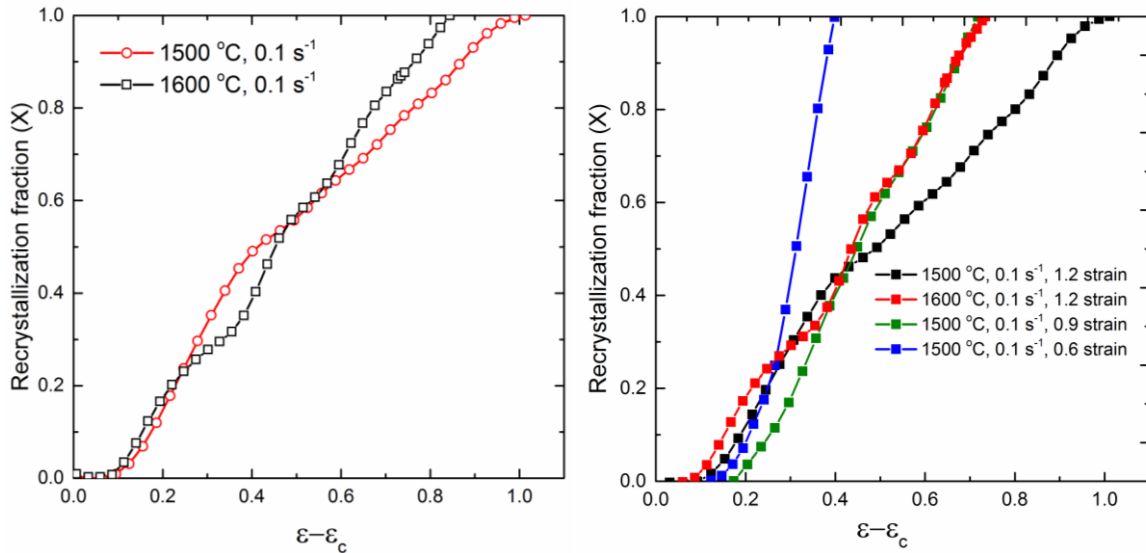


**Fig. 4.40:** Variation of recrystallization fraction with ( $\varepsilon - \varepsilon_c$ ) for Nb-1Zr-0.1C alloy.

The strain ( $\varepsilon - \varepsilon_c$ ) was converted to time using the relation

$$t = (\varepsilon - \varepsilon_c) / \dot{\varepsilon} \quad (4.11)$$

where  $\dot{\varepsilon}$  is the strain rate at which the compression test was carried out.

The Avrami plot ( $\log (\ln(1/(1-x)))$  vs.  $\log t$ ) was also constructed for all the deformation conditions as shown in Fig. 4.41. The Avrami time exponents ( $n$ ) obtained from the slope of

the curves are indicated on each plot. The  $n$  values are indicative of the nature of the nucleation sites which may be the prior grain boundaries or twin edges. For Nb-1Zr-0.1C alloy deformed at strain rate of  $0.1 \text{ s}^{-1}$ ,  $n$  was found to be about 4.8 and 5.1 for 1500 and 1600 °C respectively. The value of  $n \sim 5$  of this study correlates with ideal Avrami recrystallization for homogeneous, constant rate nucleation. Therefore this value of Avrami exponent suggests that dDRX process occurred for Nb-1Zr-0.1C alloy.

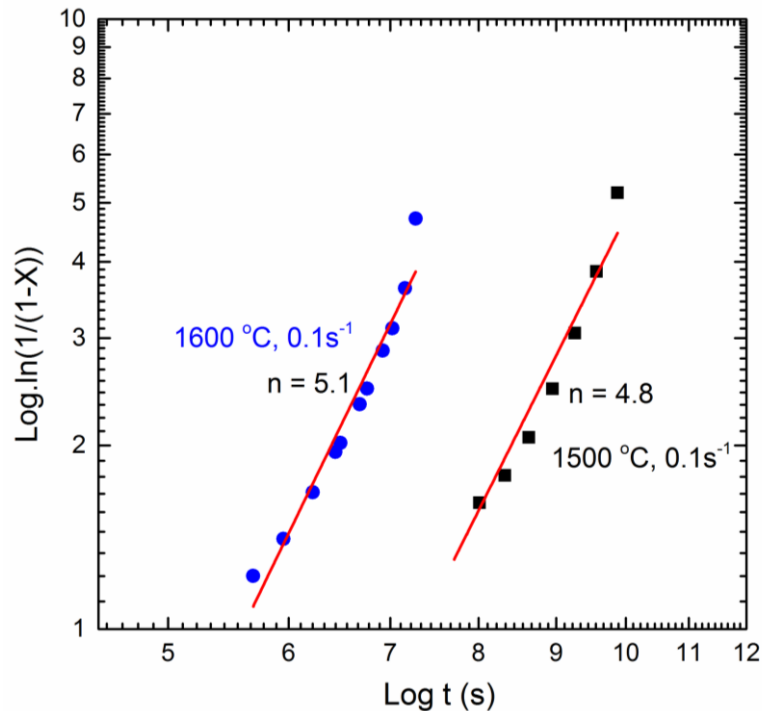


**Fig. 4.41:** Avrami plots for Nb-1Zr-0.1C alloy at different deformation conditions.

Fig. 4.42 shows the variation of recrystallization fraction with strain for 1500 and 1600 °C at strain rate of  $0.1 \text{ s}^{-1}$  as calculated from EBSD data. The increase of recrystallization fraction is more for 1500 °C than for 1600 °C. The recrystallization fraction at temperature of 1600 °C is lower than that of at 1500 °C possibly due to the low internal strain energy within the grains which retards recrystallization at this higher temperature.

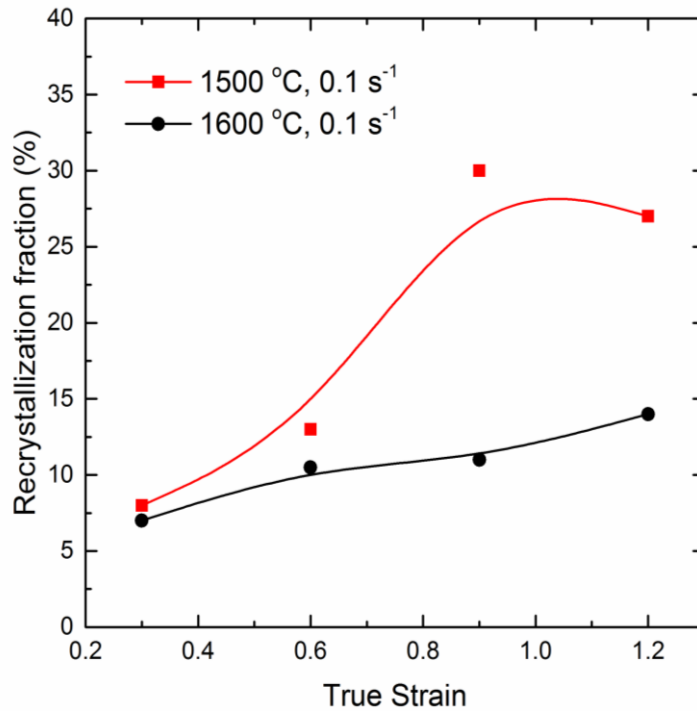


**Fig. 4.42:** Variation of recrystallization fraction with strain for 1500 and 1600 °C at strain rate of 0.1 s<sup>-1</sup> as calculated from EBSD data. The lines connecting the data points are shown for trend of data points.

### 4.3 Deformation behavior of Nb-1Zr and Nb-1Zr-0.1C from room temperature to 700 °C

The dislocation mobility mechanisms and their dependence on strain rate and temperature are the main factors that determine the strength of engineering materials. The thermally activated processes taking place during deformation can be best studied by the transient tests. Repeated transients test provide the stress dependence of the dislocation velocity and an estimation of the mobile dislocation density. The transient tests allow the measurement of microscopic activation volumes which are typical of thermally activated dislocation processes. From the strain rate change tests the strain rate sensitivity was obtained and from the multiple stress relaxation tests the apparent activation volume ( $V_a$ ) were calculated.

### 4.3.1 Strain rate change test

Figure 4.43 and 4.44 show true stress - true strain plot obtained from the strain rate change test for Nb-1Zr and Nb-1Zr-0.1C alloy from room temperature to 700 °C respectively. Strain rate during the test has been alternatively changed between  $10^{-3} \text{ s}^{-1}$  and  $10^{-2} \text{ s}^{-1}$  and  $10^{-4} \text{ s}^{-1}$ . It has been observed that by decreasing or increasing the strain rate, a new stress state is reached from which the change in stress is determined. The activation volume ( $V$ ) was calculated from the strain rate jump experiments, which allows to classify deformation mechanisms according to the material response to a strain rate change.

#### 4.3.1.1 Discussion

During the uniaxial compression test the strain rate  $\dot{\varepsilon}_1$  is suddenly increased (or decreased) to  $\dot{\varepsilon}_2$  and the resulting change in stress  $\Delta\sigma$  is recorded (Fig. 4.43 and Fig. 4.44) to calculate the strain rate sensitivity ( $m$ ) value. The idea is to characterize the materials response by activation volume defined as:

$$V = kT \left( \frac{\partial(\ln \dot{\gamma})}{\partial \tau} \right) \quad (4.12)$$

where  $\dot{\gamma}$  is shear strain rate and  $\tau$  is shear stress.

$V$  is determined experimentally by the formula:

$$V = kT \left( \frac{\partial \ln(\dot{\gamma}_1 / \dot{\gamma}_2)}{\partial \tau} \right) = MkT \left( \frac{\partial \ln(\dot{\varepsilon}_1 / \dot{\varepsilon}_2)}{\partial \sigma} \right) \quad (4.13)$$

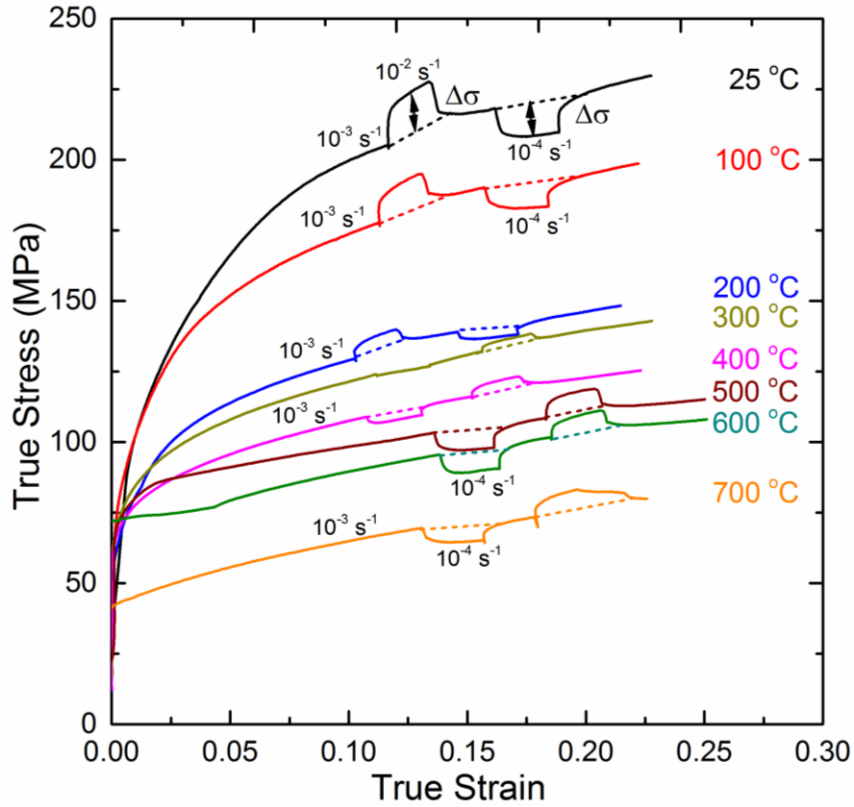


**Fig. 4.43:** Strain rate jump test of Nb-1Zr alloy at different deformation conditions as mentioned.

From the strain rate change tests strain rate sensitivity was calculated as  $m = \Delta \ln \sigma / \Delta \ln \dot{\epsilon}$  at different deformation condition (Fig. 4.43 and 4.44) and compared to other deformation domain for Nb alloys. The strain rate sensitivity ( $m$ ) is also used for the calculation of macroscopic activation volume as

$$V = \frac{MkT}{\sigma m} \quad (4.14)$$

where  $M$  is the Taylor factor taken as 2.8 (for bcc metals and alloy) and  $k$  is the Boltzmann constant.

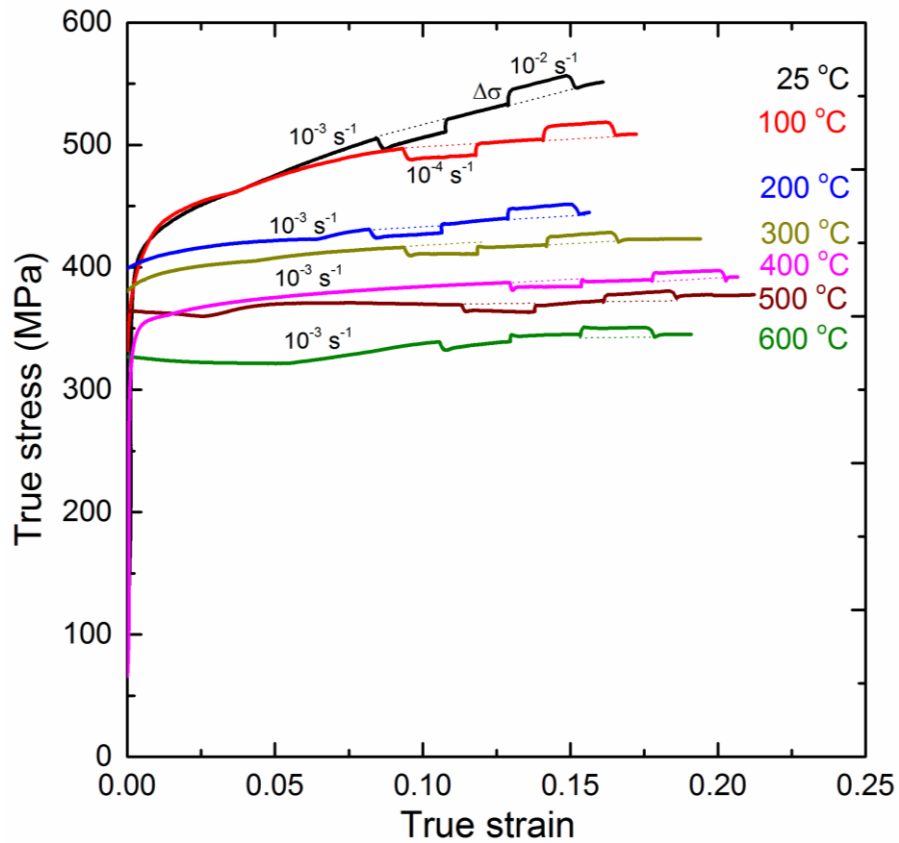


**Fig. 4.44:** Strain rate jump test of Nb-1Zr-0.1C alloy at different deformation conditions as mentioned.

The strain rate change test of Nb-1Zr-0.1C alloy at 700 °C at  $10^{-3} \text{ s}^{-1}$  was shown in Fig. 4.45. At this deformation condition the flow curve shows serrations at low strain rate of  $10^{-4} \text{ s}^{-1}$ . Also negative strain rate sensitivity was observed during the strain rate jump test which indicates the occurrence of dynamic strain aging (DSA) at temperature of 700 °C for Nb-1Zr-0.1C alloy.

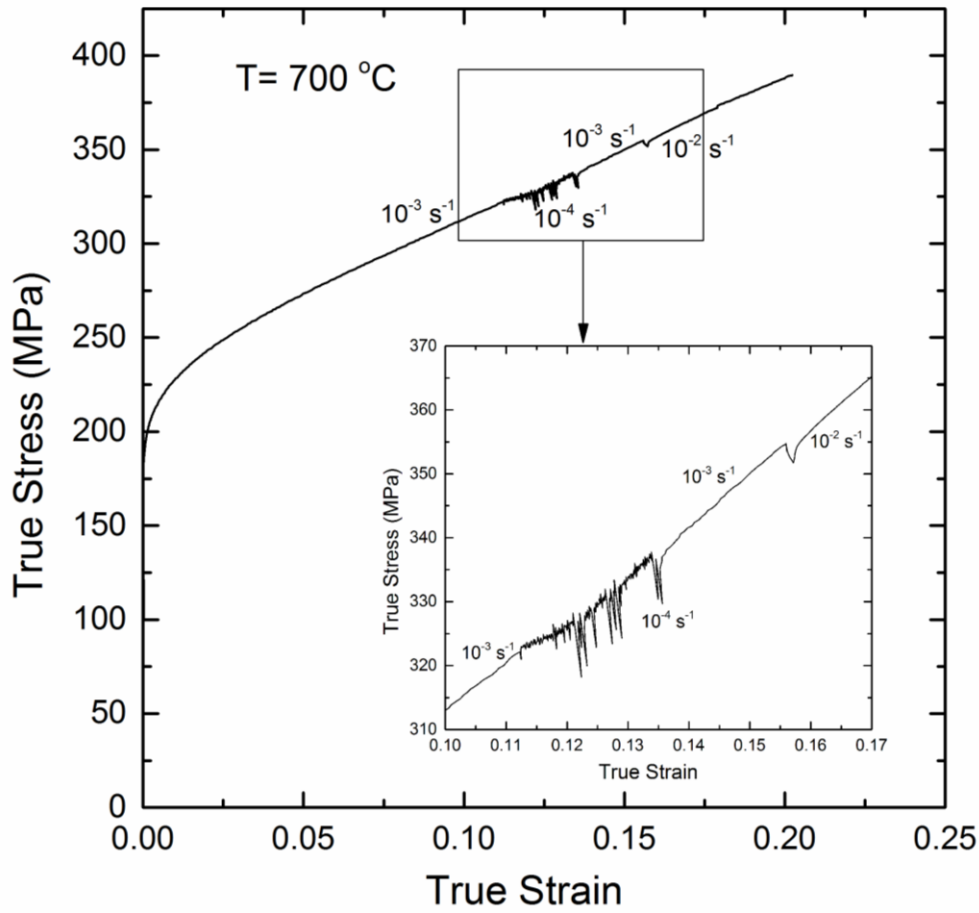


**Fig. 4.45:** Strain rate change test of Nb-1Zr-0.1C alloy at temperature of 700 °C and strain rate of  $10^{-3} \text{ s}^{-1}$ . Serrations and negative strain rate sensitivity indicate occurrence of dynamic strain aging (DSA) (Insert image).

#### 4.3.2 Stress relaxation test / multiple stress relaxation test

To identify the rate controlling mechanisms during deformation of Nb alloys activation volume was determined from the stress relaxation tests. Spattig et al. [167] suggested that multiple short-time relaxations by reloading to the same flow stress can be used to evaluate the change in structure parameter (work-hardening) during stress relaxation. At best this method is still an indirect measure of the true activation volume, and assumes that only a single obstacle species exist. A typical stress relaxation curve for Nb-1Zr-0.1C alloy at a stress of 556 MPa at room temperature was shown in Fig. 4.46. The slope of this curve was used for the determination of activation volume as per Eq. (3.9).

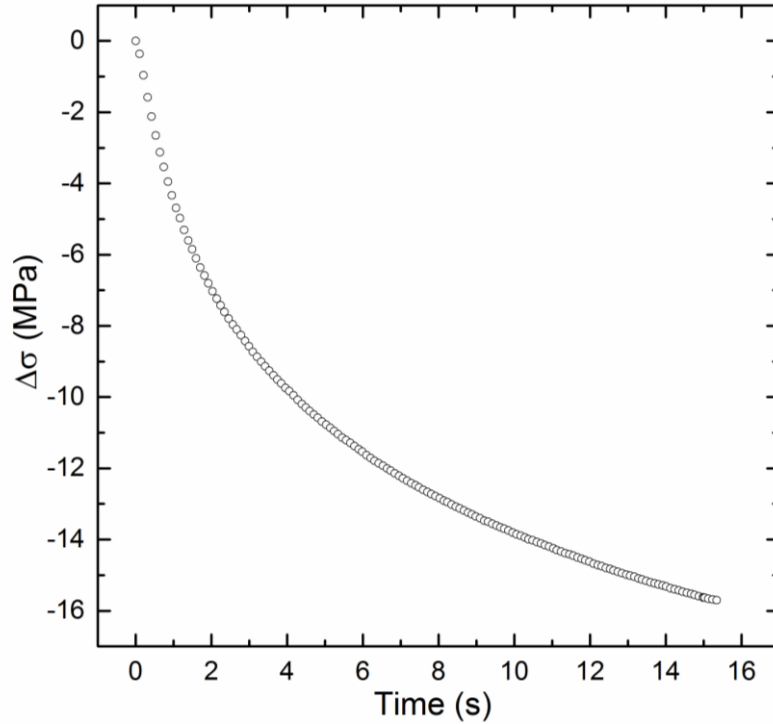


**Fig. 4.46:** Stress relaxation curve for Nb-1Zr-0.1C alloy at a stress of 556 MPa for room temperature.

At low enough temperatures and for positive work-hardening coefficients, the following features are observed from the multiple stress relaxations test (Fig. 3.3):

- i.*  $\Delta\tau_j$  decreases as  $j$ , the relaxation number in the series increases,
- ii.* analyzing the relaxation curves of the series in terms of Eq. (3.8),  $V_a$  is found to be constant, while the time constant  $c_{Tj}$  depends on  $j$ . This accounts for the shape and size changes in relaxation curves along the series.

Fig 4.47 shows a small difference in activation volume value with number of relaxations during the consecutive relaxations for Nb alloys at temperature of 25 to 600 °C. The variation of activation volume with flow stress of Nb alloys was shown in Fig. 4.48. These activation volume values were measured for strain rate of  $10^{-3} \text{ s}^{-1}$  and from room temperature to 700 °C. The activation volumes were calculated from stress relaxation data

using Eq. (3.11). The activation volume decreases as the flow stress increases for both Nb-1Zr and Nb-1Zr-0.1C alloy. As compared to the activation volumes of high temperature deformation domain, in this regime ( temperature range of 25 - 600 °C and strain rate of  $10^{-3} \text{ s}^{-1}$  ) activation volumes are low and at low temperature there is substantial difference in the activation volume of Nb-1Zr and Nb-1Zr-0.1C alloy at same deformation conditions.

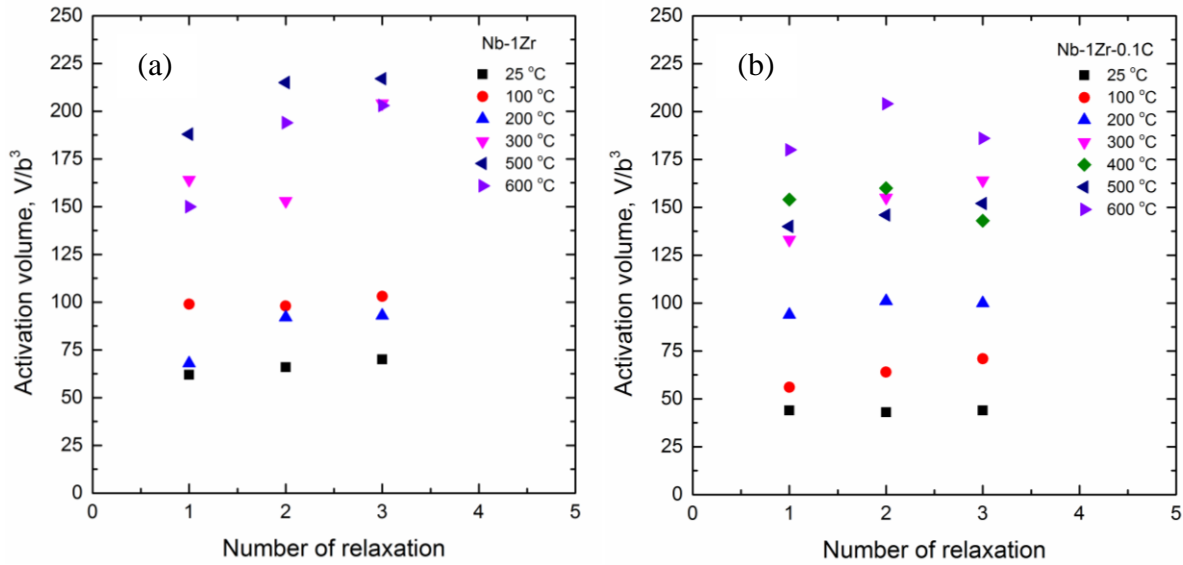


**Fig. 4.47:** Variation of activation volume with number of relaxations for Nb alloys at different temperatures as indicated.

#### 4.3.2.1 Discussion

It is known that activation volume within a range of  $1 - 10 b^3$  points at diffusion and grain boundary sliding as the controlling deformation mechanisms [168, 169]. Annihilation of dislocations at grain boundaries dominates plastic deformation if the activation volume ( $V$ ) is within a range of  $10 - 100 b^3$  [169]. Here the activation volume for Nb alloys (except at low temperature of 25 - 200 °C) were found to be within a range of  $100 - 1000 b^3$ . In case the  $V$  value is within a range of  $100 - 1000 b^3$ , the overcoming of the forest junctions by gliding dislocations is considered as the controlling deformation mechanism [168, 169].

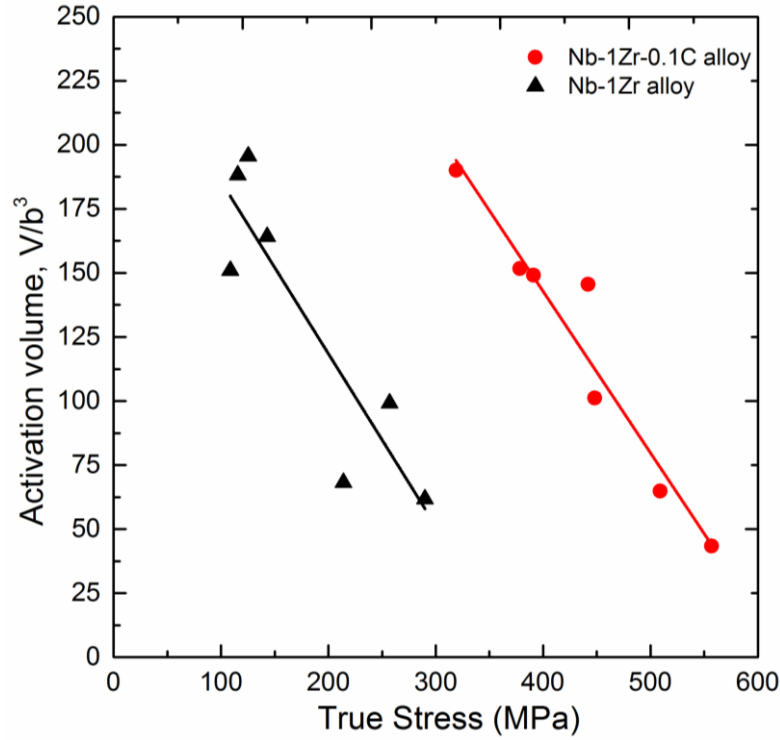


**Fig. 4.48:** Variation of activation volume with flow stress of Nb alloys. Activation volume is calculated from stress relaxation data using Eq. (3.11).

The activation volume of  $71 b^3$  for creep of Nb- 1wt.% Zr seems to lie between the anticipated activation volume for the dislocation intersection process, *i.e.*  $10^2$  to  $10^4 b^3$  [170], and that for the Peierls mechanism, *i.e.*  $10$  to  $10^2 b^3$  [7]. The activation volume of  $71 b^3$  is within a factor of 3 to the true activation volume ( $204 b^3$ ) obtained independently from a stress reduction study on Nb- 1wt.% Zr at 1300 K [171]. It should be pointed out that the true activation volume deduced from stress reduction tests refers to constant structure experiments, whereas the activation volume deduced from Eq. (3.11) (steady-state) does not [66]. The true activation area for Nb- 1wt.% Zr was obtained from the high stress sensitivity value of a semi-logarithmic plot of normalized reduced strain rate *vs.* normalized reduced stress. The true activation area was equal to  $322.5 b^2$  for an applied stress of 190 MPa and at temperature of  $1027\text{ }^\circ\text{C}$ , which is in the range of the true activation area for cutting of forest dislocations.

The high stress sensitivity values can be explained by mechanisms of forest dislocations cutting [171].

The dislocation exhaustion rates  $\rho_m / \rho_{m0}$  were obtained from the stress relaxation tests by using Eq. (3.21). The  $\Delta\rho_m$  is the decrease of the mobile dislocation density which corresponds to a decrease of one order of magnitude of the initial deformation rate. Fig. 4.49 shows the time decrease of mobile dislocation density (dislocation density exhaustion rate) during four stress relaxation cycles of Nb-1Zr-0.1C alloy at 600 °C. The dislocation exhaustion rates  $\rho_m / \rho_{m0}$  decreases rapidly to 8 percent at the end of the first relaxation of 15 second (Fig. 4.49). This high rate of dislocation exhaustion rates indicate that a large fraction of mobile dislocations get annihilated in the sample during the first relaxation. The dislocation exhaustion rates decrease subsequently for other consecutive relaxations cycles. After four consecutive relaxations cycles the dislocation exhaustion rate is close to 6 percent. This high exhaustion rate of dislocation density may arise because the number of available dislocations that can readily overcome the obstacles are used up quickly on straining.

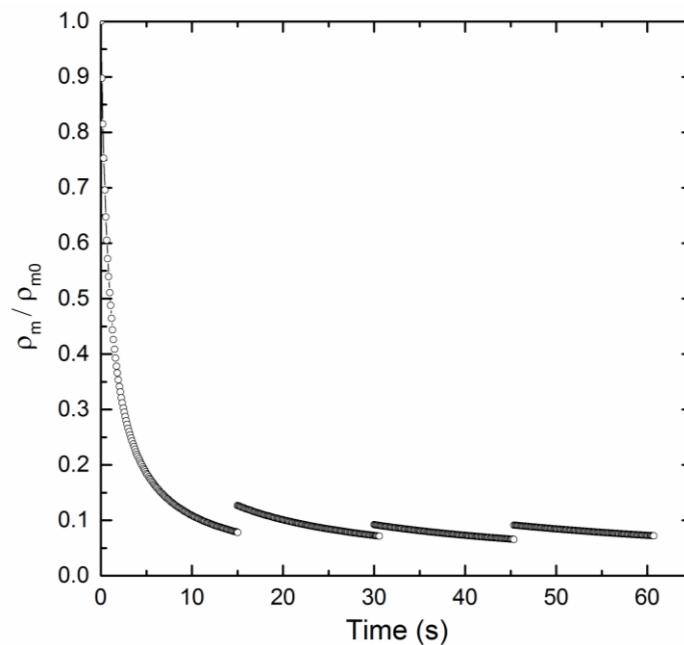


**Fig. 4.49:** The decrease of the mobile dislocation density with time (dislocation exhaustion rate) during four stress relaxation cycles of Nb-1Zr-0.1C alloy at 600 °C.

#### 4.4 High strain rate deformation

The mechanical properties of materials are strain rate and temperature dependent. High strain rate data are required for safety and structural integrity assessment of structures which undergo dynamic loading. Split Hopkinson Pressure Bar (SHPB) setup is suitable for high strain rate test in strain rate range of 100 to 10000 s<sup>-1</sup>. SHPB is used to study the high strain rate mechanical properties of Nb-1Zr and Nb-1Zr-0.1C alloys at temperatures from 25 - 400 °C.

Nb-1Zr and Nb-1Zr-0.1C alloys were tested from room temperature (25 °C) to 400 °C in the temperature interval of 100 °C up to strain of 0.25. The details of tests parameters used for Nb-1Zr and Nb-1Zr-0.1C alloys at different strain rates and temperature were given in Table 4.2 and 4.3 respectively.

**Table 4.2:** Details of high strain rate test parameters for Nb-1Zr.

S. No.	Test Temperature (°C)	Gas gun Pressure (bar)	Velocity of Striker bar (m/s)	Length of Strike bar (m)	Average strain rate (s <sup>-1</sup> )
1	27	1.76	8.97	0.5	1630
2	100	1.72	8.8	0.5	1710
3	200	1.68	8.61	0.5	1700
4	300	1.64	8.41	0.5	1770
5	400	1.6	8.19	0.5	1650

**Table 4.3:** Details of high strain rate test parameters for Nb-1Zr-0.1C.

S. No.	Test Temperature (°C)	Gas gun Pressure (bar)	Velocity of Striker bar (m/s)	Length of Strike bar (m)	Average strain rate (s <sup>-1</sup> )
1	27	2.50	12.85	0.5	1160
2	100	2.20	11.32	0.5	1125
3	200	2.09	10.71	0.5	1075
4	300	2.06	10.56	0.5	1100
5	400	2.03	10.41	0.5	1135

The variation of strain rates with strain during the SHPB test of Nb-1Zr and Nb-1Zr-0.1C alloy at temperature of 25 to 400 °C were shown Fig. 4.50 (a) and (b). From this figure it is observed that the strain rate remains constant after strain of 0.1. The average strain rates for Nb-1Zr and Nb-1Zr-0.1C alloy were obtained as 1700 s<sup>-1</sup> and 1100 s<sup>-1</sup> respectively (Fig. 4.50).

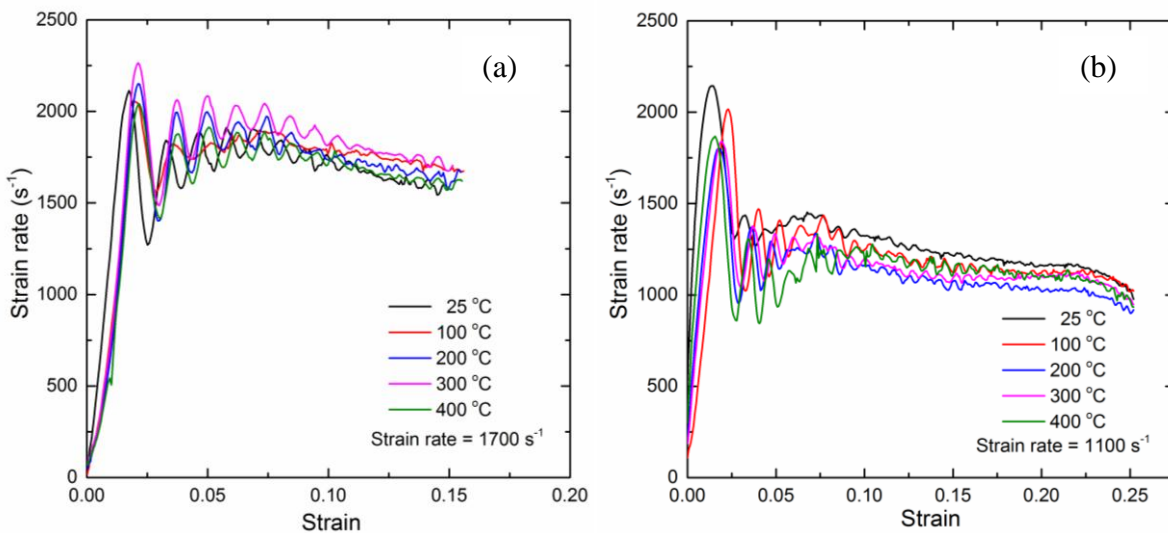


**Fig. 4.50:** Strain rate variation with strain for (a) Nb-1Zr and (b) Nb-1Zr-0.1C alloy at temperature of 25 to 400 °C.

The stress-strain curves for Nb alloys as obtained by using the procedure described in section-3.4.2 are shown in Fig. 4.51 (a) and (b). The flow curves show work-hardening behaviour of Nb-1Zr and Nb-1Zr-0.1C alloys at this high strain rate. The flow stress of Nb-1Zr at this deformation conditions is low as compared to Nb-1Zr-0.1C alloy. The flow stress of Nb alloy was seen to decrease with temperature.

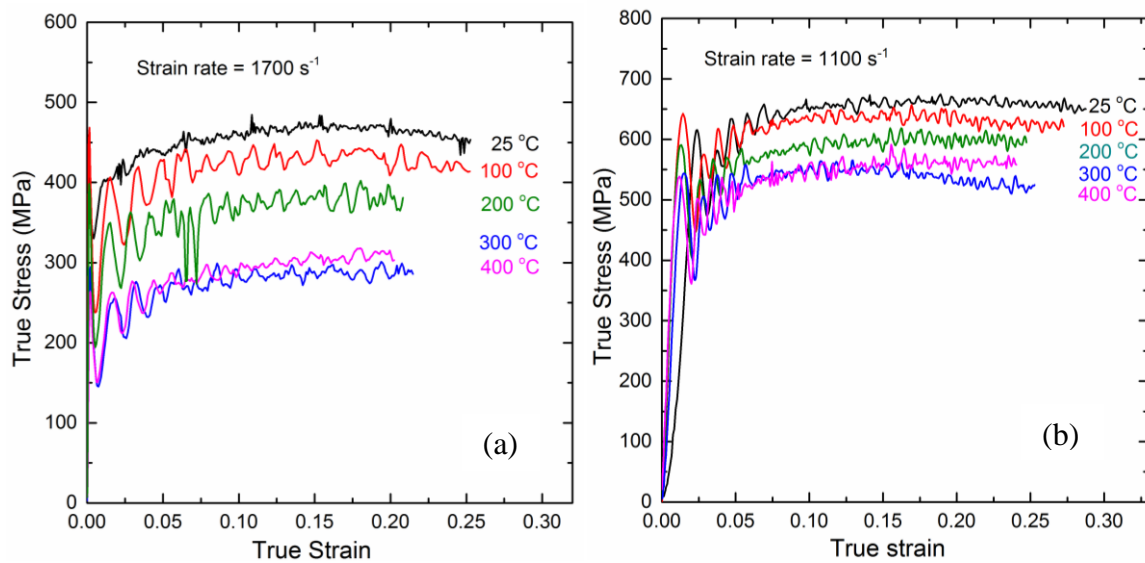


**Fig. 4.51:** True stress -true strain curve for (a) Nb-1Zr and (b) Nb-1Zr-0.1C alloy at strain rate of  $1700 \text{ s}^{-1}$  and  $1100 \text{ s}^{-1}$  respectively.

Fig. 4.52 shows the comparison of variation of flow stress of Nb-1Zr and Nb-1Zr-0.1C alloys with test temperatures at high strain rates. Both Nb alloys show the similar trend of decreasing the flow stress with temperature. However at temperature of  $400 \text{ }^{\circ}\text{C}$  the flow stress was observed to be slightly higher than that at  $300 \text{ }^{\circ}\text{C}$  for both Nb-1Zr and Nb-1Zr-0.1C alloy (Fig. 4.52). This may be due to the occurrence of DSA at these high strain rates.

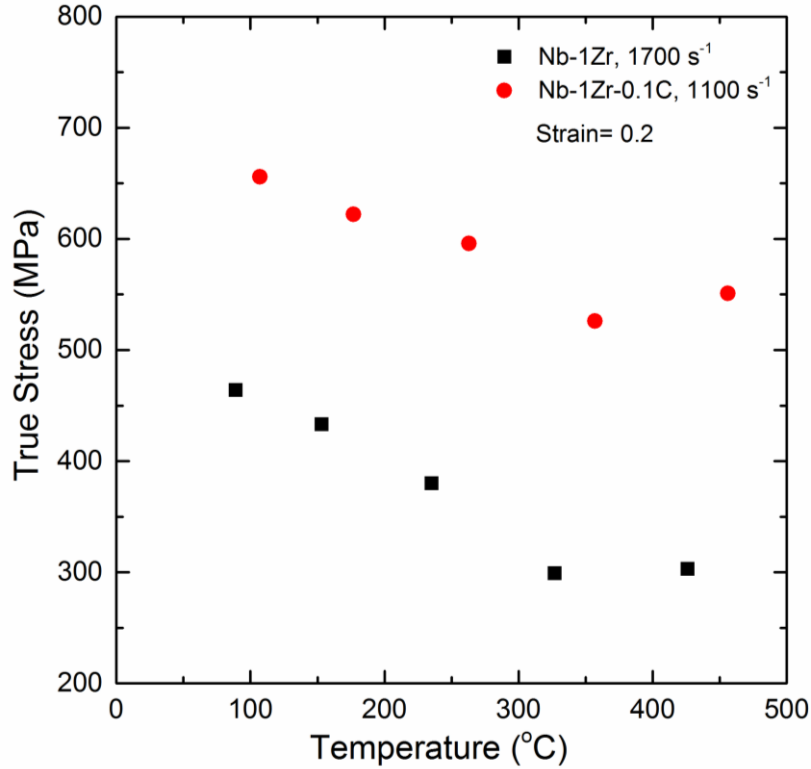


**Fig. 4.52:** The true stress variation of Nb alloys with temperature at a strain of 0.2 for high strain rates as indicated in the figure.

## 4.5 Comparative study of Nb, Nb-1Zr and Nb-1Zr-0.1C alloy

### 4.5.1 Effect of alloy addition

The major role of the alloying elements such as carbon and zirconium in Nb is to increase the mechanical strength at elevated temperatures by precipitation hardening and solid solution strengthening respectively. The stress - strain rate data of Nb-1Zr from this study was compared with data from literature for pure Nb [158] and Nb-1Zr-0.1C [47] alloy at temperature of 900 and 1000 °C as shown in Fig. 4.53. It is seen that the experimental data for Nb-1Zr of the present study follows the same trend as the Nb data from literature, which lies in the same stress range regime. However Davidson et al. [66] showed that the creep strength of Nb-1Zr was higher than that of Nb at 1027 °C. The comparison in Fig. 4.53

shows that Nb-1Zr-0.1C alloys has a higher flow stress (three fold) for given strain rate (higher creep strength) as compared to that of Nb and Nb-1Zr. The higher strength of Nb-1Zr-0.1C can be attributed to the presence of fine (Nb, Zr)C precipitates [67]. In comparison to precipitation hardening, solid solution strengthening of Zr in Nb appears insignificant.

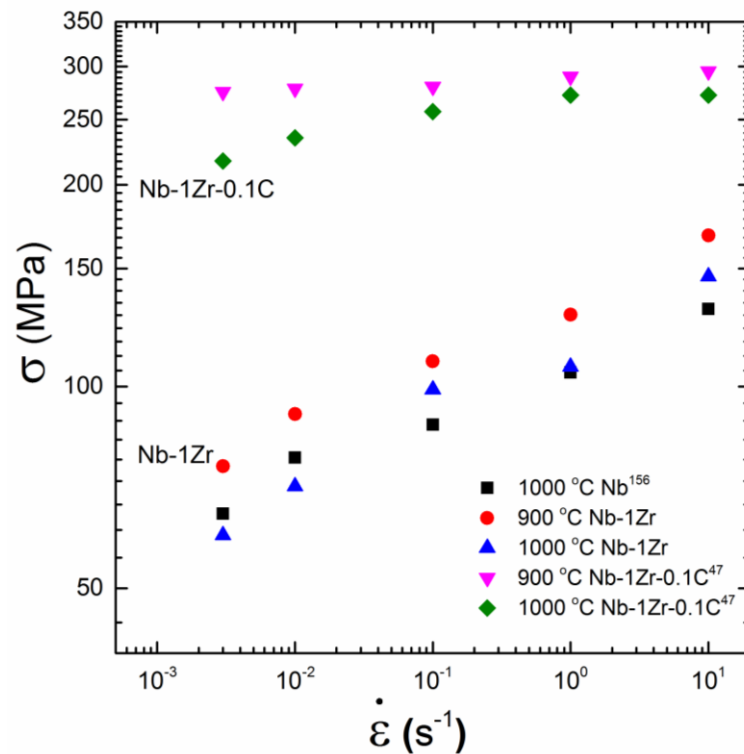


**Fig. 4.53** : Comparison of true stress vs. strain rate for Nb-1Zr, pure Nb [158] and Nb-1Zr-0.1C [47] at 900 °C and 1000 °C.

Chaudhuri et al. observed inhomogeneously distributed dynamically recrystallized grains in Nb-1Zr-0.1C alloys [73]. In the temperature range of 1500 - 1700 °C and low strain rates of 0.001 - 0.1 s<sup>-1</sup> Nb-1Zr-0.1C alloy showed a necklace microstructure typical of initiation of DRX. In the study on Nb-1Zr such necklace structure was not observed, implying that DRX was completed and grain growth had occurred at the higher temperatures and lower strain rates. A comparison of deformation parameters (data obtained from section 4.1) in the high

strain rate sensitivity domain for Nb, Nb-1Zr and Nb-1Zr-0.1C alloys are given in Table 4.4. The activation energies for deformation are similar for both Nb and Nb-1Zr alloy (around 250 kJ mol<sup>-1</sup>) and lower than that of Nb-1Zr-0.1C (360 kJ mol<sup>-1</sup>). For Nb-1Zr-0.1C alloy C is in form of carbides and the barriers to dislocation motion change from dislocation-dislocation or solute atom based process to dislocation interacting with precipitate. This possibly results in the substantial increase in  $Q$  for Nb-1Zr-0.1C as compared to Nb-1Zr. A higher activation energy for deformation implies a higher sensitivity of strain rate to changes in temperature (for a given stress)

$$Q = -R \frac{\partial \ln \dot{\varepsilon}}{\partial (1/T)} \quad (4.15)$$

An earlier study on the low temperature deformation (< 500 °C) of Nb [46] used an activation free energy of about 70 kJ mol<sup>-1</sup> to fit a physically based constitutive equation. It is expected that the 70 kJ mol<sup>-1</sup> represents the activation energy of Peierls barrier which is the short range barrier to dislocation motion in the lower temperature range. In the present study the activation energies are significantly higher than 70 kJ mol<sup>-1</sup>, suggesting that the Peierls barrier is not the short range barrier at these higher temperatures. The activation energy values match those of dislocation core diffusion [81]. A comparison of the domain of high strain rate sensitivity for Nb-1Zr and Nb-1Zr-0.1C (Fig. 3 of Ref [47]) shows a shift in the domain of DRX to higher strain rates at very high temperatures. For Nb-1Zr-0.1C the high  $m$  domain lies from 1300 to 1700 °C and 3×10<sup>-3</sup> to 0.1 s<sup>-1</sup>, whereas for Nb it lies from 1200 to 1500 °C and 10<sup>-2</sup> to 1 s<sup>-1</sup>. In the domain of hot workability the strain rate sensitivity ( $m$ ) values for both Nb-1Zr and Nb-1Zr-0.1C were found to be same.

**Table 4.4:** A comparison of deformation domain, strain rate sensitivity( $m$ ), stress exponent ( $n$ ), activation energy ( $Q$ )and activation volume ( $V/b^3$ ) values of pure Nb, Nb-1Zr and Nb-1Zr-0.1C

Material	High $m$ domain	Peak Strain rate sensitivity	$n$	$Q$ (kJ mol <sup>-1</sup> )	$V/b^3$
Nb	1200 - 1500 °C and $10^{-2}$ - $1 \text{ s}^{-1}$	0.19	7.5	246	200 - 700
Nb-1Zr	1200 - 1500 °C and $10^{-3}$ - $0.1 \text{ s}^{-1}$ and 1600 - 1700 °C and $10^{-2}$ - $1 \text{ s}^{-1}$	0.24	4.9	259	230 - 650
Nb-1Zr-0.1C	1300 - 1700 °C and $10^{-3}$ - $1 \text{ s}^{-1}$	0.25	5	361	200 - 500

The steady state strain rate vs. flow stress data of Nb, Nb-1Zr alloy from this study was compared with data from literature for pure Nb, Nb-1Zr and Nb-1Zr-0.1C alloy as shown in Fig. 4.54. As the comparison is with creep data of Mukherjee et al. [66-68, 171] at 1027 °C the present data is taken at comparable temperature of 1000 °C and plotted as strain rate vs. stress, the common visualization for creep data. It is seen that the experimental data for Nb and Nb-1Zr of the present study follows the same trend as the Nb data from literature [67]. The present data for Nb-1Zr-0.1C alloy lies in the power law breakdown regime unlike the data from Ref. [67] which lies in the power law regime. In comparison to Nb-1Zr alloys, data of which is plotted in Fig. 4.54, Nb has a lower strength (lower stress for given strain rate or higher strain rate for a given stress). The hot deformation data of Sarkar et al. [47] are in the high stress regime corresponding to the power law breakdown regime.

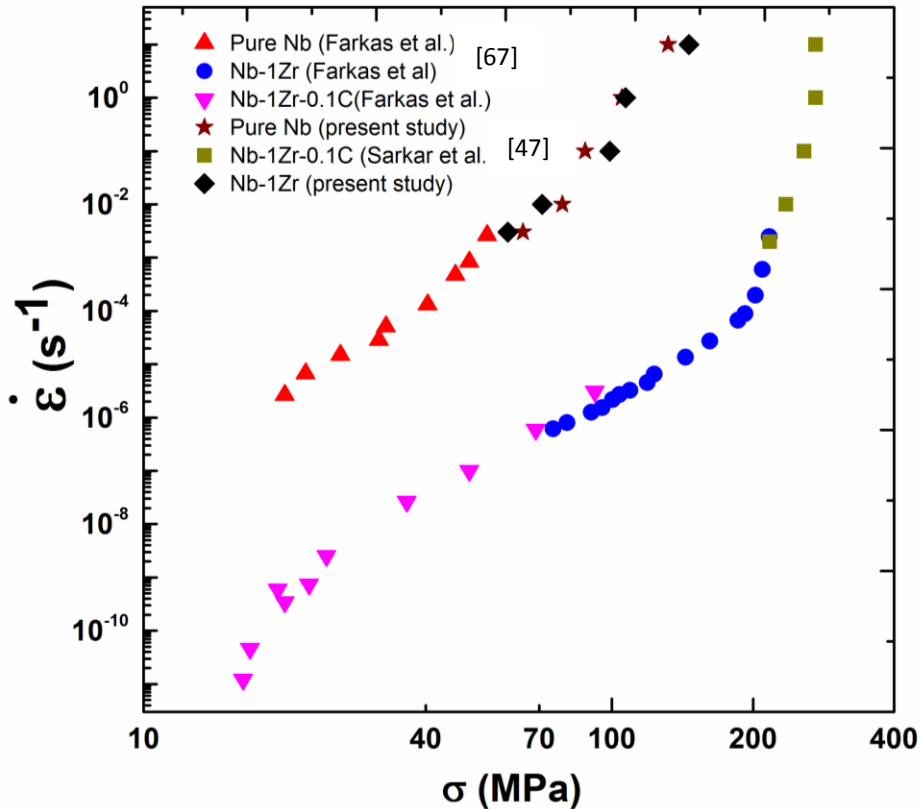


**Fig. 4.54:** Comparison of steady state strain rate vs. flow stress for pure Nb at 1000 °C (taken from experiment), Nb-1Zr-0.1C at 1000 °C and Nb-1Zr and Nb-1Zr-0.1C at 1027 °C (taken from ref. [67]).

The creep studies on Nb-1Zr alloys carried out by Davidson et al. [66] also showed that the creep strength of Nb-1Zr at 1027 °C was significantly higher than that of Nb. This was attributed to significant solid solution hardening. The addition of 0.1% C to Nb-1Zr as in the Nb-1Zr-0.1C alloy, showed no improvement in the creep strength over the Nb-1Zr alloy [67]. From the studies in literature it appeared that the lack of improvement in creep strength with the addition of C that in this stress range carbides offer no resistance to creep. It was argued by Davidson et al. [66] that the applied stress was greater than the Orowan stress required for dislocation particle bypass, hence precipitates offer no additional resistance to dislocation motion. However the present study showed that addition of C to Nb-1Zr does improve the strength at 1000 °C.

#### 4.5.2 Strain rate sensitivity and flow stress variation with temperature

Fig. 4.55 shows the comparison of variation of strain rate sensitivity with temperature for Nb-1Zr and Nb-1Zr-0.1C alloy. The strain rate sensitivity was low and nearly same for Nb-1Zr and Nb-1Zr-0.1C alloy from room temperature to 600 °C. However at higher temperature up to 1400 °C Nb-1Zr alloy has higher strain rate sensitivity than Nb-1Zr-0.1C alloy. For Nb-1Zr alloy the strain rate sensitivity increased with temperature up to 1300 °C and then decreased with temperature. Also for Nb-1Zr-0.1C alloy the strain rate sensitivity increased linearly from 900 to 1700 °C.

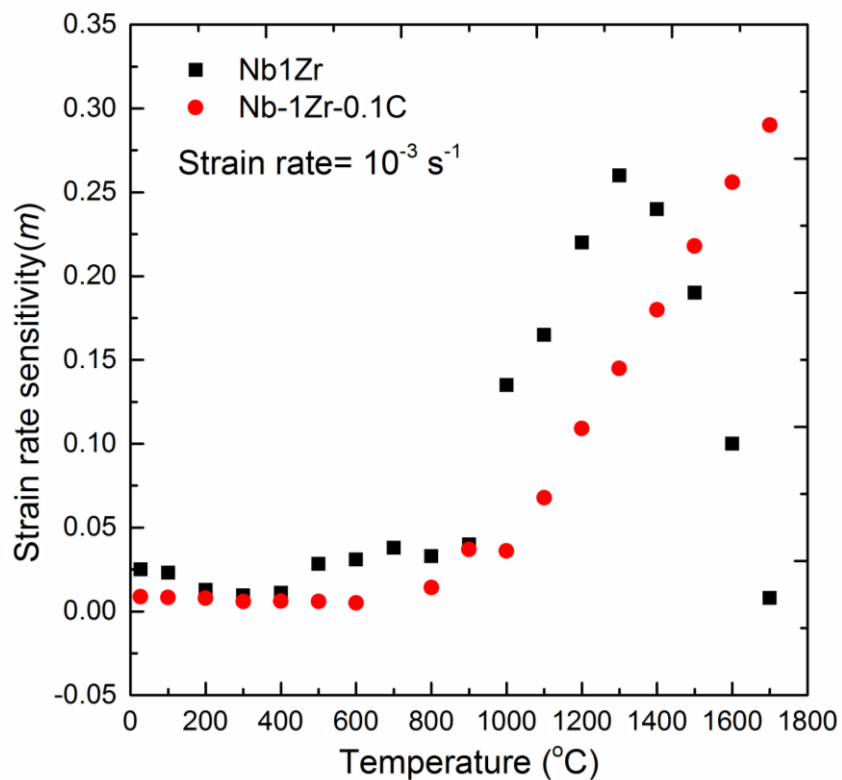


**Fig. 4.55:** The variation of strain rate sensitivity ( $m$ ) at strain rate of  $10^{-3} \text{ s}^{-1}$  with temperature for Nb-1Zr and Nb-1Zr-0.1C alloy from room temperature to 1700 °C.

The variation of flow stress from room temperature to 1700 °C for Nb alloys is shown in Fig. 4.56. For the low temperature regime the flow data for high strain rates and low strain rates are obtained for a strain of 0.25 whereas for the high temperature regime the flow data are obtained for a strain of 0.6. It is observed that in the low temperature regime the decrease of flow stress is more for both the high and low strain rates as compared to high temperature regime.

Fig. 4.57 shows the comparison of the variation of flow stress for Nb-1Zr and Nb-1Zr-0.1C alloy from room temperature to 1700 °C. The flow stress for Nb alloys features three different regime with respect to temperature variation as marked in Fig. 4.57. The three different temperature regimes are (a) low temperature regime (from room temperature to 600 °C), the intermediate temperature regime (600 - 900 °C) and high temperature regime (1000 - 1700 °C). The flow stress was observed to decrease from room temperature to 600 °C and was insensitive from 600 to 900 °C (Fig. 4.57). At temperatures higher than 1000 °C the flow stress again decreased with increasing temperature. The activation energy ( $Q$ ) for deformation for Nb alloys was determined in the low temperature regime as

$$Q = \frac{R}{m} \frac{\partial \ln \sigma}{\partial (1/T)} \quad (4.16)$$

and was shown in Table 4.5 (data obtained from Fig. 4.43 and Fig. 4.44).

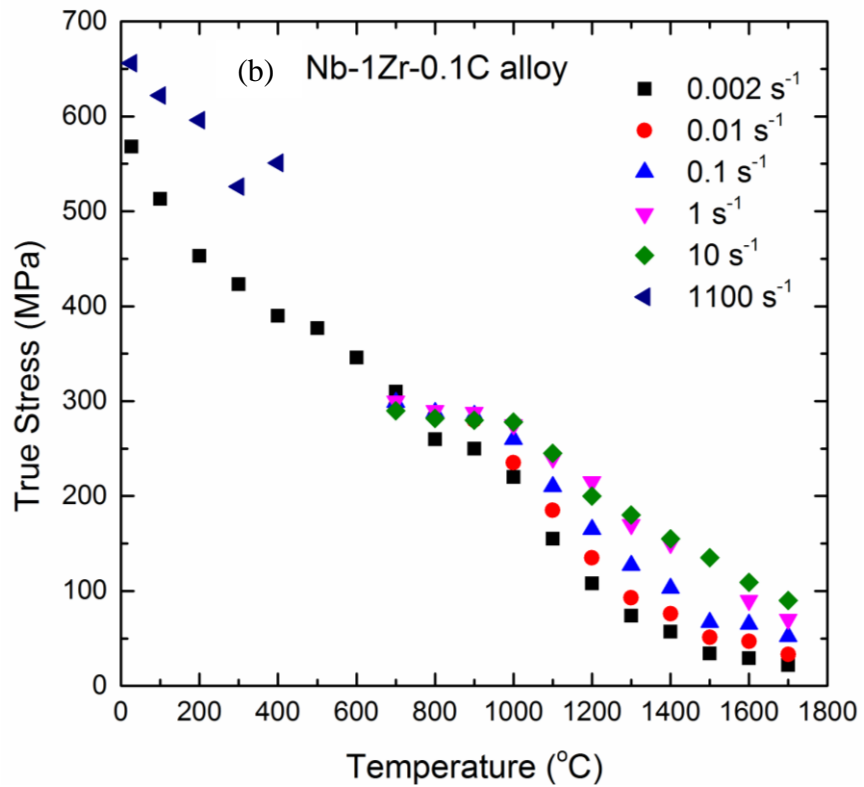
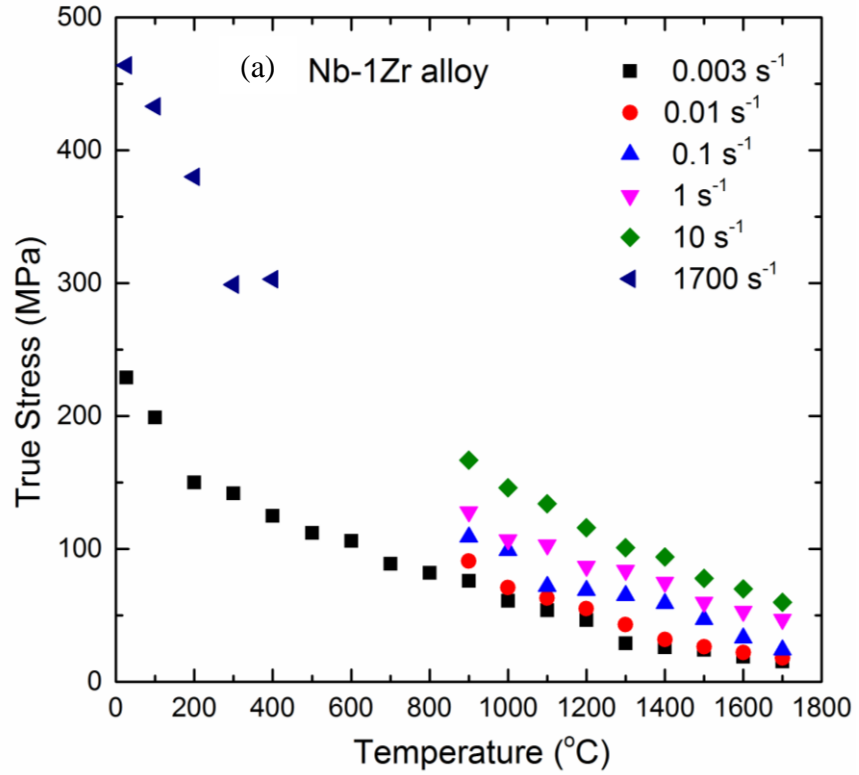


**Fig. 4.56:** The variation of true stress with temperature for (a) Nb-1Zr and (b) Nb-1Zr-0.1C alloy from room temperature to 1700 °C at different strain rates.

The activation energy for deformation of Nb-1Zr alloy at room temperature matched with that of the pure Nb and Nb-1Zr from literature [34, 46]. The activation energy for deformation of Nb alloys at these low temperature was low as compared to high temperature regime where it is 250 ~ 360 kJ mol<sup>-1</sup>. Also the activation volume for Nb alloys at these low temperature regime was found to be less than 100 b<sup>3</sup>. These values of activation volume suggest the annihilation of dislocations at grain boundaries during plastic deformation [169].

**Table 4.5:** Activation energy ( $Q$ ) for Nb-1Zr and Nb-1Zr-0.1C alloy at low temperature.

Temperature (°C)	Activation energy, $Q$ (kJ mol <sup>-1</sup> )	
	Nb-1Zr	Nb-1Zr-0.1C
25	68	141
100	122	183
200	223	229

In Fig. 4.57 the low temperature regime is related to thermally activated motion of dislocation where conservative motion takes place. In the intermediate temperature regime, where temperature is sufficient to completely overcome thermal activation, only athermal stress exists and is very weakly dependent on temperature and strain rate. In the third region again deformation becomes thermally activated but now with non-conservative dislocation motion

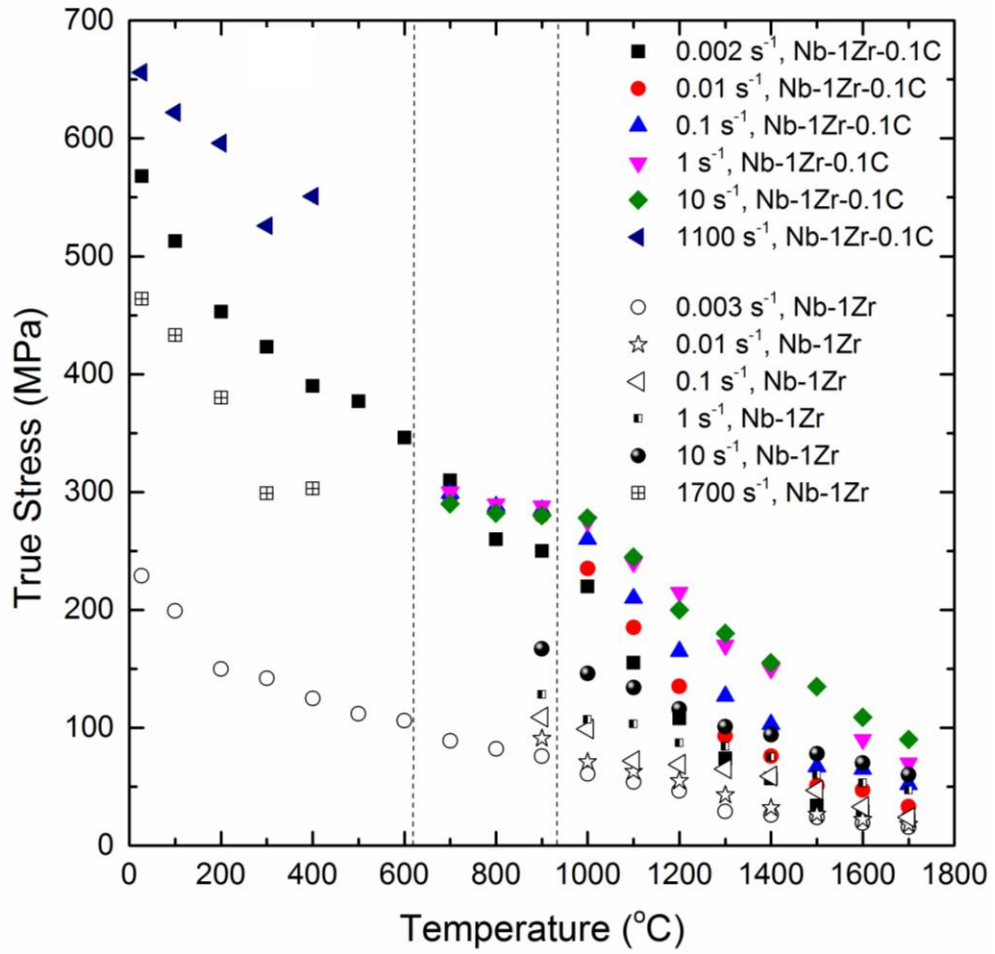


**Fig. 4.57:** Comparison of the variation of true stress at different strain rates with temperature for Nb-1Zr and Nb-1Zr-0.1C alloy from room temperature to 1700 °C.

## Chapter 5. Summary and Conclusion

### 5.1 Flow stress behavior

1. The flow curves for Nb and its alloys showed a strong dependence on deformation temperature and strain rate. In the high temperature regime the flow curves showed an initial work-hardening to a maximum stress followed by softening. This softening of flow stress after an initial hardening is evidence dynamic of recrystallisation of Nb alloys.
2. In the intermediate temperature regime the flow stress for Nb-1Zr-0.1C alloy is virtually independent of temperature and strain rate. At 700 °C and strain rate of  $10^{-3} \text{ s}^{-1}$  Nb-1Zr-0.1C alloy showed dynamic strain aging. The flow curves of Nb-1Zr alloy show work-hardening behavior at this intermediate temperature regime. At 700 °C and lower strain rates of  $3 \times 10^{-3}$  and  $10^{-1} \text{ s}^{-1}$  a sharp yield point is observed for Nb, which is indicative of strong solute dislocation interaction.
3. In the low temperature regime the flow curves show work-hardening behaviour for both low and high strain rates. The flow stress decreases with temperature more rapidly in this regime as compared to the high temperature regime.

### 5.2 Optimum of hot processing conditions

1. Two distinctly different domains were identified for niobium deformed in the temperature range of 700 - 1500 °C and the strain rate range  $10^{-3}$  -  $10 \text{ s}^{-1}$  as: (1) very small to zero strain rate sensitivity domain from 700 to 1000 °C at strain rates of  $10^{-2}$  to  $1 \text{ s}^{-1}$  and (2) the domain of hot workability as from temperature of 1200 - 1500 °C and strain rates of  $10^{-2}$  to  $1 \text{ s}^{-1}$ . In this domain the strain rate sensitivity varied from 0.12 to 0.2, the stress exponent 7.5 and activation energy  $246 \text{ kJ mol}^{-1}$ .

2. An optimum regime of hot workability was identified for Nb-1Zr alloy in the temperature range of 1200 to 1500 °C at strain rate range of  $10^{-3}$  to  $0.1 \text{ s}^{-1}$  and temperature range of 1600 - 1700 °C and strain rate range of  $10^{-1}$  to  $1 \text{ s}^{-1}$ . In this domain the strain rate sensitivity varied from 0.11 to 0.25, the stress exponent was 5 and activation energy of deformation was obtained as  $259 \text{ kJ mol}^{-1}$ .
3. A single domain of hot workability starting at about 1300 °C and maximum  $m$  at 1700 °C and  $0.002 \text{ s}^{-1}$  was identified from Nb-1Zr-0.1C alloy processing map. In this domain  $m$  increased from slightly positive value to about 0.24 with increasing temperature and decreasing strain rate.
4. The peak strain rate sensitivity ( $m$ ) was relatively high for Nb-1Zr-0.1C as compared to pure Nb and Nb-1Zr in the domain of hot workability. Nb showed a lower flow stress and an optimum hot working domain at lower temperatures as compared to Nb-1Zr and Nb-1Zr-0.1C alloy.

### 5.3 Deformation Microstructure

1. The microstructure of samples deformed within the high  $m$  domain revealed a dynamically recrystallized microstructure whereas samples deformed in the low  $m$  regime revealed strain localization. Addition of 0.1% C to Nb-1Zr alloy results in a completely modified microstructure for Nb-1Zr-0.1C.
2. The necklace structure of recrystallized grains was seen along the serrated large grain boundaries of Nb-1Zr-0.1C alloy at strain of 0.6 and 0.9 for temperature of 1500 and 1600 °C, respectively. Equiaxed microstructure was obtained for larger strain of 1.2 for both 1500 and 1600 °C test conditions for Nb-1Zr-0.1C alloy. Fine grain size distribution was observed at strain of 0.9 for both test temperatures of 1500 and 1600 °C. For Nb alloys the predominant

texture with respect to compression axis is along the  $\langle 001 \rangle$  poles for all deformation conditions of high  $m$  domain.

3. The presence of serrated grain boundaries and the necklace structure observed in Nb alloys at high temperature confirm the occurrence of discontinuous dynamic recrystallization.

#### **5.4 Deformation mechanisms and comparison of deformation parameters**

1. At high temperature the activation energies ( $Q$ ) of deformation for Nb alloys were lower than that for the activation energy for self diffusion of niobium ( $400 \text{ kJ mol}^{-1}$ ). This lower value of  $Q$  suggests dislocation core diffusion during high temperature deformation. At room temperature the activation energy for deformation for Nb-1Zr alloy is lower than that of Nb-1Zr-0.1C alloy.

2. At higher stresses the activation volume for pure Nb was similar to Nb-1Zr-0.1C, whereas at low stresses pure Nb has relatively higher activation volume. For both Nb and its alloy it was observed that the activation volume decreased with increasing stress, which suggests that the deformation is thermally activated process. The activation volume of  $200 - 700 b^3$  at higher temperature signifies the kink or jogs motion of dislocations as the rate controlling deformation mechanism. At low temperature regime the annihilation of dislocations at grain boundaries is the dominating deformation mechanisms as it reflected from the activation volume of  $10 - 100 b^3$ .

3. The flow stress for Nb-1Zr alloy is lower than that of Nb-1Zr-0.1C alloy throughout the temperature range of 25 to 1700 °C. The variation in flow stress values at the temperature range of 25 to 1700 °C for Nb-1Zr alloy is less as compared to that of Nb-1Zr-0.1C alloy.

4. In the low temperature regime (25 - 600 °C) thermally activated deformation mechanisms is identified where conservative motion of dislocations takes place. In intermediate temperature regime (600 - 900 °C) only athermal stress is operative and it is very weakly dependent on temperature and strain rate. In high temperature regime (1000 - 1700 °C) the deformation is thermally activated with non-conservative motion of dislocations.

## References

- [1] D.R. Lide, CRC hand book of chemistry and physics, 85 ed., CRC Press, 2004.
- [2] W.A. Fietz, M.R. Beasley, J. Silcox, W.W. Webb, Magnetization of Superconducting Nb-25%Zr Wire, *Physical Review*, 136 (1964) A335-345.
- [3] J.S. Park, S. Lee, B.K. Ju, J. Jang, D. Jeon, M.H. Oh, Fabrication and estimation of characteristics for Nb-silicide FEAs Asian Symposium on Information Display, 1999 pp. 49 - 52.
- [4] R. Grill, A. Gnadenberger, Niobium as mint metal: Production-properties-processing, *International Journal of Refractory Metals and Hard Materials*, 24 (2006) 275-282.
- [5] W.C. Leslie, E. Hornbogen, *Physical Metallurgy of Steels*, Chapter 17, (1981).
- [6] F.B. Pickering, *High Strength Low Alloy Steels*, *Materials Science and Technology*, Wiley-VCH Verlag GmbH & Co. KGaA, 2006.
- [7] J.K. Tien, J.P. Collier, G. Vignou, The role of Niobium and other refractory elements, *Superalloy 718 Metallurgy and Applications*, 1989, pp. 553-566.
- [8] D.C. Larbalestier, P.J. Lee, New developments in niobium titanium superconductors, *Proceedings Particle Accelerator Conference*, 1995, pp. 1276-1281 vol.1272.
- [9] J. Hebda, *Niobium alloys and high temperature applications*, *Niobium Science & Technology: Proceedings of the International Symposium Niobium 2001*, Orlando, Florida, USA, 2001.
- [10] R.H. Titran, Long-time creep behavior of Nb-1Zr alloy containing carbon, DOE/NASA/16310-4, NASA TM-100142 (1986).
- [11] E.N. Sheftel, O.A. Bannykh, Niobium-base alloys, *International Journal of Refractory Metals and Hard Materials*, 12 (1994) 303-314.

- [12] M.S. El-Genk, J.M. Tournier, A review of refractory metal alloys and mechanically alloyed-oxide dispersion strengthened steels for space nuclear power systems, *Journal of Nuclear Materials*, 340 (2005) 93-112.
- [13] A.J. Deardo, Niobium in modern steels, *International Materials Reviews*, 48 (2003) 371-402.
- [14] F. Heisterkamp, T. Carneiro, Niobium: future possibilities – technology and the market place, *Niobium Science & Technology: Proceedings of the International Symposium Niobium 2001*, Orlando, Florida, USA, 2001.
- [15] D.J. Mazey, C.A. English, Role of refractory metal alloys in fusion reactor applications, *Journal of the Less Common Metals*, 100 (1984) 385-427.
- [16] H. Matsuno, A. Yokoyama, F. Watari, M. Uo, T. Kawasaki, Biocompatibility and osteogenesis of refractory metal implants, titanium, hafnium, niobium, tantalum and rhenium, *Biomaterials*, 22 (2001) 1253-1262.
- [17] R. Cooper Jr, E. Hoffman, Refractory alloy technology for space nuclear power applications, CONF-8308130, DOE, 1984.
- [18] G. Kruger, S. Vaidyanathan, N. Deane, R. Protsik, R. Murata, SP-100 reactor design, IECEC'87; Proceedings of the Twenty-second Intersociety Energy Conversion Engineering Conference, Philadelphia, PA, Aug. 10-14, 1987. Volumes 1, 2, 3, and 4, 1987.
- [19] S.J. Zinkle, L.J. Ott, D.T. Ingersoll, R.J. Ellis, M.L. Grossbeck, Overview of materials technologies for space nuclear power and propulsion, *AIP Conference Proceedings*, 608 (2002) 1063-1073.
- [20] R.E. Gold, D.L. Harrod, Refractory metal alloys for fusion reactor applications, *Journal of Nuclear Materials*, 85-86, Part 2 (1979) 805-815.
- [21] R.H. Titran, J.R. Stephens, D.W. Petrasek, *Refractory Metal Alloys and Composites for Space Nuclear Power Systems*, DOE/NASA/16310-8 NASA TM-101364 (1988).

- [22] J.R. Distefano, Review of alkali metal and refractory alloy compatibility for rankine cycle applications, *Journal of Materials Engineering*, 11 (1989) 215-225.
- [23] M.S. El-Genk, Deployment history and design considerations for space reactor power systems, *Acta Astronautica*, 64 (2009) 833-849.
- [24] S.J. Zinkle, J.T. Busby, Structural materials for fission and fusion energy, *Materials Today*, 12 (2009) 12-19.
- [25] I.V. Dulera, R.K. Sinha, High temperature reactors, *Journal of Nuclear Materials*, 383 (2008) 183-188.
- [26] E.J. Delgrosso, C.E. Carlson, J.J. Kaminsky, Development of niobium-zirconium-carbon alloys, *Journal of Less Common Metals*, 12 (1967) 173-201.
- [27] I.V. Dulera, A. Basak, P.P. Kelkar, R.K. Sinha, Compact High Temperature Reactor, *BARC Newsletter*, 2006, pp. 172-179.
- [28] A. Rollett, F. Humphreys, G.S. Rohrer, M. Hatherly, *Recrystallization and related annealing phenomena*, Elsevier, 2004.
- [29] W.T. Read, *Dislocations in crystals*, McGraw-Hill, 1953.
- [30] U. Kocks, H. Mecking, Physics and phenomenology of strain hardening: the FCC case, *Progress in Materials Science*, 48 (2003) 171-273.
- [31] J.W. Christian, S. Mahajan, Deformation twinning, *Progress in Materials Science*, 39 (1995) 1-157.
- [32] C. Tomé, R.A. Lebensohn, U. Kocks, A model for texture development dominated by deformation twinning: application to zirconium alloys, *Acta Metallurgica et Materialia*, 39 (1991) 2667-2680.
- [33] V. Randle, Twinning-related grain boundary engineering, *Acta Materialia*, 52 (2004) 4067-4081.

- [34] G. Taylor, Thermally-activated deformation of BCC metals and alloys, *Progress in Materials Science*, 36 (1992) 29-61.
- [35] E. Orowan, Problems of plastic gliding, *Proceedings of the Physical Society*, 52 (1940) 8.
- [36] O.D. Sherby, Factors affecting the high temperature strength of polycrystalline solids, *Acta Metallurgica*, 10 (1962) 135-147.
- [37] O.D. Sherby, P.M. Burke, Mechanical behavior of crystalline solids at elevated temperature, *Progress in Materials Science*, 13 (1968) 323-390.
- [38] A.K. Mukherjee, J.E. Bird, J.E. Dorn, Experimental correlations for high-temperature creep, (1968).
- [39] A.K. Mukherjee, An examination of the constitutive equation for elevated temperature plasticity, *Materials Science and Engineering: A*, 322 (2002) 1-22.
- [40] J. Hirth, J. Lothe, *Theory of Dislocations*. 857 p, A Wiley-Interscience Publication, p571, (1982).
- [41] J. Christian, Some surprising features of the plastic deformation of body-centered cubic metals and alloys, *Metallurgical and Materials Transactions A*, 14 (1983) 1237-1256.
- [42] R.W.K. Honeycombe, The effect of temperature and alloying additions on the deformation of metal crystals, *Progress in Materials Science*, 9 (1961) 95-130.
- [43] E. Pink, R.J. Arsenault, Low-temperature softening in body-centered cubic alloys, *Progress in Materials Science*, 24 (1980) 1-50.
- [44] M.A. Meyers, D.J. Benson, O. Vöhringer, B.K. Kad, Q. Xue, H.H. Fu, Constitutive description of dynamic deformation: physically-based mechanisms, *Materials Science and Engineering: A*, 322 (2002) 194-216.
- [45] R.W. Armstrong, S.M. Walley, High strain rate properties of metals and alloys, *International Materials Reviews*, 53 (2008) 105-128.

- [46] S. Nemat-Nasser, W. Guo, Flow stress of commercially pure niobium over a broad range of temperatures and strain rates, *Materials Science and Engineering: A*, 284 (2000) 202-210.
- [47] A. Sarkar, R. Kapoor, A. Verma, J.K. Chakravarty, A.K. Suri, Hot deformation behavior of Nb-1Zr-0.1C alloy in the temperature range 700-1700 °C, *Journal of Nuclear Materials*, 422 (2012) 1-7.
- [48] I. Chou, D.A. Koss, P.R. Howell, A.S. Ramani, High-temperature deformation of a mechanically alloyed niobium-yttria alloy, *Materials Science and Engineering: A*, 222 (1997) 14-20.
- [49] L.L. Gill, B.B. Argent, Hot working of Niobium alloys, *Journal of Less Common Metals*, 3 (1961) 305-311.
- [50] H. Kiessig, U. Essmann, Flow stress of pure niobium between 2200 K and the melting point 2741 K, *Scripta Metallurgica*, 19 (1985) 989-992.
- [51] T.G. Nieh, M. Zhang, S.J. Zinkle, T.E. McGreevy, D.T. Hoelzer, S.A. Speakman, Effect of texture on the high temperature mechanical properties of Nb-1%Zr alloy, *Scripta Materialia*, 55 (2006) 719-722.
- [52] T.E. McGreevy, C.E. Duty, K.J. Leonard, F.W. Wiffen, S.J. Zinkle, The mechanical behavior of Nb-1Zr, *Proceedings of the space nuclear conference, San Diego, California, 2005*, pp. 303-308.
- [53] A. Fourdeux, A. Wronski, Some observations of the deformation mechanisms of niobium, *Journal of the Less Common Metals*, 6 (1964) 11-20.
- [54] A. Wronski, A. Fourdeux, The deformation of polycrystalline niobium at room temperature, *Journal of the Less Common Metals*, 7 (1964) 205-211.
- [55] L.I. Van Torne, G. Thomas, Yielding and plastic flow in niobium, *Acta Metallurgica*, 11 (1963) 881-898.

- [56] T.L. Briggs, J.D. Campbell, The effect of strain rate and temperature on the yield and flow of polycrystalline niobium and molybdenum, *Acta Metallurgica*, 20 (1972) 711-724.
- [57] G.R. Myneni, Physical and Mechanical Properties of Niobium for SRF Science and Technology, *AIP Conference Proceedings*, 927 (2007) 41-47.
- [58] N. Banai, V.P. Panoskaltsis, J.M. Salazar, L. Brenig, An analysis of the high temperature deformations of niobium, *Mechanics Research Communications*, 23 (1996) 483-493.
- [59] A. Zamiri, F. Pourboghrat, H. Jiang, T.R. Bieler, F. Barlat, J. Brem, C. Compton, T.L. Grimm, On mechanical properties of the superconducting niobium, *Materials Science and Engineering: A*, 435–436 (2006) 658-665.
- [60] R. Begley, J. Bechtold, Effect of alloying on the mechanical properties of niobium, *Journal of the Less Common Metals*, 3 (1961) 1-12.
- [61] H.E. McCoy, Creep properties of the Nb-1% Zr alloy, *Journal of the Less Common Metals*, 8 (1965) 20-35.
- [62] R.H. Titran, Creep strength of niobium alloys, Nb-1%Zr and PWC-11, DOE/NASA/16310-13, NASA TM-102390 (1990).
- [63] M. Uz, R.H. Titran, Processing and microstructure of Nb-1%Zr-0.1%C alloy sheet, NASA TM-105921,1993 (1993).
- [64] R.H. Titran, M. Uz, Effects of thermomechanical processing on the microstructure and mechanical properties of Nb-1Zr-C alloys, NASA TM 107207 (1993).
- [65] M. Uz, R.H. Titran, Characterization of the microstructure of Nb-1wt%Zr-0.1wt%C tubes as affected by thermomechanical processing, DOE/NASA/16310-21, NASA TM-106381 (1994).
- [66] M.J. Davidson, M. Biberger, A.K. Mukherjee, Creep of niobium and solid solution strengthened Nb-1wt%Zr, *Scripta Metallurgica et. Materialia*, 27 (1992) 1829-1834.

- [67] D.M. Farkas, A.K. Mukherjee, Creep behavior and microstructural correlation of a particle-strengthened Nb-1Zr-0.1C alloy, *Journal of Materials Research*, 11 (1996) 2198-2205.
- [68] D.M. Farkas, A.K. Mukherjee, Stress cycle testing during creep of a particle strengthened Nb-1Zr-0.1C alloy, *Materials Science and Engineering: A*, 222 (1997) 21-27.
- [69] K.J. Leonard, J.T. Busby, S.J. Zinkle, Influence of thermal and radiation effects on microstructural and mechanical properties of Nb-1Zr, *Journal of Nuclear Materials*, 414 (2011) 286-302.
- [70] H. Watanabe, K. Yasunaga, T. Muroga, N. Yoshida, F.A. Garner, The influence of heat treatments on neutron irradiated Nb-1Zr alloy, *Journal of Nuclear Materials*, 233-237 (1996) 577-580.
- [71] R. Ding, I.P. Jones, Mechanical properties and deformation behaviour of a niobium alloy with different carbon contents, *Materials Science and Engineering: A*, 497 (2008) 301-308.
- [72] R. Ding, I.P. Jones, H. Jiao, Effect of carbon on the microstructures and mechanical properties of as cast Nb-base alloy, *Materials Science and Engineering: A*, 485 (2008) 92-98.
- [73] A. Chaudhuri, A. Sarkar, R. Kapoor, R.N. Singh, J.K. Chakravartty, S. Suwas, Microstructural Features of Hot Deformed Nb-1Zr-0.1C Alloy, *Journal of Materials*, 66 (2014) 1923-1929.
- [74] N. Hansen, R.F. Mehl, New discoveries in deformed metals, *Metallurgical and Materials Transactions A*, 32 (2001) 2917-2935.
- [75] N. Hansen, Cold deformation microstructures, *Materials Science and Technology*, 6 (1990) 1039-1047.
- [76] T.L. Grobstein, R.H. Titran, Characterization of precipitates in a niobium-zirconium-carbon alloy, 1986.

- [77] M. Uz, R.H. Titran, Thermal stability of the microstructure of an aged Nb-Zr-C alloy, DOE/NASA/16310-14, NASA TM-103647 (1991).
- [78] Y. Tan, C.L. Ma, A. Kasama, R. Tanaka, J.-M. Yang, High temperature mechanical behavior of Nb–Mo–ZrC alloys, *Materials Science and Engineering: A*, 355 (2003) 260-266.
- [79] B. Vishwanadh, K. Vaibhav, S. Jha, K. Mirji, I. Samajdar, D. Srivastava, R. Tewari, N. Saibaba, G. Dey, Development of Nb–1% Zr–0.1% C alloy as structural components for high temperature reactors, *Journal of Nuclear Materials*, 427 (2012) 350-358.
- [80] M.F. Ashby, A first report on deformation-mechanism maps, *Acta Metallurgica*, 20 (1972) 887-897.
- [81] H.J. Frost, M.F. Ashby, *Deformation Mechanism Maps: The Plasticity and Creep of Metals and Ceramics*, Pergamon Press, 1982.
- [82] R. Raj, Development of a processing map for use in warm-forming and hot-forming processes, *Metallurgical and Materials Transactions A*, 12 (1981) 1089-1097.
- [83] Y.V.R.K. Prasad, H. Giegel, S. Doraivelu, J. Malas, J. Morgan, K. Lark, D. Barker, Modeling of dynamic material behavior in hot deformation: forging of Ti-6242, *Metallurgical Transactions A*, 15 (1984) 1883-1892.
- [84] Y.V.R.K. Prasad, T. Seshacharyulu, Modelling of hot deformation for microstructural control, *International Materials Reviews*, 43 (1998) 243-258.
- [85] Y.V.R.K. Prasad, Processing maps: A status report, *Journal of Materials Engineering and Performance*, 12 (2003) 638-645.
- [86] Y.V.R.K. Prasad, K. Rao, S. Sasidhar, *Hot working guide: a compendium of processing maps*, ASM international, 2015.
- [87] Y.V.R.K. Prasad, T. Seshacharyulu, Processing maps for hot working of titanium alloys, *Materials Science and Engineering: A*, 243 (1998) 82-88.

- [88] F. Montheillet, J.J. Jonas, K.W. Neale, Modeling of dynamic material behavior: A critical evaluation of the dissipator power co-content approach, *Metallurgical and Materials Transactions A*, 27 (1996) 232-235.
- [89] J.K. Chakravartty, R. Kapoor, S. Banerjee, Y.V.R.K. Prasad, Characterization of hot deformation behavior of Zr-1Nb-1Sn alloy, *Journal of Nuclear Materials*, 362 (2007) 75-86.
- [90] J.K. Chakravartty, R. Kapoor, A. Sarkar, S. Banerjee, Dynamic recrystallization in zirconium alloys, *Journal of ASTM International*, 7 (2010) 1-17.
- [91] F. Humphreys, M.Hatherly, *Recrystallization Related Annealing Phenomena*, Elsevier, 2004.
- [92] W. Nix, J. Gibeling, D. Hughes, Time-dependent deformation of metals, *Metallurgical and Materials Transactions A*, 16 (1985) 2215-2226.
- [93] T. Sakai, A. Belyakov, R. Kaibyshev, H. Miura, J.J. Jonas, Dynamic and post-dynamic recrystallization under hot, cold and severe plastic deformation conditions, *Progress in Materials Science*, 60 (2014) 130-207.
- [94] R.W.K. Honeycombe, R.W. Pethen, Dynamic recrystallization, *Journal of the Less Common Metals*, 28 (1972) 201-212.
- [95] M.J. Luton, C.M. Sellars, Dynamic recrystallization in nickel and nickel-iron alloys during high temperature deformation, *Acta Metallurgica*, 17 (1969) 1033-1043.
- [96] T. Sakai, J.J. Jonas, Overview no. 35 Dynamic recrystallization: Mechanical and microstructural considerations, *Acta Metallurgica*, 32 (1984) 189-209.
- [97] J.P. Sah, G.J. Richardson, C.M. Sellars, Grain-Size Effects during Dynamic Recrystallization of Nickel, *Metal Science*, 8 (1974) 325-331.
- [98] H.J. McQueen, Development of dynamic recrystallization theory, *Materials Science and Engineering: A*, 387–389 (2004) 203-208.

- [99] H.J. McQueen, C.A.C. Imbert, Dynamic recrystallization: plasticity enhancing structural development, *Journal of Alloys and Compounds*, 378 (2004) 35-43.
- [100] L. Blaz, T. Sakai, J.J. Jonas, Effect of initial grain size on dynamic recrystallization of copper, *Metal Science*, 17 (1983) 609-616.
- [101] B. Derby, The dependence of grain size on stress during dynamic recrystallisation, *Acta Metallurgica et Materialia*, 39 (1991) 955-962.
- [102] S. Gourdet, F. Montheillet, An experimental study of the recrystallization mechanism during hot deformation of aluminium, *Materials Science and Engineering: A*, 283 (2000) 274-288.
- [103] S. Gourdet, F. Montheillet, A model of continuous dynamic recrystallization, *Acta Materialia*, 51 (2003) 2685-2699.
- [104] D. Kuhlmann-Wilsdorf, N. Hansen, Geometrically necessary, incidental and subgrain boundaries, *Scripta metallurgica et materialia*, 25 (1991) 1557-1562.
- [105] H.J. McQueen, O. Knustad, N. Ryum, J.K. Solberg, Microstructural evolution in Al deformed to strains of 60 at 400°C, *Scripta Metallurgica*, 19 (1985) 73-78.
- [106] M.E. Kassner, S.R. Barrabes, New developments in geometric dynamic recrystallization, *Materials Science and Engineering: A*, 410–411 (2005) 152-155.
- [107] W. Blum, Q. Zhu, R. Merkel, H.J. McQueen, Geometric dynamic recrystallization in hot torsion of Al-5Mg-0.6Mn (AA5083), *Materials Science and Engineering: A*, 205 (1996) 23-30.
- [108] I. Balasundar, T. Raghu, B.P. Kashyap, Hot working and geometric dynamic recrystallisation behaviour of a near- $\alpha$  titanium alloy with acicular microstructure, *Materials Science and Engineering: A*, 600 (2014) 135-144.
- [109] S.J. Thompson, P.E.J. Flewitt, Recrystallisation of niobium, *Journal of the Less Common Metals*, 21 (1970) 456-458.

- [110] R. Sandström, R. Lagneborg, A model for hot working occurring by recrystallization, *Acta Metallurgica*, 23 (1975) 387-398.
- [111] R. Sandström, R. Lagneborg, A model for static recrystallization after hot deformation, *Acta Metallurgica*, 23 (1975) 481-488.
- [112] R. Sandström, R. Lagneborg, A controlling factor for dynamic recrystallisation, *Scripta Metallurgica*, 9 (1975) 59-65.
- [113] G. Gottstein, S. Deshpande, Dynamic recrystallization under changing loading conditions, *Materials Science and Engineering*, 94 (1987) 147-154.
- [114] M. Ueki, S. Horie, T. Nakamura, Factors affecting dynamic recrystallization of metals and alloys, *Materials Science and Technology*, 3 (1987) 329-337.
- [115] T. Sakai, M. Ohashi, Dislocation substructures developed during dynamic recrystallisation in polycrystalline nickel, *Materials Science and Technology*, 6 (1990) 1251-1257.
- [116] G. Gottstein, T. Lee, U. Schmidt, Deformation temperature and recrystallization, *Materials Science and Engineering: A*, 114 (1989) 21-28.
- [117] E.I. Poliak, J.J. Jonas, A one-parameter approach to determining the critical conditions for the initiation of dynamic recrystallization, *Acta Materialia*, 44 (1996) 127-136.
- [118] D. Ponge, G. Gottstein, Necklace formation during dynamic recrystallization: mechanisms and impact on flow behavior, *Acta Materialia*, 46 (1998) 69-80.
- [119] A.D. Rollett, M.J. Luton, D.J. Srolovitz, Microstructural simulation of dynamic recrystallization, *Acta Metallurgica et Materialia*, 40 (1992) 43-55.
- [120] J.J. Jonas, Dynamic recrystallization—scientific curiosity or industrial tool?, *Materials Science and Engineering: A*, 184 (1994) 155-165.
- [121] P. Peczak, M.J. Luton, A Monte Carlo study of the influence of dynamic recovery on dynamic recrystallization, *Acta Metallurgica et Materialia*, 41 (1993) 59-71.

- [122] F. Montheillet, O. Lurdos, G. Damamme, A grain scale approach for modeling steady-state discontinuous dynamic recrystallization, *Acta Materialia*, 57 (2009) 1602-1612.
- [123] S. Storm, D. Juul Jensen, Effects of clustered nucleation on recrystallization, *Scripta Materialia*, 60 (2009) 477-480.
- [124] S. Solhjo, Determination of critical strain for initiation of dynamic recrystallization, *Materials & Design*, 31 (2010) 1360-1364.
- [125] S. Solhjo, Determination of flow stress and the critical strain for the onset of dynamic recrystallization using a hyperbolic tangent function, *Materials & Design* (1980-2015), 54 (2014) 390-393.
- [126] J. Favre, D. Fabrègue, A. Chiba, Y. Bréchet, Nucleation of recrystallization in fine-grained materials: an extension of the Bailey–Hirsch criterion, *Philosophical Magazine Letters*, 93 (2013) 631-639.
- [127] X.G. Fan, H. Yang, Z.C. Sun, D.W. Zhang, Quantitative analysis of dynamic recrystallization behavior using a grain boundary evolution based kinetic model, *Materials Science and Engineering: A*, 527 (2010) 5368-5377.
- [128] E.I. Galindo-Nava, P.E.J. Rivera-Díaz-del-Castillo, Grain size evolution during discontinuous dynamic recrystallization, *Scripta Materialia*, 72–73 (2014) 1-4.
- [129] A. Momeni, G.R. Ebrahimi, M. Jahazi, P. Bocher, Microstructure evolution at the onset of discontinuous dynamic recrystallization: A physics-based model of subgrain critical size, *Journal of Alloys and Compounds*, 587 (2014) 199-210.
- [130] D.G. Cram, H.S. Zurob, Y.J.M. Brechet, C.R. Hutchinson, Modelling discontinuous dynamic recrystallization using a physically based model for nucleation, *Acta Materialia*, 57 (2009) 5218-5228.

- [131] A.M. Wusatowska-Sarnek, H. Miura, T. Sakai, Nucleation and microtexture development under dynamic recrystallization of copper, *Materials Science and Engineering: A*, 323 (2002) 177-186.
- [132] G. Gottstein, E. Brünger, M. Frommert, M. Goerdeler, M. Zeng, Prediction of the critical conditions for dynamic recrystallization in metals, *Zeitschrift für Metallkunde*, 94 (2003) 628-635.
- [133] K. Graetz, C. Miessen, G. Gottstein, Analysis of steady-state dynamic recrystallization, *Acta Materialia*, 67 (2014) 58-66.
- [134] J. Wang, H.T. Yang, X.G. Wang, H. Xiao, A new mathematical model for predicting flow stress up to the critical strain during hot deformation, *Materials & Design (1980-2015)*, 65 (2015) 637-643.
- [135] R. Ding, Z.X. Guo, Coupled quantitative simulation of microstructural evolution and plastic flow during dynamic recrystallization, *Acta Materialia*, 49 (2001) 3163-3175.
- [136] U. Andrade, M.A. Meyers, K.S. Vecchio, A.H. Chokshi, Dynamic recrystallization in high-strain, high-strain-rate plastic deformation of copper, *Acta Metallurgica et Materialia*, 42 (1994) 3183-3195.
- [137] C.W. Price, Comments on kinetic models for recrystallization, *Scripta Metallurgica*, 19 (1985) 669-673.
- [138] C.W. Price, Comments on the extent of simultaneous recovery during recrystallization and its effect on recrystallization kinetics, *Scripta Metallurgica*, 23 (1989) 1273-1276.
- [139] H.P. Stüwe, A.F. Padilha, F. Siciliano, Competition between recovery and recrystallization, *Materials Science and Engineering: A*, 333 (2002) 361-367.
- [140] S.H. Zahiri, C.H.J. Davies, P.D. Hodgson, A mechanical approach to quantify dynamic recrystallization in polycrystalline metals, *Scripta Materialia*, 52 (2005) 299-304.

- [141] R.B. Godiksen, S. Schmidt, D.J. Jensen, Effects of distributions of growth rates on recrystallization kinetics and microstructure, *Scripta Materialia*, 57 (2007) 345-348.
- [142] R. Kapoor, S. Nemat-Nasser, Determination of temperature rise during high strain rate deformation, *Mechanics of Materials*, 27 (1998) 1-12.
- [143] F. Guiu, P.L. Pratt, Stress Relaxation and the Plastic Deformation of Solids, *physica status solidi (b)*, 6 (1964) 111-120.
- [144] A. Seeger, J. Diehl, S. Mader, H. Rebstock, Work-hardening and work-softening of face-centred cubic metal crystals, *Philosophical Magazine*, 2 (1957) 323-350.
- [145] J. Martin, B.L. Piccolo, T. Kruml, J. Bonneville, Characterization of thermally activated dislocation mechanisms using transient tests, *Materials Science and Engineering: A*, 322 (2002) 118-125.
- [146] S. Sharma, V. Chavan, R. Agrawal, R. Patel, R. Kapoor, J. Chakravartty, Split-Hopkinson Pressure Bar: An Experimental Technique for High Strain Rate Tests, BARC, E/013 (2011).
- [147] R.E. Reed-hill, M.J. Kaufman, On evaluating the flow stress in niobium of commercial purity, *Acta Metallurgica et Materialia*, 43 (1995) 1731-1739.
- [148] R.E. Reed-Hill, S.C. Park, L.P. Beckerman, Application of a model for strain aging under stress to niobium, *Acta Metallurgica*, 31 (1983) 1715-1720.
- [149] A. Sarkar, J.K. Chakravartty, B. Paul, A.K. Suri, Kinetics of dynamic recrystallization in cobalt: A study using the Avrami relation, *physica status solidi (a)*, 208 (2011) 814-818.
- [150] A. Sarkar, A. Marchattiwari, J.K. Chakravartty, B.P. Kashyap, Kinetics of dynamic recrystallization in Ti-modified 15Cr-15Ni-2Mo austenitic stainless steel, *Journal of Nuclear Materials*, 432 (2013) 9-15.
- [151] T. Sakai, M.G. Akben, J.J. Jonas, Dynamic recrystallization during the transient deformation of a vanadium microalloyed steel, *Acta Metallurgica*, 31 (1983) 631-641.

- [152] X.M. Chen, Y.C. Lin, D.X. Wen, J.L. Zhang, M. He, Dynamic recrystallization behavior of a typical nickel-based superalloy during hot deformation, *Materials & Design*, 57 (2014) 568-577.
- [153] C.M. Sellars, W.J. McTegart, On the mechanism of hot deformation, *Acta Metallurgica*, 14 (1966) 1136-1138.
- [154] E.W. Hart, Theory of the tensile test, *Acta Metallurgica*, 15 (1967) 351-355.
- [155] J.D. Campbell, Plastic instability in rate-dependent materials, *Journal of the Mechanics and Physics of Solids*, 15 (1967) 359-370.
- [156] J.J. Jonas, R.A. Holt, C.E. Coleman, Plastic stability in tension and compression, *Acta Metallurgica*, 24 (1976) 911-918.
- [157] C.M. Sellars, W.J.M. Tegart, Relationship between strength and structure in deformation at elevated temperatures, *Mem. Science Review Met.*, 63 (1966) 731-745.
- [158] A.N. Behera, R. Kapoor, A. Sarkar, J.K. Chakravarty, Hot deformation behaviour of niobium in temperature range 700-1500 °C, *Materials Science and Technology (United Kingdom)*, 30 (2014) 637-644.
- [159] G. Glover, C.M. Sellars, Recovery and recrystallization during high temperature deformation of alpha iron, *Metall. Trans.*, 4 (1973) 765-775.
- [160] Q. Wei, S. Cheng, K.T. Ramesh, E. Ma, Effect of nanocrystalline and ultrafine grain sizes on the strain rate sensitivity and activation volume: fcc versus bcc metals, *Materials Science and Engineering A*, 381 (2004) 71-79.
- [161] H. Sun, Y. Sun, R. Zhang, M. Wang, R. Tang, Z. Zhou, Hot deformation behavior and microstructural evolution of a modified 310 austenitic steel, *Materials & Design*, 64 (2014) 374-380.

- [162] Y.C. Lin, D.G. He, M.S. Chen, X.M. Chen, C.Y. Zhao, X. Ma, Z.L. Long, EBSD analysis of evolution of dynamic recrystallization grains and  $\delta$  phase in a nickel-based superalloy during hot compressive deformation, *Materials & Design*, 97 (2016) 13-24.
- [163] A.K. Koul, G.H. Gessinger, On the mechanism of serrated grain boundary formation in Ni-based superalloys, *Acta Metallurgica*, 31 (1983) 1061-1069.
- [164] Y.C. Lin, X.Y. Wu, X.M. Chen, J. Chen, D.X. Wen, J.L. Zhang, L.T. Li, EBSD study of a hot deformed nickel-based superalloy, *Journal of Alloys and Compounds*, 640 (2015) 101-113.
- [165] J.J. Jonas, X. Quelellenc, L. Jiang, É. Martin, The Avrami kinetics of dynamic recrystallization, *Acta Materialia*, 57 (2009) 2748-2756.
- [166] H. Mecking, U.F. Kocks, Kinetics of flow and strain-hardening, *Acta Metallurgica*, 29 (1981) 1865-1875.
- [167] P. Spätig, J. Bonneville, J.L. Martin, A new method for activation volume measurements: application to Ni<sub>3</sub> (Al, Hf), *Materials Science and Engineering: A*, 167 (1993) 73-79.
- [168] P. Rodriguez, Grain size dependence of the activation parameters for plastic deformation: influence of crystal structure, slip system, and rate-controlling dislocation mechanism, *Metallurgical and Materials Transactions A*, 35 (2004) 2697-2705.
- [169] D. Caillard, J.L. Martin, *Thermally activated mechanisms in crystal plasticity*, Elsevier, 2003.
- [170] H. Conrad, Thermally activated deformation of metals, *JOM*, 16 (1964) 582-588.
- [171] M. Biberger, M.J. Davidson, A.K. Mukherjee, Stress reduction tests on Nb-1wt.%Zr at 1300 K, *Materials Science and Engineering: A*, 159 (1992) 181-185.

